IJOER
RESEARCH JOURNAL

ISSN
2395-6992

International Journal of Engineering Research & Science

www.ijoer.com
www.adpublications.org

Volume-3! Issue-7 ! July, 2017 www.ijoer.com ! info@ijoer.com

Preface

We would like to present, with great pleasure, the inaugural volume-3, Issue-7, July 2017, of a scholarly journal, *International Journal of Engineering Research & Science*. This journal is part of the AD Publications series *in the field of Engineering, Mathematics, Physics, Chemistry and science Research Development*, and is devoted to the gamut of Engineering and Science issues, from theoretical aspects to application-dependent studies and the validation of emerging technologies.

This journal was envisioned and founded to represent the growing needs of Engineering and Science as an emerging and increasingly vital field, now widely recognized as an integral part of scientific and technical investigations. Its mission is to become a voice of the Engineering and Science community, addressing researchers and practitioners in below areas

Chemical Engineering	
Biomolecular Engineering	Materials Engineering
Molecular Engineering	Process Engineering
Corrosion Engineering	
Civil Engineering	
Environmental Engineering	Geotechnical Engineering
Structural Engineering	Mining Engineering
Transport Engineering	Water resources Engineering
Electrical Engineering	
Power System Engineering	Optical Engineering
Mechanical Engineering	
Acoustical Engineering	Manufacturing Engineering
Optomechanical Engineering	Thermal Engineering
Power plant Engineering	Energy Engineering
Sports Engineering	Vehicle Engineering
Software Engineering	
Computer-aided Engineering	Cryptographic Engineering
Teletraffic Engineering	Web Engineering
System Engineering	
Mathematics	
Arithmetic	Algebra
Number theory	Field theory and polynomials
Analysis	Combinatorics
Geometry and topology	Topology
Probability and Statistics	Computational Science
Physical Science	Operational Research
Physics	
Nuclear and particle physics	Atomic, molecular, and optical physics
Condensed matter physics	Astrophysics
Applied Physics	Modern physics
Philosophy	Core theories

Chemistry	
Analytical chemistry	Biochemistry
Inorganic chemistry	Materials chemistry
Neurochemistry	Nuclear chemistry
Organic chemistry	Physical chemistry
Other Engineering Areas	
Aerospace Engineering	Agricultural Engineering
Applied Engineering	Biomedical Engineering
Biological Engineering	Building services Engineering
Energy Engineering	Railway Engineering
Industrial Engineering	Mechatronics Engineering
Management Engineering	Military Engineering
Petroleum Engineering	Nuclear Engineering
Textile Engineering	Nano Engineering
Algorithm and Computational Complexity	Artificial Intelligence
Electronics & Communication Engineering	Image Processing
Information Retrieval	Low Power VLSI Design
Neural Networks	Plastic Engineering

Each article in this issue provides an example of a concrete industrial application or a case study of the presented methodology to amplify the impact of the contribution. We are very thankful to everybody within that community who supported the idea of creating a new Research with IJOER. We are certain that this issue will be followed by many others, reporting new developments in the Engineering and Science field. This issue would not have been possible without the great support of the Reviewer, Editorial Board members and also with our Advisory Board Members, and we would like to express our sincere thanks to all of them. We would also like to express our gratitude to the editorial staff of AD Publications, who supported us at every stage of the project. It is our hope that this fine collection of articles will be a valuable resource for *IJOER* readers and will stimulate further research into the vibrant area of Engineering and Science Research.

Mukesh Arora

(Chief Editor)

Board Members

Dr. S.R.Boselin Prabhu

Ph.D, Wireless Sensor Networks, M.E. Network Engineering, Excellent Professional Achievement Award Winner from Society of Professional Engineers Biography Included in Marquis Who's Who in the World (Academic Year 2015 and 2016). Currently Serving as Assistant Professor in the department of ECE in SVS College of Engineering, Coimbatore.

Dr. Maheshwar Shrestha

Postdoctoral Research Fellow in DEPT. OF ELE ENGG & COMP SCI, SDSU, Brookings, SD Ph.D, M.Sc. in Electrical Engineering from SOUTH DAKOTA STATE UNIVERSITY, Brookings, SD.

Zairi Ismael Rizman

Senior Lecturer, Faculty of Electrical Engineering, Universiti Teknologi MARA (UiTM) (Terengganu) Malaysia Master (Science) in Microelectronics (2005), Universiti Kebangsaan Malaysia (UKM), Malaysia. Bachelor (Hons.) and Diploma in Electrical Engineering (Communication) (2002), UiTM Shah Alam, Malaysia

Dr. D. Amaranatha Reddy

Ph.D.(Postdocteral Fellow,Pusan National University, South Korea), M.Sc., B.Sc. : Physics.

Dr. Dibya Prakash Rai

Post Doctoral Fellow (PDF), M.Sc.,B.Sc., Working as Assistant Professor in Department of Physics in Pachhuncga University College, Mizoram, India.

Dr. Pankaj Kumar Pal

Ph.D R/S, ECE Deptt., IIT-Roorkee.

Dr. P. Thangam

BE(Computer Hardware & Software), ME(CSE), PhD in Information & Communication Engineering, currently serving as Associate Professor in the Department of Computer Science and Engineering of Coimbatore Institute of Engineering and Technology.

Dr. Pradeep K. Sharma

PhD., M.Phil, M.Sc, B.Sc, in Physics, MBA in System Management, Presently working as Provost and Associate Professor & Head of Department for Physics in University of Engineering & Management, Jaipur.

Dr. R. Devi Priya

Ph.D (CSE),Anna University Chennai in 2013, M.E, B.E (CSE) from Kongu Engineering College, currently working in the Department of Computer Science and Engineering in Kongu Engineering College, Tamil Nadu, India.

Dr. Sandeep

Post-doctoral fellow, Principal Investigator, Young Scientist Scheme Project (DST-SERB), Department of Physics, Mizoram University, Aizawl Mizoram, India- 796001.

Mr. Abilash

MTech in VLSI, BTech in Electronics & Telecommunication engineering through A.M.I.E.T.E from Central Electronics Engineering Research Institute (C.E.E.R.I) Pilani, Industrial Electronics from ATI-EPI Hyderabad, IEEE course in Mechatronics, CSHAM from Birla Institute Of Professional Studies.

Mr. Varun Shukla

M.Tech in ECE from RGPV (Awarded with silver Medal By President of India), Assistant Professor, Dept. of ECE, PSIT, Kanpur.

Mr. Shrikant Harle

Presently working as a Assistant Professor in Civil Engineering field of Prof. Ram Meghe College of Engineering and Management, Amravati. He was Senior Design Engineer (Larsen & Toubro Limited, India).

Table of Contents

Optimal Well Locations using Genetic Algorithm for Tushki Project, Western Desert, Egypt

S. Khalaf[1], M.I. Gad[2]

[1]Irrigation and Hydraulics Dept., Faculty of Engineering, Mansoura University, Egypt.
[2]Prof. Dr., Hydrology Division, Desert Research Center, Cairo, Egypt

Abstract— *The well location problem is challenging due to the non-linear, discrete and often multi-modal objective function. The optimal distribution of productive well locations mitigates the groundwater productivity problem that threats the national projects in arid countries like Egypt. In this paper, a trial to mitigate this problem in Tushki National Project, south western desert, Egypt is supposed via delineating the optimal well locations and optimal pumping rates. The methodology of combination between simulation and optimization techniques is applied. The simulation outputs of groundwater flow system by Visual MODFLOW model is linked by the constructed Fortran Code for Optimal well Location using Genetic Algorithm (OLGA Code) for obtaining the optimum management of groundwater resources in this project. Two management cases are considered by running the model domain with adopted steady and transit calibrated parameters. The first management case deals with the present well locations and predicts the optimal value of the objective function (maximum pumping rate). In the second case, the optimal new well locations resulted from the OLGA Code is predicted from flexible well location with the moving well option. Also, the prediction of the future changes in both head and flow are studied in steady and transient states.*

Keywords— Groundwater, Optimization, Genetic Algorithm, Tushki project.

I. INTRODUCTION

Selecting optimal well sites is a valuable problem to solve; maximizing groundwater recovery increases oil reserves and minimizing costs improves profitability. One of the best methods of selecting optimal sites is the combined use of simulation and optimization (S/O) models. While simulation models basically provide solutions of the governing equations of groundwater flow, optimization models identify an optimal management and planning strategy from a set of feasible alternative strategies. The genetic algorithm (GA) is widely used to modify the parameters of groundwater flow models (Yan et al., 2003; Yao et al., 2003) and to solve the management models of groundwater resources (Mckinney and Lin, 1994; Liu et al., 2002; Zhu et al., 2003). Rana et al, (2008) conducted a study on a spatio-temporal optimization of agricultural drainage, using groundwater model and GA. Guan et al. (2008) proposed an improved genetic algorithm (IGA) to solve optimization problems with equality and inequality constraints. Hamid et al. (2009) presented a paper focusing on the S/O for conjunctive use of surface water and groundwater on a basin-wide scale, the Najafabad plain in west-central Iran. Gad et al., (2011), and Moharram et al., (2012) used an optimization model based on the combination of MODFLOW simulation with GA to maximize the total pumping rate from the Nubian sandstone aquifer in El-Dakhla and El-Farafra depressions, Egypt. Saafan et al., (2011) applied multi-objective genetic algorithm (MOGA) Code in El-Farafra depression, Egypt to study the maximum pumping rate and minimum operation cost. Gad and Khalaf, (2013) used MOGA model to develop the maximum pumping rate and minimum operation cost in the Miocene aquifer of Wadi El-Farigh, West Delta, Egypt.

In the other side, there are limited studies for the determination of optimal operating strategy, including unknown well locations and pumping rates, for groundwater systems to the best of our knowledge (Wang and Ahlfeld, 1994, Karahan and Ayvaz, 2005, and Ayvaz and Karahan, 2008). Saffi and Cheddadi (2007) developed an algebraic expression which gave the matrix of transient influence coefficients for one-dimensional semi-confined aquifer model and solved the governing equation by using a mixed compartment model. Tung and Chou (2004) integrated pattern classification and tabu search to optimize the average zonal groundwater pumping for an aquifer. As a general, the research conducted in this field dealt with the identification of locations and released histories of unknown groundwater pollution sources (Mahar and Datta, 2000, 2001; Aral et al., 2001; Ruperti, 2002; Singh et al., 2004; Sun et al., 2006), pumping well optimization for optimum remediation design (Wang and Ahlfeld, 1994; Huang and Mayer, 1997; Guan and Aral, 1999; Zheng and Wang, 1999; Mantoglou and Kourakos, 2007; Chang et al., 2007), and optimum well locations and pumping rates in the coastal sides (Park and Aral, 2004; Ferreira da Silva and Haie, 2007). Meira, et al. (2016) proposed technique for decision-making process in optimal well location including a step of risk analysis associated with the uncertainties present in the variables of the

problem. The proposed technique was applied to two benchmark cases and the results, evaluated by experts in the field, indicated that the obtained solutions were richer than those identified by previously adopted manual approaches.

Due to the few of scientific researches related to optimal well locations especially in our national governmental and invest mental agricultural projects, a trial was carried out in this paper to through a light on the optimal location for new fourteen production wells in Tushki project required for irrigation of 25 thousand acres which will drill under the strategy of reclamation of 1.5 million acres project.

II. DESCRIPTION OF CASE STUDY

2.1 Site description

Tushki area, is a part of the Western Desert of Egypt; between latitudes 22° 14' 24.75" and 22° 50' 6.10" N and longitudes 31° 0' 44.06"and 31° 50' 4.05E, with total area of 2268 km^2. Tushki project, one of the national governmental and invest mental agricultural projects, aims to reclaim 540,000 acres using both surface water from El-Sheikh Zaid artificial canal (1.5 km^3/year) and groundwater extracted from about 316 productive wells for cultivating 36000 acres. Moreover, the agricultural development in the north and south of Abu-Simbel area, which depends only on the groundwater resource, will extract 22.5 million m^3/year from the present 75 productive wells (Figure 1). This operation policy is expected to have its side effect on groundwater regime of **N**ubia **S**andstone **A**quifer in **A**bu-**S**imbel **A**rea (**NSAASA**) due to the absence of optimal well locations which will be the fulcrum of this research.

2.2 Geomorphological and geological settings

Referring to the geomorphological studies prepared by El-Shazly, et al., (1980), CONOCO, (1987), and Aggour et al., (2012), five geomorphologic units are distinguished in the study area. Nasser lake, the Nile valley, Wadi Kurkur pediplain, Tushki depression and West Dungul plain. Wadi Kurkur pediplain represents most parts of the area. The pediplain surface is covered mainly by nearly horizontal beds of Nubia sandstone, with outcrops of igneous and metamorphic rocks as well as several volcanic exposures. Tushki depression area is an elongated featureless smooth plain bounded by the topographic contour line of 200m above sea level and is generally representing a topographic depression with an average absolute elevation of less than 200m. It is bounded from the north and east by limestone plateau and from the south and the west by sandy pediplain and peneplain respectively.

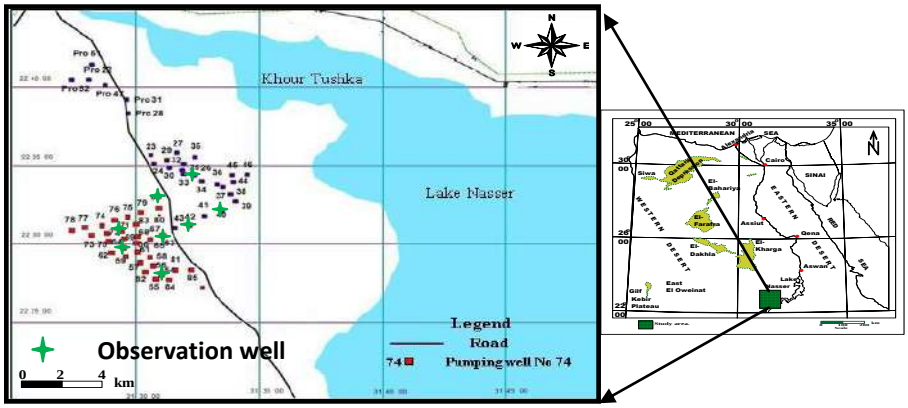

FIGURE1. LOCATION MAP OF ABU SIMBEL AREA SHOWING THE LOCATION OF 75 PRODUCTIVE WELLS AND 9 OBSERVATION WELLS

Geologically, the main geological units in Tushki area are the Precambrian Basement rocks and sedimentary succession. The basement rocks constitute some of the conspicuous ridges and high peaks in the area such as G. Umm Shaghir (318 m asl). The lithostratigraphic sedimentary succession is dominated by Cretaceous, Oligocene and Quaternary sediments (Figure 2). The Lower Cretaceous rocks are differentiated into the Abu Simbel, Lake Nasser and Sabaya formations. The Abu Simbel Formation covers vast parts south of Khour Tushki with thickness ranges from 30m to 87.45m (Aggour et al., 2012). The Lake Nasser Formation is underlain by the Abu Simbel Formation and overlain by the Sabaya Formation. In addition, the Upper Cretaceous rocks are represented by Kiseiba Formation with 150m thick. The Oligocene basalt rocks are widespread near the head of Khour Tushki. Moreover, the Quaternary deposits are represented by sand accumulations and Alluvial sediments. As a general, various structural elements are present, among which are the uplift of the basement (Nakhlai-Aswan uplift trending NE-SW with 300 km long), E-W faults (north of Khour Tushki) and NW-SE faults (south of Khour Tushki),

E-W and NE-SW folds, the Ring forms and the structural lineation. The fault systems play an important role in recharging the NSAASA from Lake Nasser especially the NW-SE. They act as conduits and help in transmitting the groundwater within the NSAASA supporting the hydraulic connection between the aquifer units (Aggour et al., 2012).

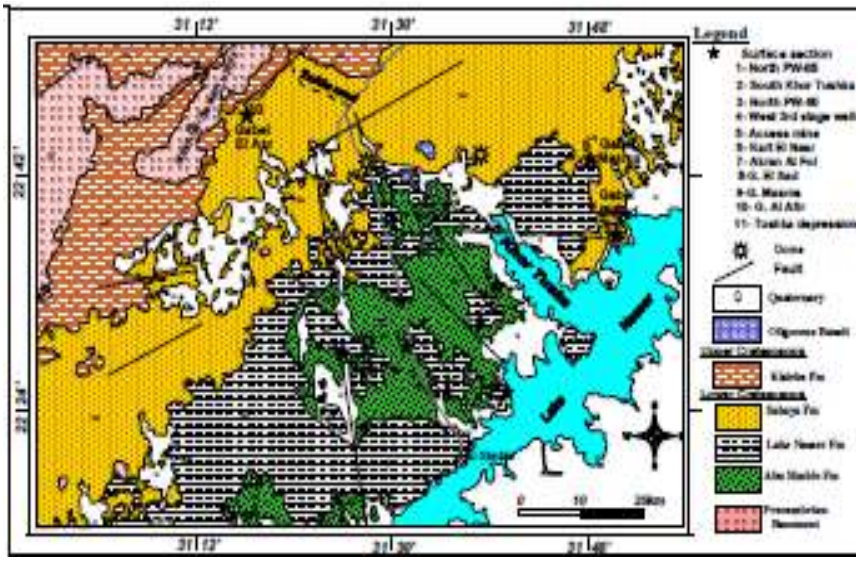

FIGURE 2: GEOLOGICAL MAP OF THE STUDY AREA (AFTER

2.3 Hydrogeological aspects

The **NSAASA** is mainly composed of three successive water-bearing units, namely; the Gilf, Abu Simbel and Lake Nasser. The middle unit is an aquiclude that extends under the lake and the lower unit overlying the granitic basement is a confined aquifer of fluvial sandstones (Figure 3). The groundwater of **NSAASA** exists under unconfined to semi-confined conditions. The **NSAASA** maximum thickness reaches 400 m and decreases towards north and NW. The transmissivity of the **NSAASA** ranges between **389** and **1322** m^2/day (Table 2), and increases from SW to NE. The constructed equipotential contour maps (Figure 4) show that the local recharge of the NSAASA depends upon the leakage from the Lake Nasser due west direction. The estimated groundwater flow rate based on these contour maps (Figure 4) reaches 0.054 m/day near Nasser Lake and decreases to 0.044 m/day towards northwestern parts.

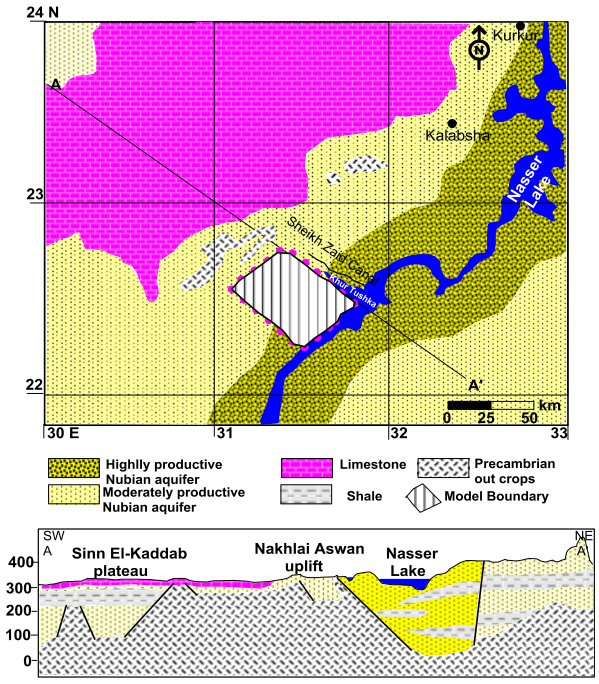

FIGURE 3: NSAASA POTENTIALITY MAP AND SW-NE CROSS-SECTION SHOWING AQUIFER THICKNESS

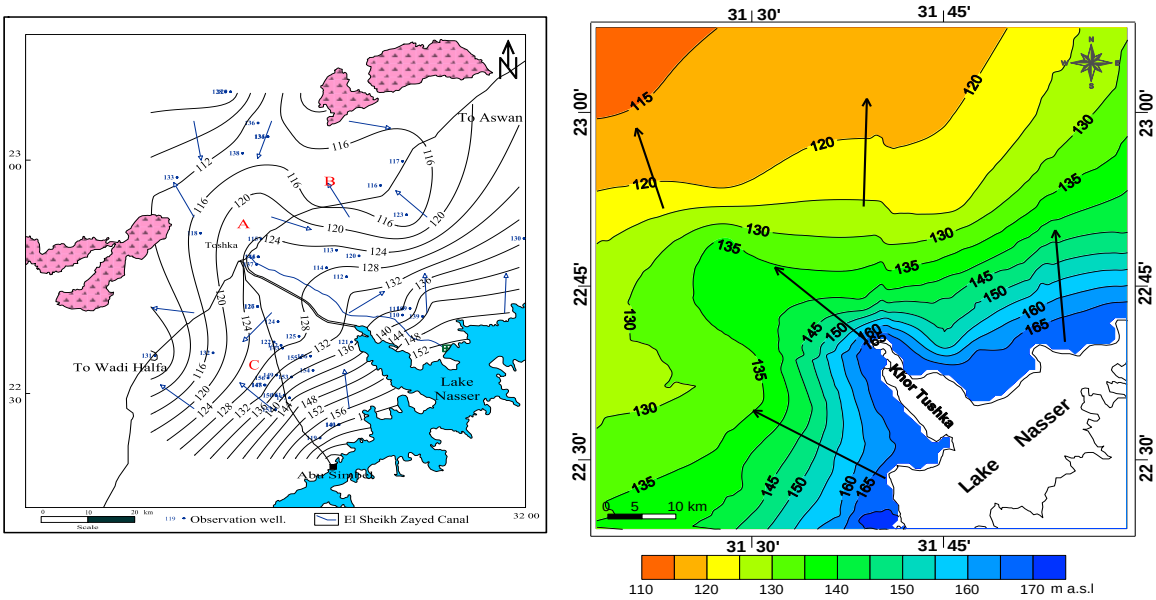

FIGURE 4: THE GROUNDWATER EQUIPOTENTIAL MAPS OF NSAASA DURING 2008 (LEFT MAP AFTER EL-SABRI ET. AL., 2010) AND DURING 2010 (RIGHT MAP-AFTER AGGOUR ET. AL., 2012)

III. MATERIALS AND METHODS

3.1 Field trip and data collection

The materials used in this paper are collected through carrying out four field trips in Abu Simbel area during the period 2010-12. The basic hydraulic parameters of NSAASA are estimated based on carrying out one step test and 13 long duration pumping tests (Tables 1 and 2). The different hydrologic data are obtained during the field trips. These materials also include collection of archival data (well drilling reports, WRRI 2002), registration of discharge, distribution of wells, proposed operating systems for both groundwater supply and reclaimed area beside recording depth to water for groundwater level changes.

TABLE 1
RESULTS OF STEP DRAWDOWN TEST ANALYSIS IN NSAASA

Step No	Step time Duration (hour)	Well discharge Q (m^3/day)	Total DD (s) (m)	s/ Q (day/m^2)
I	1.5	1080	8.32	0.008666667
II	1.5	1200	11.8	0.009833333
III	1.5	1368	13.38	0.009291667
IV	1.5	1488	15.82	0.01063172

TABLE 2
RESULTS OF LONG DURATION PUMPING TESTS ANALYSIS IN NSAASA

Well No	Pumping rate (m^3/h)	Depth to water (m)	Total DD (m)	Screen (m)	Hydraulic parameters		
					K (regional) (m/day)	K (local) (m/day)	T (m^2/day)
W27	105	79.4	5.67	80.5	6.88	12.45	1003
W30	120	76.79	7.89	80.5	4.9	9.09	732
W38	173	60.88	11.81	80.5	4.94	10.07	812
W40	120	62.59	10.01	80.5	9.21	16.42	1322
W43	112	71.26	-	80.5	-	-	878
W45	160	55.6	16.28	80.5	5.19	10.41	839
W50	172	30.64	17.53	74.75	2.19	5.64	422
W55	123	58.6	24.87	57.5	-	9.28	534
W 57	110	63.15	20.84	57.5	-	8.06	464
W 60	100	74.07	13.17	135	-	7.11	389
W75	107	72.7	14.5	57.5	-	10.01	576
W80	110	68.8	11.25	57.5	-	-	912
W85	130	58.2	-	57.5	-	-	340

The methodological approach used in this paper is based on the mathematical modeling techniques which combines between simulation and optimization model. A computer programming with FORTRAN language has been originally established to apply the principles of the genetic algorithm for studying the optimal location of the groundwater productive wells as a principal tool for groundwater resources management. The Optimal well Location applying Genetic Algorithm (OLGA Code) links MODFLOW with genetic algorithm technique to establish a simulation optimization groundwater model.

3.2 Simulation technique

Groundwater flow simulation is carried out applying MODFLOW software. It describes groundwater flow of constant density under non-equilibrium conditions in three-dimensional heterogeneous and anisotropic medium according to the following equation (Bear, 1979):

$$\frac{\partial}{\partial x}\left(K_{XX}\frac{\partial h}{\partial x}\right)+\frac{\partial}{\partial y}\left(K_{YY}\frac{\partial h}{\partial y}\right)+\frac{\partial}{\partial Z}\left(K_{ZZ}\frac{\partial h}{\partial Z}\right)-W=S_s\frac{\partial h}{\partial t} \quad (1)$$

in which;

K_{xx}, K_{yy} and K_{zz} are values of hydraulic conductivity ($L\,T^{-1}$); along the x, y, and z coordinate axes; h is the potentiometric head (L); W is the volumetric flux per unit volume and represents sources and/or sinks of water (T^{-1}); S_s is the specific storage of the porous material (L^{-1}); and t is time (T).

3.2.1 Conceptual Model

The conceptual model of the NSAASA is based on the geology of the study area which is comprised of Nubian sandstone sediments. The hydrogeologic system is concerned two hydraulically connected through fault planes layers. The top hydrostratigraphic unit (Gilf Formation) is considered to be a sandy unconfined aquifer zone up to 95 meters maximum thick. The second confined aquifer zone of fluvial sandstones is separated from the sandy unconfined aquifer zone by aquiclude, and had maximum thickness of 79 meters. The scattered new communities around the asphaltic road in the N-S direction of the Abu Simbel area are primarily planned for agriculture.

3.2.2 Model domain

The model domain of NSAASA is selected to cover 3315 km^2 (51x65 Km-Figure 3). It is discretized using 130 rows × 102 columns rectangular cells. This discrimination produces 13260 cells in the model layer. The width of the cells along rows (in x-direction) is 500m and along columns (in y-direction) is 500 m. The grid geometry is shown in (Figure 5).

3.2.3 Boundary conditions

The hydraulic conditions at the boundaries of the model domain are specified (Figure 5). Based on the groundwater flow pattern of the NSAASA (Figure 4) and the field measurements of the groundwater head in the present productive wells (Table 2), the initial and boundary conditions of the local model is defined. The lower boundary (water body of Lake Nasser) is considered a time-constant head at level of 175 m asl (DRC 2012). The equipotential contour line of 130m asl characterizing to the upper boundary (Figure 5) is far enough from the well fields to be genral head boundary condition. The left and right boundaries are assumed to be no flow boundaries due to the regional flow direction from SE to the NW.

The impermeable Basement rock is assumed to be the bottom boundary of the model domain with no flow and maximum depth 236.45m (Table 3 and Figure 6). The hydraulic heads and hydraulic conductance are assigned to boundary cells. These heads vary during the simulation process according to different stresses applied on the modeled area.

3.2.4 Aquifer properties

The aquifer material properties of the NSAASA include the transmissivity, the storage coefficient and the hydraulic conductivity. The transmissivity ranges from 389 and 1322 m^2/day (Table 2) and the storage coefficient from $1.2x10^{-4}$ to $5x10^{-4}$ (El-Sabri et. Al., 2010). Vertical heterogeneity is assumed adequate to allow treatment as multi layered aquifer. The vertical hydraulic conductivity, estimated from the aquifer thickness (Figure 6-left) and aquifer transmissivity values, is varied from 5.64 to 16.42 m/day. Furthermore, the availability of a relatively complete database of 75 groundwater drilled wells and 9 observation wells in the NSAASA help in constructing the present model. In addition, the initial piezometric heads are computed from the absolute ground elevation values of the model domain extracted from the Digital Elevation Model (DEM) of the study area (Figure 6-right).

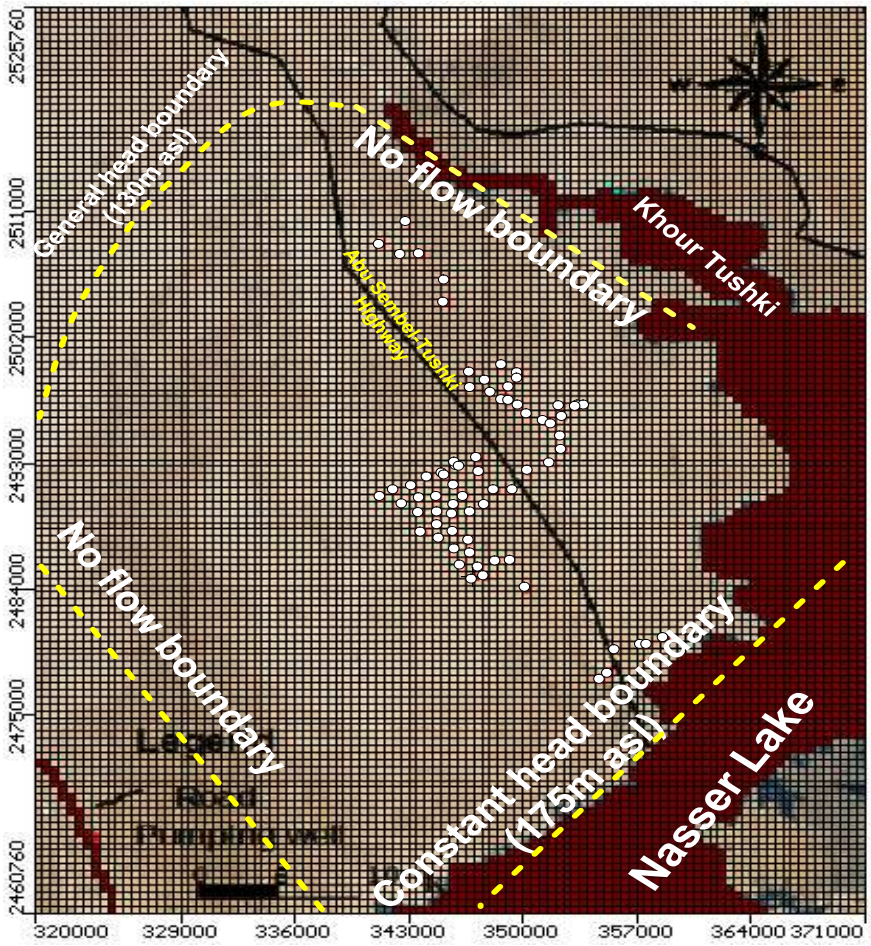

FIGURE 5. FLOW MODEL DOMAIN GRID AND THE BOUNDARY CONDITIONS OF THE NSAASA

TABLE 3
UPPER SURFACE OF BASEMENT ROCK (AMSL) IN ABU SIMBEL AREA

Well name	Ground elevation (m)	Basement level (m)	Well name	Ground elev. (m)	Basement level (m)
Akaria well	185.07	-34	O.B No11	85	-236.45
Well No 4	193.57	-176	O.B No 3	225	+107
Well No 5	204.72	-176	O.B No 3	225	0.0
Well No 13	194.05	+10	O.B No 6"	201	-129
Well No 21	195	-4	O.B No 7	165	-86
KADCO No 1	230	-2	O.B No 8	215	-9
KADCO No 2	233	+8	O.B No 10"	165	+75
KADCO No 3	233	+15	O.B No 18	190	-42
El Masria well	164	+92	O.B No 18"	190	-116
Akaria well 2	198.06	-124	O.B No 19	193	0.0
O.B No 4	193.05	-168	O.B No 20	165	+51
O.B No 10	186.07	-45	O.B No 25	183	-41

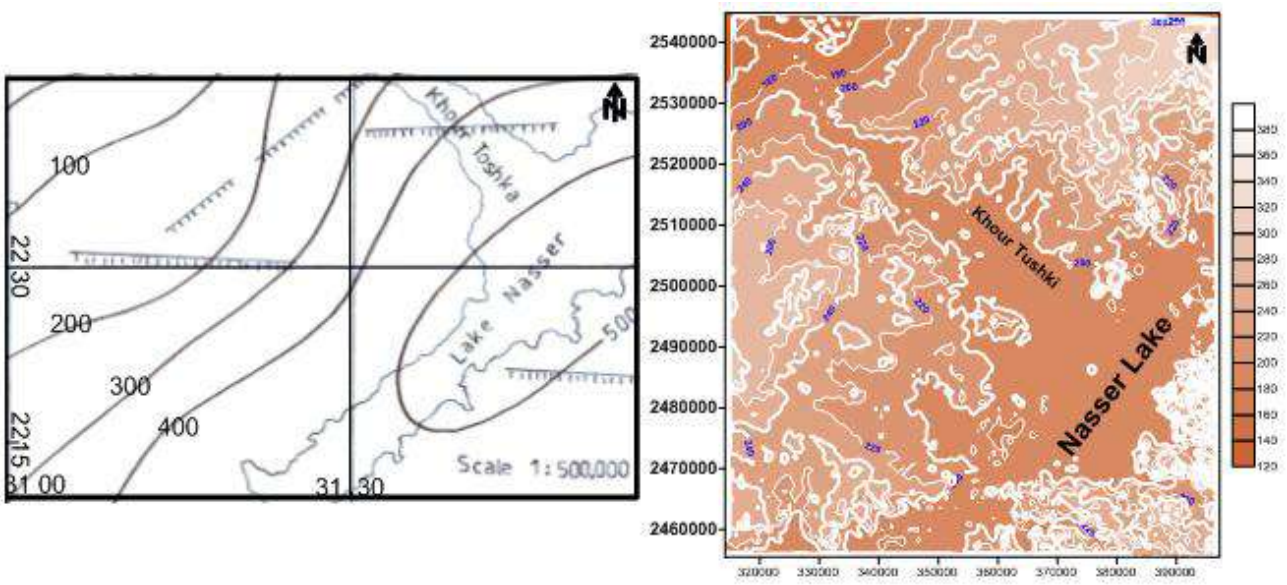

FIGURE 6: AQUIFER THICKNESS CONTOUR MAP (LEFT MAP) AND GROUND ELEVATION EXTRACTED FROM DEM (RIGHT MAP)

3.2.5 Model calibration

Calibration involves modification of the parameters, and forcing functions in the model in such a way as to assure that the model reproduced observed-head values (Hill, 1998 & 2000). The calibration process typically involves calibrating to steady-state and unsteady state conditions. The performed steady state calibration permits the adjustment of the hydraulic conductivity, where NSAASA storage changes are not significant. The relation between the calculated and observed heads is checked from the calculated-observed head curve and the variance appears as 45.966 % (Figure 8). This large value indicates great difference between the heads calculated by the model and actual measured heads. After many times of changing the k values, the variance between the observed and calculated heads is minimized to 3.61 % and the calculated head values is very closely related to the field-measured head values (Figure 7). Based on the calibrated model, the estimated hydraulic conductivity values are ranging from 4.33 to 7.60 m/day. These values are generally more slightly than the values calculated from the field data. The difference may relate to the benchmarks, uncertainty and grid refinement.

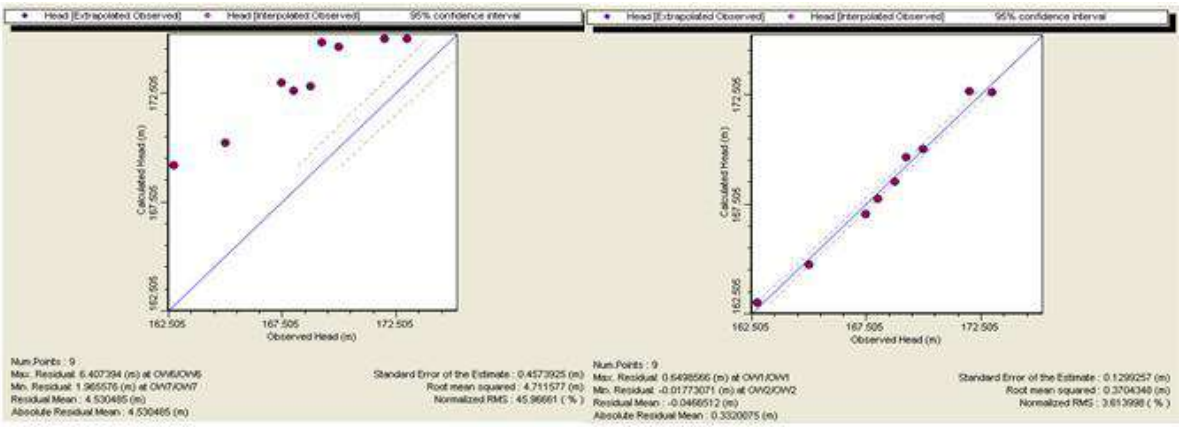

FIGURE 7: THE CALCULATED AND OBSERVED HEADS OF THE MODEL DOMAIN OF NSAASA FOR STEADY STATE

Transient state, specific yield values are modified on a trial and errors basis, until a good match between the observed heads in the years 2002 and 2012 (sited in Kim and Sultan, 2002 and Aggour et. Al., 2012) and the calculated heads are achieved. The range of the resulted specific yield after the final calibration of the transient state is found to be varying from 0.14 to 0.34 (Fig. 8). It can be seen that, in general, there is a good agreement between the observed and simulated head values.

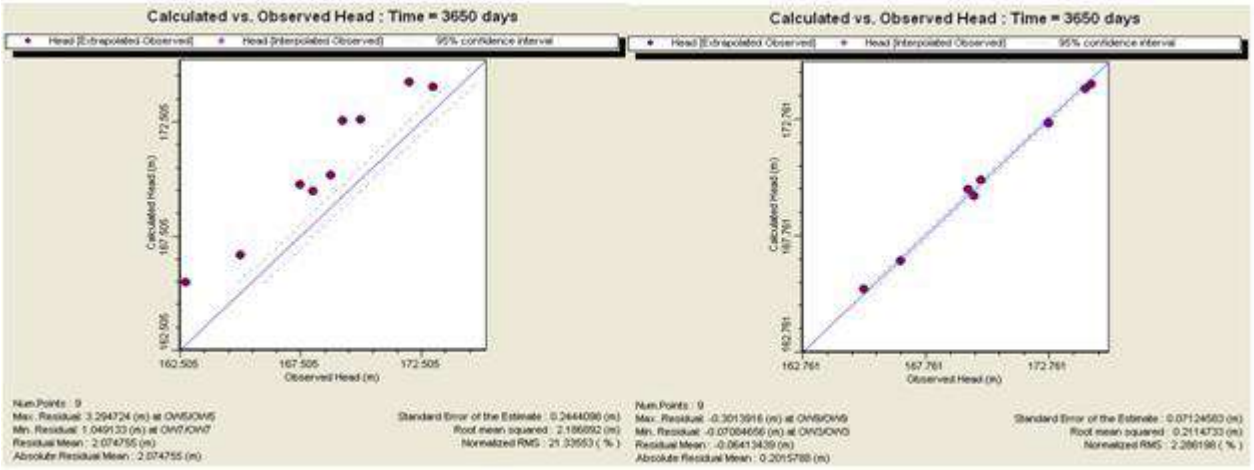

FIG. 8: THE CALCULATED AND OBSERVED HEADS OF THE MODEL DOMAIN OF NSAASA FOR UNSTEADY STATE

3.3 Optimization Technique

Genetic Algorithms (GA) are adaptive heuristic search algorithm premised on the evolutionary ideas of natural selection and genetic. The basic concept of GA is designed to simulate processes in natural system necessary for evolution. A solution for a given problem is represented in the form of a string, called "chromosome", consisting of a set of elements, called "genes", that hold a set of values for the optimization variables (the decision variables). The fitness of each chromosome is determined by evaluating it against an objective function. The chromosome represents a feasible solution for the problem under study. The length of the chromosome equals the number of variables. A Gene value is real coding (actual values). The concept of GA is based on the initial selection of a relatively small population. Each individual in the population represents a possible solution in the parameter space. The fitness of each individual is determined by the value of the objective function, calculated from a set of parameters. The natural evolutional processes of reproduction, selection, crossover, and mutation are applied using probability rules to evolve the new and better generations. The probabilistic rules allow some less fit individuals to survive. The objective of this study is to maximize the benefit function Z with respect to pumping rate to obtain optimal location of wells, Q_j as design variable, where:

$$\text{Max} \qquad Z = \sum_{j=1}^{N_w} Q_j - P_j \tag{2}$$

in which:, N_w is the total number of pumping wells and P_j is penalty.

Moreover, the management objectives must be achieved within a set of constraints. The constraints may be decision variables. The objective function is subjected to the following constrains:

3.3.1 Objective function constraints

3.3.1.1 Pumping constraint

The pumping rates at potential pumping wells in the water demand are constrained to values between some minimum (Q_j^{min}) and maximum (Q_j^{max}) permissible pumping rates as the following:

$$Q_j^{min} \le Q_j \le Q_j^{max} \quad j = \ldots\ldots,N_w \tag{3}$$

In the GA simulation, this constraint can be easily satisfied by restricting the population space of the design variables to be within the proposed limits. Hence, no special treatment is needed for this constraint.

3.3.1.2 Drawdown constraint

This constraint normally means to protect the ecosystem by avoiding excessive drawdown. In this work, the drawdown constraints were formulated to avoid mining and formulated as follows:-

at arbitrary point 1, Drawdown constraint = $r_{w1} + r_{w2} + r_{w3} + r_{w4} + r_{w5} + \ldots\ldots\ldots + r_{w68}$

at arbitrary point 2, Drawdown constraint = $r_{w1} + r_{w2} + r_{w3} + r_{w4} + r_{w5} + \ldots\ldots\ldots + r_{w68}$

at arbitrary point 3, Drawdown constraint = $r_{w1} + r_{w2} + r_{w3} + r_{w4} + r_{w5} + \ldots\ldots\ldots + r_{w68}$

at arbitrary point N_c, Drawdown constraint = $r_{w1} + r_{w2} + r_{w3} + r_{w4} + r_{w5} + \ldots\ldots\ldots + r_{w68}$

Accordingly, it postulates the relation;

$$\sum_{j=1}^{N_w} r_j \leq d_i \tag{4}$$

In which: r_{w1} is drawdown at point 1 due to pumping well no 1, r_{w2} is drawdown at point 1 due to pumping well no 2, r_{w3} is drawdown at point 1 due to pumping well no 3, N_c no of control points, *rj* is the drawdown at control point *i* caused by a pumping rate from pumping well *j* (value of *rj* in Table 4 to 6), *di* is the permissible drawdown at control point *i* equals to 30 m.

3.3.1.3 Water demand constraint

The NSAASA is considered as the sole source of water. This, therefore, means that the designed optimal pumping strategy must supply at least the minimum water demand. It is formulated as follows:

$$\sum_{j=1}^{N_w} Q_j \geq Q_D \tag{5}$$

In which Q_D is water demand.

3.3.1.4 Distance between wells constraint

This constraint obeys the relation:

$$D_i \geq D_{all} \tag{6}$$

Where D_i is actual distance between wells and D_{all} is minimum distance between wells.

3.3.1.5 Location of wells

The locations of wells constraint is to be decided by the model itself within a user defined region of the model grid until the optimal location is reached (Figure 9).

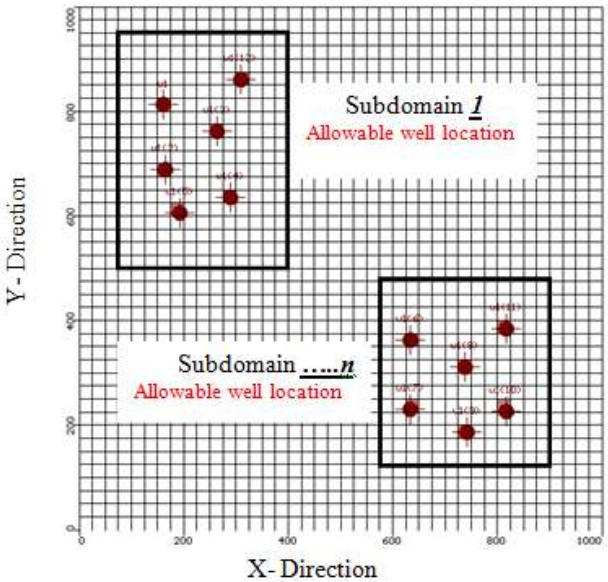

FIG. 9: PLAN VIEW SHOWING FINITE DIFFERENCE GRID WITH SUB-DOMAIN FOR WELL LOCATIONS

3.4 Optimization Procedure of the Simulation-Optimization model

In groundwater management problems, there are two sets of variables, decision variables and state variables, where the decision variable is the pumping and injection rates of wells. Also other decision variables include well locations and the on/off status of a well. By optimization techniques the decision variables can be managed to identify the best combination of them. Moreover, hydraulic head is the state variable. The simulation model updates the state variables, and the optimization model determines the optimal values for all decision variables. In this work, MODFLOW FORTRAN code is used as the simulation of groundwater flow which links with GA optimization (OLGA Code). The flowchart for simulation-optimization model is given in (Fig. 10).

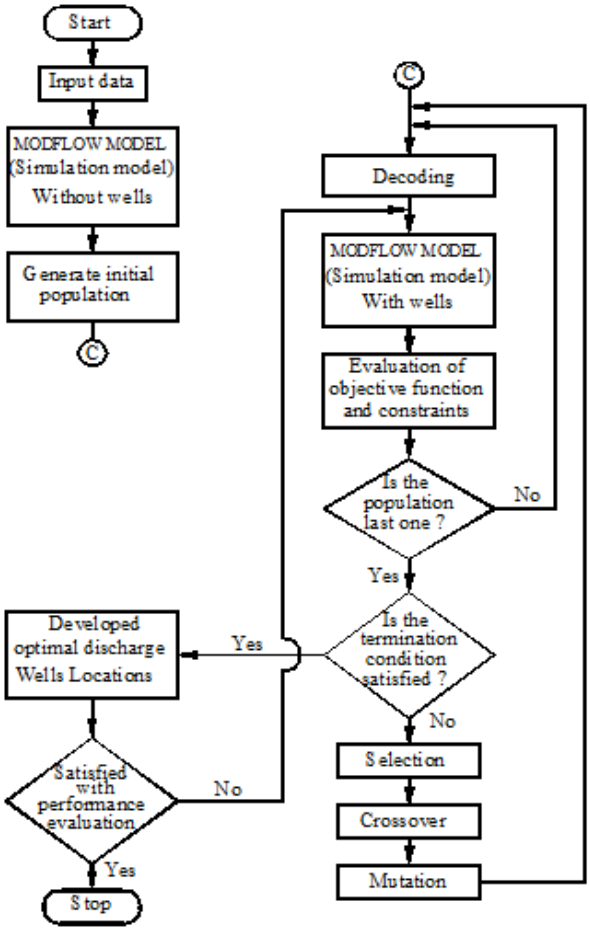

FIGURE 10: FLOWCHART FOR THE SIMULATION/OPTIMIZATION MODEL

It must refer that MODFLOW simulation without wells is used to generate the initial head, but initial population is generated from GA via random number for each well according to constraints and number of chromosome.

3.4.1 Checking the termination criterion

The optimization algorithm continues to be executed by iterating until the given termination criteria are satisfied (Fig. 10). Note that different termination criteria can be used to stop the computation. These may be: Stopping the computation after a given number of iterations; reaching a specific objective function value; no improvement in the objective function value for a specified number of passed iterations; or after limited time. In this study, the relative error definition is used to check the convergence of iterations. Thus, the convergence criterion is defined as,

$$\frac{f_1 - f_0}{f_0} \leq \varepsilon \tag{7}$$

Where ε is a tolerance for the convergence of iterations, if two consecutive objective values (f1, f_o) satisfy the criterion.

3.5 Testing scenarios

The testing scenarios include three proposed pumping rates and well locations policies. The first scenario estimates the pumping rates from 75 productive wells with their present locations. The second scenario checks the present locations for these 75 productive wells and the optimality of their pumping rates. The third one proposes water exploitation policy aimed at increasing the present productive wells by 14 wells, as a result of the increase in reclamation activities (new 25 thousand acres), and delineates the optimal locations of these new wells and keeping the present locations of the other 75 present wells besides estimating the optimal pumping rates for all.

IV. RESULTS AND DISCUSSIONS

The expected interference between cones of depression of the present productive wells due to their configurations around the highway roads of the Abu Simbel area will affect the groundwater productivity of the NSAASA. Accordingly, the need to determine optimal well location strategy for the new drilled wells required for future expansion of the project (1.5 million acres national project) is essential.

In addition, applying the constructed OLGA Code for solving the optimization problems related to the optimal pumping rates and the optimal well locations, the initial pumping rates are assigned to each well as more than 700 m^3/day and less than 1000 m^3/day and then the optimization procedure explained before is used. The GA parameters used in the optimization problem are given in Table 4. The optimal well location and pumping rate are determined, based on OLGA Code, from one feasible solution to the other according to the calculated residual errors values where they improve quickly in the early iterations and change slowly in subsequent iterations till satisfying the constraints.

TABLE 4
THE GA SOLUTION PARAMETERS APPLYING OLGA CODE

Continuous GA Parameter	Value
Population size	200
Mutation ratio	0.006
Type of crossover	uniform crossover
Crossover probability	0.7
Tolerance for the convergence of iterations	0.01

On the other side, the results of the three testing optimal policies applying OLGA Code show the future predictions in the optimal pumping rates after 5, 10, 15, 20, 25, 30, 40 and 50 years. The first scenario investigates the proposed pumping rates from the 75 productive wells penetrating the NSAASA under their current locations. The OLGA simulation results show that the optimal pumping rates, under the present conditions of water demand Q_D of 60000 m^3/day, range from 57585 to 50144 m^3/day with corresponding total drawdown ranges from 3.42 to 13.73 m during the simulation period of 50 years (Table 5).

TABLE 5
OPTIMAL PUMPING RATE FOR FIRST SCENARIO

Year	5	10	15	20	25	30	40	50
N	75	75	75	75	75	75	75	75
r (m)	3.42	5.62	6.78	7.88	8.93	9.96	11.85	13.73
$Q_{min}/well$	746.8	726.4	708.6	695.6	645.2	629.2	613.8	605.7
$Q_{max}/well$	1000	1000	1000	1000	1000	1000	1000	1000
Q_{opt} (m^3/day)	57585	56033	54511	53021	52292	51568	50852	50144

N is number of operation wells, r is maximum drawdown, $Q_{min}/well$ is min optimal pumping rate for well, $Q_{max}/well$ is max optimal pumping rate for well and Q_{opt} total optimal pumping rate for all wells.

Moreover, by running the developed OLGA Code for time step of 5 years, the predicted head distribution maps of the NSAASA under the current pumping rates at years 2015, 2025, 2035 and 2060 are shown in (Figure 11). It is noticed from (Figure 11) that the groundwater levels change from 164.5 masl to 161.3 masl in the center of the cone of depression. Few productive wells in the southwestern part of the model domain show relatively slight drawdown amounts to 13 m at East El-Emaratiah Company well field. This is mainly attributed to the effect of increasing the thickness of water bearing formation towards the northwestern and western parts. In addition, one large cone of depression will develop in the cultivated areas.

This cone is in the central part of Abu Simbel-Tushki road and may attribute to the present extraction rates from the reclaimed areas.

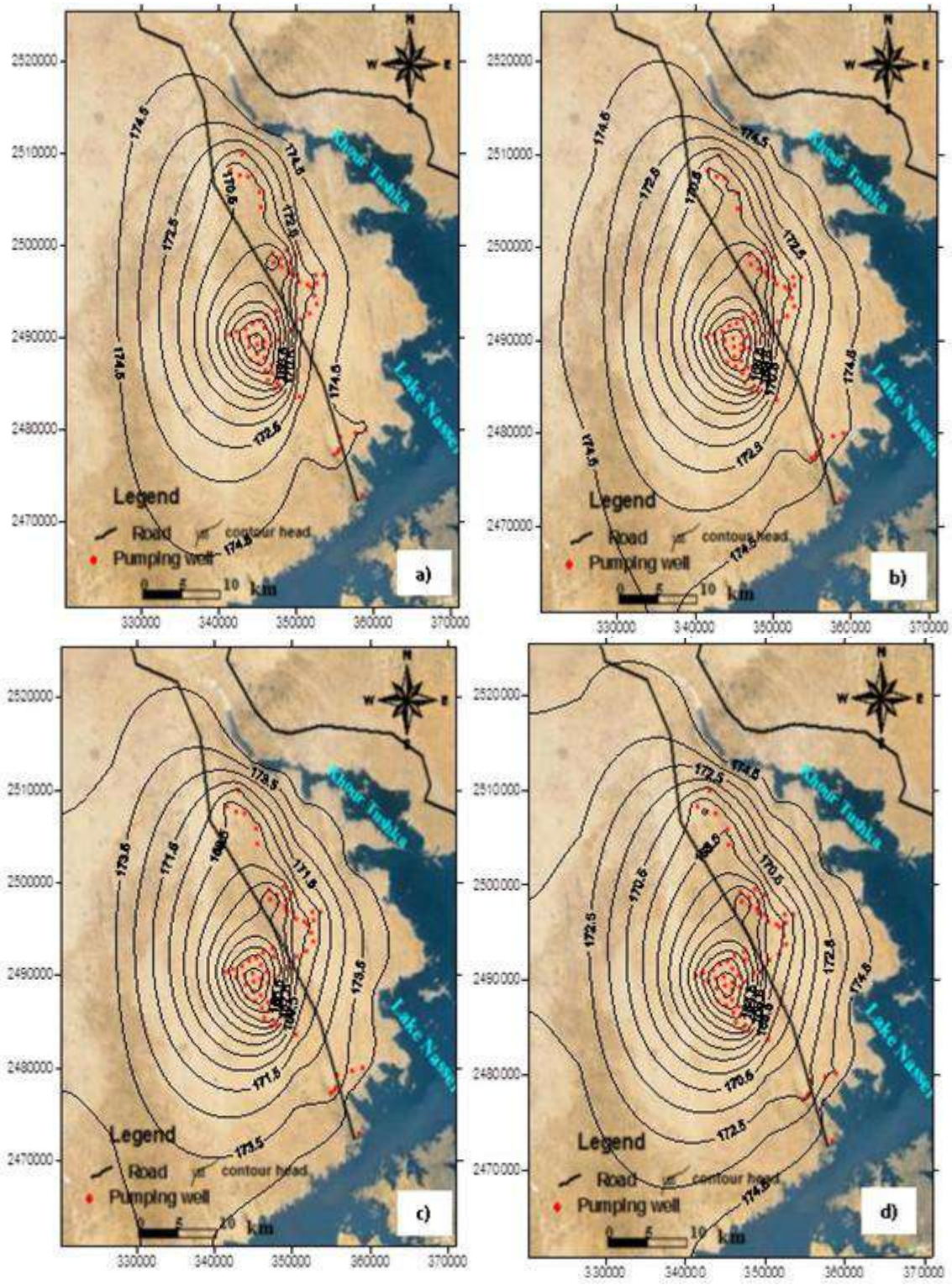

FIGURE 11: PREDICTED HEAD DISTRIBUTION MAP OF THE NSAASA FOR OPTIMAL PUMPING RATES APPLYING 1ST SCENARIO a) at 2015, b) at 2025, c) at 2035, and d) at 2060

Otherwise, the second scenario seems to be theoretical more than practical since it studies the optimal locations of already 75 present productive wells under the present constraint of water demand Q_D of 120000 m^3/day and predict their optimal pumping rates. The GA parameters used in this optimization case are given in (Table 6). The initial pumping rates are assigned to each well as less than 1500 m^3/day and the optimal pumping rates after 5, 10, 15, 20, 25, 30, 40 and 50 years are

predicted (Table 6). It is noticed from (Table 6) that the number of the total operating wells N is still constant (75 wells), and the maximum drawdown (r) ranges from 2.22 to 12.13 m while Q_{min}/well begins with 1460.6 and ends by 1053.2 m^3/day for the simulation period. The total optimal pumping rate for all wells (Q_{opt}) ranges between 102038 and 100773 m^3/day (Table 6).

TABLE 6
OPTIMAL PUMPING RATE FOR THE 2ND SCENARIO APPLYING OLGA CODE

Year	5	10	15	20	25	30	40	50
N	75	75	75	75	75	75	75	75
r (m)	2.22	4.32	5.43	6.63	7.73	8.64	10.53	12.13
Q_{min}/well	1460.6	1369.5	1301.6	1286.4	1201.3	1183.2	1102.4	1053.2
Q_{max}/well	1500	1500	1500	1500	1500	1500	1500	1500
Q_{opt} (m^3/day)	102038	101797	101561	101330	101103	100992	100882	100773

In the same side, the results of the OLGA Code based on this scenario show that the predicted optimal location of the productive wells differ more or less from the present location (Figure 12). Although the proposed OLGA approach successfully identified all the well locations and pumping rates of the present numerical study, identification of all the well locations and pumping rates may not be feasible for real-world applications since the number of pumping wells is usually very high. Instead, the proposed procedure may be applied to the suspected illegal pumping areas as noticed in the field trips. As an extension of this study, the performance of the proposed OLGA Code should be tested on a real field system in a future study.

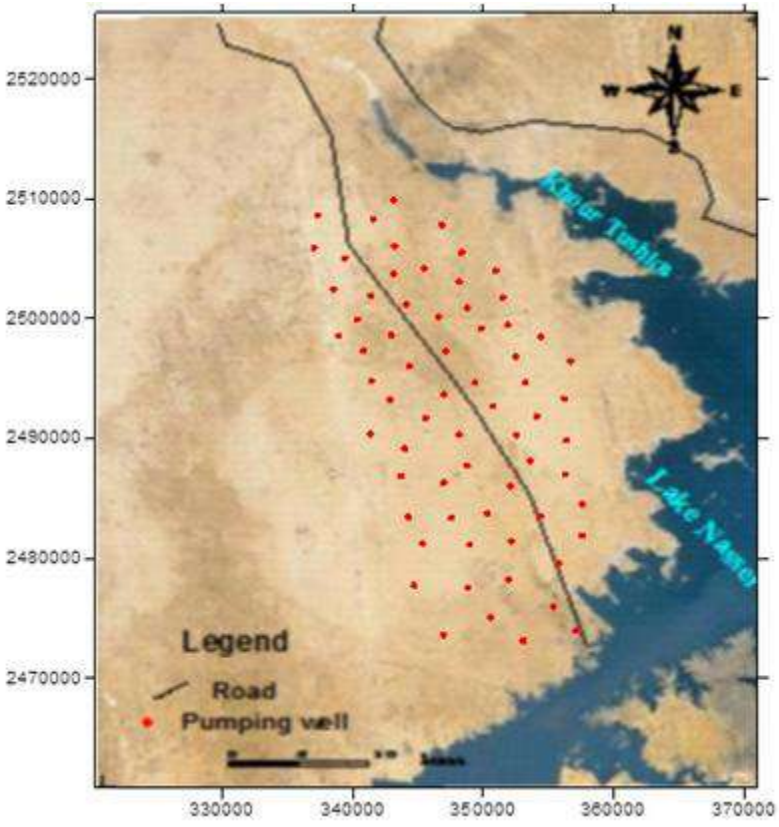

FIGURE 12: OPTIMAL LOCATION OF PRESENT WELLS (2ND SCENARIO)

Otherwise, the predicted head distribution maps of the NSAASA under the 2nd scenario (Figure 13) show groundwater levels change from 165.5 masl to 162.5 masl in the center of the cone of depression. It is noticed from (Figure 13) that the normal decline in the groundwater levels (3 m) may attribute to the small thickness and low hydraulic conductivity of the NSAASA in these localities. Moreover, the cone of depression will appear in the cultivated areas during the simulation time (with diameter of 2.5 to 4 km approximately). While the southern and western cultivated parts of the model domain does not be

affected with this scenario. This may attribute to the effect of the great aquifer thickness and the presence of thin clay layers in the southern and western parts rather than the geologic structure impact. Accordingly, this reflects the low potentiality of the northern cultivated parts for positive response to this scenario.

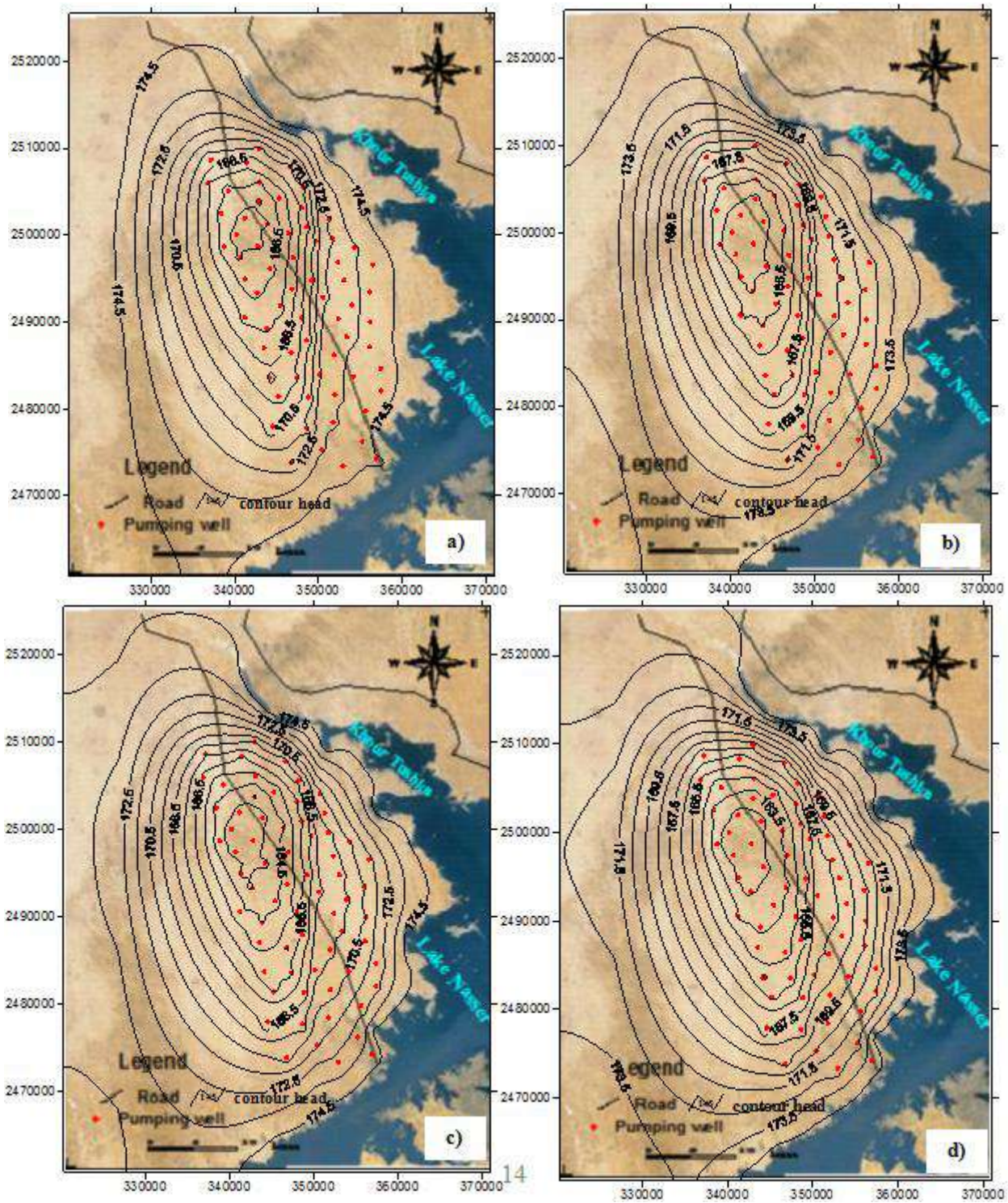

FIGURE 13: PREDICTED HEAD DISTRIBUTION MAPS OF THE NSAASA FOR OPTIMAL WELL LOCATIONS APPLYING 2ND SCENARIO A) AT 2015, B) AT 2025, C) AT 2035, AND D) AT 2060

The third scenario proposes water exploitation policy aimed at increasing the present productive wells by 14 wells, as a result of the increase in reclamation activities, under the constraints of 500 m as minimum distance between wells and 900000 m^3/day as water demand Q_D, and delineates the optimal locations of these new productive wells and keeping the present locations of the other 75 present productive wells, besides estimating the optimal pumping rates for all. The GA parameters

used in this optimization case are given in (Table 7). The OLGA Code runs for time step of 5 years. The predicted optimal location of the new productive wells is checked (Figure 14) and the predicted head distribution maps of the NSAASA for the optimal pumping rates at years 2015, 2025, 2035 and 2060 are shown in (Figure 15).

TABLE 7
OPTIMAL PUMPING RATE FOR THIRD SCENARIO

Year	5	10	15	20	25	30	40	50
N	89	89	89	89	89	89	89	89
r (m)	4.27	6.47	7.63	8.72	9.77	10.80	12.68	14.56
Q_{min}/well	923.2	913.3	902.8	879.6	823.6	813.2	800	800
Q_{max}/well	1500	1500	1500	1500	1500	1500	1500	1500
Q_{opt} (m^3/day)	87187	85635	84114	82623	81894	81171	80454	79747

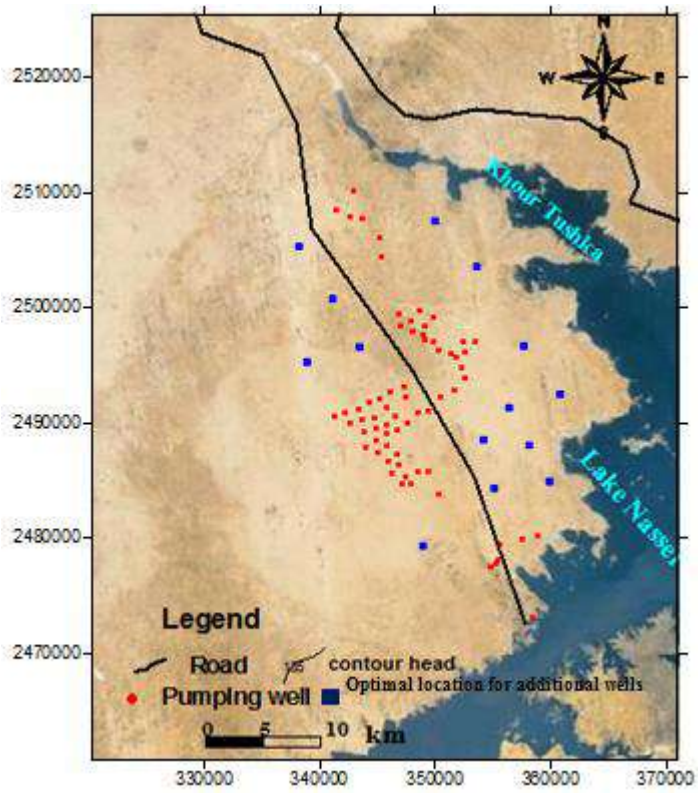

FIG. 14: OPTIMAL LOCATION OF THE NEW PRODUCTIVE WELLS (BLUE COLORED) (3RD SCENARIO)

It is noticed from (Table 7) that the maximum drawdown r ranges from 4.27 to 14.56 m while Q_{min}/well begins with 923.2 and ends by 800 m^3/day in case of number of total operating wells N of 91 productive wells. Moreover, Q_{min}/well begins with 923.2 and ends by 800 m^3/day during the simulation period. The total optimal pumping rate for all wells (Q_{opt}) ranges between 87187 and 79747 m^3/day.

However, it is noticed from the predicted head distribution maps (Figure 15) that the groundwater level decreases from 163m asl in the beginning of the simulation period (the year 2015) to 158m asl in the end of the simulation period (the year 2060). The depression cones related to the first and the second scenarios are mitigated in the northern part of the model domain. Moreover, limits are placed on the total optimal pumping rates of the productive groundwater wells beside its optimal locations in the reclaimed areas. Accordingly, it is preferred to extend the future reclamation activities parallel to the western side of the Khour Tushki area. Although the results of this scenario provide more or less good degree of confidence in the optimal location of the new productive wells and optimal pumping rates, the expected sharp decline in groundwater levels in the concerned area assumes more applied studies. The Q_{opt} in the 3rd scenario is actually lower than that in the 2nd scenario because the second scenario studies the optimal locations for these 75 productive wells and their optimal pumping rates. The third one proposes water exploitation policy aimed at increasing the present productive wells by 14 wells. The predicted value of (r) based on the 3rd scenario is more or less similar to the results of the other two scenarios although the number of the operating wells is increased by 19%. This reflects the great importance to apply the optimal well location concept in any

new reclamation projects. As a result of the above discussion of the OLGA Code optimal well location and pumping rates results, it can be concluded that the groundwater withdrawal from the NSAASA under this optimization study could be safely conducted.

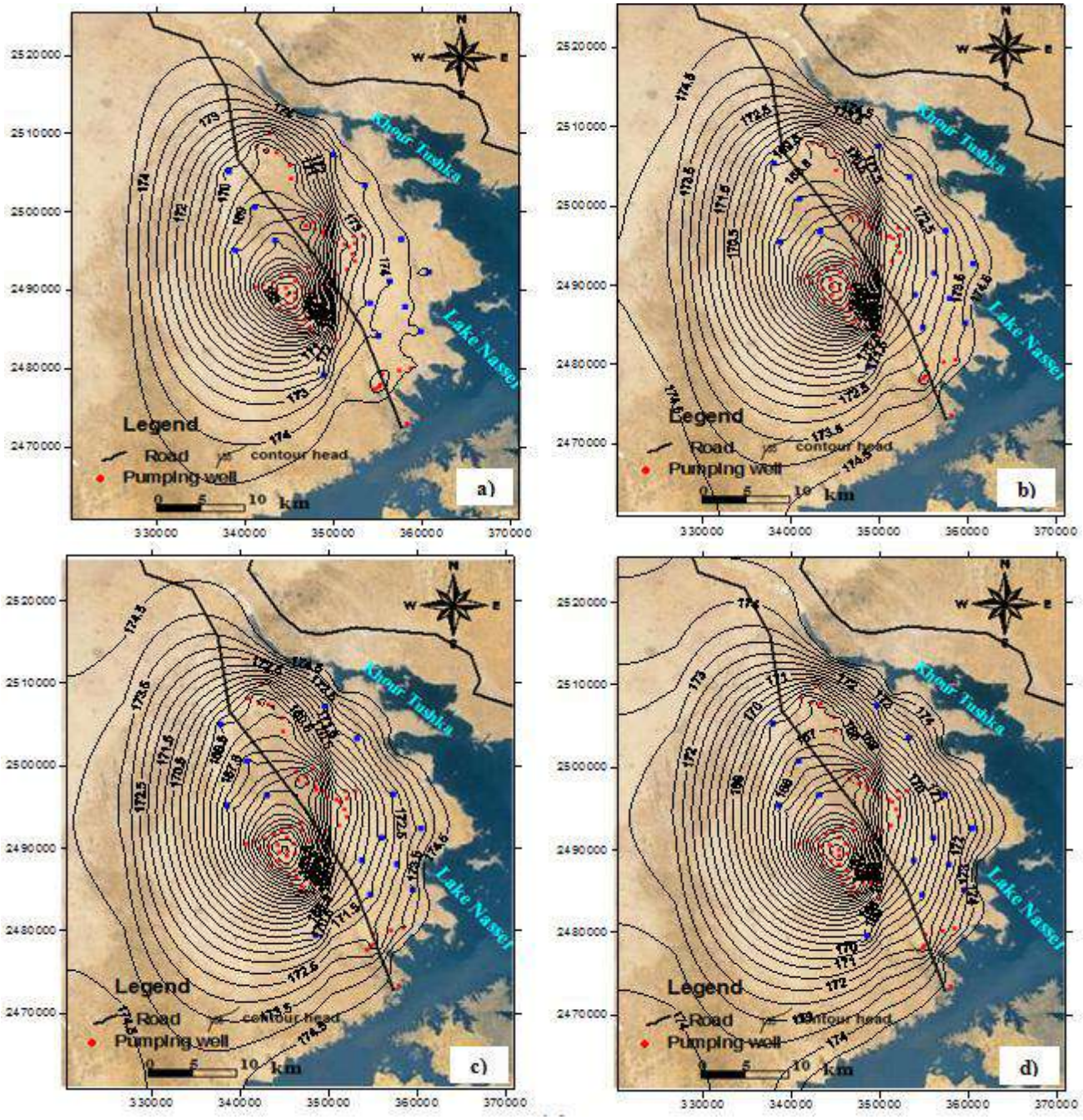

FIGURE 15: PREDICTED HEAD DISTRIBUTION MAPS OF THE NSAASA FOR OPTIMAL WELL LOCATIONS APPLYING 3RD SCENARIO a) at 2015, b) at 2025, c) at 2035, and d) at 2060

V. CONCLUSION AND RECOMMENDATION

This paper is devoted to propose an assisted methodology to identify representative models for optimal well locations. To do so, first a mathematical equations were developed to model the representativeness of a subset of constrains with respect to the full set that characterizes the well location problem. Then, an optimization tool was implemented to identify the representative constrains of any problem, considering not only the main output variables, but also the probability distribution of the attribute-levels of the problem. Accordingly, OLGA Code was linked MODFLOW with genetic algorithm technique to establish a simulation optimization groundwater model. This model was applied for NSAASA to develop the optimal location of the groundwater productive wells with maximum pumping rate. Three scenarios were tested to choose the proper

water exploitation policy. For the first scenario, the predicted groundwater drawdown after simulation period of 50 years ranged from 3.42 to 13.73 m while the corresponding optimal pumping rates ranged from 57585 to 50144 m^3/day. Under the second proposed scenario, the predicted drawdown (r) and the corresponding total optimal pumping rate for all wells (Q_{opt}) ranged from 2.22 to 12.13 m and between 102038 and 100773 m^3/day, respectively. Moreover, the predicted value of (r) based on the 3rd scenario was more or less similar to the results of the other two scenarios although the number of the operating wells was increased by 19%. Computational restrictions were common and likely the cause of the systemic lack of algorithm benchmarking for well location optimization. Still, some valuable insight can be gained from these results that could guide further investigation.

Based on the results of the OLGA model, it is highly recommended to choose the new productive well locations in staggered system parallel to the western side of the Khour Tushki area. More applied studies are needed for verification the results of this optimal well location model. Also, this study should be extended to contain more test cases and more comprehensive selection of algorithms including interpolation methods, ad joint methods and hybrid methods.

ACKNOWLEDGEMENTS

The data of this work were presented from Desert Research Center Station in Abu Simbel through Development of South Wadi Project, Egypt (Tushki project) which carried out by the team work of DRC. Assistance from project team work and Groundwater Sector Office is gratefully acknowledged. I'm indebted to them, especially Prof Himida and Dr El-Sheikh, for their help in performing field works and providing the required data. I appreciate the insightful comments and suggestions of the editor and anonymous reviewers, which greatly improved this manuscript.

REFERENCES

[1] Aggour, T. A., Korany, E. A., Mosaad, S., and Kehew, A., (2012): Geological conditions and characteristics of the Nubia Sandstone aquifer system and their hydrogeological impacts, Tushka area, south Western Desert, Egypt. Egy. J. Pure & Appl. Sci. (2012) 027-037.

[2] Aral, M. M., Guan, J. B., Maslia, M. L., (2001): Identification of contaminant source location and release history in aquifers. Journal of Hydrologic Engineering 6 (3), 225–234.

[3] Ayvaz MT, Karahan H, (2008) "Simultaneous parameter identification of a heterogeneous aquifer system using artificial neural networks". Hydrogeology Journal 16: 817–827.

[4] Bear, J., (1979): Hydraulics of groundwater. McGraw-Hill, New York, 569 p.

[5] Chang, L. C., Chu, H. J., Hsiao, C. T.,(2007): Optimal planning of a dynamic pump-treat-inject groundwater remediation system. Journal of Hydrology 342, 295–304.

[6] CONOCO, (1987): Geological map of Egypt, NF 36 NW El Sad El-Ali. Scale 1:500000. The Egyptian General Petroleum Corporation. Conoco Coral.

[7] Desert Research Center (DRC) (2012) "Evaluation of Hydraulic Parameters of Nubia Sandstone Aquifer", unpublished internal report, submitted, MARA – 65 p.

[8] El-Sabri, M. A. Sh., El-Sheikh, A. E., and El-Osta, M. M., (2010): The hydrogeological connection between Lake Nasser and the Nubian Sandstone aquifer in Tushka area, South Western Desert, Egypt. Egyptian Journal of Aquatic Research, 2010. 36 (2), 245-262.

[9] El-Shazly, E. M., Abdel Hady, M. A., El Ghawaby, M. A., Soliman, A. B., El-Kassas, I. A., Khawaski, S. M., El Amin, H., El Rakaiby, M. M., El Aasy, I. E., Abdel Megid, A. A., and Mansour, S. I., (1980): The geologic map of Egypt, the structural lineation map of Egypt, and the drainage map of Egypt based on LANDSAT-1 Imagery interpretation and field investigations: Remote Sensing Center, Academy of Scientific Research and Technology, Cairo: Oklahama state University, Stillwater, Oklahama and United Nations Environment Program (GEMS): 12 maps. Scale 1:100000.

[10] Ferreira da Silva, J., Haie, N., (2007): Optimal locations of groundwater extractions in coastal aquifers. Water Resources Management 21 (8), 1299–1311.

[11] Gad, M. I., and Khalaf. S., (2013): Application of sharing genetic algorithm for optimization of groundwater management problems in Wadi El-Farigh, Egypt. Journal of Applied Water Science. 3:701–716.

[12] Gad, M. I., El-Sheikh, A., and El-Osta. M. M., (2011): Optimal management for groundwater of Nubian aquifer in El-Dakhla depression, Western Desert, Egypt. Journal of Water Resources and Environmental Engineering, Vol. 3(14), pp. 393-409.

[13] Guan, J., Kentel, E., and Aral, M. M., (2008): Genetic algorithm for constrained optimization models and its application in groundwater resources management. J., Water Resour Plann., Manag., 134 (1) : 64–72.

[14] Guan, J., Aral, M.M., (1999): Optimal remediation with well locations and pumping rates selected as continuous decision variables. Journal of Hydrology 221, 20–42.

[15] Hamid, R. S., Fatemeh, D., Miguel, A. M., (2009): Simulation-Optimization Modeling of Conjunctive Use of Surface Water and Groundwater. Water Resour. Manage, DOI 10.1007/s11269-009-9533-z.

[16] Hill, M. C., (1998): Methods and Guidelines for Effective Model Calibration. U.S. Geological Survey Water-Resources Investigations Report 98-4005.

[17] Hill, M. C., (2000):Methods and Guidelines for Effective Model Calibration. Proceedings EWRI, ASCE, 2000.

[18] Huang, C., Mayer, A.S., (1997): Pump-and-treat optimization using well locations and pumping rates as decision variables. Water Resources Research 33 (5), 1001–1012.

[19] Karahan H, Ayvaz MT "Groundwater parameter estimation by optimization and dual reciprocity finite differences method". J Porous Media 8(2):211–223, 2005

[20] Kim, J., and Sultan, M., (2002): Assessment of the long-term hydrologic impacts of Lake Nasser and related irrigation projects in southwestern Egypt. J. Hydrol. 262, 68–83.

[21] Liu, Q., Zou, L., Li, (2002): The application of genetic algorithms in groundwater management. World Geology 21(2):145–149.

[22] Mahar, P. S., Datta, B., (2000): Identification of pollution sources in transient groundwater systems. Water Resources Management, 14, 209–227.

[23] Mahar, P. S., Datta, B., (2001): Optimal identification of ground-water pollution sources and parameter estimation. Journal of Water Resources Planning and Management 127 (1), 20–29.

[24] Mantoglou, A., and Kourakos, G., (2007): Optimal groundwater remediation under uncertainty using multi-objective optimization. Water Resources Management 21, 835–847.

[25] Mckinney, D. C., Lin, M., (1994): Genetic algorithm solution of groundwater management models. Water Resour Res 30(6):1897–1906.

[26] Meira, L.A.A., Coelho, G. P., Santos, A.A.S., and Schiozer, D.J. (2016). Selection of Representative Models for Decision Analysis Under Uncertainty. Computers & Geosciences J.V(88), 67-82.

[27] Moharram, S. H., Gad, M. I., Saafan, T. A., and Khalaf, S., (2012): Optimal Groundwater Management Using Genetic Algorithm in El-Farafra Oasis, Western Desert, Egypt. Water Resour. Manage. 10.1007/s11269-011- 9865-3.

[28] Park, C. H., and Aral, M. M., (2004): Multi-objective optimization of pumping rates and well placement in coastal aquifers. Journal of Hydrology 290, 80–99.

[29] Rana, T., Khan, S., Rahimi, M., (2008): Spatio-temporal optimization of agricultural drainage using groundwater models and genetic algorithms: an example from the Murray Irrigation Area, Australia. Hydrogeology Journal, 16: 1145–1157.

[30] Ruperti, N. J., (2002): Estimation of the release history of a contaminant source in 2-D groundwater systems. In: Fourth International Conference on Inverse Problems in Engineering, Rio de Janeiro, Brazil.

[31] Saafan, T. A., Moharram, S. H., GAD, M. I., and Khalaf, S.,(2011): A multi-objective optimization approach to groundwater management using genetic algorithm. Journal of Water Resources and Environmental Engineering, Vol. 3(7), pp. 139-149, August 2011.

[32] Saffi, M., Cheddadi, A., (2007): Explicit algebraic influence coefficients: a one-dimensional transient aquifer model. Hydrological Sciences Journal-Journal Des Sciences 52 (4), 763–776.

[33] Singh, R. M., Datta, B., and Jain, A., (2004): Identification of unknown groundwater pollution sources using artificial neural networks. Journal of Water Resources Planning and Management 130 (6), 506–514.

[34] Sun, A. Y., Painter, S. L., Wittmeyer, G. W., (2006): A robust approach for iterative contaminant source location and release history recovery. Journal of Contaminant Hydrology 88, 181–196.

[35] Tung, C. P., Chou, C. A., (2004): Pattern classification using tabu search to identify the spatial distribution of groundwater pumping. Hydrogeology Journal 12 (5), 488–496.

[36] Wang, W., Ahlfeld, D. P., (1994): Optimal groundwater remediation with well location as a decision variable – model development. Water Resources Research 30 (5), 1605–1618.

[37] Yan, T., Wu, J., and Xue, Y., (2003): A comparison of genetic algorithm and trial-and-error approach in solving the hydrogeologic inverse problem. In: Proceedings of the international Symposium on Water Resources and the Urban Environment. China Environment Science Press, Beijing, pp 137–141.

[38] Yao, L., Li, J., and Li, Z., (2003): Parameter identification of groundwater flow numerical modeling by means of improved genetic algorithm. J Hydraul. Eng. 34(12):40–46.

[39] Zheng, C. M., and Wang, P. P., (1999): An integrated global and local optimization approach for remediation system design. Water Resources Research 35 (1), 137–148.

[40] Zhu, X., Wu, J., Ye, S., Zhao, J., and Wu, M., (2003): Evaluation of groundwater resource in deep aquifers of the Yangtze Delta (south of the Yangtze Delta). In: Proceedings of the international Symposium on Water Resources and the Urban Environment. China Environment Science Press, Beijing, pp 467–473.

Process and Device for Generating High Purity Hydrogen Based on Hydrolysis Reaction of Aluminum Dross

E. David[1], J. Kopac[2]

[1]National Institute of Research and Development for Cryogenic and Isotopic Technologies, Street Uzinei No.4; P.O Râureni; P.O.Box 7; 240050 Rm.Vâlcea, Romania

[2]Faculty of Mechanical Engineering, University of Ljubljana, Askerceva 6, SI-1000 Ljubljana, Slovenia

Abstract-*This paper presents an efficient process to generate hydrogen, using aluminum dross particles activated by mechano-chemical methods and tap water with a pH value ≥ 10.4, obtained by adding of NH_3 aqueous solution 25 wt%/L. The effect of pH value and aluminum amount on hydrogen yield has been studied. For these tests pure aluminium particles and aluminum dross were employed, and SEM analysis was used to study the changes in surface properties of metal occurring due to metal hydrolysis and hydrogen release. The obtained results show that the rate of hydrogen generation increases with the increasing of pH value and aluminum quantity. A hydrogen continuous device was designed and operated. The economical and environmental key aspects associated with the production of hydrogen, using Al dross, are discussed. The data obtained in this research can provide the basis for scale implementation of the aluminum dross hydrolysis process to generate H_2 of high purity (>99.5 vol.%).*

Keywords: aluminum dross; aluminum-water reaction; hydrogen generating; tap water; mechano-chemical activation;

I. INTRODUCTION

Progress of energy systems depends on the development of new efficient and environmentally sustainable sources of clean energy. There are several ways to develop such sources. One way of perspective is based on the generation of hydrogen [1-3]. Hydrogen is known as one of the best clean energy carrier because of its minimal impact on the environment regarding to greenhouse gas emissions such as carbon dioxide and other gases [1, 4-6]. Hydrogen can be used directly in molecular form , (i.e. as a fuel for vehicles) or indirectly to generate electricity for other industrial applications [4-7] .A major advantage which it has over other fuels is that not cause pollution because of its burning reaction results only water. Hydrogen is also an almost ideal fuel gas and in terms of reducing smog when it is burned. However, safe storage and generation at low cost are technical challenges that need to be considered. For these reasons there are sought new ways to produce hydrogen at low cost from other sources than are known [8-10].The alkali metals (such as sodium, potassium, lithium) and alkaline earth (calcium, strontium, aluminum, magnesium, etc.) are very active when they come in contact with water, react spontaneously, generating hydrogen and heat. Based on this chemical property, the hydrolysis reaction of pure aluminum powder is commonly used for high purity hydrogen generation [6, 11,12,13, 14].Although the use of pure aluminum in reaction with water to produce hydrogen is a viable method, it is expensive, if it takes into account the cost of producing pure aluminum and the use of an alkali metal hydroxide, also an expensive product. The alkali metal hydroxide is used to remove the protective layer of aluminum oxide on the surface of the aluminum particles, which prevent the contact between the metal and water, and thus slow down or substantially avoid reaction between the aluminum and water [15, 16, 17, 18] .As a result, other methods should be studied and utilized to activate the surface of the aluminum particles, to initiate and accelerate the reaction of hydrolysis. Different methods to enhance the rate of aluminum reaction and other metals with water have been developed [19,20, 21, 22].One such method is mechanical activation (crushing, cutting, grinding). This is a method not so expensive and leads to removal of aluminum oxide layer and obtaining a surface clean and active. Also, the replacement of an alkali metal hydroxide with less expensive other chemical compound [19] can be effective. Another way to reduce the costs is to replace pure aluminum with another source of aluminum. As is known from the literature, large amounts of aluminum are present in the solid metal wastes resulting from the production of aluminum, or from recycling processes, this being known as dross or slag [10, 12.13]. The use of this source of aluminum to generate hydrogen has both benefits to environment by waste recycling, and to the cost of hydrogen producing, that decreases substantially. In this work, we have investigated the hydrolysis properties of Al powder and Al dross mechanically treated by ball milling to form a fresh chemically active metal surface, with the use of tap water, in which was added a small amount of ammonia solution 25 wt %, to increase the pH (i.e. from 6.95 to 10.45) and to create a strong alkali environment that determines the metal surface activation. The aim is to accelerate the hydrolysis rate and to improve the hydrogen yields of the mixture in water. Removal of the aluminum oxide layer on aluminum particle surface by mechanical means, sustains aluminum assisted water split reaction. In addition, the presence in dross composition of an effective amount of nitride (AlN), salts, especially KCl, NaCl,

and oxides such as CaO and MgO, with metal, more so in Al dross, play the role of catalysts for the reaction between Al and water. Once contacted with water, these compounds cause substantial increase of pH (i.e. create a higher alkaline environment, increasing the pH value from 10.45 over 12.4) which accelerates the corrosion of Al with accompanying of hydrogen release. The activated aluminum can then react spontaneously with water, even at room temperature, without adding any chemicals to the water and hydrogen is produced.

II. MATERIALS AND METHODS

The aluminum dross used in our experiments was supplied by S.C. AL Mina Com SRL, Bucharest, Romania. The samples consisted of rounded lumps up to approximately 10-15 mm in size (as well as some smaller metallic fragments) and had a slight smell of ammonia. The samples were grinded and for this it was used a Fritsch planetary mill, with stainless steels balls and vials and then the ground material were sieved through a 100-µm aperture screen. A sample before and after grinding is shown in Fig. 1(a, b).

(a) (b)

FIGURE 1. Sample of aluminum dross before (a) and after grinding (b)

The chemical analysis of the elements of raw aluminum dross was carried out by atomic absorption spectrometry method using an analyzer type Analytic Yena Nova 300, X-ray diffraction, using a Philips PW 1710 diffractometer with Ni filter and Cu kα radiation and the morphology of the powders was analyzed using scanning electron microscope JSM-7500F (JOEL-Japan) operated at 10Kv, and X-ray fluorescence (XRF) method, using an analyzer type Bruker S1 Titan 600. A composition is presented in Table 1.

TABLE 1
The composition of raw aluminum dross

Composition	Al	Al_2O_3	AlN	MgO	Fe_2O_3	KCl	NaCl	SiO_2	CaO
Mass wt%	15.27	43.71	7.2	4.28	4.35	5.94	7.38	10.09	1.78

Other starting materials used in experiments were: powder of pure Al, size approximately 45-100 µm (99.5% purity) supplied by Alfa Aesar, a Johnson Mathey Company; nitrogen and argon gases (N_2, Ar) with a purity of 99.99% purchased from Linde Company, ammonia solution 25 wt% supplied by Adra Chim SRL Bucharest, Romania, ferrous sulfate supplied by Sigma-Aldrich, zeolite molecular sieve 5Å from Linde Company.

Surface of aluminum particles were activated by mechanical grinding and also using tap water with an alkaline pH ≥10.4. First, by adding 2 ml aqueous ammonia solution 25wt% / L_{H2O}, the pH value of water increased from initial value of 6.95 to a value of 10.45. This tap water with high pH, in contact with Al dross particles, which contain appreciable amounts of AlN, salts and other alkaline oxides , accelerates the hydrolysis reaction of AlN and these compounds leading to releasing of high soluble alkaline compounds which also determines the increase the pH value over 12.4.Consequently, this high alkaline environment accelerates the corrosion process of Al particles and releases hydrogen.

For experiments it was used a laboratory system consisting of a flat-bottomed glass flask with a volume of 500 ml., a hot plate with magnetic stirrer and water bath, (Fig. 2). The reaction started by introducing of 200 ml alkaline tap water (obtained by adding 2 ml ammonia aqueous solution of 25wt% /$L_{tap\ water}$) or tap water without adding ammonia solution, through the central vessel neck over 1 to 3 g of pure Al particles or over 6.548 to 19.646 g of Al dross particles respectively, also containing an amount of Al of 1 to 3 g and which were poured in the flask from beforehand. After Al particles or aluminum dross particles were introduced, the neck of flask was immediately corked and before tap water or tap water solution introducing, the entire system was purged with nitrogen gas at a flow of 60 ml/sec for 10 min. This operation was

performed to remove air from the system and to prevent formation of an explosive mixture with the hydrogen released from reaction. The temperature of the process was measured and for this it used a Chromel/Alumel thermocouple.

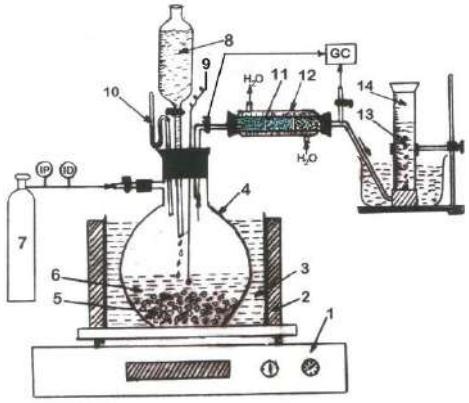

FIGURE 2. Laboratory experimental system:(1) magnetic stirrer ; (2) electric stove ; (3) water bath; (4) flat-bottomed glass flask ; (5) pure Al powder or Al dross powder; (6) tap water or alkaline tap water solution; (7) tank containing nitrogen under pressure; (8) burette containing tap water or alkaline tap water solution; (9) thermocouple; (10) manometer; (11) filter containing zeolite molecular sieve 5Å and iron sulphate ;(12) cooler; (13) gas burette graduated at room temperature in 0.1 ml increments, filled with deionized water for hydrogen gas volume collecting; (14) hydrogen volume collected; (GC) gas chromatograph; (IP) pressure indicator; (ID) flowmeter.

The flat-bottomed glass was placed in bath filled with water maintained at room temperature to prevent overheating. The gas was passed through a filter to remove water content and to retain ammonia, and then the volume of hydrogen was measured. For this, the outer walls of the filter were cooled using colder water (5-10 ^{O}C), and the filter was filled with layers consisting from zeolite molecular sieve 5Å and iron sulphate ($FeSO_4.7H_2O$). The volume of hydrogen released was determined by the water trap method and corrected at standard temperature and pressure (STP). Atmospheric pressure was established of local weather office. All experiments were performed at a temperature of 20^{O}C and an atmospheric pressure of 759 mm of Hg. The hydrogen gas released was directed into an inverted burette of 1000 to 2000 ml, containing deionized water. The hydrogen gas has displaced the water from burette, and the changing of the water level in the burette was noted as a function of time. The rate of change of the water level in the burette is determined by the production rate of hydrogen in the hydrolysis reaction and the difference between the initial and final water level represents the total volume of hydrogen generated. At regular intervals (1.2, 3 or 5 minutes) were collected gas samples, using gas-tight syringe of 1 ml. Then it was determined gas composition and the purity of H_2 released from reaction. The gas composition was established bygas chromatography method, using agas chromatograph type HewlettPackard5890A. This was equipped with two detectors, (flame ionization and thermal conductivity) two columns (Porapak-Q and5Amolecular sieve) and it was used as carrier as argonor helium, depending on the components which were determined. To study the hydrolysis reaction between aluminum and water were made two types of experiments. In the first set of experimental tests has been used the laboratory system shown in Figure 2, pure aluminum powder and aluminum powder dross. The data obtained were compared between them regarding the volume of hydrogen released from the reaction of aluminum with tap water, with or without addition of ammonia. The influence of parameters such as pH value and aluminum amount on aluminum-water reaction rate and hydrogen yield was studied. As a result of this original process, it was designed and assembled a hydrogen generation device and then it was evaluated the process of continuous release of hydrogen from the reaction of the mechanically milled aluminum dross with alkaline tap water(containing 2 ml ammonia aqueous solution of 25wt% /$L_{tap\ water}$).

III. RESULTS AND DISCUSSION

3.1 Reaction of aluminum with water

The concept of hydrogen production by the hydrolysis reaction of alkaline or alkaline-earth metals with water is known [2, 3]. More recently, these researches were enhanced and this is reflected in an increased number of publications and patents that are directed to the hydrogen production, through reactions between water and aluminum based metal [5-7]. All of the aluminum based approaches propose activation methods to remove the protective layer of aluminum oxide, thus allowing the hydrolysis reaction to start and proceed. The following exothermic reactions are possible when activated aluminum particles come in contact with water:

$$2Al + 6H_2O \rightarrow 2Al(OH)_3 + 3H_2 + \Delta H \quad (1)$$

$$2Al + 4H_2O \rightarrow 2AlO(OH) + 3H_2 + \Delta H \quad (2)$$

$$2Al + 3H_2O \rightarrow Al_2O_3 + 3H_2 \quad + \Delta H \tag{3}$$

The first reaction forms the aluminum hydroxide ($Al(OH)_3$) known as bayerite and hydrogen, from the second reaction results the aluminum hydroxide (AlO(OH)) known as boehmite and hydrogen , and from the third reaction results aluminum oxide (Al_2O_3) known as alumina and hydrogen. All above reactions are thermodynamically possible from room temperature till the aluminum melting point (660^OC) and are highly exothermic. The thermodynamic of all above reactions indicate that aluminum could spontaneously react with water, but in practice if a piece of aluminum is dropped into water under room temperature or even with boiling water conditions will not react, because the aluminum surface has an adhering and thin coherent layer of oxide (Al_2O_3), which prevents the reaction. Therefore, the key to starting and maintaining the reaction of water with aluminum at room temperature is the permanent disruption and removal of the hydrated alumina thin layer on the surface. In this work the activation method of aluminum dross particle surface is based on mechano-chemical technique, including the mechanical milling method and analkaline environment with high pH value. Bymechanical milling of aluminum dross are obtained particles to size ≤ 100 μm and was removed the protective layeron the surface of aluminum particles, thus favoring the onset of reaction. Also, the presence of nitride (AlN), salts in sufficient quantity, in particular KCl, NaCl, and oxides such as CaO, MgO (Table 1), when mixed with metals other than aluminum, acts as a catalyst for the reaction between Al and water. Also, a strong alkaline medium dissolves the oxide layer on the surface of the aluminum particles. In most studies this alkaline environment is created by adding an alkali hydroxide (NaOH or KOH)[4, 11]. Analyzing the dross composition (Table 1) it can be seen that contains AlN and Na and K salts (NaCl, KCl). As shown in other studies [22,23]on hydrolysis behavior of AlN in water and different solutions it was found that this hydrolyzes faster and more efficient in alkaline solutions. Hydrolysis process occurs according to the reactions:

$$AlN + 2H_2O \rightarrow AlOOH + NH_3 \tag{4}$$

$$NH_3 + H_2O \rightarrow NH_4^+ + OH^- \tag{5}$$

$$AlOOH + H_2O \rightarrow Al(OH)_3 \tag{6}$$

According to the reaction (4) by hydrolysis of AlN result NH_3 that rapidly dissolves, according to the reaction (5) and leads to an increase in pH value of the water and helps to solubilize and remove the protective oxide layer. In our experiments, the high alkaline environment was created , first, by adding of 2 ml NH_3aqueous solution of 25wt% /$L_{tap\ water}$ to stimulate the hydrolyze of AlN, and then by salts of sodium, potassium and calcium oxides , which are present in the initial composition of the dross (Table 1) and in contact with water also hydrolyze and cause an increase in pH value. In Fig. 3 is presented the changing in pH value, using different amounts of ammonia aqueous solution of 25wt% / $L_{tap\ water.}$

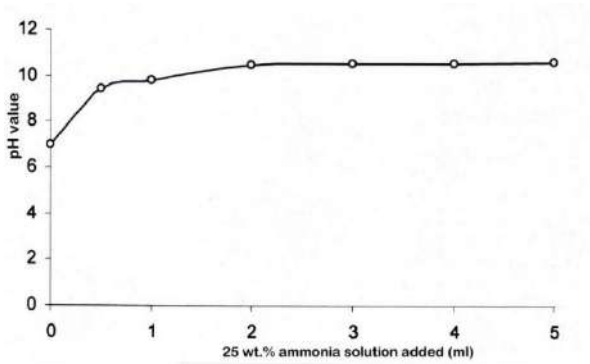

FIGURE 3. The pH value variation by adding of different quantity of NH_3 aqueous solution of 25wt% /$L_{tap\ water}$

By adding 0.5 ml, 1 ml and 2 ml aqueous ammonia solution 25wt% / $L_{tap\ water}$, the pH value of tap water increased from initial value of 6.95 to a value of 9.43, 9.81 and 10.45 respectively. Further increase in the amount of 25 wt% aqueous ammonia solution / L has not led to a substantial increase in pH value, this remaining almost constant (Fig. 3).As a result, the amount of 2 ml aqueous ammonia solution 25wt% / $L_{tap\ water}$ has been used to create a water with an pH of 10.45, enough to accelerate the AlN, NaCl, KCl, CaO and MgO hydrolysis reactions and to lead to an increase of pH value (≥12.4). This higher alkaline environment accelerates the Al corrosion process, removing the oxide layer on the Al particle surface by its solubilizing and releasing the hydrogen.

Using the laboratory system presented in Fig. 2, some experiments were performed in order to get more details on hydrolysis reaction regarding certain factors affecting the reaction rate and hydrogen yield, such as pH value and aluminum amount. In a

first experiment , 71.1ml of gas was obtained in 15 min, using 1 g of Al powder (≤ 100 µm) with 200 ml tap water having the value pH of 6.95, at the room temperature (Fig 4a, Table 2).

TABLE 2
Hydrogen volume released from reaction of 1g Al powder (≤ 100µm) with 200ml tap water (without NH_3 solution 25wt.%), pH= 6.95

Time (min)	1	2	3	4	5	6	7	8	9	10	11	12	13	14	15	16
$H_{2released}$(ml)	7.6	26.4	38.1	47.3	53.8	59.5	61.4	65.2	69.2	69.9	70.6	71.1	71.3	71.2	71.2	71.23

TABLE 3
Hydrogen volume released from reaction of 1g Al powder (≤ 100µm) with 200ml tap water (with 2 ml NH_3 solution 25wt.%/$L_{tap\ water}$), pH= 10.45

Time (min)	1	2	3	4	5	6	7	8	9	10	11	12	13	14	15	
$H_{2released}$(ml)	20.4	48.7	66.8	74.9	83.5	167.1	250.5	334.2	417.5	503.2	584.5	667.8	751.2	853.2	919.6	

In this case, the hydrolysis reaction rate was found to be slowly. Figure 4b and Table 3 present the rate of hydrogen production using 1 g Al powder, 200 ml tap water having the pH value of 10.45, at the room temperature. Analyzing this experiment, it may be observed that the rate of H_2 production during the first minutes is high, that means the rate of Al corrosion particles is also high. From first minute to 12th minute, the production rate goes on increasing and after the production remains almost constant with time. The morphology of initial Al powder is presented in the SEM images, Fig. 5. It can be observed that it consists of a lot of spherical particles of different size diameters, from 20 µm to 100 µm. Reacted Al particles coexist with the unreacted particles, and there are even the particles partially covered with products of hydrolysis reactions.

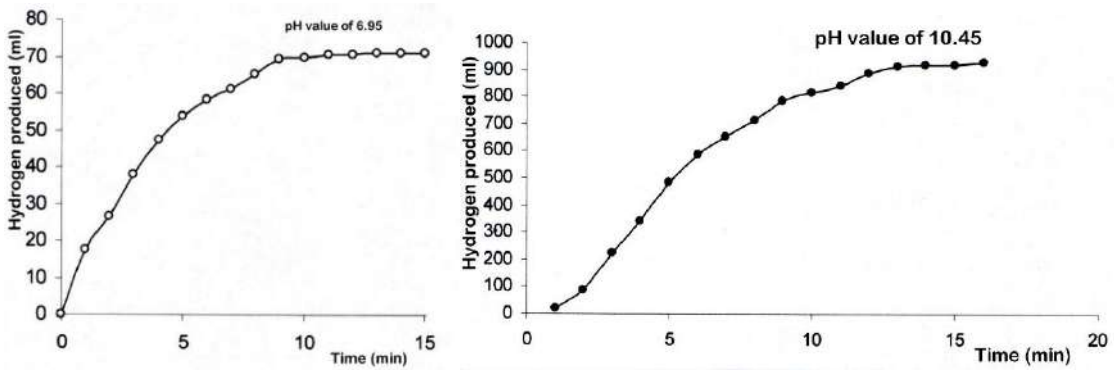

(a) (b)

FIGURE 4. Hydrogen production using 1 g Al powder with particle size ≤100 µm, 200 ml tap water having the pH value of 6.95 without ammonia solution adding (a) and the pH value of 10.45, by adding 2 ml ammonia solution of 25%/$L_{tap\ water}$ (b), at room temperature.

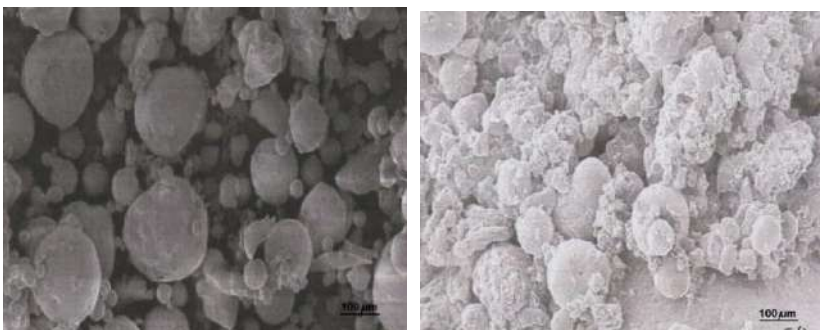

(a) **(b)**

FIGURE 5. SEM images of microstructures of Al particle surfaces: initial Al particles (a) and after hydrolysis with tap water at pH 10.45 for 15 mins (b) at room temperature

Catalytic reaction of aluminum with water produces an important heat quantity and hydrogen gas. As was stated, the presence in dross composition of an effective amount of nitride (AlN), salts (NaCl, KCl), oxides such as CaO, MgO, they play a role of catalyst. Starting at 20^{O}C, the temperature in the reactor was modified according to the graph from Fig. 6. There is a period of a few minutes for the heating phase, after which the temperature is stabilized at about 45.2 ^{O}C. After about 18 minutes, the temperature drops, reaching within minutes at about 21 ^{O}C, indicating the exhaustion amount of aluminum in reaction with the water.

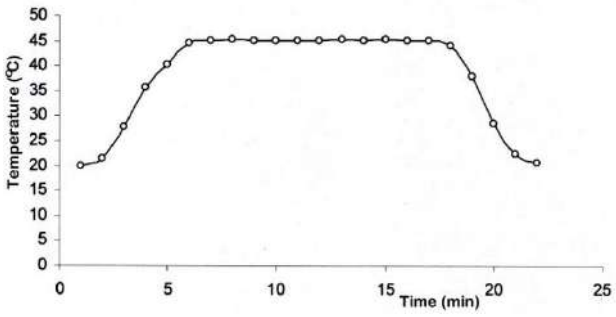

FIGURE 6. Variation of temperature over time for the reaction of hydrogen gas production (temperature of 20^{O}C; 1 g Al powder with particle size ≤100 µm, 200 ml tap water with a pH of 10.45)

Fig. 7 and Table 4 show the hydrogen volume produced using different aluminum amounts (1, 2 or 3 g Al powder respectively) and 200 ml tap water having a pH value of 10.45 for each experiments, obtained by adding 2 ml ammonia solution of 25%/$L_{tap\ water.}$

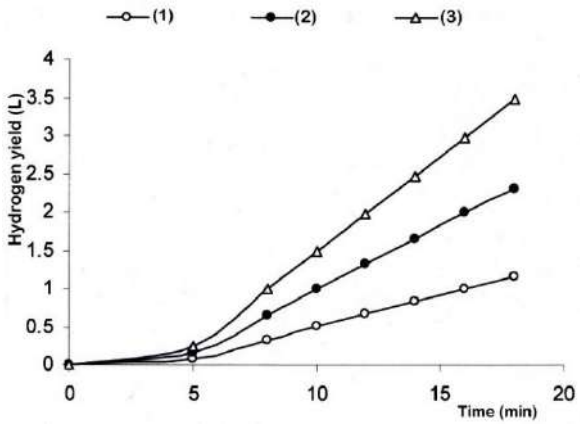

FIGURE 7.Hydrogen production using 1 g, 2g and 3g Al powder respectively ,with particle size ≤100 µm, 200 ml tap water having a pH value of 10.45 obtained by adding 2 ml NH_3 solution of 25%/L , at room temperature.

TABLE 4
Hydrogen volume released from reaction of 1g, 2g and 3g Al powder (≤ 100µm) and 200 ml tap water (with 2 ml NH_3 solution 25wt.%/$L_{tap\ water}$), pH= 10.45

Time (min)		H_2 (L) $_{calc}$ Yield,η (%)								
		5	8	10	12	14	16	18	(18 min)	
$H_{2released}$ (L)	(1g Al)	0.083	0.334	0.503	0.667	0.835	1.002	1.169	1.244	93.97
	(2gAl)	0.163	0.661	0.991	1.322	1.648	1.990	2.311	2.488	92.88
	(3g Al)	0.247	0.997	1.491	1.971	2.478	2.976	3.486	3.732	93.41

Average efficiency = 93.42 %

Analyzing the data obtained from these experiments, it may be concluded that the H_2 production is high. From first minute to five minutes, the H_2 volume produced increases slightly, after the H_2 volume produced increases rapidly; the production rate

is nearly constant (Table 4).The H_2 volume produced is close to that theoretical. The effect of increasing of Al amount on the hydrogen volume produced also can be seen in Fig. 7 and Table 4. The amount of hydrogen produced increases almost linearly with the amount of aluminum used. For example, when using 2 or 3 g Al, at the same reaction time, the hydrogen volume released is almost double or triple, compared to that obtained from 1 g Al, the reaction efficiency being higher than 93%.

3.2 Reaction of aluminum dross with water

Using the same laboratory system (Fig. 2) the pure Al powder was replaced by an appropriate amount of Al dross (Table 1) that to contain the same amount of Al such as: 6.548g Al dross containing1 g Al;13.097g dross, containing 2 g Al and 19.646 g dross containing 3 g Al, respectively. Fig. 8 and Table 5 show the hydrogen volume produced using these aluminum dross amounts and 200 ml tap water containing 2 ml NH_3aqueous solution of 25wt% /$L_{\text{tap water}}$, having a pH value of 10.45.

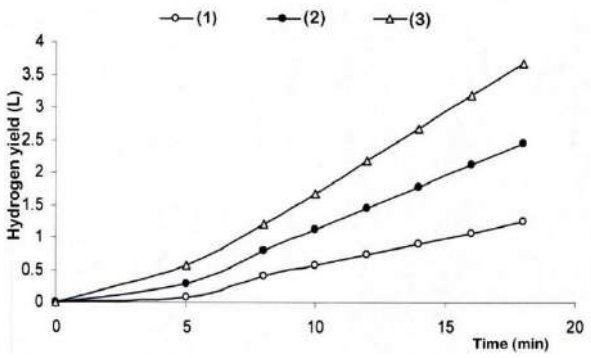

FIGURE 8. Hydrogen production using 6.548, 13.097 and 19.646 g Al dross respectively, size particles ≤100µm, tap water with pH value of 10.45, room temperature.

TABLE 5
Hydrogen volume released from reaction of 6.548g, 13.097g and 19.646g Al dross powder (≤ 100µm) and 200 ml tap water (with 2 ml NH_3 solution 25wt.%/$L_{\text{tap water}}$), pH= 10.45

Time (min)	H_2 (L) $_{calc}$ Yield,η (%)							
	5	8	10	12	14	16	18	(18 min)
$H_{2released}$ (L)	(6.548g Al dross)	0.089	0.402	0.566	0.734	0.897	1.067	1.235	1.244	99.29
	(13.097gAl dross)	0.277	0.798	1.123	1.453	1.784	2.114	2.447	2.488	98. 37
	(19.646g Al dross)	0.565	1.197	1.683	2.184	2.673	3.176	3.672	3.732	98.39

Average efficiency = 98.68%

Adding 200 ml of tap water having a pH value of 10.45 over 6.548g; 13.097g and 19.646 g Al dross respectively, the pH value was increased (≥ 12.4), this increase being due to hydrolysis of AlN, salts, calcium and magnesium oxides present in the dross composition. Increasing of the pH value leads to speeding up the activation surface of aluminum particles, potentially reactive with water, according to reactions (1, 2, 3). In Figure 8 is shown the H_2 volume released during the reaction of Al dross powder ,size particles ≤100µm, with 200 ml tap water containing 2 ml ammonia aqueous solution of 25wt% /L and having a pH value of 10.45, at room temperature. Al dross powder showed almost no apparent reaction with tap water of 6.95 pH, whereas in tap water of 10.45 pH, aluminum exhibits effervescent reaction with hydrogen release. Analyzing the data obtained from these experiments, it may be concluded that the H_2 production is high. From first minute to five minutes, the H_2 volume produced increases slightly, after the H_2 volume produced increases rapidly; the production rate is also nearly constant (Table 5).The H_2 volume produced is very close to that theoretical. The effect of increasing of Al dross amount on the hydrogen volume produced also can be seen in Figure 8. The volume of hydrogen produced increases almost linearly with the amount of aluminum dross used. For example, when using 13.097, 19.646 g Al dross, at the same reaction time, the hydrogen volume released is almost double or triple, compared to that obtained from 6.548 g Al dross, the reaction efficiency is > 98% and this being higher than that in case of using pure Al powder (>93%), see Table 4 .This could

be explained by creating a higher alkaline environment that resulted from solubilization of AlN, sodium and potassium salts, as well as of CaO, MgO in reaction with the water (e.g achieving a pH of 12.45 instead of 10.45 pH value) and which accelerates the activation process of Al surface and Al reaction with water, releasing hydrogen, or even the hydrolysis reaction of the other metals present in the composition of the dross, releasing of hydrogen as well. The composition of the gas product was determined at the exit of the reactor and an average is: 98.42 vol.% H_2; 1.26 vol.% NH_3; 0.11 vol.% N_2; 0.21 vol% H_2O.The hydrogen purity after passed through the filter, where was retained the moisture and NH_3 was also determined . An average value obtained was 99.73vol.% H_2. The HN_3 was removed by chemosorption process using ferrous sulfate, according to the reaction (7)

$$3[FeSO_4.7H_2O] + 3NH_3 \rightarrow 3(NH_4)_2SO_4 + Fe_3O_4 + 17H_2O + H_2\uparrow \quad (7)$$

The reaction is fully, the entire quantity of NH_3 from hydrogen produced is retained. The calculation of the necessary quantity of $FeSO_4.7H_2O$ was done in accordance with the reaction stoichiometry. Humidity has been reduced from 0.21vol. % to 0.05 vol. %, by adsorption on zeolite molecular sieve 5A. Hydrogen generation rate is very important in this process and it can be determined by variables that can be controlled as hydrogen yield calculated with equation (8):

$$\eta\%H_2 = (nH_2(t)/nH_2O)x100 \quad (8)$$

where nH_2O is the number of water moles consumed in the reaction and reaction rate is given by equation (9):

$$v(H_2) = dv(t)/dt \quad (9)$$

3.3 Hydrogen generating device based on aluminum dross hydrolysis process

Based on experimental data obtained, a continuous hydrogen generating device was designed and assembled and hydrogen volume produced during the hydrolysis reaction of mechanically milled aluminum dross with tap water containing 2 ml ammonia aqueous solution of 25 wt% /L was evaluated. The scheme of the steps taken for hydrogen production is presented in Fig. 9 and the schematic device is shown in Fig. 10. The characteristics of reactor were described in reference [24]. The cartridge was designed as a perforated basket, lined with felt on the inside wall and it was filled with aluminum powder dross (≤100μm). Lining cloth was used to prevent the passage of dross particles through the holes of basket wall and to ensure continuous absorption of water from the tank and also to allow the leakage of the gas released from the reaction of aluminum particles with water through holes.

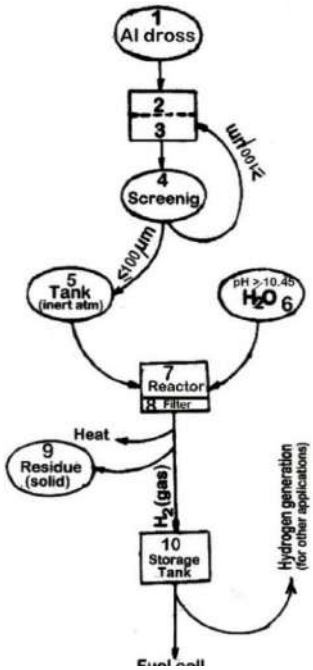

FIGURE 9. Schematic representation of the steps taken for hydrogen production process using aluminum dross and water

Hydrogen generating process as schematically is presented in Fig. 9, is based on the reaction of aluminum dross with water and includes several stages. The use as raw material of the aluminum dross is expected to result in the form of pieces of

different sizes (Fig. 1 a) from the primary and secondary production of aluminum metal from or (bauxite) or recovered scrap from various sectors such as automotive, cans, beer, construction, etc. Hard dross (1) is crushed by crushing (2) and then converted into powder by milling (3), for this operation using a ball mill. Milling stage is followed by screening stage(4) for fraction separation containing particles with size $\Phi \leq 100$ μm , which are stored in the tank (5) under an inert atmosphere of argonto maintain the active surface of the aluminum metal particles. Fraction consisting of particles $\Phi \geq 100$μmsizeis returnedin(3) for regrinding and resorting. Powder in the tank (5) with $\Phi \leq 100$ μm particle sizes is used to fill the reactor cartridge (6). From the tank (7) it is inserted into the reactor (6) water (tap or industrial water, containing 2 ml NH_3 solution of 25 wt. %/L). At contact between water and aluminum particles, which were activated on the surface by mechanical grinding, inreactor (6) takes place first the phenomenon of hydrolysis of AlN, salts of Na, K and oxides of Ca and Mg, present in the composition of the dross, resulting in an increase of alkaline pH from 10.45 to ≥12.4) in the reaction area, an environment that favors the onset of the reaction between metal particles of active Aland water to obtain hydrogen of high concentration(> 99.5% vol) and release heat , according to reactions(1 - 3).

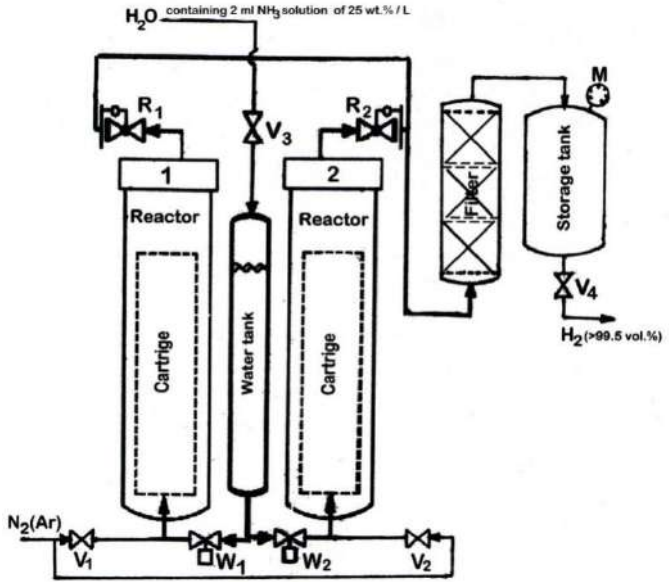

FIGURE 10: A schematic representation of hydrogen production system: (1) and (2) reactors containing fuel cartridge filled with Al dross powder; water tank; filter containing zeolite molecular sieve 5Å and $FeSO_4.7H_2O$; M – manometer; R_1, R_2 –three-way valves; V_1,V_2,V_3, V_4 – valves; W_1,W_2-water valves;

A schematic representation of hydrogen generating device is presented in Fig. 10. The capacity of the device is of about 2 kg of Al dross powder (≤ 100 μm) for each reactor, which contains about 305.4 g Al. The initial temperature is room temperature. The gas released from the reaction passes through the layers consisting of molecular sieve 5A and ferrous sulphate from the filter. Here, the hydrogen gas is purified by removing moisture and ammonia. Further, the hydrogen is collected in the storage tank. First reactor unit worked continuously ≈ 9 h at a hydrogen generation rate of about 0.735 L/min. The purity of hydrogen produced was 99.58vol %. After about 9 hours of operation, the reactor (1) was disconnected by closing water valves (W_1) and R_1, while was connected the reactor (2) by opening water valves (W_2) and R_2, thus ensuring continuous operation of the device. Hydrogen gas resulted can be taken by the user (eg. a fuel cell or industrial applications, Fig. 9).The data obtained in our research can provide the basis for scale implementation of the aluminum dross hydrolysis process to generate hydrogen. We have reached the very important conclusion that by hydrolysis process of aluminum waste such as Al dross can be obtained hydrogen of high purity (>99.5 vol.%).

IV. KEY ASPECTS ASSOCIATED WITH THE PRODUCTION OF HYDROGEN USING Al DROSS

As mentioned, thhydrolysis reaction of the pure aluminum metalis typically used for the production of hydrogen. Although the use of pure aluminum in reaction with water to produce hydrogen is a viable method, it is expensive, if it is considered the cost of producing aluminum in the form of pure metal and alkali hydroxide consumption, also an expensive product. The key aspects associated with the production of hydrogen using the aluminum metal-water reaction are as follows: Aluminum required: 9kg Al per 1kg H_2 produced, considering 100% yield; A gravimetric hydrogen capacity of 3.7 wt.% (materials only); A volumetric hydrogen capacity of 36-46 khH_2/L (materials only); Reaction kinetics: $2x10^{-4}$gH_2/sec/g of Al [25];A production cost: ≈ € 5.7 per kg H_2 (based on the cost of electricity for aluminum production and considering only the reduction of alumina to metal aluminum step) [25,26].If there are considered and the steps required to produce alumina from bauxite and alkali hydroxide consumption required in hydrolysis reaction, certainly the costs are much higher. From published data to date [25, 26],the worldwide the aluminum industry produces over 4.5 billion kilograms of aluminum waste per year. Each type of waste has unique physical and chemical characteristics, and the waste value is determined by the level

of impurities contained and the cost required for metal recovering. Taking into account the chemical composition of aluminum dross presented in Table 1, it follows that1 kgof dross contains 0.1527kgAl, amount that can react with water to produce hydrogen and aluminum oxy-hydroxide or other Al compounds. Alkali hydroxide consumption is zero, in this case , the alkaline reaction medium is ensured by adding of 2 ml ammonia aqueous solution of 25wt% /L water used, (meaning a very small quantity), and this being much cheaper than an alkali hydroxide and also by the content of AlN , Na, K salts and Ca, Mg oxides, present in the dross composition(as we noted in the description presented above).By extrapolation, 9 kgAl needed to produce1 kgH_2 (considering 100% yield) corresponding to an amount of≈ 59 kg dross. Since this is a waste (with negative consequences on the environment by landfill), its use to produce hydrogen and other high value products (aluminum oxy-hydroxide, alumina, etc.) leads to a viable and advantageous solution because capitalizes a possible hazardous waste to the environment and people and reduces significantly the cost of hydrogen production. Also, it solves an environmental issue by reducing the negative environmental impact and it leads to lower energy and raw materials consumptions necessary for obtaining pure aluminum metal and alkali hydroxide, materials involved in the reaction with water to release hydrogen. Other resulting benefits cover issues such as reducing the volume of aluminum waste disposed in landfills, conserving energy and natural resources used to produce new aluminum amounts, reducing landfill disposal fees, generating of new renewable energy sources and encouraging the recycling of other kinds of wastes. Recycling aluminum waste can only bring benefits to society at lowering the cost of production for a big number of products that are used every day, among them being and the hydrogen. Maybe people should be encouraged to reuse this material if they know some basic statistics such as that a piece of aluminum naturally disappear after 100 years, but by recycling it could save energy to produce 20 pieces of recycled. The ore from which obtain aluminum is bauxite and current reserves of bauxite are sufficient for another 400 years, but recycling 1kg of aluminum it could save ≈ 8 kg of bauxite, 4 kg of chemicals and 14 kWh of electricity[26],obvious benefits both economical and energetical. Also, the fact that hydrogen will become certainly clean energy source for the future, should be supported the processes of its obtaining , starting from such sources of cheap raw materials, which will lead to reduction in the cost of production.

V. CONCLUSIONS

An investigation of hydrogen production using aluminum dross and tap water with high pH value (≥10.45) was made. The experiments conducted at laboratory scale allowed determining the amount of hydrogen generated and processing temperature. Data obtained showed that the fast and self sustained hydrolysis reaction of activated Al dross particles with tap water, whose pH was increased from 6.95 to 10.45 by adding of 2 ml ammonia aqueous solution of 25wt% /L, takes place, starting from the room temperature and can release hydrogen of high purity(>99.5 vol.%). Based on experimental laboratory data, a continuous hydrogen generating device was designed and operated. Its operation shows clearly that Al dross can be successfully used for producing hydrogen of high purity. The key aspects associated with the production of hydrogen, using Al dross, certainly present only benefits to society, contributing to lowering the cost of hydrogen production and to solve an environmental issue by reducing the negative impact. The data obtained in our research can provide the basis for scale implementation of the aluminum dross hydrolysis process to generate hydrogen. This process is based on aluminum hydrolysis, consuming only water and aluminum dross which are cheap raw materials. As a consequence, this process could be a feasible alternative for CO_2 free hydrogen production for fuel cell or other applications.

ACKNOWLEDGMENTS

Financial support for this research was provided by the National Agency of Scientific Research and Innovation from Romania, National Plan of Research & Development in Energy and Environment field, project PN 09 19 01 19/2015

REFERENCES

[1] N.Z. Muradov, T.N.Veziroglu , Green path from fossil-based to hydrogen economy: an overview of carbon-neutral technologies. Int J Hydrogen Energy (33)2008,pp.6804-6839.
[2] J.Turner, G.Sverdrup, M.K. Mann , P.C. Maness , B. Kroposki , M. Ghirardi et al. Renewable hydrogen production. Int J Energy Res (32)2008, pp.379-407.
[3] M.Ball M, Wietschel M. The future of hydrogen -opportunities and challenges. Int J Hydrogen Energy 2009;34:615-627.
[4] A.G.Stern, Design of an efficient, high purity hydrogen generation apparatus and method for a sustainable, closed clean energy cycle.Int J Hydrogen Energy(40) 2015,pp.9885-9990.
[5] M.H. Grosjean , M. Zidoune, L. Roue , J.Y. Huot . Hydrogen production via hydrolysis reaction from ball-milled Mg based materials. Int J Hydrogen Energy (31)2006pp.109-119.
[6] O.V. Kravchenko , K.N. Semenenko , B.M. Bulychev , K.B. Kalmykov . Activation of aluminum metal and its reaction with water. J Alloys Compd (397)2005,pp.58-62.
[7] H.Z. Wang , D.Y.C. Leung , M.K.H. Leung , M.Ni , A review on hydrogen production using aluminum and aluminum alloys.Renew Sustain Energy Rev (13) 2009, pp. 845-853.
[8] T. Hiraki , M.Takeuchi , M. Hisa , T. Akiyama . Hydrogen production from waste aluminum at different temperatures with LCA. Mater Trans (46) 2005, pp.1052-1057.

[9] A.V. Parmuzina , O.V. Kravchenko, Activation of aluminum metal to evolve hydrogen from water. Int J Hydrogen Energy(33) 2008, pp3073-3076.
[10] E. David, J. Kopac,. Aluminium recovery as a product with high added value using aluminium hazardous waste.J Haz Mat (261)2013, pp.316-324.
[11] N. S. Ahmad Zauzi, M. Z. H. Zakaria, R. Baini, M. R. Rahman, N. Mohamed Sutan, and S. Hamdan, Influence of alkali treatment on the surface area of aluminium dross, Advances in Materials Science and Engineering,Volume 2016,http://dx.doi.org/10.1155/2016/6306304
[12] B. Alinejad, K. Mahmoodi . A novel method for generating hydrogen by hydrolysis of highly activated aluminum nanoparticles in pure water. Int J Hydrogen Energy, (34) 2009,pp.7934-7938.
[13] L. Soler , J. Macana , M. Munoz, J. Casado , Aluminum and aluminum alloys as sources of hydrogen for fuel cell applications. J Power Sources(169) 2007,pp.144-149.
[14] L..Soler, A.M. Candela , J. Macanas , M. Munoz , J. Casado, Hydrogen generation from water and aluminum promoted by sodium stannate. Int J Hydrogen Energy , (35)2010, pp.1038-1048.
[15] Z.Y. Deng, Y.B.Tang, L.L. Zhu, Y. Sakka , J.H. Ye, Effect of different modification agents on hydrogen-generation by the reaction of Al with water. Int J Hydrogen Energy, (35) 2010, pp.9561-9568.
[16] M. Kitano, K. Tsujimaru, M. Anpo, Hydrogen production using highly active titanium oxide-based photocatalysts. Top Catal (49) 2008, pp.4-17.
[17] Z.Y. Deng, J.M.F. Ferreira, Y. Sakka , Hydrogen-generation materials for portable applications. J Amer Ceram Soc., (91)2008, pp.3825-3834.
[18] U. K. Sultana, F. Gulshan, M. A. Gafur, and A. S. W. Kurny,"Kinetics of recovery of alumina fromaluminium casting wastethrough fusion with sodium hydroxide," American Journal of Materials Engineering and Technology, vol. 1, no. 3,2013, pp. 30–34.
[19] P.Dupiano , D. Stamatis , E.L. Dreizin, Hydrogen production by reacting water with mechanically milled composite aluminum-metal oxide powders. Inter J Hydrogen Energy, (36) 2011, pp.4781-4791.
[20] H.W.Wanga, H.W. Chung, H.T. Teng , G. Cao, Generation of hydrogen from aluminum and water end effect of metal oxide nanocrystals and water quality. Inter J Hydrogen Energy, (36) 2011pp.15136-15144.
[21] S.Duman, S. Ozkar, Hydrogen generation from the dehydrogenation of ammonia-borane in the presence of ruthenium(III) acetylacetonate forming a homogeneous catalyst. Inter J Hydrogen Energy, (38) 2013,pp.180-187.
[22] A.V. Ilyukhina , A.S. Ilyukhin , E.I. Shkolnikov , Hydrogen generation from water by means of activated Aluminum, Inter J Hydrogen Energy,(37) 2012, pp.16382-16387.
[23] P. Li , M. Guo1, M. Zhang , L.D.Teng, S.L. Seetharaman, Leaching process investigation of secondary aluminium dross: Investigation of AlN hydrolysis behaviour in NaCl solution, Min Proc Extractive Metallurgy (Trans. Inst. Min. Metall. C), 121(3) 2012,pp.140-146.
[24] E. David, J. Kopac , Hydrolysis of aluminum dross material to achieve zero hazardous waste. J Haz Mat, (209) 2012, pp.501-509.
[25] S. Satyapal , J. Petrovic , C. Read ,G.Thomas , G. Ordaz ,The U.S. Department of Energy's National Hydrogen Storage Project: Progress towards meeting hydrogen-powered vehicle requirements, Catalysis Today,(120)2007,pp.246-256.
[26] F.Habashi, "A short history of hydrometallurgy". Hydrometallurgy 2005;79:15–22. *doi:10.1016/j.hydromet.2004.01.008*

Temperature Distribution and Numerical Modeling of Heat Transfer in Block 276 P1-Sand – Part I

R. Trabelsi[1*], A. C. Seibi[2], F. Boukadi[3], W. Chalgham[4], H. Trabelsi[5]

University of Louisiana, Dept. of Petroleum Engineering, Lafayette LA, USA

Abstract**—** *Eugene Island (EI) 276 fields presents an interesting case study of overpressure caused by uncompacted porosity, in addition to heat. Mechanics of sand deposition, transgressive shale, surrounding faults, overlying shale barriers and underlying salt diapirs have caused temperature anomalies in the P1-sand. Plio-Pleistocene sandstone reservoirs are supplied with mature hydrocarbons by migration of fluids from overpressured shales upwards along an active fault system. The heat carried by climbing fluids and the existence of highly conductive salt diapirs generate strong temperature variances disturbing the entire mini-basin. A COMSOL Multiphysics thermal simulation model has been developed to duplicate temperature variation in well #12, drilled in the proximity of a fault and a salt diapir. Recorded temperatures show a variation in the order of 42 ^{o}F across a shale barrier separating the reservoir from top formation. Heat conduction originating from the salt dome was found to be the dominant heat transfer mechanism, transgressive shale and shale barriers contributed to entrapment and led to overheating.*

Keywords**— Eugine Island, thermal analysis, heat transfer, temperature distribution.**

I. INTRODUCTION

EI330 oil field in the Northern Gulf of Mexico is a nearby giant oil and gas accumulation (Fig. 1), southwest of EI276. It was stated that the field has been the focus of an exceptional interdisciplinary effort to comprehend the changing aspects of an active oil field. The largest Pleistocene oil field in the world [Anderson *et* al., 1994], EI330 is at the staple of a dynamic growth fault system. Over the 30 years since discovery, multiple indications have revealed that hydrocarbons have been migrating along the fault during the recent history and are still flowing. This has been proven by: 1) the presence of hydrocarbon oozes at the sea floor, 2) differences between oil maturity in the multiple reservoirs, and 3) sequential changes in the composition of oils produced over the last 20 years [Anderson *et* al., 1994 and Holland *et* al., 1990]. Identifying the mechanisms of overpressure caused by heat will help direct future drilling and delineation activities in Block 276.

It was stated that unlike seismic traits, formation temperature can be an excellent indicator of long-term fluid circulation. The temperature variation is caused by a combination of possible fluid migration along faults and the presence of heterogeneous structures such as salt diapirs (domes) and transgressive shale, common in the Gulf of Mexico. In this study, we will be utilizing COMSOL to model heat transfer to justify temperature variation in well #12 and better interpret overpressure in P1-sand.

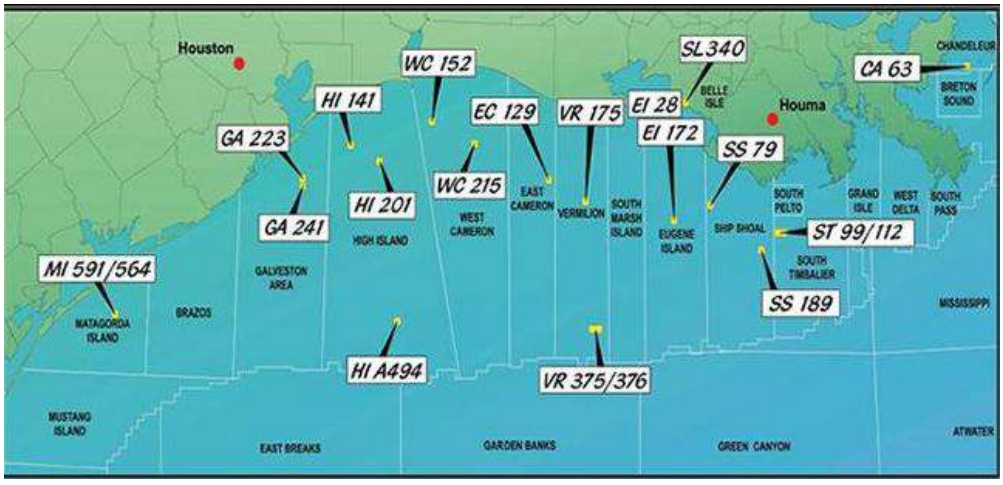

FIG. 1: EUGENE ISLAND FIELD LOCATION

II. GEOLOGICAL SETTINGS

EI276 is offshore St. Mary Parish, Louisiana, 65 miles from shore, under 170 ft of water. Shallowest salt was encountered at a depth of 4962 ft, the deepest salt was met at a depth of 14,150 ft. The deepest well, EI275, is Texaco OCS-G-0988 #4 drilled to a total depth (TD) of 14,495 ft. EI276 field neighbors EI330 lying under 246 ft of water, approximately 170 mi southwest of New Orleans, near the southern edge of the Louisiana Outer Continental Shelf.

The rapid influx of Upper Cretaceous and Lower Tertiary terrigeneous sediments from the ancestral Mississippi delta has mobilized the Jurassic Louann salt, which left a trail of isolated salt dome across the shelf, and formed semicontinuous salt uplifts under the slope of the Gulf Coast margin [Woodbury *et* al., 1973]. EI330 study area is made of nine property blocks located at the transition between these two salt provinces [Holland et al., 1990], with two salt diapirs underneath the South-East and the North-West corners of the study area. The Tertiary and Quaternary sediments overlying the salt define three main facies representative of the normal evolution of a deltaic system prograding across a continental margin [Selley, 1988; Holland *et* al., 1990, Alexander and Flemings, 1995]: 1) directly over the salt, massive shales and turbidites were deposited in a prodelta environment. 2) They are overlain by a sequence of proximal deltaic sands and transgressive shales deposited during sea-level fluctuations when the delta slope was located nearby. The most productive reservoirs of the field are in this interval [Holland *et* al., 1990]. 3) The uppermost section was deposited after the delta had prograded southward, and is composed of fluvial massive sands. The transitions between the different sedimentation phases were identified in the 3D seismic data by reflectors corresponding to transgressive episodes. Biostratigraphic markers Cristellaria "S" (Cris S) and Small Gephyrocapsa (2) (Sm Gep (2)) [Alexander and Flemings, 1995] define the bottom and the top of the proximal deltaic phase, respectively.

Structurally, the EI276 field is a classic salt-withdrawal shelf minibasin [Alexander and Flemings, 1995]. It is bounded by 4 main fault zones (see Fig. 2). The northern, western and southern boundaries are defined by normal faults, while the eastern border is defined by a fault that developed as extensional compensation during the salt withdrawal to the south. Oil and gas reservoirs are trapped under two rollover anticlines.

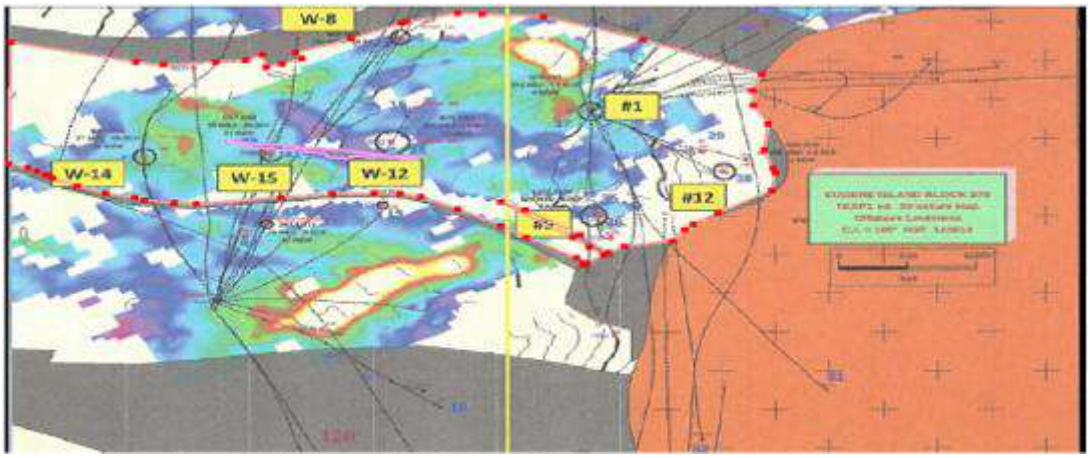

FIGURE 2: EUGENE ISLAND TOP STRUCTURAL MAP

III. TEMPERATURE DISTRIBUTION

Nagihara and Smith [2008] indicated that nearly 600 bottom-hole temperature data from the northern continental shelf of the Gulf of Mexico, each corrected for drilling disturbance, yielded a regional map of geothermal gradient down to approximately 3.7 mi sub–sea floor. Two geographic trends were seen on the map. First, from east to west, the geothermal gradient changes from values between 0.014 and 0.016°F/ft off the Alabama–Mississippi shore to lower values of 0.008 – 0.014°F/ft off eastern Louisiana and to higher values of 0.016 – 0.033°F/ft off western Louisiana through Texas. Second, thermal gradients tend to be lower toward the outer continental shelf (less than 0.0112°F/ft). The authors believe that the observed variations are primarily attributable to the thermal effect of rapid and regionally variable sediment accumulation during the Cenozoic era, which resulted in the occurrence of the geopressured zone in the Texas–Louisiana shelf. In the eastern Louisiana shelf, where accumulation was fastest, sediments down to about 3.7 mi are relatively young (about <15 Ma) and have not had enough time to fully equilibrate with deeper, hotter sediments. That resulted in the low thermal gradient. As the depocenter migrated farther offshore, younger sediments accumulated more in the outer shelf and resulted in an even lower thermal gradient there. However, this mechanism alone cannot explain the fact that geothermal gradients in the

Texas shelf are higher than those in the Alabama shelf, where Cenozoic sedimentation has been much slower. It may be suggested that the contrasting sedimentation history between the Texas and Alabama shelves has resulted in some difference in overall thermal conductivity of sediment, and that the geothermal gradients reflect such difference. However, it is more plausible if additional mechanisms enhance heat flow through sediment in the Texas shelf, such as (1) upward migration of pore fluid expelled from deep, overpressured sands and/or (2) a greater amount of heat released from the igneous basement. Deep sedimentary temperatures in the high-thermal-gradient areas suggest higher risks of hydrogen sulfide occurrence and reservoir quality degradation because of quartz cementation.

Leipper [1954] presented the average outer continental sea surface temperatures for the months of February and August. According to Leipper, the main feature of the average winter pattern is a gradual drop from approximately 75 ^{o}F in the South to an average of 65 ^{o}F in the North, in all parts of the Gulf of Mexico. In the Summer time, Leipper indicated that average temperatures are nearly constant at around 84 ^{o}F. It was also stated [Weatherford, 2009] that sea floor temperature in the Gulf of Mexico at Block 276 depths is at around an average of 60 ^{o}F.

Using well logs from W-4, W-8, W-12, W-15, #1, #9 and #12 in block 276 P1-sand, and an average sea floor temperature of 60 ^{o}F, the temperature gradient taken at depths greater than a shale barrier divide was calculated to be at 1.23 ^{o}F/100 ft (see well log temperature gradient plot in Fig. 3, below). This confirms the theory that a hotter gradient is active in well #12 and any future drilling and delineations have to be planned away from the eastern flank of Block #276, away from the salt diapir.

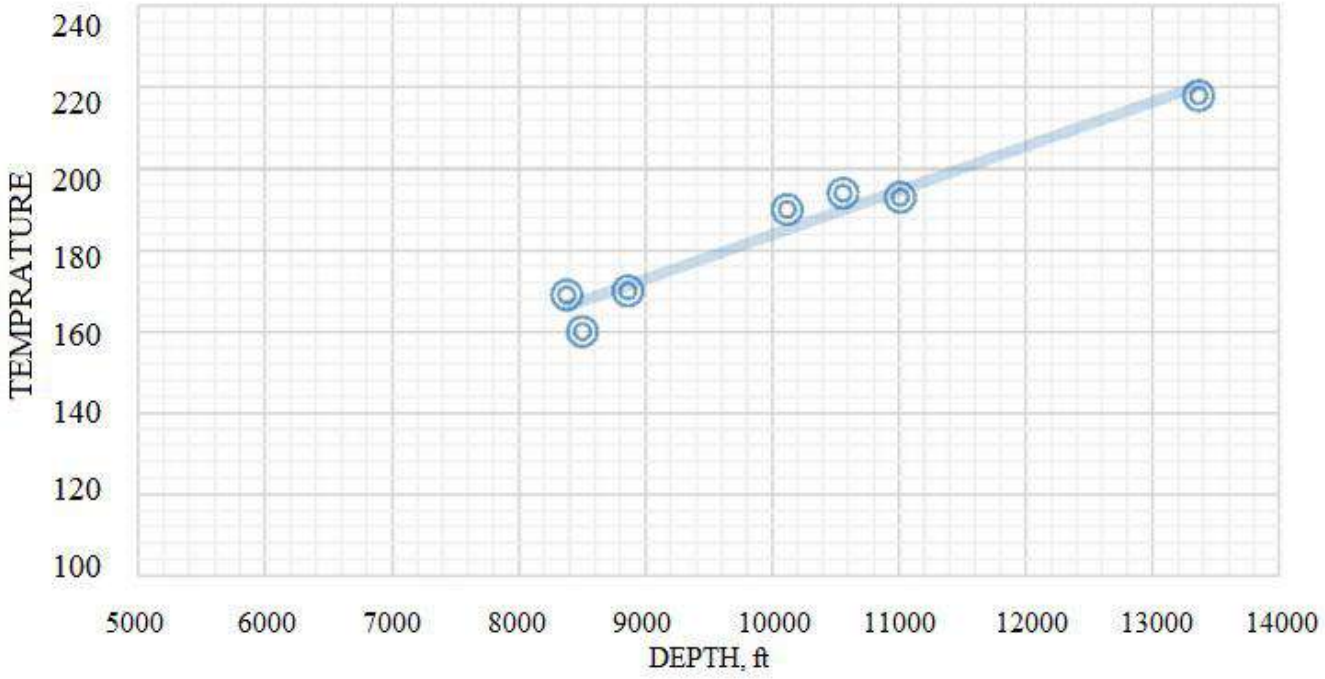

FIGURE 3: TEMPERATURE GRADIENT IN BLOCK 276 P1 SHALY SAND PORTION

Additionally, The P1-sand has seen a resistivity shift at the paleo marker at about 7500 ft [Lane and Macpherson, 1976]. This has also been observed from well testing information (see Fig. 4 below). Temperature has increased from 133 ^{o}F at a true vertical depth sub-sea (TVDSS) of 7573 ft to 165 ^{o}F at 7621 ft in well #12 (the closest well to the salt dome). The shift in temperature indicates that a heat source, transgressive shale, a barrier and obviously oil and gas accumulations, preventing heat dissipation and causing warming, exist. For that matter, resistivity logs from well #12 indicate that a shale barrier exits between the measured depths of 7573 and 7621 ft (see Fig. 5, below); thereby, resulting in heat entrapment.

The same could be said about transgressive shale in P1-sand depths of 7415 to 7680 ft (Fig. 5). The shift in temperature also indicates that a heat source leading to a hotter temperature is located nearby. Just below well #12, a salt diapir is the source of the heat (see top view of a section of Block 276 in Fig. 2, above).

Additionally, the following 3-D view (Fig. 6) also confirms that well #12 is in a hotter zone and that development wells should be planned on the downdip, western flank of the reservoir to prevent drilling hazards and future production problems. According to Forrest et al. [2007], the same phenomenon has been observed in EI292 with a temperature shift at Base Mud Line Depths (BMLD) between 2000 and 4000 feet (see Fig. 7).

FIGURE 4: TEMPERATURE PROFILE REVERSAL AT BOTTOM OF WELL #12 IN BLOCK 276 P1-SAND

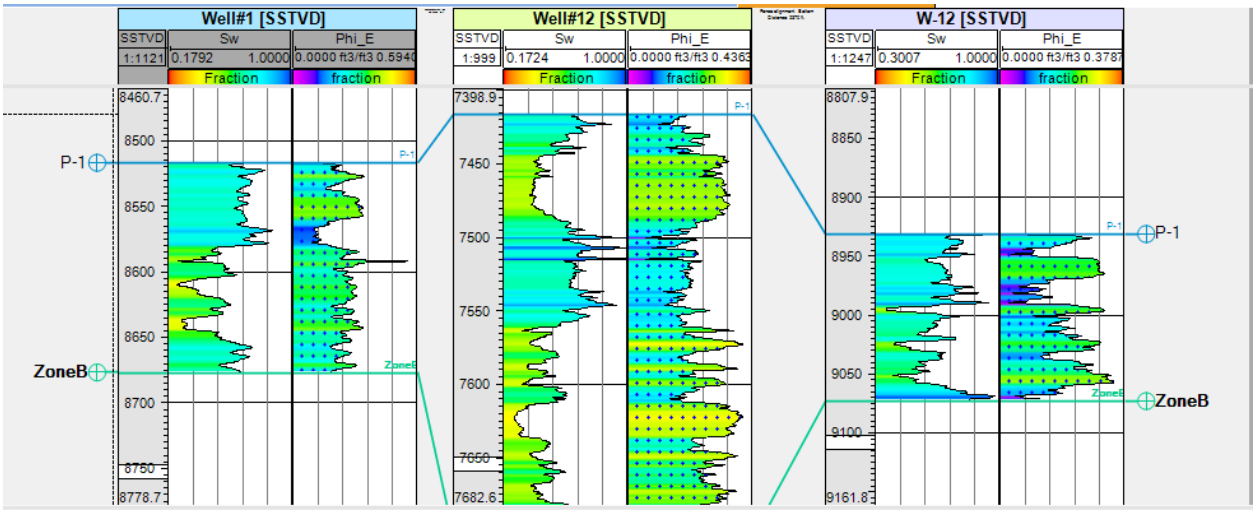

FIGURE 5: TRANSGRESSIVE SHALE AT DEPTHS (7415-7680 FT) CAUSING HEAT ENTRAPMENT

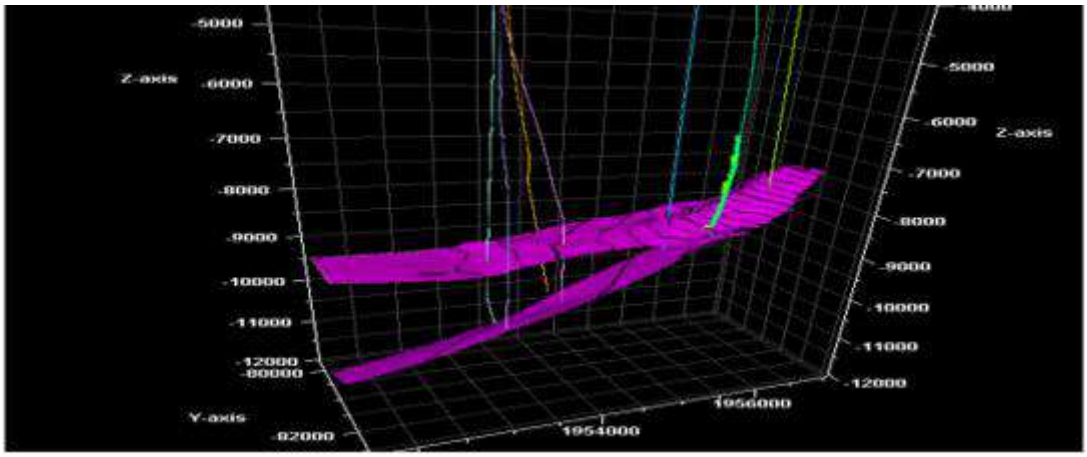

FIGURE 6: WELL #12 (FAR RIGHT, UPSTRUCTURE) CLOSE TO THE SALT DIAPIR

In their study of geothermal gradients and subsurface temperatures in the Northern Gulf of Mexico, the authors calculated geothermal gradients for 1131 fields and wells, and a map has been prepared showing the below-mudline depth to the 300°F subsurface isotherm over the northern Gulf of Mexico. The authors stated that since the 300°F isotherm values are a direct reflection of thermal gradient, thermal conductivity, and heat flow, the map may be considered as a portrayal of subsurface temperature distribution. They noted that based on interpreted vertical and horizontal temperature patterns, the northern Gulf can be subdivided into six thermal domains. The authors added that the moderately high temperatures and a pattern of isotherm contours related to salt features characterize the Louisiana shelf domain, in particular. To model temperature

discrepancy around well #12, COMSOL Multiphysics was used to conduct thermal analysis and validate the theory of heat entrapment.

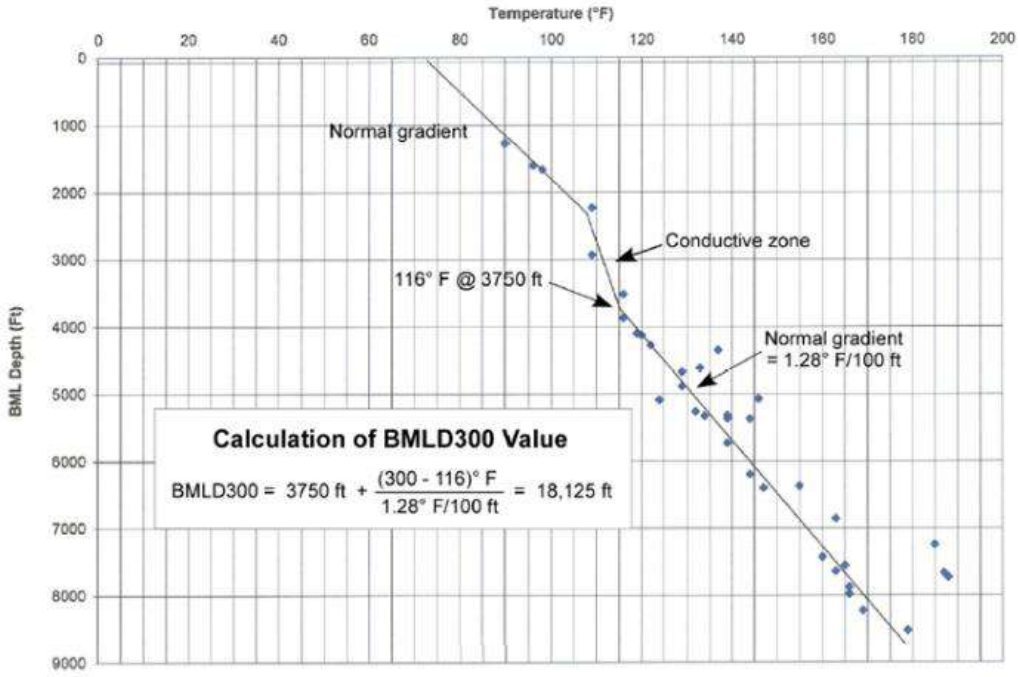

FIGURE 7: AVERAGE TEMPERATURE-DEPTH PLOT OF SANDS IN EI292 FIELD. DATA FROM MMS ATLAS OF NORTHERN GULF OF MEXICO GAS AND OIL SANDS [2001]

IV. HEAT TRANSFER IN SEDIMENTARY BASINS

Heat transfer in sedimentary formations can be described by the following equation of conservation of energy:

$$\int_V \frac{\partial(\rho CT)}{\partial t} dV = \int_S \lambda \nabla T \, dS - \int_S \rho_f C_f T V_d \, dS + \int_V H \, dV \tag{1}$$

where V and S are, respectively, the volume and the external surface of an arbitrary unit of sediments and dS is the normal to S. The left side of the equation is the variation of internal energy which is a function of bulk density (ρ), specific heat of the sediments (C), and temperature (T). The first term on the right symbolizes heat transfer by conduction defined by Fourier's law and proportional to thermal conductivity of the minerals (λ) and to the temperature gradient (∇T) across the surface S. This term is typically the dominant heat transfer component in sedimentary basins [Rybach, 1981] causing strong variance in the presence of geological bodies of high thermal conductivity like salt despairs [Mello *et* al., 1994]. The second term represents the heat carried by fluids of specific heat (C_f) and density(ρ_f) flowing with Darcy velocity(V_d). It is assumed that the pore space is fluid-saturated and that the volumetric flow rate can be expressed using Darcy's law for single phase fluid flow, $V_d = -\frac{k}{\mu}[\nabla P - \rho_f g]$ where, ∇P is the pressure gradient, k, the permeability of the sediments, μ, the dynamic viscosity of the fluid and g, the acceleration of gravity. The last term in the heat transfer equation (1) is the heat created by eventual sources of volumetric strength H.

To simulate heat transfer, we assume that the temperature distribution is continuous and varies smoothly at grid block's scale. Equation (1) is discretized as follows:

$$\frac{\partial(\rho CT)}{\partial t} = \nabla(\lambda \nabla T) - \nabla(\rho_f C_f T V_d) + H \tag{2}$$

4.1 Heat sources

In this study, it was considered that the heat flux has been generated by the combined dominant effects of (1) radiogenic heat (2) heat produced by chemical reactions and (3) sedimentation. The radiogenic heat produced by decay of radioactive

isotopes of Potassium, Thorium and Uranium, the heat produced by chemical reactions (like diagenesis and hydrocarbon generation), and also the effect of sedimentation was discarded.

Sedimentation is active and taking place at a rate of 1.0 mm/year. However, salt movement in the Eugene Island area has stopped about 1.5 million years ago. It was also stated that temperature change over the last 100,000 years is less than 0.2°C, almost in steady state after stoppage of salt movement, and is practically constant at present time [Alexander and Flemings, 1995]. Moreover, we will consider that fluid flow via faults into the reservoir is extremely small; thereby, it can be assumed that V_d is negligible. As such, Equation (2) reduces to the following:

$$\frac{\partial(\rho CT)}{\partial t} = \nabla(\lambda \nabla T) \tag{3}$$

4.2 Analysis of temperature distribution around well #12

The reservoir under study consists of three distinct regions i) a clean sand at the top of the reservoir, ii) a shaly sand in the bottom portion, and iii) a shale barrier, sandwiched between the two (see Fig. 8, below). Fig. 8 also describes the model that will be used to predict the thermal variation along the depth of P1-sand. The three regions are characterized by lower temperatures for thin sand-rich formations, whereas, higher temperatures distinguish thick shaly formations, since sand-rich sections have a higher thermal conductivity.

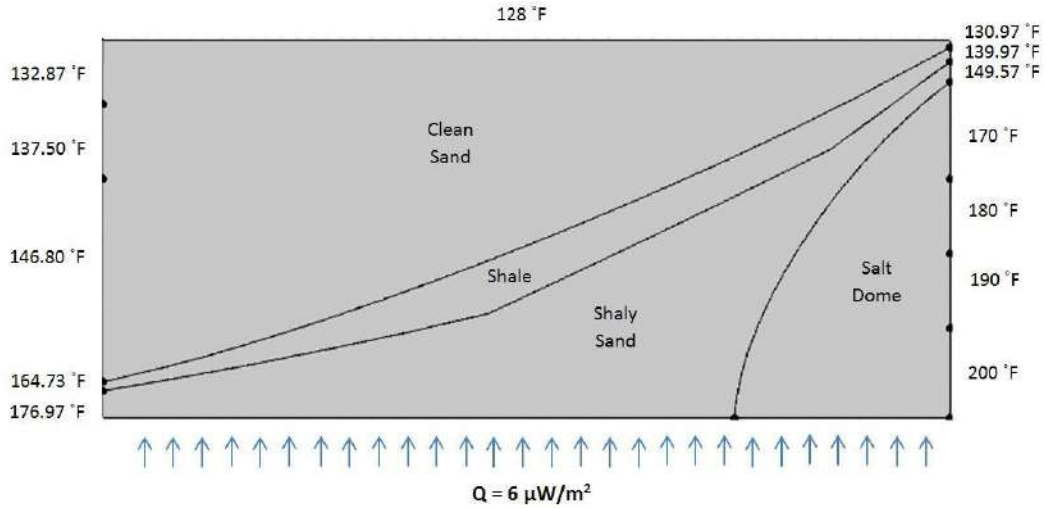

FIGURE 8: SCHEMATIC OF MODEL USED FOR COMSOL MUTIPHYSICS SIMULATION

It was assumed that a uniform heat flow from the basement (salt dome) through a sequence of shaly sand, shale, then clean sand formations. The thick shaly sand on top of the salt dome maintains higher temperatures. A drastic temperature drop, across the shale and into the clean-rich sand, is in the neighborhood of 43 ^{o}F. Temperatures at the outer eastern and western boundaries, delimited by faults, have been set to vary at a constant temperature gradient. It was stated that high thermal conductivity of the salt compared to the surrounding sediments (4-6 W/mK vs. 1-3 W/mK, [Mello et al., 1994]) and the high amplitude of salt topography, described by Anderson et al. [1994] as the most rugged topography on earth can generate significant temperature anomalies [Mello et al., 1994].

Coelho et al. [1996] confirmed that presence of oil and gas decreases thermal conductivity, leading to thermal draping that increases temperature underneath reservoirs. The authors indicated that influence of hydrocarbons could cause a positive temperature difference, as high as 15 ^{o}C below the main reservoirs, and could explain by itself the recorded differences. However, using their theory, it was found that such blanketing would require about 60% of gas distributed uniformly in a pore space with an average porosity of about 40 % between 1,000 and 2,000 mbsf (meter below sea floor, also known as TVDSS). This does not represent P1-sand, deeper and mostly oil-saturated.

V. THERMAL ANALYSIS

Heat generated by conduction is the dominant component in Equation (1). It was assumed that conduction governs heat flow across the faults (surrounding the reservoir) and dominates the influence of the salt dome. Average values for salt conductivity and density and specific heat of the fluids are λ=6 W/mK, ρ_f=1000 kg/m^3 and C_f=1.5 J/Kkg^3, respectively.

5.1 Numerical Analysis

Using a control volume fixed with regard to the shallowest horizon of the P1-sand (see Fig. 8).

In permanent regime, this can be written as:

$$\int_S \lambda \nabla T dS - \int_S \rho_r C_r T U dS = 0 \tag{4}$$

where U represents type of sediment (whether salt, clean sand, shaly sand or shale), ρ_r and C_r are the density and specific heat of the sediment. Tables in the Appendix summarize property values used in the analysis of temperature distribution, vertically in the well #12 area of interest. Using a finite difference formulation for a surface S with n gridblocks, each having the same dimensions Δx and Δz, one can write the following:

$$\sum_{i=b,t,e,w} k_i S_i \frac{(T_i - T_{i-1})}{d_i} + \sum_{i=b,t,e,w} \rho_r C_r U \Delta x \Delta z \left[\frac{(T_t + T_{i-1})}{2} - \frac{(T_b + T_{i-1})}{2} \right] = 0 \tag{5}$$

where the subscript i represents direction and b, t, e, and w all represent bottom, top, east and west bounds of two neighboring blocks i and $i-1$. The terms d_i and S_i are the grid dimensions along and surface orthogonal to direction, d, respectively. Thermal conductivity between two neighboring blocks is the harmonic "in series" average of the thermal conductivity of i and $i-1$:

$$k_i = \frac{2\lambda_i \lambda_{i-1}}{\lambda_i + \lambda_{i-1}} \tag{6}$$

The centered space over-relaxation method [Press, 1994] that is used to solve Equation (5) is an iterative algorithm where an initial temperature value is attributed to all nodes at initial step (T^0). Temperature T^{n+1} at step $(n+1)$ for any node is calculated from values of previous step (n) at adjacent nodes, until reaching a convergence limit, ε. In the control unit, where node dimensions are $\Delta x\, \Delta y$ and Δz, the recurrent formula is:

$$T_i^{n+1} = (1-\alpha) T_i^n + \beta \left[\Delta x \Delta y (T_t^n k_t + T_b^n k_b + \gamma (T_t^n - T_b^n)) + \Delta y \Delta z (T_e^n k_e + T_w^n k_w) \right] \tag{7}$$

with, $\beta = \frac{\alpha}{\Delta x \Delta y (k_t + k_b) + \Delta y \Delta z (k_e + k_w)}$ and $\gamma = \frac{U \rho v C}{2}$

where, α is the over-relaxation coefficient taken between 1.0 and 2.0 for unconditional convergence [Press, 1994].

VI. RESULTS AND DISCUSSION

In the developed model, four different types of formation with specific attributes were used. These correspond to the main facies associated with the development of the minibasin, from bottom up: the salt diapir (1) overlain by sand and transgressive shale (2) a shale barrier (3), and an uppermost section composed of clean sands (4), as depicted in Fig. 8 above.

Neither fine gridding nor a complete reproduction was attempted; the idea was to develop a better understanding of heat dissipation in block EI276.

The initial and boundary conditions were chosen to be representative of recorded well testing bottomhole temperatures in well #1 and #12, both sit on the top of the semi-anticline on the eastern boundary portion of the reservoir in the vicinity of faults and the salt dome. Temperature at the top of the control surface was extrapolated to 128 ^{o}F, using a cold temperature gradient of 1.0 ^{o}F/100 ft (clean sand). A null heat flux across the lateral boundaries (null horizontal gradients) was used.

Temperatures on the eastern and western fault boundaries were extrapolated from obtained data using observed gradients across the different formations. These are 1.0 ^{o}F/100 ft in clean sand and 1.23 ^{o}F/100 ft in the shaly deeper sand beds, respectively. A uniform vertical heat flow at the bottom boundary (60 $\mu W/m^2$, from Anderson *et* al. [1991]) was also utilized to simulate salt dome conduction.

COMSOL results showed a 41 ^{o}F temperature anomaly between temperatures in Well #12 producing from sand and transgressive shale, located in the vicinity of a salt dome, and a shallower well #1 producing from clean sand and more remote from the conductive salt dome source. The influence of salt dome is significant and conduction played a major role in

temperature rise in well #12. Transgressive shale, shale, oil and gas have also contributed to temperature entrapment (Fig. 9). It can be observed that shale acted like a thermal barrier where there are two distinctive thermal regions (above and below shale layer) that exhibit various temperature gradients (1.0 and 1.23 ^{o}F/100 ft).

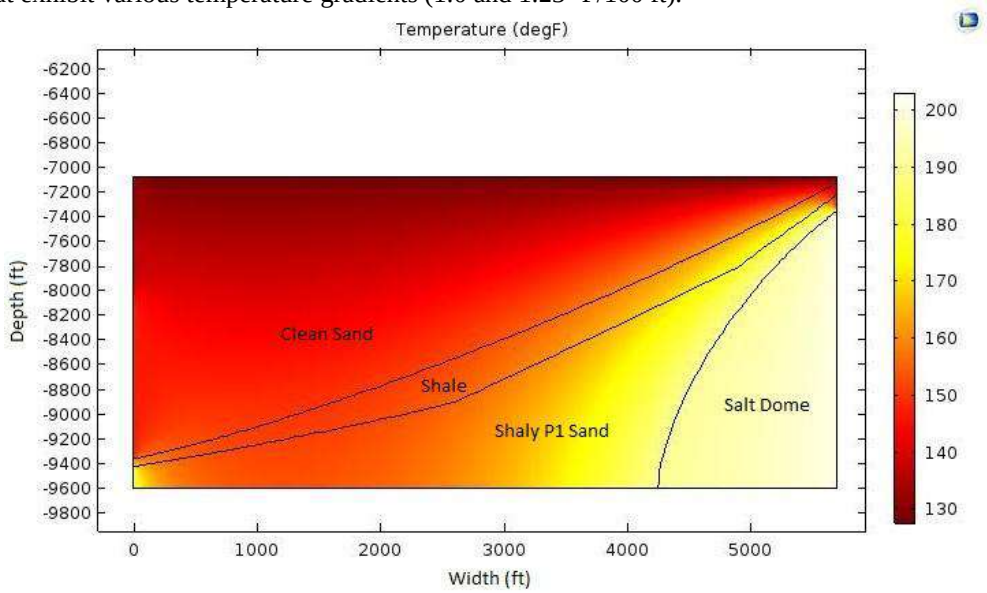

FIGURE 9: HEAT TRANSFER SIMULATION CONTROL VOLUME

The isothermal contours lines shown in Fig. 10 clearly show a temperature discrepancy in the salt dome and across the shale barrier. The observed temperature drop across the shale barrier of 43 ^{o}F was reproduced with a calculated simulation drop of 41 ^{o}F. That corresponds to an absolute error of 5.7% indicating that the simulation results agree with the reported data and consolidated the hypothesis that salt domes are the major source of heat and that the dominant mechanism of heat transfer in the Eugene Island area is by conduction.

A sensitivity analysis on heat influx magnitude and dome temperature was performed. COMSOL reproduction of observed data was achieved for a heat influx value of 6.0 $\mu W/m^2$ and a dome temperature gradient of 7.5 ^{o}F/100 ft on the eastern side of the structure. A 1.6 ^{o}F/100 ft on the western side of the structure was utilized in the clean sand portion of the P1-sand. Another temperature gradient of 2.2 ^{o}F/100 ft along the shaly-sand portion (resulting in a high temperature concentration at the left bottom corner of the control volume) was used to match the observed temperature profile. Figure 8 is an illustration of the sensitivity analysis parameters.

Pertinent modeling data are all summarized Tables 1 to 4 in Appendix A.

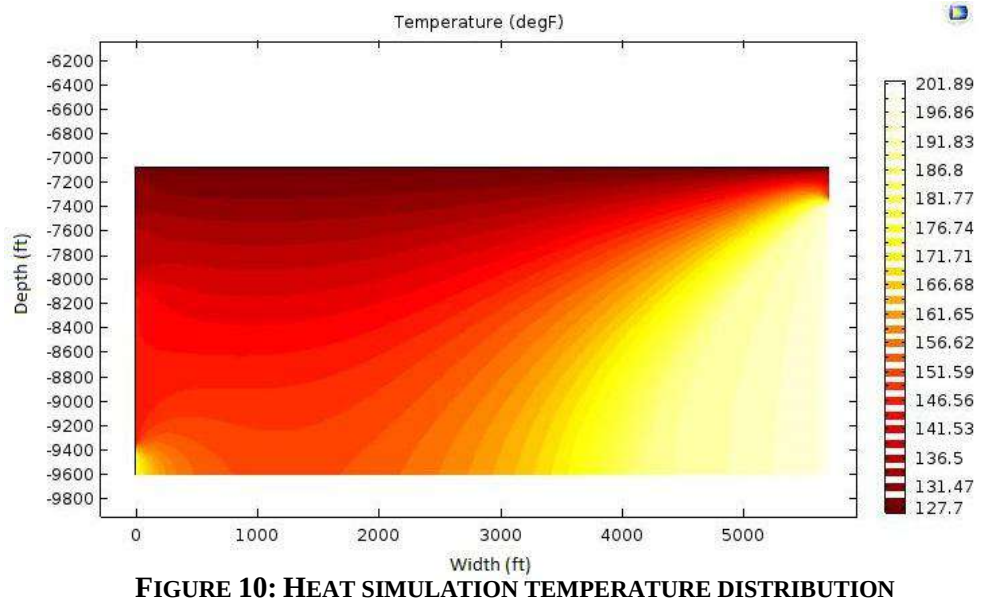

FIGURE 10: HEAT SIMULATION TEMPERATURE DISTRIBUTION

VII. CONCLUSIONS

A thermal analysis of the vicinity of well #12 was conducted using COMSOL multiphysics to predict temperature variation along the P1-sand depth. The developed model validated the variation in temperature between cold clean and hotter shaly sands and predicted a temperature contrast of 41 ^{o}F across the shale barrier. This is in agreement with the observed temperature departure of 43 ^{o}F. The temperature variation indicated that salt diapirs transferred heat by conduction to the reservoir, increased temperature around nearby wells. COMSOL simulation results also confirmed that shale acted as a thermal barrier and helped retaining heat in the shaly sand.

REFERENCES

[1] L. L. Alexander, P.B. Flemings, "Geologic evolution of a Plio-Pleistocene salt withdrawal Mini-Basin: Block 330, Eugene Island," South Addition, Offshore Louisiana, AAPG Bull., 79(12), 1995, pp. 1737-1756.

[2] R. N. Anderson, P. B. Flemings, S. Losh, J. Austin, R. Woodhams, "Gulf of Mexico Growth fault drilled, seen as oil, gas migration pathway," Oil and Gas Journal, June 6, 1994, pp. 97-103.

[3] D. Coelho, A. Erendi, L. M. Cathles, "Temperature, pressure and fluid flow modelling in Block 330, South Eugene Island using 2D and 3D finite element algorithms," Annual Meeting Abstracts - AAPG and SEPM, v. 5, 1996, pp. 28.

[4] J. Forrest, E. Marcucci, P. Scott, "Geothermal gradients and subsurface temperatures in the Northern Gulf of Mexico," GCAGS Transactions, v. 55, 2007, pp. 233-248.

[5] R. A. Lane, L. A. Macpherson, "A review of geopressure Evaluation from well logs – Louisiana Gulf Coast," Journal of Petroleum Technology, 1976, pp. 963-971.

[6] D. S. Holland, J. B. Leedy, D. R. Lammlein, "Eugene Island Block 330 field, offshore Louisiana, in Beaumont, E.A., and Foster, N. H., compilers, Structural traps III, tectonic fold and fault traps," AAPG Treatise of Petroleum Geology Atlas of Oil and Gas Fields: 1990, pp. 103-143.

[7] D. F. Leipper, "Physical oceanography of the Gulf of Mexico, Fishery Bull., 55(89): 1954, pp. 119-138.

[8] S. Nagihara, M. A. Smith, "Regional overview of deep sedimentary thermal gradients of the geopressured zone of the Texas–Louisiana continental shelf,: AAPG Bull. 92, 2008, pp. 1-14.

[9] U. T. Mello, R. N. Anderson, G. D. Carner, "Salt restrains maturation in subsalt plays, Oil and Gas Journal, 31, 1994, pp. 101-107.

[10] W. H. Press, S. A. Teukolsky, W. T. Vetterling, B. P. Flannery, "Numerical recipes in C: the art of scientific computing" 2nd edition, Cambridge University Press, New York, 1992.

[11] L. Rybach, "Geothermal Systems, Conductive Heat Flow, in Geothermal Systems: principles and case histories, L. Rybach and L.J.P. Muffler, John Wiley and Sons, Ltd, 1981.

[12] R. C. Selley, "Applied Sedimentology. xii + 446 pp. London: Academic Press, 1988.

[13] H. O. Woodbury, I. B. Murray, P. J. Pickford, W. H. Akers, "Pliocene and Pleistocene depocenters, outer continental shelf. Louisiana and Texas: *AAPG Bull.*, 57, 1973, pp. 2428-2439.

Appendix A
Materials properties used in COMSOL multiphysics.

TABLE 1
MATERIAL PROPERTIES OF SHALE BARRIER

Material Contents

Property	Name	Value	Unit	Property group
Thermal conductivity	k	1.043633...	W/(m·K)	Basic
Density	rho	2322.677...	kg/m^3	Basic
Heat capacity at constant pressu...	Cp	803.8656	J/(kg·K)	Basic
Ratio of specific heats	gamma	1	1	Basic

TABLE 2
MATERIAL PROPERTIES OF P1-SAND

Material Contents

Property	Name	Value	Unit	Property group
Thermal conductivity	k	0.95	W/(m·K)	Basic
Heat capacity at constant pressu...	Cp	766.1844	J/(kg·K)	Basic
Density	rho	2178.511	kg/m^3	Basic
Ratio of specific heats	gamma	1	1	Basic

TABLE 3
MATERIAL PROPERTIES OF SALT

Material Contents

Property	Name	Value	Unit	Property group
Thermal conductivity	k	6	W/(m·K)	Basic
Heat capacity at constant pressu...	Cp	880	J/(kg·K)	Basic
Density	rho	2200	kg/m^3	Basic
TD	TD	1.99e-9		Basic
Ratio of specific heats	gamma	1	1	Basic

TABLE 4
MATERIAL PROPERTIES OF CLEAN SAND

Material Contents

Property	Name	Value	Unit	Property group
Heat capacity at constant pressu...	Cp	773.72	J/(kg·K)	Basic
Thermal conductivity	k	0.91	W/(m·K)	Basic
Density	rho	2274.62	kg/m^3	Basic
Ratio of specific heats	gamma	1	1	Basic

Numerical Investigation of Over pressure Causes in Eugene Island P1 Sand – Part II

R. Trabelsi[1*], A. C. Seibi[2], F. Boukadi[3], W. Chalgham[4], H. Trabelsi[5]

University of Louisiana, Dept. of Petroleum Engineering, Lafayette LA, USA

***Abstract*—** *Eugene Initial reservoir pressures from well test information were found to be higher than the calculated hydrostatic pressures. Three wells in Block 276 P1-sand had higher observed pressures than what was expected, implying pore pressures greater than anticipated. It is thought that under compaction in shaly sand and thermal dissipation from salt diapirs are the main reasons causing over pressurization. Both effects have been studied and under compaction was found to be the dominant mechanism causing pore overpressure. Transgressive shale in P1-sand, resulting from ocean transgression, acted as plastic barriers; thereby, negating the transfer of lithostatic load to deeper formations. This has resulted in constant porosities with respect to depth. A developed COMSOL multiphysics model has also indicated that temperature effects from underlying salt diapers have also affected pore pressure and that pore over pressurization by conduction was found to range from 3 – 15%.*

***Keywords*— Eugine Island, transgressive shale, over pressure.**

I. INTRODUCTION

EI330 Normal reservoir pressure is the pressure necessary to sustain a column of water to surface (Fertl, 1976]. Normal pressures range between 0.43 and 0.50 psi/ft. Normal drilling muds weigh about 9 ppg (pounds per gallon) and exert a bottom hole pressure of approximately 0.47 psi/ft of depth. Overpressure refers to pressures higher than normal. Pressures lower than normal are called subnormal. Dickey et al. [1968] identified the location of abnormal pressures in southern Louisiana and noted that the continental and deltaic facies contain sandy beds and that the neritic (nearshore) facies also comprise a few silty and sandy beds that connect laterally to the deltaic facies. The authors added that shelf facies contains almost no sandy beds, and the pore fluids cannot escape. It was also highlighted that growth faults are seals that stop the lateral flow of pore water toward the neritic facies.

Abnormal pressure is defined as any departure from normal hydrostatic pressure at a given depth [Bruce and Bowers, 2002]. Abnormal subsurface pressures, either overpressure (geopressure) or unde rpressure, are found in hydrocarbon basins throughout the world in all lithologies, from all geologic ages, and at all depths [Fertl et al., 1994].

Timely and reliable detection of geopressure is imperative to avoid or mitigate potential drilling and safety hazards, e.g.:

- Shallow water flow
- Blowouts
- Shale instability

During drilling, advanced warning of approaching geopressuring enables mud engineers to adjust the mud weight to prevent well and reservoir damage and to determine casing points. This is a particular concern in deepwater wells where the pressure difference; i.e., the operating window, between the hydrostatic gradient and the fracture gradient is very narrow.

For most cases, shale and shaly sands are formations that exhibit over pressurization. Shale is abundant in Block 276 P1-sand with an average net to gross of 46 to 48%. A better understanding of porosity mechanics in Block 276 is of interest for many reasons, namely:

1) Shale is the dominant lithology in the block of interest basin.
2) Expulsion of pore waters from shale could affect the pressure distribution and flow of pore waters and hydrocarbons throughout the block of interest basin.
3) In many cases, shale porosity depends only on effective stress (lithostatic stress minus pore pressure), and excess shale porosity provides a useful measure of pore fluid pressure.
4) Over pressured shales pose drilling hazards and stimulate slumping and fault movement.
5) Shale porosity profiles can replicate the history of over pressuring and the time of seal formation in the area.

To interpret shale porosity, we need to know how shales compact when pore fluid pressure is hydrostatic. Hunt et al. [1998] have suggested that, in wells where fluid pressure is hydrostatic, porosity decreases linearly with depth until porosities of about 10% are reached.

At greater depths, as in the case in Block 276 P1-sand, porosity changes slightly. It goes up and down, but does not portray signs of degradation with depth. The boundary between linear (stage 1) compaction and no (stage 2) compaction occurs when the shale pores have been condensed to the thickness of about 3 mono-layers of water. For shales with a high percentage of high surface area clays (illite + smectite + illite-smectite) the limit of normal compaction can be 15-20% or even greater, according to Hunt et al. [1998). For shales with a low percentage of high surface area clays, the limit of compaction can be as low as 3%. Once shales reach stage 2 compaction, shale porosity is independent of effective stress. If pore pressure is then increased (by hydrocarbon maturation, for example), porosity will not increase and overpressures will not be revealed in shale porosity. Hunt et al. [1998] showed several examples where the top of overpressure lies in stage 2 compaction zone and porosity remains unchanged, despite the large surge in pore pressure. The perception that there is a natural limit to shale compaction provides a sound justification of these interpretations.

This contradicts with a considerable literature suggesting that porosity data can be used to predict excess (above hydrostatic) pore pressures [Magara, 1978; Fertl, 1976; Bray and Karig, 1985; Shi and Wang, 1988; Bangs et al., 1990; Luo and Vasseur, 1992, 1993; Bour et al., 1995; Gordon and Flemings, 1998; and Stump et al., 1998].

In addition, Revil et al. [1998] examined porosity-depth profiles and mud weight data in 89 wells in the Eugene Island area to determine whether the intervals of approximately constant porosity are caused by compaction reaching its natural limit or by fluid overpressure. By comparing the fluid pressures predicted from shale porosity to those computed from mud weight data, Revil et al. [1998] found that constant porosity intervals are in a state of disequilibrium compaction. The porosities were controlled by pore pressure as Gordon and Flemings [1998] reported, from an analysis of several wells in the area.

To analyze and infer the pattern of compaction, Revil et al. [1998] developed theoretical relations against which departures from hydrostatic compaction can be measured. They found that the pattern of subsurface shale porosity is spatially logical on a local scale but varies over the study area. They defined a surface where porosity commences to depart from the hydrostatic compaction trend. This surface parallels the H. sellii transgressive shale over the study area. It was proposed that the sediments become impermeable when hydrocarbon fluids entered the area and capillary seals formed [Cathles, 2001 and Shosa and Cathles, 2001], but alternative explanations are also likely.

II. RESERVOIR SIMULATION AND HISTORY MATCHING

In the attempts to history match reservoir pressure in P1-sand, pressure profiles (Fig. 1) show a significant divergence between wells #1, #12 and W-12 observed (solid) and estimated (dashed) pore pressures, during early production time. Early departures are indicative of hydrocarbon overpressure caused by under compaction and possibly heat dissipation from salt diapers in the vicinity of Block 276. The late time matching could possibly be explained by wells producing under normal hydrostatic regime after over pressured hydrocarbons have all been depleted.

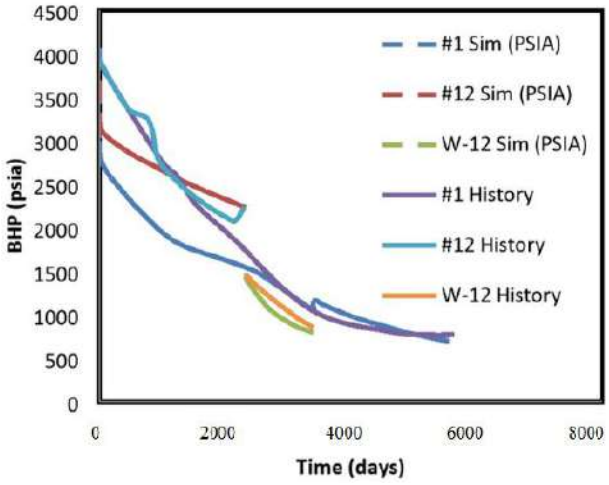

FIGURE 1: PRESSURE PROFILES IN P1 SAND, OBSERVED AND SIMULATED

In this work, it is intended to study under compaction in P1-sand, thought to be the dominant mechanism behind overpressure in Block 276. Temperature effects on pressure are also investigated.

III. ARRESTED COMPACTION

In Fig. 2 below, the depth at which porosity departs from normal compaction trend is what is referred to as fluid retention depth. At that particular depth, porosity remains constant as is the case in Block 276 P1-sand depths of 7621 to 9600 ft. It is also the depth at which pore pressure departs from the hydrostatic pressure trend and fluids become over pressured. The main attribute is what is called disequilibrium compaction.

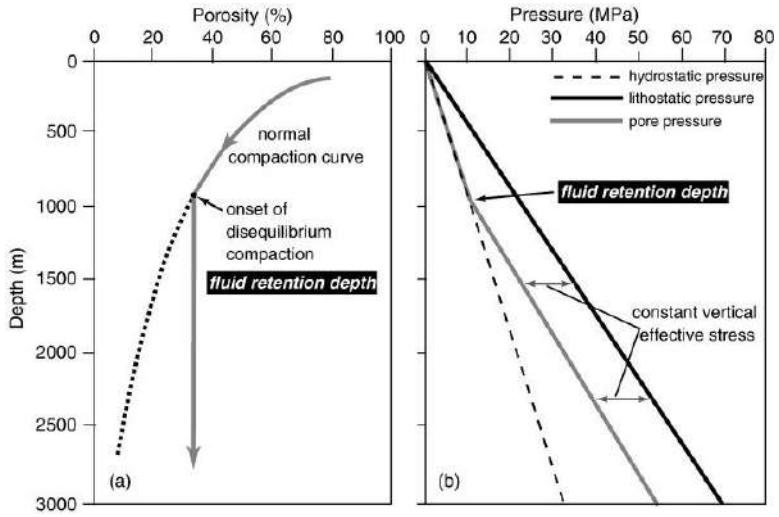

FIGURE 2: RELATIONSHIP BETWEEN (a) porosity and depth and (b) pressure and depth for a shale that becomes over pressured by disequilibrium compaction at the fluid retention depth. Modified from Harrold et al. [1999]

According to Lash and Blood [2006], the fluid retention depth in the Gulf of Mexico varies from as shallow as 0.3 mi. to as deep as 0.9 mi (Fig. 3). At that depth, shaly sandstone composition sees a drastic shift in its mineral structure. Smectite replaces most of the illite leading into water expulsion. That translates to a higher hydrocarbon storativity and higher pore pressure.

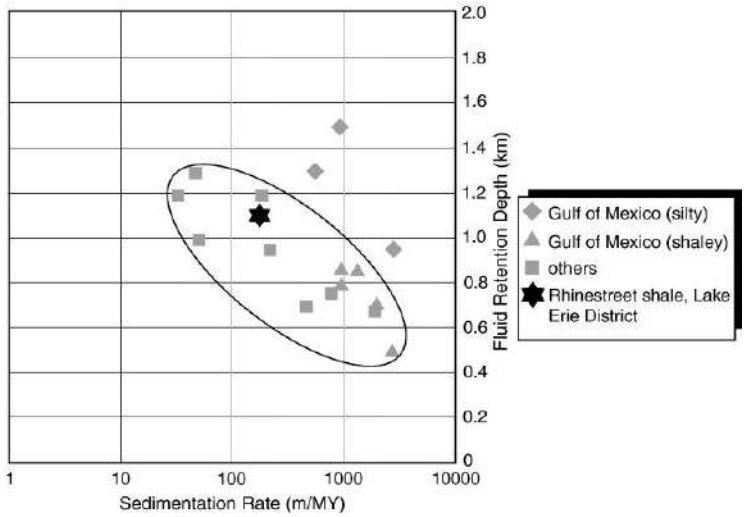

FIGURE 3: FLUID RETENTION DEPTH AS A FUNCTION OF SEDIMENTATION RATE, LASH AND BLOOD [2006]

Besides, when the sediments subside rapidly as in Fig. 3 above and in Block 276 P1-sand, fluids in the sediments can only be partially expelled. The remaining fluid in the pores must sustain all or part of the weight of overly sediments, causing the pressure of pore fluids to increase (abnormally high pore pressure). In this case, porosity decreases less rapidly than it should be with depth, and formations are said to be under-compacted or in compaction disequilibrium.

Furthermore, and according to Hunt [1996], disequilibrium compaction is caused by stepwise transformation to mixed-layer clays and illite. This releases more water into the rock and causes a slower compaction of smectite-rich rocks. Overpressures can be generated by many mechanism, such as compaction disequilibrium (under-compaction), hydrocarbon generation and gas cracking, aquathermal expansion, tectonic compression (lateral stress), mineral transformations (e.g., illitization), and osmosis, hydraulic head and hydrocarbon buoyancy [Gutierrez et al., 2006; Swarbrick and Osborne, 1998]. In nearly all cases where compaction disequilibrium has been determined to be the primary cause of over pressuring, the age of the rocks is geologically young. Examples of areas where compaction disequilibrium is cited as the primary reason of abnormal pressure include the U.S. Gulf Coast, Alaska Cook Inlet; Beaufort Sea, Mackenzie Delta, North Sea, Adriatic Sea, Niger Delta, Mahakam Delta, the Nile Delta, Malay Basin, Eastern Venezuelan Basin (Trinidad) and the Potwar Plateau of Pakistan [Law and Spencer, 1998; Burrus, 1998; Heppard et al., 1998; Powley, 1990; Nelson and Bird, 2005; Morley et al., 2011]. In these areas, the abnormally pressured rocks are mainly located in Tertiary and late Mesozoic sedimentary formations (146 to 65 mya, million years ago), the depositional setting is dominantly deltaic, and the lithology is dominantly shale, as is the case of Block 276, where sedimentary formations, Pliocene-Pleistocene (5.3 mya to 11,000) is even younger.

Additionally, Mouchet and Mitchell [1989] noted that one of major reasons of abnormal pore pressure is caused by abnormal formation compaction (compaction disequilibrium or under-compaction). When sediments compact normally, formation porosity is reduced at the same time as pore fluid is expelled. The authors added that during burial, increasing overburden pressure is the prime cause of fluid expulsion. They explained that if the sedimentation rate is slow, normal compaction occurs, i.e., equilibrium between increasing overburden and the reduction of pore fluid volume due to compaction (or ability to expel fluids) is maintained. They said that this normal compaction causes hydrostatic pore pressure in the formation. The authors explained that rapid burial, however, leads to faster expulsion of fluids in response to rapidly increasing overburden stress.

Swarbrick et al. [2002] added that the overpressures generated by under-compaction in mudrock-dominated sequences may reveal an abnormal pore pressure change with depth. They noted that the compaction disequilibrium is known by higher than expected porosities at a given depth and that the porosities deviated from the normal porosity trend.

Zhang [2011] looked at overpressure from a different angle. He plotted shale resistivity as a function of depth to explain the departure of pore pressure from the normal hydrostatic trend. The author identified under compaction as the main reason behind over pressurization. He showed that the inclined line in Fig. 4(a), above, represents the resistivity in normally compacted formation (normal resistivity, R_n). He noted that in the under-compacted section resistivity (R) reversal occurs, indicating an over pressured formation in Fig. 4(b). He showed a lower resistivity in the under compacted/over pressured section. In the figure, R_n is the normal resistivity trendline, σ_V is the lithostatic or overburden stress, σ_e is the effective vertical stress, p_n is the normal pore pressure, and p is the pore pressure.

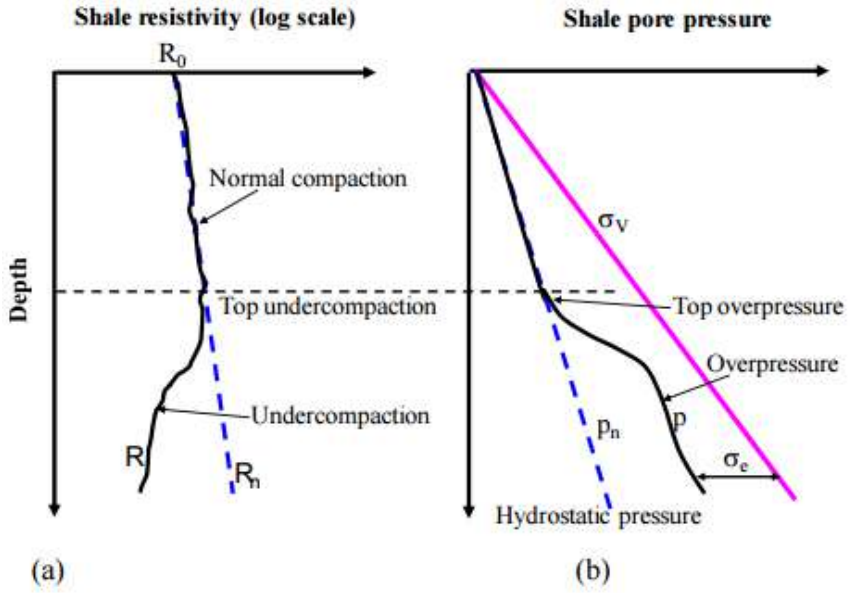

FIGURE 4: SCHEMATIC OF RESISTIVITY (A) AND PORE PRESSURE (B) IN AN UNDERCOMPACTED BASIN, ZHANG [2011]

In Fig. 5, Zhang [2011] plotted porosity as a function of depth, to prove his hypothesis. The dashed porosity profile in (a) represents normally compacted formation. In the over pressured section, the porosity reversal occurs (heavy line). In the over pressured section, porosity is larger than that in the normal compaction trendline (ϕ_n) and under compaction is apparent.

In addition, Fig. 6 below shows different tracks of porosity. Porosity of shales and normal compaction trendline. Shales do not follow the normal compaction trend.

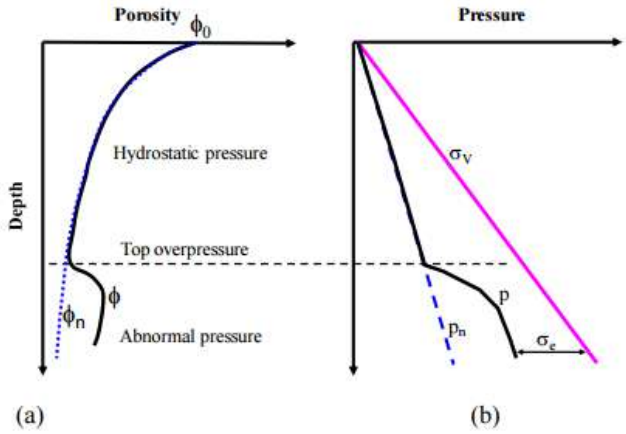

FIGURE 5: SCHEMATIC OF POROSITY (A) AND CORRESPONDING PORE PRESSURE (B) IN A SEDIMENTARY BASIN [ZHANG, 2011]

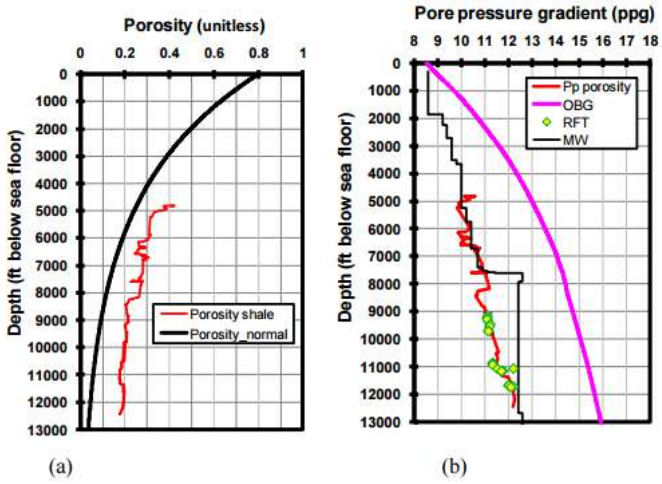

FIGURE 6: POROSITY AND PRESSURE PREDICTION FROM THE POROSITY [ZHANG, 2011]

In Fig. 7, Shaly P1-sand porosity profile shows the same behavior. No clear trend of compaction and porosity hovers around an average of 30% and stays constant with increasing depth. In Fig. 6 the normal compacted porosity should range between 12 to 10% in P1 sand.

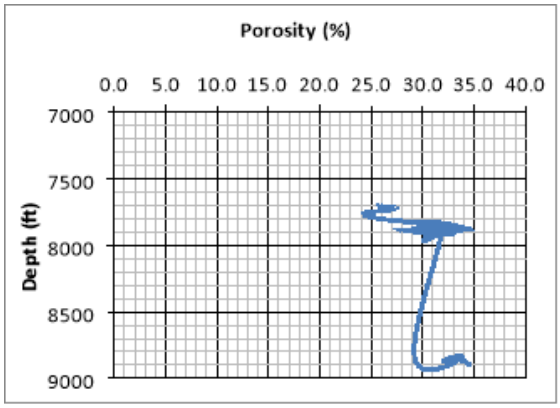

FIGURE 7: P1-SAND SIDEWALL CORE POROSITY PROFILE

Permeability profiles can also be used in justifying under compaction. Fig. 8 is an illustration of permeability variation with depth in P1-sand. A lower permeability at the top of the formation explains the occurrence of transgressive shale, a primary cause of ceased compaction. Permeability is lower in the shaly P1-sand and sees a drastic shift in the bottom of the reservoir and indicates a facies change.

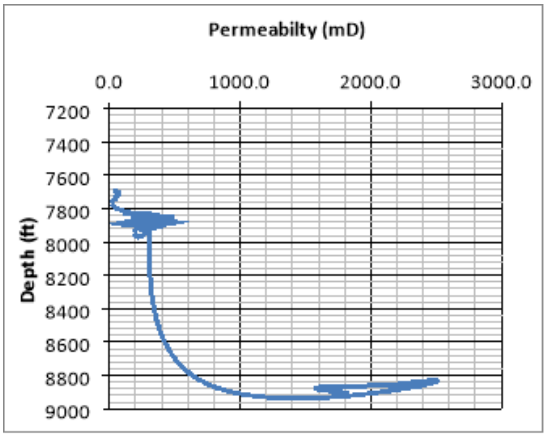

FIGURE 8: P1-SAND SIDEWALL CORE PERMEABILITY PROFILE

High water saturation distribution in layer 1 (Fig. 9) is another indication of transgressive shale in large quantities and that P1-sand is overlain by a shale barrier, as seen in Fig. 7 and 8 above.

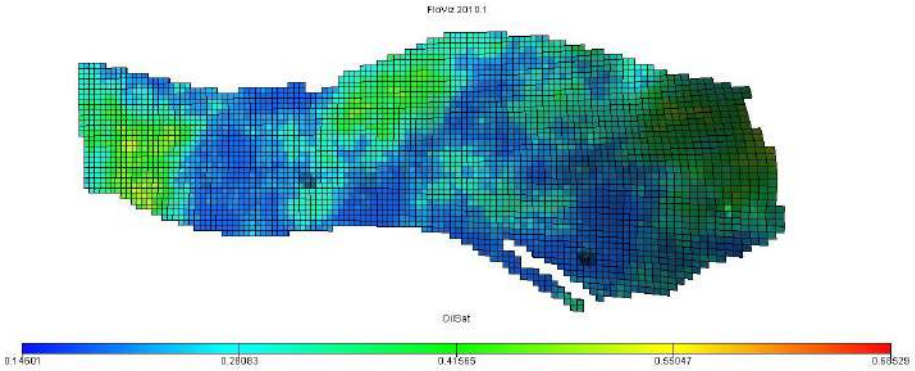

FIGURE 9: WATER SATURATION DISTRIBUTION IN LAYER 1

Techlog generated porosity and water saturation (Fig. 10) and volume of shale (Vshale) and net-to-gross (NTG) logs (Fig. 11) in wells #1, #12 and W-12 also indicate that no clear trend of compaction is evident in the shaly transgressive sand and that the porosity is under compacted (Fig. 10).

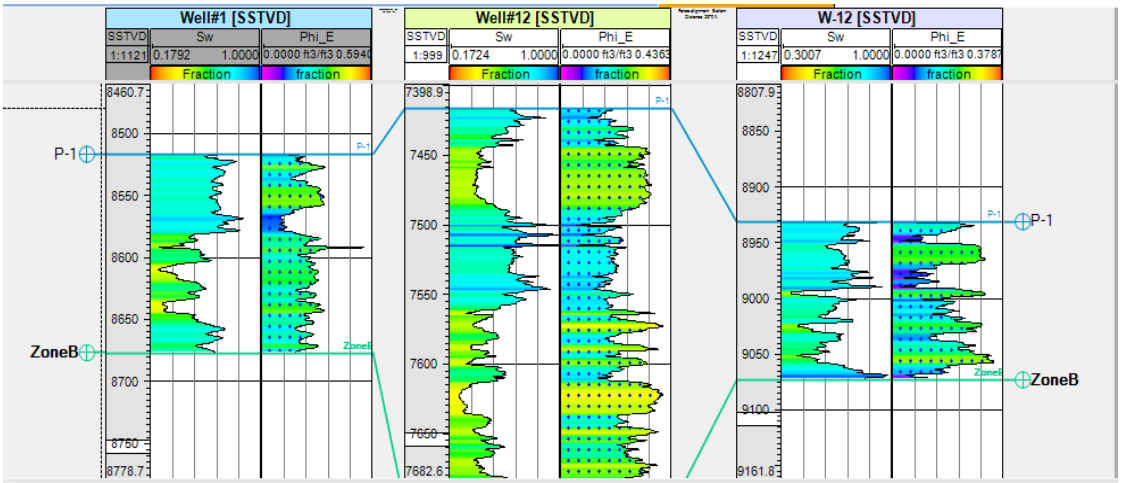

FIGURE 10: NO CLEAR TREND OF POROSITY DEGRADATION IN P1-SAND

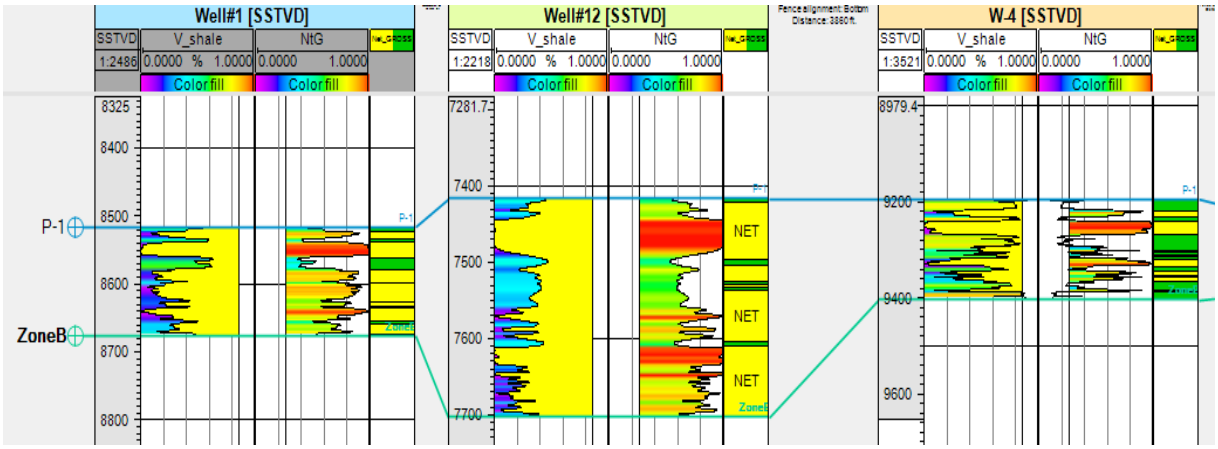

FIGURE 11: EVIDENCE OF INTERBEDDED (TRANSGRESSIVE) SHALE

To better describe porosity variation with depth and under compaction, a mathematical model is used.

IV. MATHEMATICAL MODEL

The relationship between the in-situ, porosity, $\emptyset$, and the uncompacted porosity, $\emptyset_o$, is given by [Revil *et* al., 1998]:

$$\emptyset = 1 - (1 - \emptyset_o) exp(\frac{z}{z_c}) \tag{1}$$

where, z is a depth of interest and

$$\frac{1}{z_c} = g(\rho_g - \rho_f)\emptyset_o \beta$$

where β is the compaction coefficient with β=4.8x10^{-12} psi in the Eugene Island minibasin.

In addition, we assume that fluid pressures have not increased for reasons unrelated to compaction, (2) solid material has not been dissolved and removed, (3) buoyant pressures are not transmitted horizontally or vertically.

Porosity is deduced from density logs using;

$$\rho = (1 - \emptyset)\rho_g + \emptyset\rho_f \tag{2}$$

where, ρ is the sediment density, ρ_g is the sediment grain density, and ρ_f is the pore fluid density. Generally, grain density is taken as 165.4 lb/ft^3 and pore fluid density as 62.4.

We assume that changes in porosity, $\partial\emptyset$, are explicitly related to changes in effective stress, $\partial\sigma_{eff}$:

$$\partial\emptyset = -\emptyset_o \beta \partial\sigma_{eff} \tag{3}$$

where, $\emptyset_o$ is the uncompacted porosity and β is the long term compressibility. The effective stress equals the lithostatic stress, P, minus the pore pressure p:

$$\sigma_{eff} = P - p \tag{4}$$

Lithostatic stress is related to density of mineral grains, ρ_g, density of pore fluid, ρ_f, and sediment porosity, $\emptyset$, by:

$$\partial P_z = (\rho_g(1 - \emptyset) + \rho_f\emptyset)g\Delta z \tag{5}$$

The interpretation method is straightforward. Equation (5) implies that instead of a decreasing porosity in line with normal hydrostatic compaction, a constant porosity with increasing depth implies excess fluid causing pore over pressurization. To make sure that over pressurization was mostly caused by under compaction; a stress analysis was conducted using COMSOL

to study the effect of gravity and temperature on pressure and whether the shale barrier was acting as lithostatic gradient absorber, limiting compaction in P1-sand.

V. EFFECT OF TEMPERATURE ON PRESSURE VARIATION IN P1-SAND

A finite element model using COMSOL multiphysics was developed to study the effect of temperature on the effective stress (see Fig. 12). This study will also explain whether the shale barrier overlain the sand was the main reason behind under compaction. A two-dimensional model of the P1-sand was built using quadrilateral elements to determine the thermal stresses caused by heat dissipated from the salt dome and thermal boundaries. A thermal analysis was initially conducted to determine the temperature distribution within the P1-sand from which thermal stresses were obtained. To mimic the overburden stress, a pressure gradient of 1 psi/ft was assumed and an equivalent pressure of 7500 psi was applied to the top of the elemental volume. Gravity of the different sedimentary strata was also considered. The eastern and western boundaries of the reservoir were constrained from moving laterally and allowed to move vertically; whereas, the bottom side of the model was constrained from moving in all directions.

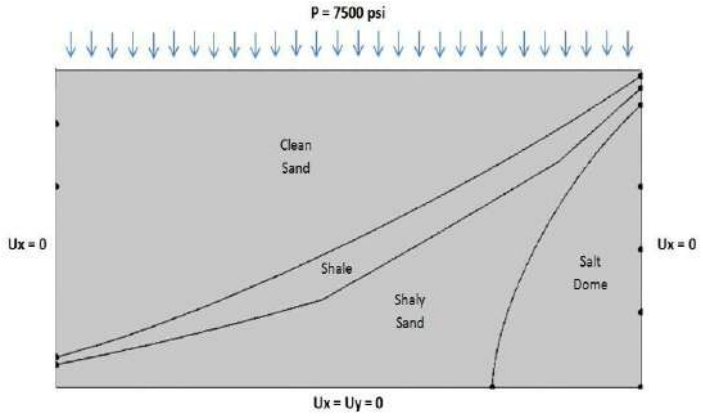

FIGURE 12: BOUNDARY CONDITIONS USED IN THE FINITE ELEMENT MODEL

Fig. 13 shows the displacement field under mechanical and thermal loads. It can be seen that the highest vertical displacement of -6.43 ft occurred at the top of the section (clean sand at a depth of 7500 ft) with least displacement below the shale layer, which acts as a visco-plastic medium; thereby, sustaining the overburben pressure causing under compaction in P1-sand. Fig. 13 also shows that shale, a visco-plastic medium, absorbs most of the stress and acts as a load carrier structure leading to under compaction in the underlain shaly sand portion of the reservoir.

To understand the effect of temperature on the pore pressure, the effective stress and pressure contours for both thermo-mechanical (gravity + temperature) and mechanical loading (gravity only) were examined. Fig.s 13(a) and (b) show the effective stress contour and pressure for gravity alone; while Figs. 13(c) and 13(d) portray the contours for gravity and temperature. A comparison between the effective stress contours reveals that temperature effect was found to contribute to the increase in pore pressure up to 20.5% increase throughout the whole field.

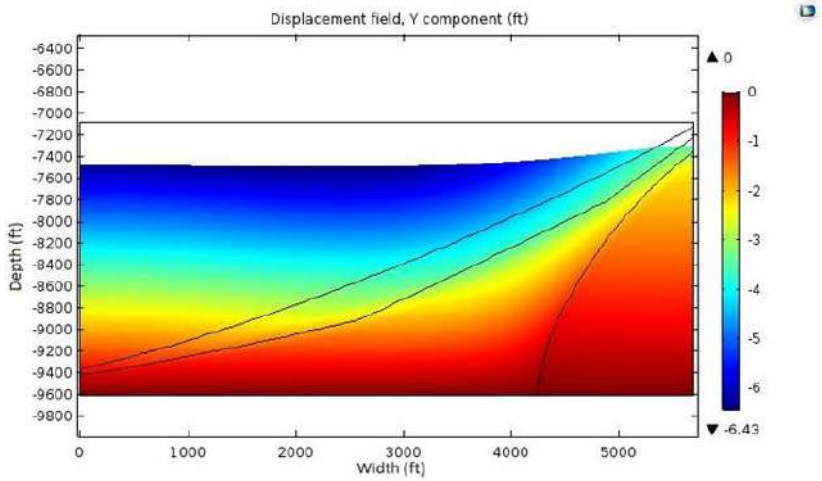

FIGURE 13: DISPLACEMENT SIMULATION CONTOUR

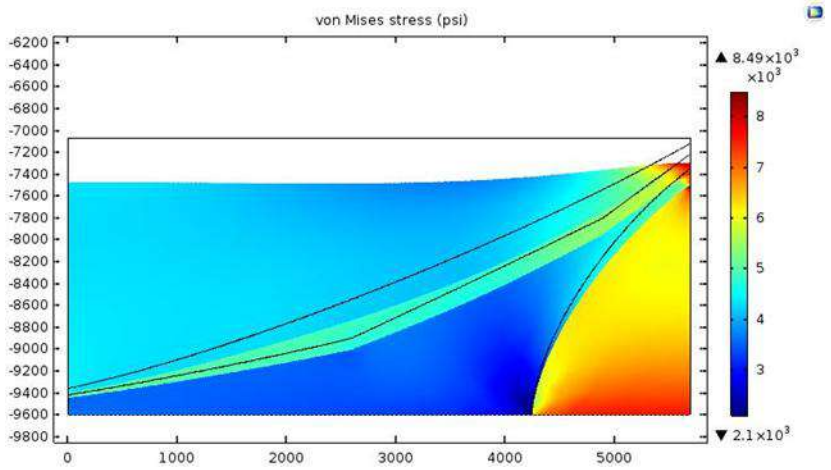

FIGURE 14(A): STRESS DISTRIBUTION IN SIMULATION CONTROL VOLUME, GRAVITY ONLY

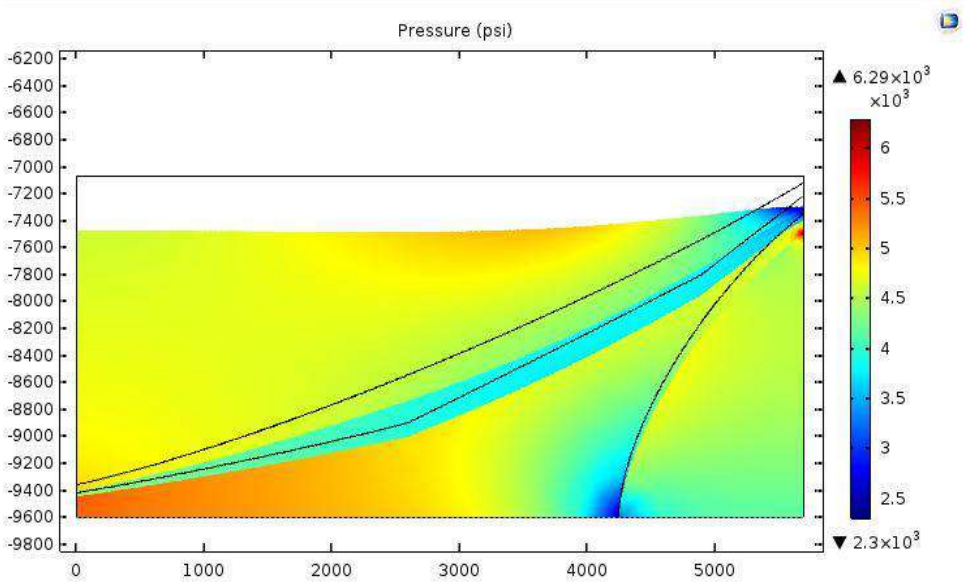

FIGURE 14(B): PRESSURE DISTRIBUTION IN SIMULATION CONTROL VOLUME, GRAVITY ONLY

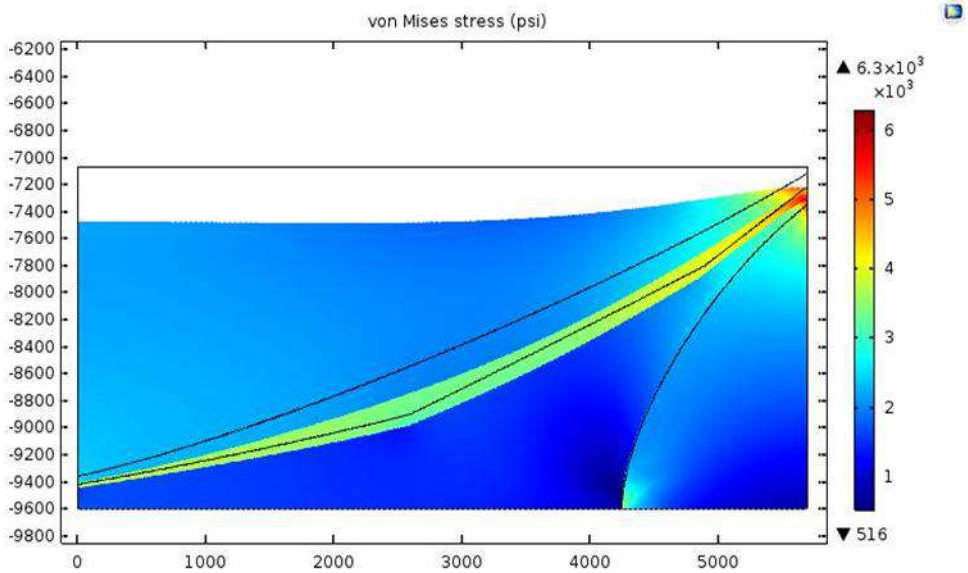

FIGURE 14(C): STRESS DISTRIBUTION IN SIMULATION CONTROL VOLUME, GRAVITY + TEMPERATURE

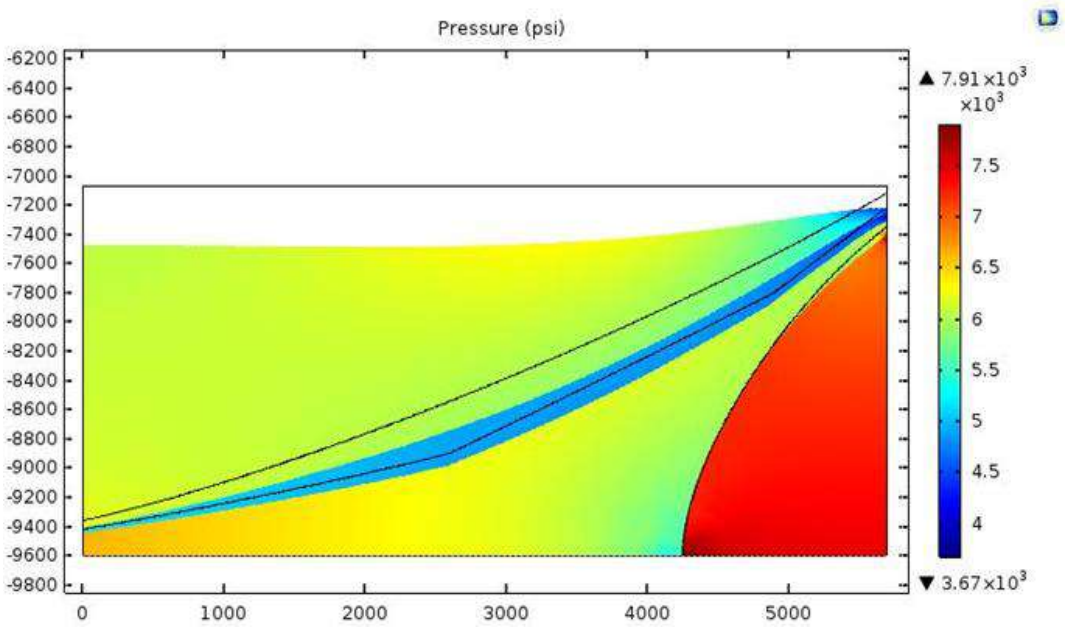

FIGURE 14(D): PRESSURE DISTRIBUTION IN SIMULATION CONTROL VOLUME, GRAVITY + TEMPERATURE

A close examination of Fig.s 13(a) and (c) exhibit that P1-sand (dark blue) is subjected to the lowest effective stress indicating that the pore pressure gets higher in this zone as compared to the clean sand layer (light blue); thereby, confirming the theory of under compaction (overpressure) presented in Equation (6).

$$\sigma_{ob} = \sigma_{eff} + p_f \tag{6}$$

Fig. 14 shows a vertical line along which pressure values were taken at different depths. It passes through well 12 in the reservoir which located below the shale layer. Fig. 15 shows the pressure profile as a function of depth for both loading cases (mechanical only versus mechanical and thermal). The plot clearly portrays that convection is insignificant (blue line lays on top of the orange). Temperature generated from the salt dome has, however, affected reservoir pressure and partially caused over pressurization. Gray and orange lines departure of 500 in clean sand, 30 in the shale barrier, and 350 in shaly sand is a clear indication that over pressurization of the P-1 sand is a combined effect of under compaction and temperature. It is worth noting that shale layer acted as a thermal barrier, indicated by the minimal temperature effect on pressure variation. Moreover, the shale layer acted as a load carrier as explained by its insignificant deformation (compaction).

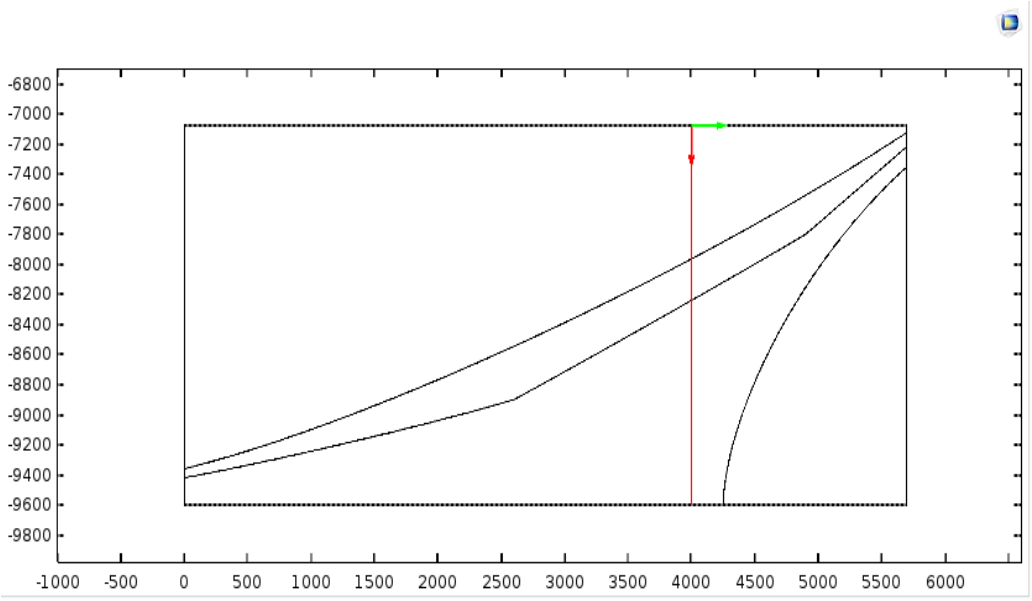

FIGURE 15: SCHEMATIC OF WELL LOCATION USED IN COMSOL SIMULATION

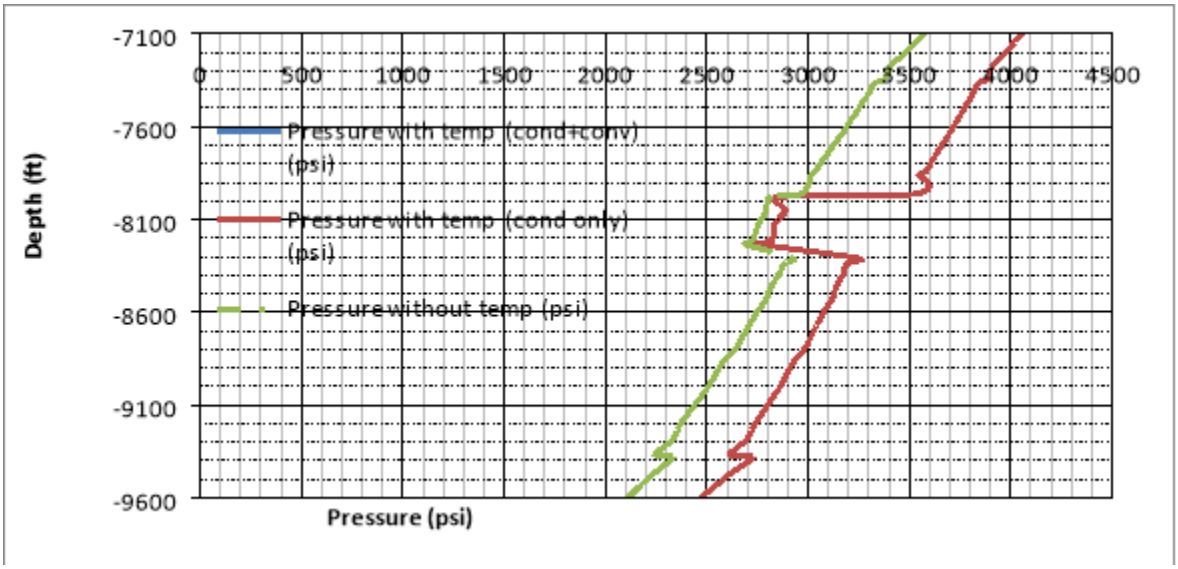

FIGURE 16: SIMULATED PRESSURE PROFILE

VI. CONCLUSIONS

Analysis of the Block 276 P1-sand porosity, permeability, shale content, and pressure show that departures of shale porosity from hydrostatic compaction trend are coherent and provide significant new information on the possible nature of under compaction. It was concluded that over pressuring is strongly controlled by depositional environment. A COMSOL Multiphysics model was also used to demonstrate that temperature effect from nearby salt diapers also contributes to over pressurization but not as much as under compaction, the dominant over pressurization mechanism. It was observed that the temperature effect on pore pressure ranges from 3 to 15%. Thereby, drilling engineers must pay attention to this increase whenever they plan for any drilling activity.

REFERENCES

[1] N. L. Bangs, G. K. Westbrook, J. W. Ladd, P. Bulh, "Seismic velocities from the Barbados Ridge complex: indicators of high pore pressures in an accretionary complex," J. Geophys. Res., v. 95, 1990, pp. 8767-8782.

[2] O. Bour, I. Lerche, D. Grauls, "Quantitative models of very high fluid pressure: the possible role of lateral stress," Terra Nova, v. 7, 1995, pp. 68-79.

[3] C. J. Bray, D. E. Karig, "Porosity of sediments in accretionary prisms and some implications for dewatering processes," J. Geophys. Res., v. 90, 1985, pp. 768-778.

[4] B. Bruce, G. Bowers, "Pore Pressure Terminology," The Leading Edge 21 (2), 2002, pp. 170–173.

[5] J. Burrus, "Overpressure models for clastic rocks, their relation to hydrocarbon expulsion: a critical reevaluation," AAPG Memoir 70: Abnormal Pressures in Hydrocarbon Environments, 1998.

[6] G. F. Ulmishek, V. I. Slavin, "Abnormal pressures in hydrocarbon environments," AAPG Memoir 70, 735 Chapman Petroleum geology, Elsevier1983, pp. 35–63.

[7] L. M. Cathles, "Capillary seals as a cause of pressure compartmentation in sedimentary basins," GCSSEPM, Foundation 21st Annual Research Conference, Petroleum Systems of Deep-Water Basins Dec. 2001, pp. 561-571.

[8] P. A. Dickey, C. R. Shriram, W. R. Paine, "Abnormal pressures in deep wells of southwestern Louisiana," Science, May 10, v. 160, 1968, pp. 609–615.

[9] B. A. Eaton, B.A., "Fracture gradient prediction and its application in oilfield operations," Paper SPE2163. JPT, 1968, pp. 25-32.

[10] W. H. Fertl, "Abnormal formation pressure, implications for exploration, drilling, and production of oil and gas resources," Elsevier, Amsterdam, 1976.

[11] W. H. Fertl, R. E. Chapman, R. F. Holz, "Studies in Abnormal Pressure, 1-454," Amsterdam: Elsevier, Developments in Petroleum Science No. 38, 1994.

[12] D. S. Gordon, P. B. Flemings, "Two dimensional modeling of groundwater flow in an evolving deltaic environment," Soc., Sedimentary Geol., v. 62, 1998, pp. 301-312.

[13] M. A. Gutierrez, N. R. Braunsdorf, B. A. Couzens, "Calibration and ranking of pore-pressure prediction models," The leading Edge, 2006, pp. 1516-1523.

[14] T. W. D. Harrold, R. E. Swarbrick, N. R. Goulty, "Pore pressure estimation from Mudrock porosities in Tertiary Basins," Southeast Asia. Am. Assoc. Petrol. Geol. Bull., 83, 1999, pp. 1057-1067.

[15] P. D. Heppard, H. S. Cander, E. B. Eggertson, "Abnormal pressure and the occurrence of hydrocarbons in offshore eastern Trinidad, West Indies," Abnormal pressures in hydrocarbon environments: AAPG Memoir 70, 1998, pp. 215–246.

[16] J. M. Hunt, "Petroleum Geochemistry and Geology," W.H. Freeman, New York, 1996.

[17] J. M. Hunt, J. K. Whelan, L. B. Eglinton, L. M. Cathles III, "Relation of shale porosities, gas generation, and compaction to deep overpressures in the U.S. Gulf Coast," Abnormal pressures in hydrocarbon environments, AAPG Memoir 70, 1998, pp. 87-104.

[18] G. Lash, R. Blood, "Origin of early overpressure in the Upper Devonian Catskill Delta Complex," Western New York state, Basin Research, 19(1), 2006, pp. 51-66.

[19] B. E. Law, C. W. Spencer, "Abnormal pressures in hydrocarbon environments," Abnormal pressures in hydrocarbon environments: AAPG 777 Memoir 70, 1998, pp. 1–11.

[20] X. R. Luo, G. Vasseur, "Contributions of compaction and aquathermal pressuring to geopressure and the influence of environmental conditions," AAPG Bull., v. 76, 1992, pp. 1150-1159.

[21] X. R. Luo, G Vasseur, G., "Contributions of compaction and aquathermal pressuring to geopressure and the influence of environmental conditions," AAPG Bull., v. 77, 1993, pp. 2011-2014.

[22] K. Magara, "Compaction and Fluid Migration, Practical Petroleum Geology," Elsevier, New York, 1978.

[23] C. K. Morley, R. King, R. Hillis, M. Tingay, G. Backe, "Deepwater fold and thrust belt classification, tectonics, structure and hydrocarbon prospectivity: A review," Earth-Science Reviews, 2001, pp. 104: 41–91.

[24] J. P. Mouchet, A. Mitchell, "Abnormal Pressures While Drilling: Origins, Prediction, Detection, Evaluation," Paris: Elf EP-Editions, Editions Technip, 1989.

[25] H. N. Nelson, K. J. Bird, "Porosity-depth trends and regional uplift calculated from sonic logs, National Reserve in Alaska," Scientific Investigation Report 2005-5051, U.S. Dept. of the Interior and USGS, 2005.

[26] D. E. Powley, "Pressures and hydrogeology in petroleum basins," Earth-Sci. Rev., 29, 1990, pp. 215-226.

[27] A. Revil, L. M. Cathles, J. D. Shosa, P. A. Pezard, F. D. de Larouziers, "Capillary sealing in sedimentary basins: a clear field example, Geophys. Res. Letters, v. 25 (3), 1998, pp. 389-392.

[28] Y. Shi, C. Wang, "Generation of high pore-pressures in accretionary prism: inferences from the Barbados subduction complex," J. Geophys. Res., v. 93, 1988, pp. 8893-8910.

[29] J. D. Shosa, L. M. Cathles, "Experimental investigation of capillary blockage of two-phase flow in layered porous media," Petroleum Systems of Deep-Water Basins: Global and Gulf of Mexico Experience, GCSSEPM Proceedings Volume, 2001.

[30] B. B. Stump, P. B. Flemings, T. Finkbeiner, M. D. Zoback, "Pressure differences between overpressured sands and bounding shales at the Eugene Island 330 field (offshore Louisiana, USA) with implications for fluid flow induced by sediment loading," Overpressures in Petroleum, 1998.

[31] R. E. Swarbrick, M. J. Osborne, "Mechanisms that generate abnormal pressures: an overview," Abnormal pressures in hydrocarbon environments: AAPG Memoir 70, 1998, p. 13–34.

[32] R. E. Swarbrick, M. J. Osborne, G. S. Yardley, "Comparison of overpressure magnitude resulting from the main generating mechanisms," Pressure regimes in sedimentary basins and their prediction: AAPG Memoir 76, 2002, pp. 1–12.

[33] J. Zhang, "Pore pressure prediction from well logs: methods, modifications, and new approaches," the Science Reviews, 108(1), 2011, pp. 50-63.

Numerical treatment and Global Error Estimation of a MHD Flows of an Oldroyd 6-Constant Nano-Fluid through a non-Darcy Porous medium with Heat and Mass Transfer

Abeer A. Shaaban

Department of Mathematics, Faculty of Education, Ain Shams University, Roxy, Cairo, Egypt
Department of Management Information Systems, Faculty of Business Administration in Rass, Qassim University, Qassim, KSA

Abstract— *Explicit Finite-Difference method was used to obtain the solution of the system of the non-linear ordinary differential equations which transform from the non-linear partial differential equations. These equations describe the steady magneto-hydrodynamic flow of an oldroyd 6-constant non-Newtonian nano-fluid through a non-Darcy porous medium with heat and mass transfer. The numerical formula of the velocity, the temperature, the concentration, and the nanoparticles concentration distributions of the problem were illustrated graphically. The effect of Darcy number D_a, Forchheimer number F_s, magnetic field parameter M, local temperature Grashof number G_r, local nanoparticle Grashof B_r, Prandtl number P_r, Dufour number N_d, Brownian motion parameter N_b, Thermophoresis parameter N_t, Lewis number L_e, Sort number L_d, Chemical reaction parameter R_c, and Chemical reaction order m on those formula were discussed at the values of material parameters ($\alpha_1 = 8$, $\alpha_2 = 2$) specially in the case of pure Coutte flow. Then, the effects of modified pressure gradients on those formulas were discussed in the case of pure Poiseuille flow and the generalized Couette flow. Also, an estimation of the global error for the numerical values of the solutions is calculated by using Zadunaisky technique.*

Keywords— Finite-difference method, Heat and Mass transfer, MHD flows, Non-Darcy Porous medium, Oldoryd 6-Constant non-Newtonian nano-Fluid.

I. NOMENCLATURE

A	Chemical Reaction rate constant	R_c	Chemical reaction parameter, defined by Eq. (42)
B_r	Local nanoparticle Grashof number, defined by Eq. (42)	S	The dimensionless concentration
c^*	Forchheimer number	t	The time
C	The concentration of the fluid	T	The fluid temperature
C_1	The concentration at lower plate ($y = 0$)	T_1	The temperature at lower plate ($y = 0$)
C_2	The concentration at upper plate ($y = H$)	T_2	The temperature at upper plate ($y = H$)
C_s	Nanoparticle susceptibility	$\underline{V}$	The velocity vector
D_a	Darcy number, defined by Eq. (42)		
D_B	Brownian diffusion coefficient		
D_T	Thermophoretic diffusion coefficient		**Greek symbols**
$\underline{E}$	Electrical field	$\hat{\phi}$	The nanoparticles phenomena
$\underline{F}$	The external force	Φ	The dissipation function
F_s	Forchheimer number, defined by Eq. (42)	ϕ	The dimensionless nanoparticles
G	Gravitational acceleration	θ	The dimensionless temperature
G_r	Local temperature Grashof number, defined by Eq. (42)	α_1 , α_2	The non-Newtonian parameters , defined by Eq. (36)
$\underline{H}$	The magnetic field		
$\underline{J}$	The current density	∇	Gradient operator
k	Thermal conductivity	∇^2	Laplacian operator

k^*	Permeability constant	μ	the dynamic viscosity of fluid
K_T	Thermal diffusion ratio	μ_e	the magnetic permeability
L_e	Lewis number, defined by Eq. (42)	ν	The kinematic viscosity (μ/ρ_f)
L_d	Sort number, defined by Eq. (42)	c_p	The specific heat capacity at constant pressure
M	Chemical Reaction order	ρ_f	The density of the fluid
M	Magnetic field parameter, defined by Eq. (42)	ρ_p	The density of the particle
N_b	Brownian motion parameter, defined by Eq. (42)	$(\rho c)_f$	heat capacity of the fluid
N_d	Dufour numbe, defined by Eq. (42)	$(\rho c)_p$	effective heat capacity of the nanoparticle material
N_t	The thermophoresis parameter, defined by Eq. (42)	σ	Electrical conductivity of the fluid
P	The fluid pressure	τ	The Cauchy Stress tensor
P_r	Prandtl number, defined by Eq. (42)	α_T , α_C	Volumetric thermal and solute expansion coefficients of the base fluid

II. INTRODUCTION

The study of non-Newtonian fluids has gained much attention recently in view of its promising applications in engineering and industry. Such fluids exhibit a non-linear relationship between the stresses and the rate of strain. Due to non-linear dependence, the analysis of the behavior of the non-Newtonian fluids tends to be much more complicated and subtle in comparison with that of Newtonian fluids. Flow of fluids with complex microstructure (e. g. molten polymer, polymer solutions, blood, paints, greases, oils, ketchup, etc.) cannot be described by a single model of non-Newtonian fluids. Many models that exist are based either on natural modifications of established macroscopic theories or molecular considerations. In general, the equations of motion for non-Newtonian fluids are of higher order than the Navier-Stokes equations and thus one need conditions in addition to the usual adherence boundary condition [28].

Guillope and Saut [2] has established existence results for some shearing motions of viscoelastic fluids of Oldroyd type. Some exact solutions of an Oldroyd 3-constant fluid are studied in [4], [5], [11], [13]. Baris [21] investigated the steady flow of an Oldroyd 6-constant fluid between intersecting planes using the series expansion method. Hayat et al. [23] studied the Couette and Poiseuille flows of an Oldroyd 6-constant fluid with magnetic field by using the Homotopy analysis method. Hayat et al. [25] studied the steady flow of a magneto-hydrodynamic Oldroyd 6-constant fluid by the motion of an infinite plate using the Homotopy analysis method. Wang et al. [30] investigated the non-linear magnetohydrodynamic problems of an Oldroyd 6-constant fluid by using analytical method and the finite-difference discretization method. Hayat et al. [24] studied the effect of the slip condition on flows of an Oldroyd 6-constant fluid. Rana et al. [14] studied the Hall effects on hydromagnetic flow of an Oldroyd 6-constant fluid between concentric cylinders by the finite difference method. Hayat et al. [26] investigated the exact solution of a thin film flow of an Oldroyd 6-constant fluid over a moving belt by the Homotopy perturbation.

Investigation of nanofluid flow has received special focus in the past due to its relevance in numerous industrial applications. The researchers not only discovered unexpected thermal properties of nanofluids but also proposed mechanisms behind the enhanced thermal properties of nanofluids and thus identified unusual opportunities to develop them as next generation coolants for computers and safe coolants for nuclear reactors. A combination of nanofluid with biotechnological components can provide potential applications in agriculture, pharmaceuticals and biological sensors. Various types of nanomaterials including nanoparticles, nanowires, nanofibers, nanostructures, and nanomachines are used in biotechnological applications. The commercialization of nano-biotechnological products seems to have a potential future and within next a few years many new products of this nature are likely to be used. Nano and micro-fluidics is a new area which has potential for engineering applications, especially for the development of new biomedical devices and procedures [1].

The magnetic nanofluids possess both liquid and magnetic properties. These fluids have key importance in modulators, optical switches, optical gratings and tunable optical fiber filters. The magnetic nanoparticles are significant in medicine, construction of loud speakers, sink float separation, cancer therapy and tumor analysis. Nowadays, the sustainable energy generation is one of the most important issues across the globe. Perhaps the solar energy is also one of the best sources of renewable energy with minimal environment impact. Solar power is a direct way obtaining heat, water, and electricity from the nature. Researchers concluded that heat transfer and solar collection processes can be improved through the addition of nanoparticles in the fluids. Fluid heating and cooling are required in many industrial fields such as power manufacturing and transportation. Effective cooling techniques are needed for cooling any sort of high energy device. Common heat transfer fluids such as ethylene glycol, water and engine oil have limited heat transfer capabilities due to their low heat transfer properties and thus cannot meet the modern cooling requirements [1].

The terminology of nanofluid was first used by Choi [22] when he experimentally discovered a significant improvement in the heat transfer performance through the addition of small amount nanometer sized particles in the base fluids. This addition also causes scattering of the incident radiation which allows a deeper absorption within the fluid. Recently, Trieb and Nitsch [3] proposed the idea of solar thermal collectors by using nanofluids to directly absorb the solar radiation.

The phenomenon of thermal conductivity enhancement by dispersing nanoparticles in the liquid was also observed by Masuda et al. [7]. Buongiorno [9] recognized that the two main effects namely the Brownian motion and thermophoretic diffusion of nanoparticles contribute to the massive increase in the thermal conductivity of the liquids. He also proposed the modifications in the transport equations due to these effects.

Vajravelu et al. [12] investigated heat and mass transfer properties of three-layer fluid flow in which nano-fluid layer is squeezed between two clear viscous fluid. Farooq et al. [27] studied heat and mass transfer of two-layer flows of third-grade nano-fluids in a vertical channel. Abou-zeid et al. [16] obtained numerical solutions and Global error estimation of natural convection effects on gliding motion of bacteria on a power-law nano-slime through a non-Darcy porous medium. El-Dabe et al. [17] investigated magneto-hydrodynamic non-Newtonian nano-fluid flow over a stretching sheet through a non-Darcy porous medium with radiation and chemical reaction.

Magneto-hydrodynamic (MHD) is concerning the mathematical and physical scaffold that introduces magnetic-dynamics in electrically conducting fluids (e.g. in plasmas and liquid metals). The applications of Magneto-hydrodynamic incompressible viscous flow in science and engineering involving heat and mass transfer under the influence of chemical reaction is great importance to many areas of science and engineering. This frequently occurs in agriculture, engineering, plasma studies and petroleum industries [15].

Flow through porous media plays an important role in countless practical applications such as ground water flows, enhanced oil recovery processes, contamination of soils by hazardous wastes, pollution movement [20]. An understanding of the dynamics of fluids in a porous medium is of principal interest because these flows are quite prevalent in nature. Such flows have attracted the attention of number of scholars due to their applications in many branches of science and technology, viz. in the fields of agricultural engineering to study the underground water resources; seepage of water in river beds; in petroleum technology to study the movement of natural gas, oil, and water through the oil reservoirs. In the widely used continuum approach to transport processes in a porous media, the differential equation governing the macroscopic fluid motion is based on the experimentally established Darcy law [8], which accounts for the drag exerted on the fluid by porous medium [29].

The objective of this work is to investigate the numerical solution by using Explicit Finite Difference method [6] for the system of non-linear differential equations which arises from magneto-hydrodynamic flows of an Oldroyd 6-constant Nano-fluid with a magnetic field through a non-Darcy porous medium with heat and mass transfer. We obtained the distributions of the velocity, the temperature, the concentration, and the Nanoparticles. Numerical results are found for different values of various non-dimensional parameters in the case of pure Coutte flow ($U_0 = 1$, $\frac{d\bar{P}}{dx}=0$). The effects of modified pressure gradients on those formulas were discussed in the case of pure Poiseuille flow and the generalized Couette flow. The results are shown graphically and discussed in detail. Also, the global error estimation for the error propagation is obtained by Zadunaisky technique [19].

III. FLUID MODEL

For an Oldroyd 6-constant fluid, the Cauchy stress tensor τ is given by [30]

$$\tau = -PI + S^*, \tag{1}$$

$$S^* + \lambda_1 \frac{DS^*}{Dt} + \frac{\lambda_3}{2}(S^*A_1 + A_1S^*) + \frac{\lambda_5}{2}(tr\, S^*)A_1 = \mu\left[A_1 + \lambda_2 \frac{DA_1}{Dt} + \lambda_4 A_1^2\right]. \tag{2}$$

Where,

$$A_1 = L + L^T \quad , \quad L = grad\, V\,. \tag{3}$$

$-PI$ is the indeterminate part of the stress due to the constraint of incompressibility, S^* is the extra stress tensor, A_1 is the first Rivlin-Ericksen tensor, L is the velocity gradient, $\underline{V}$ is the velocity vector, and μ, λ_i $(i = 1, 2, \ldots\ldots, 5)$ are the six material constants.

The contra variant convected derivative $\frac{D}{D\,t}$ satisfying the principle of material frame in difference in terms of the material $\frac{d}{d\,t}$ is defined by the following equation

$$\frac{DS^*}{Dt} = \frac{dS^*}{dt} - L\,S^* - S^*L^T. \tag{4}$$

in which the superscript T is used for the transpose operation.

It should be noted that when $\lambda_i = 0$ $(i = 1, 2, 3, 4, 5)$ the model reduces to the classical linearly viscous model of Newtonian fluid. For $\lambda_i = 0$ $(i = 3, 4, 5)$ a 3-constant model of an Oldroyd-B fluid is described, while for $\lambda_i = 0$ $(i = 2, 3, 4, 5)$ a Maxwell model is formulated. For $\lambda_i = 0$ $(i = 1, 3, 4, 5)$ the model describes a second-grade fluid.

IV. MATHEMATICAL FORMULATION

We consider magnetohydrodynamic flows of an Oldroyd 6-constant Nano-fluid through a non-Darcy porous medium between two parallel plates (see FIG. 1). We take in our consideration the presence of heat and mass transfer with chemical reaction.

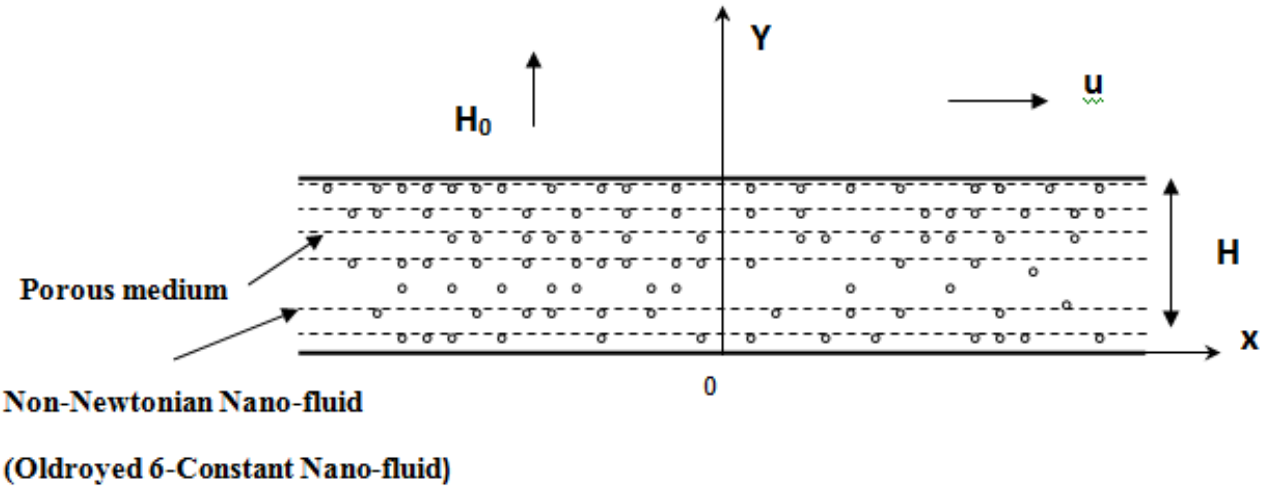

FIGURE 1: MAGNETOHYDRODYNAMIC FLOWS OF AN OLDROYD 6-CONSTANT NANO-FLUID THROUGH A NON-DARCY POROUS MEDIUM BETWEEN TWO PARALLEL PLATES

V. BASIC EQUATIONS

The basic equations governing the flow of an incompressible fluid are the following equations [10, 18],

The continuity equation

$$\nabla.\underline{V} = 0 \quad , \tag{5}$$

The momentum equation

$$\rho_f \frac{d\underline{V}}{dt} = \nabla.\tau + \mu_e\left(\underline{J} \wedge \underline{H}\right) - \rho_f c^* \underline{V}|\underline{V}| - \frac{\mu}{k^*}\underline{V} + \underline{F} \ , \tag{6}$$

The energy equation

$$\left(\rho c_p\right)_f \left[\frac{dT}{dt}\right] = k\,\nabla^2 T + \Phi + \left(\rho c_p\right)_p \left[D_B\left(\nabla T.\nabla\hat{\phi}\right) + \frac{D_T}{T_1}(\nabla T)^2\right] + \frac{\rho_f D_B \kappa_T}{C_s}, \tag{7}$$

The concentration equation

$$\frac{dC}{dt} = D_B\,\nabla^2 C + \frac{D_T \kappa_T}{T_1}\,\nabla^2 T - A(C - C_2)^m \quad , \tag{8}$$

The nanoparticles concentration equation

$$\frac{d\hat{\phi}}{dt} = D_B \nabla^2 \hat{\phi} + \frac{D_T}{T_2}\nabla^2 T \quad . \tag{9}$$

Where, $\frac{d}{dt} = \left[\frac{\partial}{\partial t} + \left(\underline{V}.\nabla\right)\right]$ denotes the material time derivative, $\underline{J} = \sigma\left(\underline{E} + \mu_e\,\underline{V} \wedge \underline{H}\right)$, and $\underline{E} = 0$.

For a simple one-dimensional shearing flow considered in this work, the extra stress tensor and the velocity are of the form

$$S(y,t) = \begin{pmatrix} S_{xx} & S_{xy} & S_{xz} \\ S_{yx} & S_{yy} & S_{yz} \\ S_{zx} & S_{zy} & S_{zz} \end{pmatrix} \quad , \quad V(y,t) = \begin{pmatrix} u(y,t) \\ 0 \\ 0 \end{pmatrix} \quad . \tag{10}$$

Also, the constant magnetic field, the temperature, the concentration, and the nanoparticles are of the form

$$\underline{H} = (0, H_0, 0) \ , \ T = T(y,t) \ , \ C = C(y,t) \ , \ \hat{\phi} = \hat{\phi}(y,t) \ . \tag{11}$$

For steady motion, it is clear that with the simplified dependence (10-11), the continuity equation (5) is satisfied identically, and equations (1-3) and (6) become,

$$\frac{\partial P}{\partial x} = \frac{dS_{xy}}{dy} - \sigma\,\mu_e^2\,H_0^2\,u - \rho c^* u^2 - \frac{\mu}{\kappa^*}u + \rho_f g \alpha_T (T - T_2) + \rho_f g \alpha_C (C - C_2) \quad , \tag{12}$$

$$\frac{\partial P}{\partial y} = \frac{dS_{yy}}{dy} \quad , \tag{13}$$

$$\frac{\partial P}{\partial z} = \frac{dS_{zy}}{dy} \quad , \tag{14}$$

$$S_{xx} + (\lambda_3 - 2\lambda_1) S_{xy} \frac{du}{dy} = \mu(\lambda_4 - 2\lambda_2)\left(\frac{du}{dy}\right)^2 \quad , \tag{15}$$

$$S_{xy} - \lambda_1 S_{yy} \frac{du}{dy} + \left(\frac{\lambda_3 + \lambda_5}{2}\right)\left(S_{xx} + S_{yy}\right)\frac{du}{dy} + \frac{\lambda_5}{2} S_{zz} \frac{du}{dy} = \mu\left(\frac{du}{dy}\right) \quad , \tag{16}$$

$$S_{zx} + \left(\frac{\lambda_3 - 2\lambda_1}{2}\right) S_{zy} \frac{du}{dy} = 0 \quad , \tag{17}$$

$$S_{yy} + \lambda_3 S_{xy} \frac{du}{dy} = \mu \lambda_4 \left(\frac{du}{dy}\right)^2 \quad , \tag{18}$$

$$S_{zy} + \frac{\lambda_3}{2} S_{zx} \frac{du}{dy} = 0 \quad , \tag{19}$$

$$S_{zz} = 0 \quad . \tag{20}$$

by addition of two equations (15) and (18) we have,

$$S_{xx} + S_{yy} = 2\mu(\lambda_4 - \lambda_2)\left(\frac{du}{dy}\right)^2 - 2(\lambda_3 - \lambda_1) S_{xy} \frac{du}{dy} \quad . \tag{21}$$

from equations (17) and (19) we get

$$S_{zx} = S_{zy} = 0 \quad . \tag{22}$$

Substituting (18) – (22) in (14) and (16) we have

$$\frac{\partial P}{\partial z} = 0 \quad , \tag{23}$$

$$S_{xy} = \frac{\left(\mu\frac{du}{dy}+\mu\,\alpha_1\left(\frac{du}{dy}\right)^3\right)}{\left(1+\alpha_2\left(\frac{du}{dy}\right)^2\right)} \quad . \tag{24}$$

where,

$$\alpha_1 = \lambda_1\lambda_4 - (\lambda_3+\lambda_5)(\lambda_4-\lambda_2) \quad , \tag{25}$$

$$\alpha_2 = \lambda_1\lambda_3 - (\lambda_3+\lambda_5)(\lambda_3-\lambda_1) \quad . \tag{26}$$

Defining the modified pressure

$$\hat{P} = P - S_{yy} \quad , \tag{27}$$

and using (12) – (14) and (24) we arrive at

$$\frac{\partial \hat{P}}{\partial x} = \frac{d}{dy}\left[\frac{\left(\mu\frac{du}{dy}+\mu\,\alpha_1\left(\frac{du}{dy}\right)^3\right)}{\left(1+\alpha_2\left(\frac{du}{dy}\right)^2\right)}\right] - \sigma\,\mu_e^2\,H_0^2\,u - \rho c^* u^2 - \frac{\mu}{\kappa^*}u + \rho_f g\alpha(T-T_2) + \rho_f g\alpha(C-C_2) \quad , \tag{28}$$

$$\frac{\partial \hat{P}}{\partial y} = \frac{\partial \hat{P}}{\partial z} = 0 \quad . \tag{29}$$

The dissipation function Φ can be written as follows

$$\Phi = \tau_{ij}\frac{\partial V_i}{\partial x_j} \quad . \tag{30}$$

By using the definitions (10) we have,

$$\Phi = S_{xy}\frac{du}{dy} \quad . \tag{31}$$

Then, equations (7 - 9) can be written as follows:

$$\kappa\frac{d^2T}{dy^2} + \frac{\rho_f D_B \kappa_T}{C_s}\frac{d^2C}{dy^2} + \left(\rho c_p\right)_p\left[D_B\frac{dT}{dy}\frac{d\hat{\phi}}{dy} + \frac{D_T}{T_1}\left(\frac{dT}{dy}\right)^2\right] + \left[\frac{\left(\mu\frac{du}{dy}+\mu\,\alpha_1\left(\frac{du}{dy}\right)^3\right)}{\left(1+\alpha_2\left(\frac{du}{dy}\right)^2\right)}\right]\frac{du}{dy} = 0 \quad , \tag{32}$$

$$D_B\frac{d^2C}{dy^2} + \frac{D_T\kappa_T}{T_1}\frac{d^2T}{dy^2} - A(C-C_2)^m = 0 \quad , \tag{33}$$

$$D_B\frac{d^2\hat{\phi}}{dy^2} + \frac{D_T}{T_2}\frac{d^2T}{dy^2} = 0 \quad . \tag{34}$$

The boundary conditions of the problem are given by:

$$u = 0 \;,\quad T = T_1 \;,\; C = C_1 \;,\; \hat{\phi} = \hat{\phi}_1 \qquad at \quad y = 0 \;,$$

$$u = u_0 \;,\quad T = T_2 \;,\; C = C_2 \;,\; \hat{\phi} = \hat{\phi}_2 \qquad at \quad y = H \;. \tag{35}$$

We shall now write the field equations (28), (32 – 34) and the boundary conditions (35) in terms of a set of dimensionless variables and, for this purpose, we choose H and U as the characteristic length and velocity and introduce the following

dimensionless variables of both:

$$\bar{y} = \frac{y}{H} \ , \ \bar{u} = \frac{u}{U} \ , \ \bar{\alpha}_1 = \frac{\alpha_1}{\left(H/U\right)^2} \ , \ \bar{\alpha}_2 = \frac{\alpha_2}{\left(H/U\right)^2} \ , \ \bar{x} = \frac{x}{H} \ , \ \bar{\hat{P}} = \frac{\hat{P}}{\left(\frac{\mu U}{H}\right)} \ , \ \bar{\kappa}^* = \frac{\kappa^*}{H^2} \ ,$$

$$\theta = \frac{T-T_2}{T_1-T_2} \ , \ S = \frac{C-C_2}{C_1-C_2} \ , \ \phi = \frac{\hat{\phi}-\hat{\phi}_2}{\hat{\phi}_1-\hat{\phi}_2} \ . \tag{36}$$

Thus, the system of our non-linear differential equations (28), (32 – 34) and the boundary conditions (35) can be rewritten in a non-dimensional forms:

$$\frac{d}{d\bar{y}}\left[\frac{\left(\frac{d\bar{u}}{d\bar{y}} + \bar{\alpha}_1\left(\frac{d\bar{u}}{d\bar{y}}\right)^3\right)}{\left(1+\bar{\alpha}_2\left(\frac{d\bar{u}}{d\bar{y}}\right)^2\right)}\right] - \frac{\partial \bar{\hat{P}}}{\partial \bar{x}} - F_s\,\bar{u}^2 - \left(M + \frac{1}{D_a}\right)\bar{u} + G_r\,\theta + B_r\,S = 0 \quad , \tag{37}$$

$$\frac{1}{P_r}\frac{d^2\theta}{d\bar{y}^2} + N_d\frac{d^2S}{d\bar{y}^2} + N_b\left(\frac{d\theta}{d\bar{y}}\right)\left(\frac{d\phi}{d\bar{y}}\right) + N_t\left(\frac{d\theta}{d\bar{y}}\right)^2 + \left[\frac{\left(\frac{d\bar{u}}{d\bar{y}} + \bar{\alpha}_1\left(\frac{d\bar{u}}{d\bar{y}}\right)^3\right)}{\left(1+\bar{\alpha}_2\left(\frac{d\bar{u}}{d\bar{y}}\right)^2\right)}\right]\frac{d\bar{u}}{d\bar{y}} = 0 \ , \tag{38}$$

$$\frac{1}{L_e}\frac{d^2S}{d\bar{y}^2} + L_d\frac{d^2\theta}{d\bar{y}^2} - R_c\,S^m = 0 \quad , \tag{39}$$

$$N_b\frac{d^2\phi}{d\bar{y}^2} + N_t\frac{d^2\theta}{d\bar{y}^2} = 0 \quad . \tag{40}$$

with the dimensionless boundary conditions:

$$\bar{u} = 0 \ , \ \theta = 1 \ , S = 1 \ , \phi = 1 \quad at \quad \bar{y} = 0 \ ,$$

$$\bar{u} = \bar{U}_0 \ , \ \theta = 0 \ , S = 0 \ , \phi = 0 \quad at \quad \bar{y} = 1 \ . \tag{41}$$

Where, the dimensionless parameters are defined by

$$D_a = \frac{\kappa^*}{H^2} \ , \quad F_s = \frac{\rho c^* U H^2}{\mu} \ , \quad M = \frac{\sigma\,\mu_e^2\,H_0^2 H^2}{\mu} \ , \ G_r = \frac{g\,\alpha_T\,H\,(T_1-T_2)}{U^2} \ , \quad B_r = \frac{g\,\alpha_C\,H\,(C_1-C_2)}{U^2} \ ,$$

$$P_r = \frac{\mu\,U^2}{\kappa(T_1-T_2)} \ , \ N_d = \frac{D_B\kappa_T(C_1-C_2)}{C_s\,c_p\,\nu\,(T_1-T_2)} \ , \ N_b = \frac{D_B\left(\hat{\phi}_1-\hat{\phi}_2\right)}{\nu} \ , \quad N_t = \frac{D_T\,(T_1-T_2)}{T_1\,\nu} \ ,$$

$$L_e = \frac{\nu}{D_B} \ , \quad L_d = \frac{D_T\,\kappa_T\,(T_1-T_2)}{T_1\,\nu\,(C_1-C_2)} \ , \ R_c = \frac{H^2 A(C_1-C_2)^{m-1}}{\nu} \quad . \tag{42}$$

For convenience, we shall drop the bars that identify the dimensionless quantities. The system of non-linear ordinary differential equations (37) – (40) with the boundary conditions (41), will be solved numerically by using the explicit finite-difference method. And, we computed the global error for the solutions of the problem.

VI. NUMERICAL SOLUTION

The equations (37) – (40) can be written after applied explicit finite difference schemes [6] as:

$$\left(\frac{u[i-1]-2u[i]+u[i+1]}{h^2}\right) - \frac{\left[\frac{d\bar{P}}{dx}+F_S(u[i])^2+\left(M+\frac{1}{D_a}\right)u[i]-G_r\,\theta[i]-B_r\,S[i]\right]\cdot\left[1+\alpha_2\left(\frac{u[i]-u[i-1]}{h}\right)^2\right]^2}{\left[1+3\alpha_1\left(\frac{u[i]-u[i-1]}{h}\right)^2-\alpha_2\left(\frac{u[i]-u[i-1]}{h}\right)^2+\alpha_1\alpha_2\left(\frac{u[i]-u[i-1]}{h}\right)^4\right]} = 0 \quad , \tag{43}$$

$$\left(\frac{\theta[i-1]-2\theta[i]+\theta[i+1]}{h^2}\right) + P_r\,N_d\left(\frac{S[i-1]-2S[i]+S[i+1]}{h^2}\right) + P_r\,N_b\left(\frac{\theta[i]-\theta[i-1]}{h}\right)\left(\frac{\phi[i]-\phi[i-1]}{h}\right) + P_r\,N_t\left(\frac{\theta[i]-\theta[i-1]}{h}\right)^2 + P_r\left[\frac{1+\alpha_1\left(\frac{u[i]-u[i-1]}{h}\right)^2}{1+\alpha_2\left(\frac{u[i]-u[i-1]}{h}\right)^2}\right]\left(\frac{u[i]-u[i-1]}{h}\right)^2 = 0 \quad , \tag{44}$$

$$\left(\frac{S[i-1]-2S[i]+S[i+1]}{h^2}\right)+L_e\,L_d\,\left(\frac{\theta[i-1]-2\theta[i]+\theta[i+1]}{h^2}\right)-L_e\,R_c\,(S[i])^m=0\quad,\tag{45}$$

$$\left(\frac{\phi[i-1]-2\phi[i]+\phi[i+1]}{h^2}\right)+{N_t}/{N_b}\left(\frac{\theta[i-1]-2\theta[i]+\theta[i+1]}{h^2}\right)=0\,.\tag{46}$$

Where the index i refers to y and the $\Delta y=h=0.04$. According to the boundary conditions (41) we can solved equations (43) – (46) numerically, then a Newtonian iteration method continues until either of goals specified by accuracy goal or precision goal is achieved.

VII. ESTIMATION OF THE GLOBAL ERROR

We used Zadunaisky technique [19] for calculating the global error, which can be explained in the following steps:

1. We fined the interpolating polynomial of $u\,,\,u',\,\theta,\,\theta',\,S,\,S',\,\phi,\,\phi'$ from the values of them which came from the explicit finite-difference method. Then we named it $P_i(x)$, $(i=1,2,3,\dots\dots\dots\dots,8)$, and we found the interpolating functions of u'', θ'', S'', and ϕ'', and we named them as:

$$u''=q_1(x),\quad \theta''=q_2(x),\quad S''=q_3(x),\quad \phi''=q_4(x)\,,$$

$$q_1(x)=\frac{\left[\frac{d\tilde{P}}{dx}+F_S\left(P_1(x)\right)^2+\left(M+\frac{1}{Da}\right)P_1(x)-G_rP_3(x)-B_r\,P_5(x)\right].\left[1+\alpha_2\left(P_2(x)\right)^2\right]^2}{\left[1+3\alpha_1\left(P_2(x)\right)^2-\alpha_2\left(P_2(x)\right)^2+\alpha_1\alpha_2\left(P_2(x)\right)^4\right]}\quad,$$

$$q_2(x)=\frac{1}{(1-P_r\,N_d\,L_e\,L_d)}\left[-P_rN_dL_eR_c\left(P_5(x)\right)^m-P_r\,N_b\,P_4(x)\,P_8(x)-P_r\,N_t\,\left(P_4(x)\right)^2-P_r\left[\frac{1+\alpha_1\left(P_2(x)\right)^2}{1+\alpha_2\left(P_2(x)\right)^2}\right]\left(P_2(x)\right)^2\right]\quad,$$

$$q_3(x)=-L_e\,L_d\,q_2(x)+L_e\,R_c\,\left(P_5(x)\right)^m\quad,$$

$$q_4(x)=-{N_t}/{N_b}\,q_2(x).\tag{47}$$

2. We calculate the defect functions $D_i(x)$, $(i=1,2,3,\dots\dots,8)$, which can be written as follows:

$$D_1(x)=P_1'(x)-P_2(x)=0\ ,\ D_2(x)=P_1''(x)-q_1(x)\ ,$$

$$D_3(x)=P_3'(x)-P_4(x)=0\ ,\ D_4(x)=P_3''(x)-q_2(x)\ ,$$

$$D_5(x)=P_5'(x)-P_6(x)=0\ ,\ D_6(x)=P_5''(x)-q_3(x)\ ,$$

$$D_7(x)=P_7'(x)-P_8(x)=0\ ,\ D_8(x)=P_7''(x)-q_4(x)\ .\tag{48}$$

3. We add the defect functions $D_i(x)$, $(i=1,2,3,\dots\dots,8)$ to the original problem.
4. We solved the pseudo-problem (new problem) by the same method which is used for solving the main problem, and we will have the new solutions.
5. We calculate an estimation of the global error from the formulas,

$$\underline{e}_n=\underline{f}_n-\underline{f}(x_n)=\underline{f}_n-\underline{P}(x_n)\quad,\quad(n=0,1,2,\dots\dots\dots,25)\tag{49}$$

In this relation, $\underline{f}_n$ is the approximate solutions of the new problem (the pseudo-problem) at the point x_n , and $\underline{f}(x_n)$ is the exact solutions of pseudo-problem at x_n.

The values of global error for the solutions of the problem which solved by the explicit finite difference method are shown in table (1). The error in table (1) based on using 26 points to find interpolating polynomials $P_i(x)$ of degree 25. In order to achieve the above task, we used the Mathematica package.

TABLE 1
DIFFERENT VALUES OF THE DIMENSIONLESS PHYSICAL QUANTITIES

The global error by using finite difference technique								
y	**u =Y1**	**error (e1n)**	**θ =Y3**	**error (e3n)**	**S=Y5**	**error (e_{5n})**	**ϕ=Y7**	**error (e7n)**
0	0.00E+00	0.00E+00	1.00E+00	0.00E+00	1.00E+00	0.00E+00	1.00E+00	0.00E+00
0.08	0.084677	2.45938E-06	1.0654	1.06548E-05	0.877711	4.73414E-06	0.832759	9.45491E-06
0.16	0.167804	4.11468E-06	1.10363	1.91716E-05	0.765806	8.26993E-06	0.681824	1.69842E-05
0.24	0.249488	5.13257E-06	1.11623	2.58221E-05	0.662794	1.08326E-05	0.546264	2.28215E-05
0.32	0.329882	5.63641E-06	1.10429	3.07583E-05	0.567513	1.25695E-05	0.425427	2.71033E-05
0.4	0.40918	5.70977E-06	1.06848	3.40436E-05	0.479077	1.35718E-05	0.318913	2.98941E-05
0.48	0.487619	5.39798E-06	1.00906	3.56739E-05	0.39684	1.38901E-05	0.226562	3.12032E-05
0.56	0.565479	4.70768E-06	0.925913	3.55924E-05	0.320364	1.3545E-05	0.148452	3.09962E-05
0.64	0.64308	3.60483E-06	0.818507	3.37017E-05	0.249402	1.25357E-05	0.0848959	2.92048E-05
0.72	0.720789	2.019E-06	0.685922	2.98767E-05	0.183879	1.0847E-05	0.0364469	2.57363E-05
0.8	0.799017	9.48686E-08	0.526812	2.39868E-05	0.123881	8.45801E-06	0.00391268	2.04927E-05
0.88	0.878223	2.40736E-06	0.339383	1.59365E-05	0.0696485	5.37175E-06	-0.0116299	1.34196E-05
0.96	0.958919	2.76915E-06	0.121352	5.76248E-06	0.0215698	1.761E-06	-0.00881092	4.69398E-06
1	1.00E+00	0.00E+00	0.00E+00	0.00E+00	0.00E+00	0.00E+00	0.00E+00	0.00E+00

VIII. NUMERICAL RESULTS AND DISCUSSION

In this paper we generalized the problem of MHD flows to include the non-Newtonian Nano-fluid obeying Oldroyd 6-constant model through a porous medium of non-Darcy type with heat and mass transfer. The system of non-linear ordinary differential equations (37) – (40) with the boundary conditions (41) was solved numerically by using an Explicit finite Difference method. The functions $u, \theta, S,$ and ϕ are obtained and illustrated graphically as shown in figures (a-1 – a-5), (b-1 – b-13), (c-1 – c-13), and (d-1 – d-13) for different values of the parameters of the problem in the case of pure Couette flow $\left(U_0 = 1, \frac{d\hat{P}}{dx}=0\right)$, at the values of non-Newtonian parameters $(\alpha_1 = 8, \alpha_2 = 2)$. And, figures (e-1 – e-4) show the effects of modified pressure gradients on those formula in the case of pure Poiseuille flow $(U_0 = 0)$, at the values of non-Newtonian parameters $(\alpha_1 = 8, \alpha_2 = 2)$. And, figures (f-1 – f-4) show the effects of modified pressure gradients on those formula in the case of generalized Couette flow $(U_0 = 1)$, at the values of non-Newtonian parameters $(\alpha_1 = 8, \alpha_2 = 2)$.

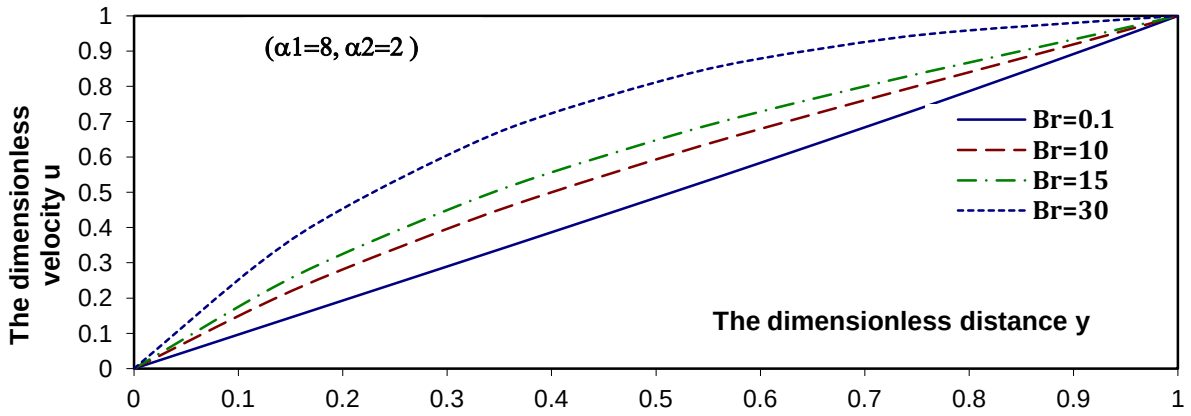

FIG. A-1: Profiles of the velocity u(y) for a pure Couette flow with various values of Br for a system have the particulars M=0.1, Da=1, Fs=0.5, Gr=0.1, Pr=0.7, Nd=2, Nb=0.5, Nt=0.3, Le=2, Ld=0.1, Rc=0.5, m=2.

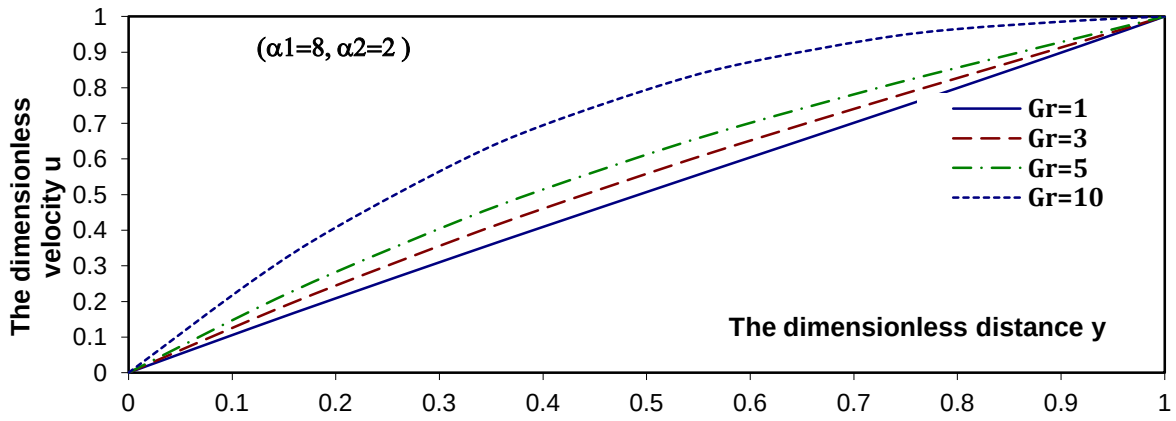

FIG. A-2: Profiles of the velocity u(y) for a pure Couette flow with various values of Gr for a system have the particulars M=0.1, Da=1, Fs=0.5, Br=0.1, Pr=0.7, Nd=2, Nb=0.5, Nt=0.3, Le=2, Ld=0.1, Rc=0.5, m=2.

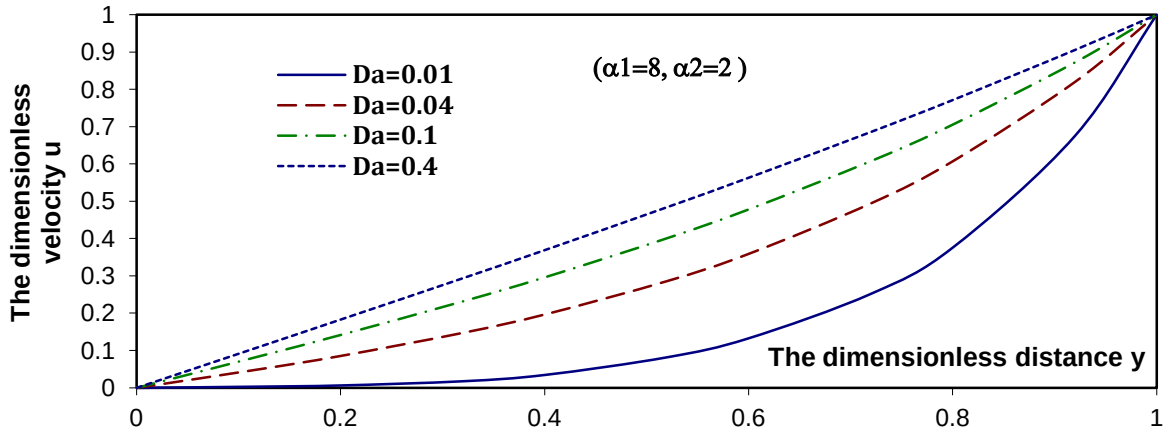

FIG. A-3: Profiles of the velocity u(y) for a pure Couette flow with various values of Da for a system have the particulars M=0.1, Fs=0.5, Nt=0.3, Gr=0.1, Br= 0.1, Pr=0.7, Nd=2, Nb=0.5, Nt=0.3, Le=2, Ld=0.1, Rc=0.5, m=2.

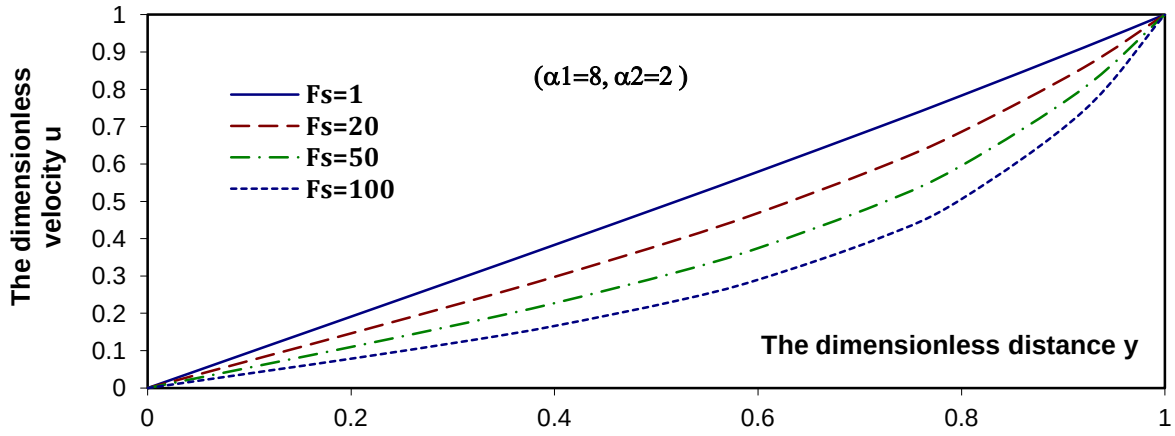

FIG. A-4: Profiles of the velocity u(y) for a pure Couette flow with various values of Fs for a system have the particulars M=0.1, Da=1, Nt=0.3, Gr=0.1, Br=0.1, Pr=0.7, Nd=2, Nb=0.5, Nt=0.3, Le=2, Ld=0.1, Rc=0.5, m=2.

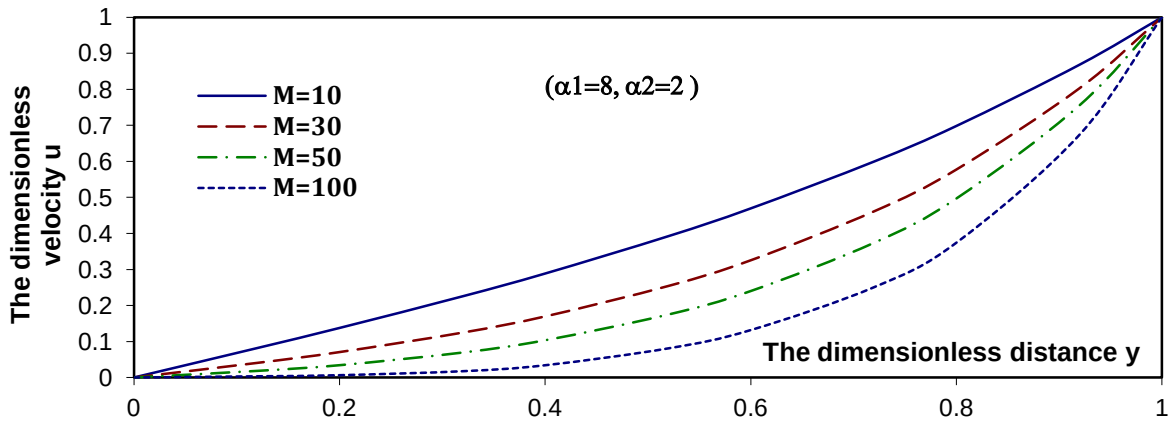

FIG. A-5: Profiles of the velocity u(y) for a pure Couette flow with various values of M for a system have the particulars Da=1, Fs=0.5, Nt=0.3, Gr=0.1, Br= 0.1, Pr=0.7, Nd=2, Nb=0.5, Nt=0.3, Le=2, Ld=0.1, Rc=0.5, m=2.

8.1 Couette flow

Considering the Couette flow of an Oldroyd 6-constant fluid between two infinite parallel plates, for which the lower plate is fixed and the top plate moves with the velocity ($U_0 = 1$), it is assumed that the flow is driven only by the motion of the top plate. The modified pressure gradient in the flow direction vanishes instant ($\frac{d\hat{P}}{dx}=0$). Figures (a-1 – a-5), (b-1 – b-13), (c-1 – c-13), and (d-1 – d-13) will show the effect of the problem parameters on the problem solutions in this case.

Figures (a-1 – a-5) show the distributions of the velocity profile u at different values of some parameters of the problem. It is clear that, the velocity increases by increasing each of local temperature Grashof number G_r, local nanoparticle Grashof B_r, and Darcy number D_a. But, the velocity decreases by increasing each of Forchheimer number F_s, magnetic field parameter M.

Figures (b-1 – b-13) describe the distributions of the temperature profile θ at different values of some parameters of the problem. It is noted that, as the local nanoparticle Grashof B_r, local temperature Grashof number G_r, and Darcy number D_a increase, the temperature increases in the region $0 \leq y \leq 0.58$ and, it returns decrease to $0.58 \leq y \leq 1$. The temperature increases by increasing each of Sort number L_d, Lewis number L_e, Brownian motion parameter N_b, Dufour number N_d, Thermophoresis parameter N_t, Prandtl number P_r, and Chemical reaction parameter R_c. And, as Forchheimer number F_s increases, the temperature decreases in the region $0 \leq y \leq 0.7$ and, it returns increase to $0.7 \leq y \leq 1$. Also, as magnetic field parameter M increases, the temperature decreases in the region $0 \leq y \leq 0.5$ and, it returns increase to $0.5 \leq y \leq 1$. Finally, the temperature decreases by increasing Chemical reaction order m.

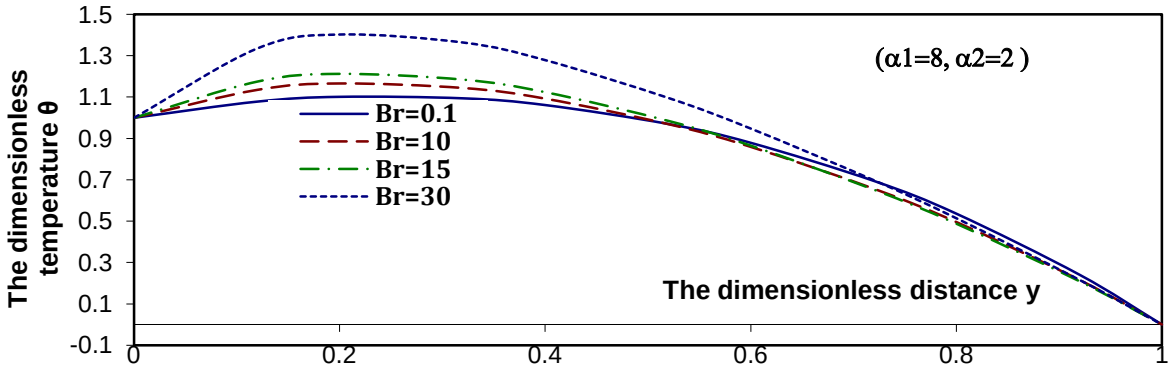

FIG. B-1: Profiles of the temperature θ(y) for a pure Couette flow with various values of Br for a system have the particulars M=0.1, Da=1, Fs=0.5, Gr=0.1, Pr=0.7, Nd=2, Nb=0.5, Nt=0.3, Le=2, Ld=0.1, Rc=0.5, m=2.

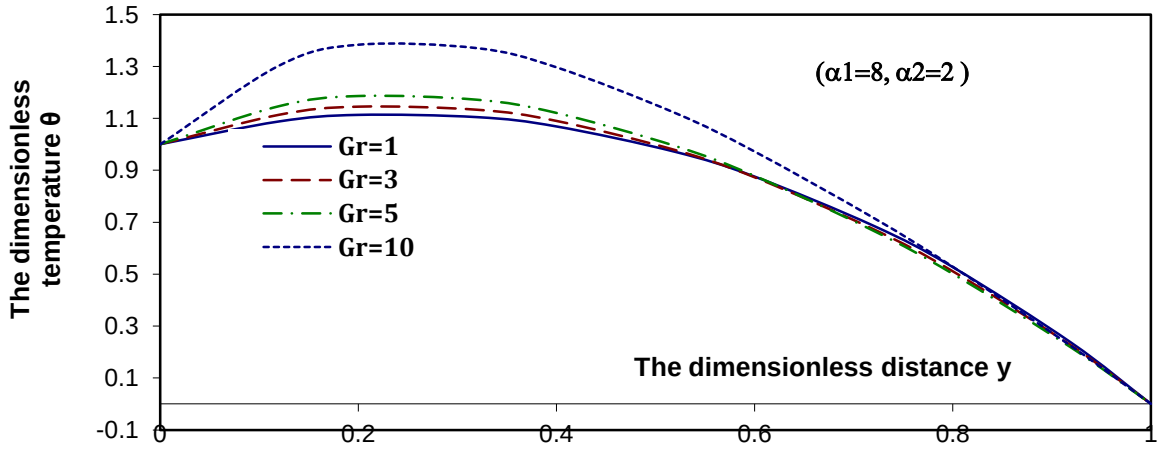

FIG. B-2: Profiles of the temperature θ(y) for a pure Couette flow with various values of Gr for a system have the particulars M=0.1, Da=1, Fs=0.5, Br=0.1, Pr=0.7, Nd=2, Nb=0.5, Nt=0.3, Le=2, Ld=0.1, Rc=0.5, m=2.

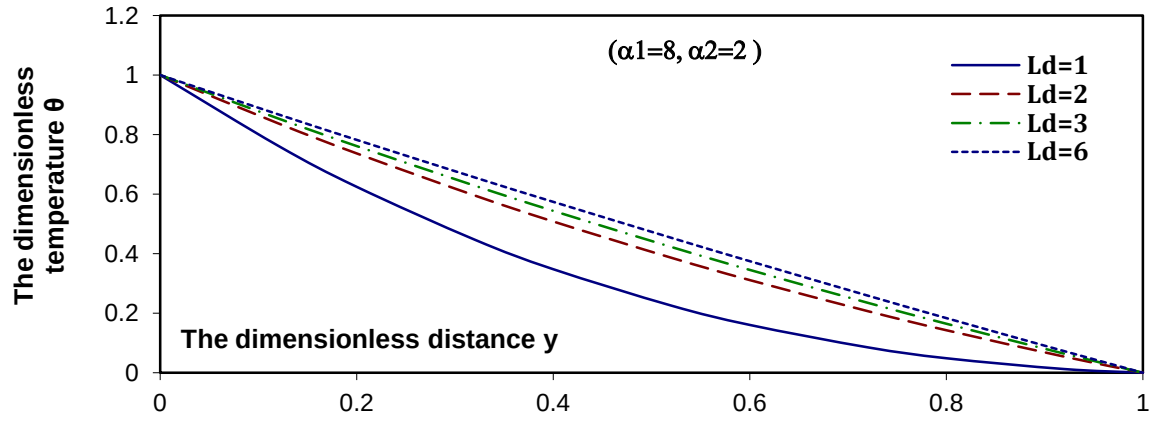

FIG. B-3: Profiles of the temperature θ(y) for a pure Couette flow with various values Ld for a system have the particulars M=0.1, Da=1, Fs=0.5, Gr=0.1, Br=0.1, Pr=0.7, Nd=2, Nb=0.5, Nt=0.3, Le=2, Rc=0.5, m=2.

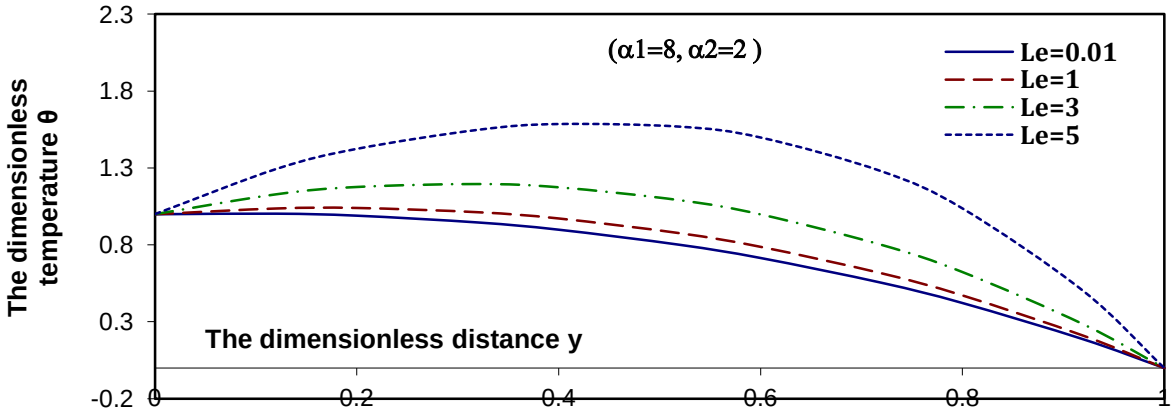

FIG. B-4: Profiles of the temperature θ(y) for a pure Couette flow with various values of Le for a system have the particulars M=0.1, Da=1, Fs=0.5, Gr=0.1, Br=0.1, Pr=0.7, Nd=2, Nb=0.5, Nt=0.3, Ld=0.1, Rc=0.5, m=2.

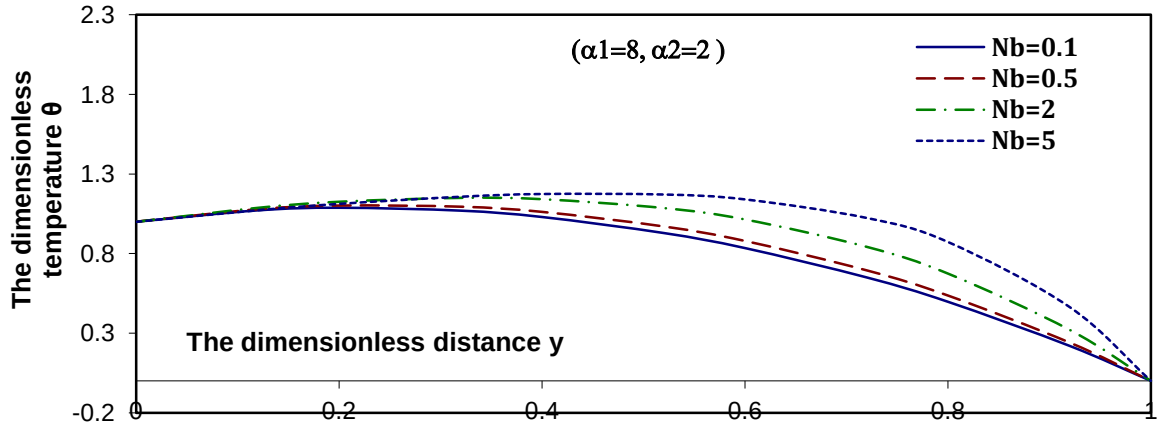

FIG. b-5: Profiles of the temperature θ(y) for a pure Couette flow with various values of Nb for a system have the particulars M=0.1, Da=1, Fs=0.5, Gr=0.1, Br=0.1, Pr=0.7, Nd=2, Le=2, Nt=0.3, Ld=0.1, Rc=0.5, m=2.

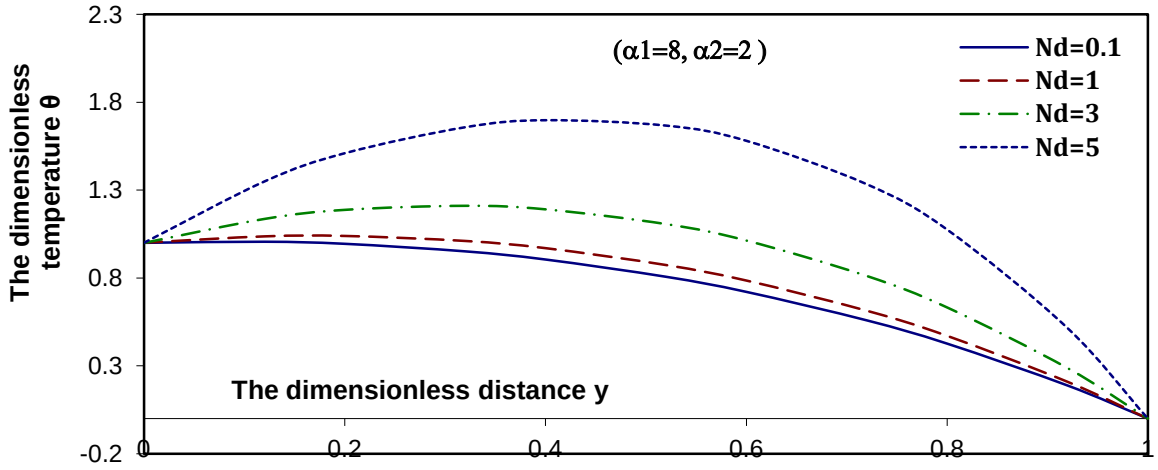

FIG. b-6: Profiles of the temperature θ(y) for a pure Couette flow with various values of Nd for a system have the particulars M=0.1, Da=1, Fs=0.5, Gr=0.1, Br=0.1, Pr=0.7, Nb=0.5, Le=2, Nt=0.3, Ld=0.1, Rc=0.5, m=2.

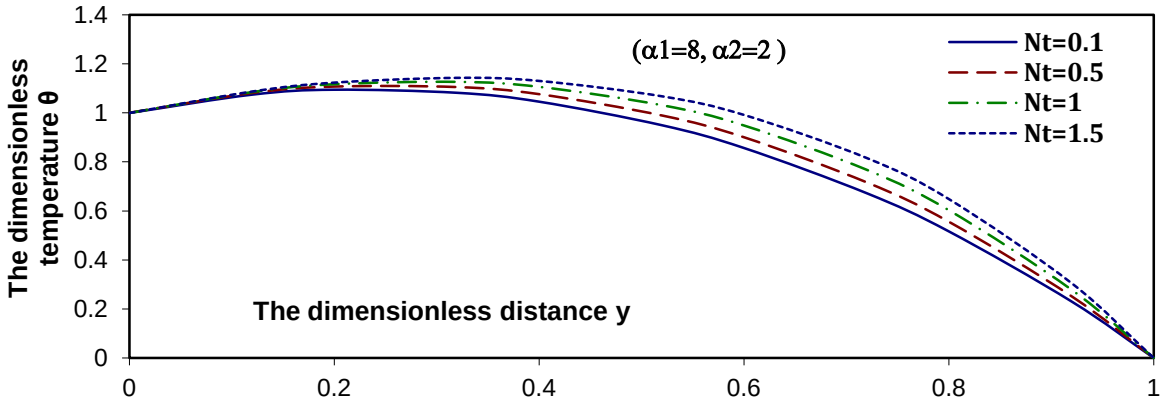

FIG. b-7: Profiles of the temperature θ(y) for a pure Couette flow with various values of Nt for a system have the particulars M=0.1, Da=1, Fs=0.5, Gr=0.1, Br=0.1, Pr=0.7, Nb=0.5, Le=2, Nd=2, Ld=0.1, Rc=0.5, m=2.

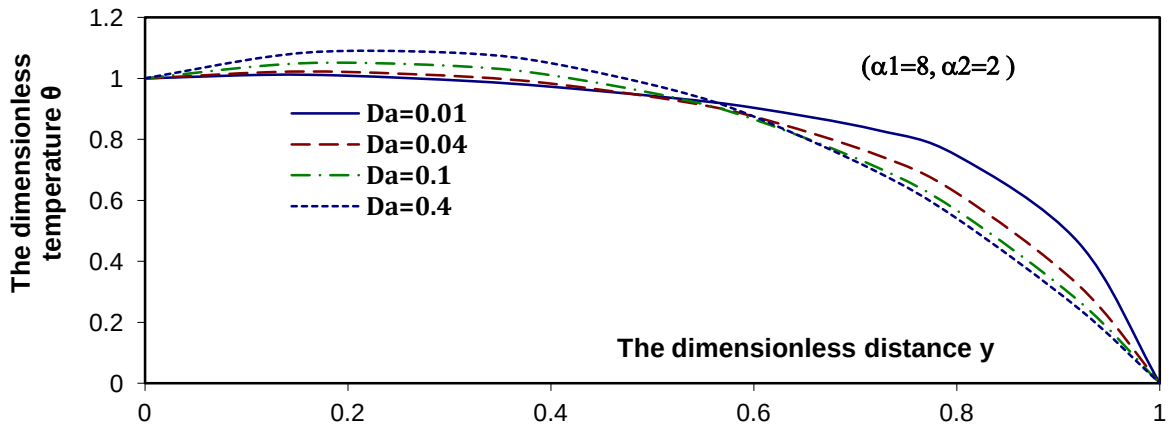

FIG. b-8: Profiles of the temperature θ(y) for a pure Couette flow with various values of Da for a system have the particulars M=0.1, Fs=0.5=1, Nt=0.3, Gr=0.1, Br=0.1, Pr=0.7, Nd=2, Nb=0.5, Nt=0.3, Le=2, Ld=0.1, Rc=0.5, m=2.

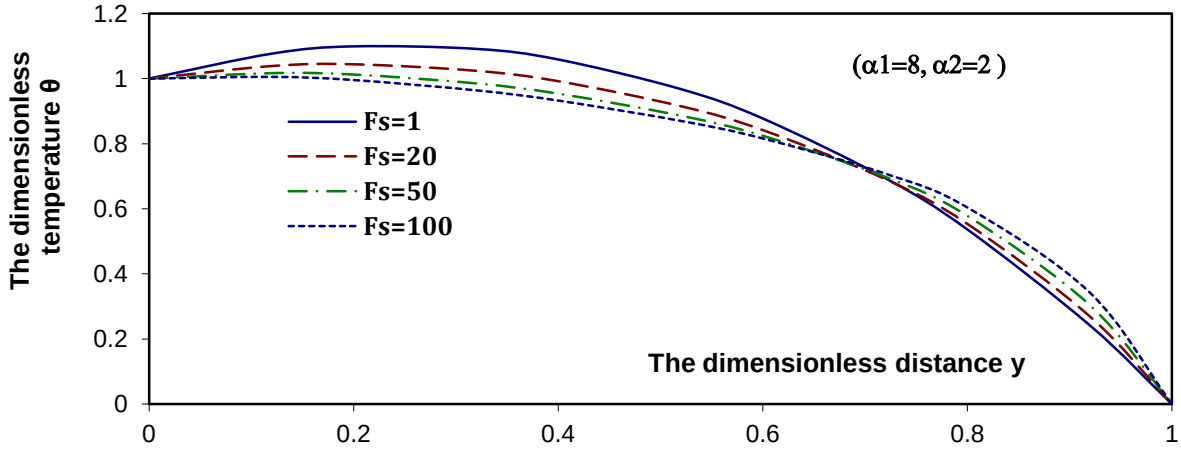

FIG. b-9: Profiles of the temperature θ(y) for a pure Couette flow with various values of Fs for a system have the particulars M=0.1, Da=1, Nt=0.3, Gr=0.1, Br=0.1, Pr=0.7, Nd=2, Nb=0.5, Nt=0.3, Le=2, Ld=0.1, Rc=0.5, m=2.

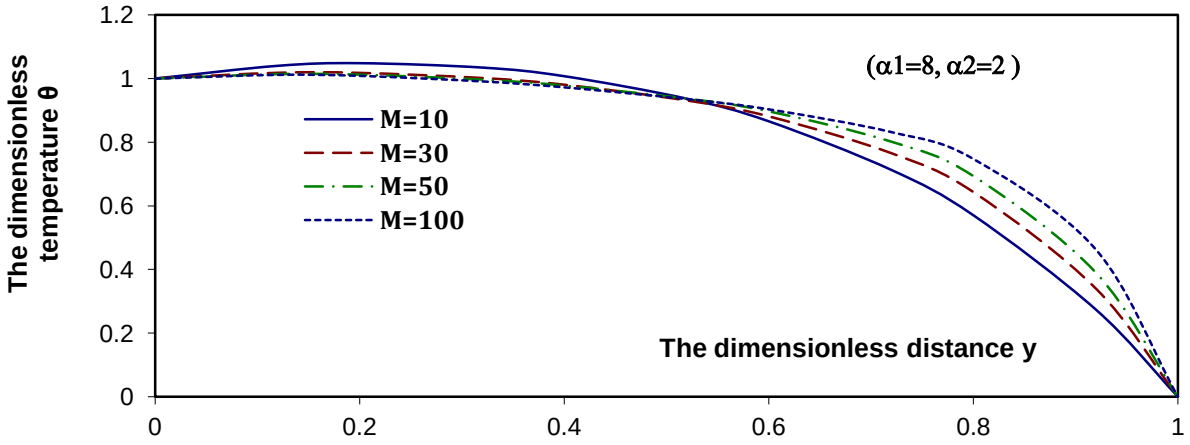

FIG. b-10: Profiles of the temperature θ(y) for a pure Couette flow with various values of M for a system have the particulars Da=1, Fs=0.5=1, Nt=0.3, Gr=0.1, Br=0.1, Pr=0.7, Nd=2, Nb=0.5, Nt=0.3, Le=2, Ld=0.1, Rc=0.5, m=2.

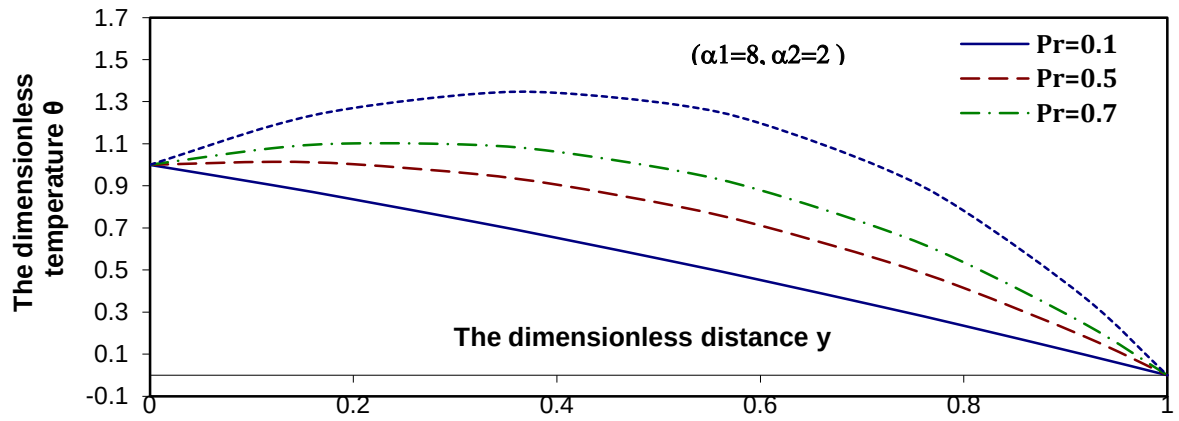

FIG. b-11: Profiles of the temperature θ(y) for a pure Couette flow with various values of Pr for a system have the particulars Da=1, Fs=0.5=1, Nt=0.3, Gr=0.1, Br=0.1, M=0.1, Nd=2, Nb=0.5, Nt=0.3, Le=2, Ld=0.1, Rc=0.5, m=2.

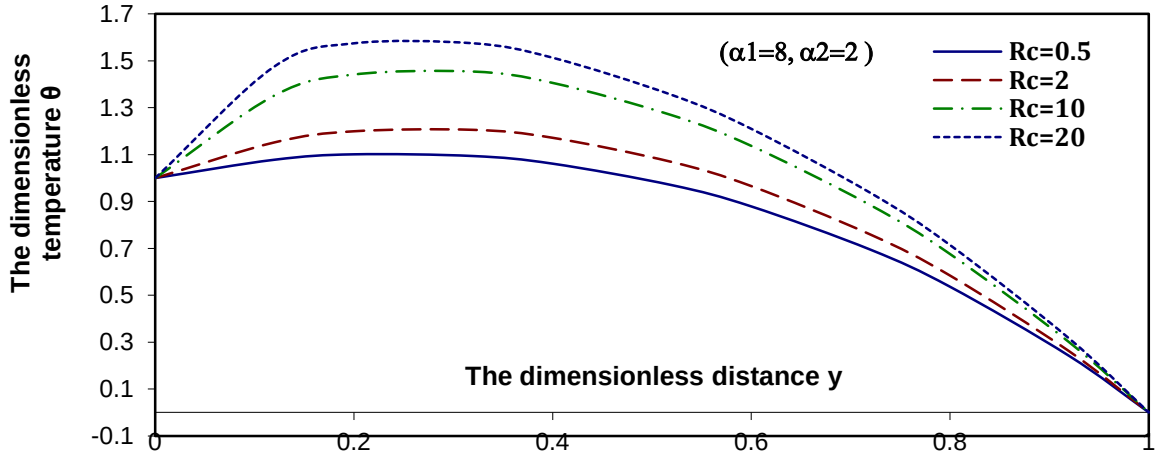

FIG. b-12: Profiles of the temperature θ(y) for a pure Couette flow with various values of Rc for a system have the particulars Pr=0.7, Da=1, Fs=0.5=1, Nt=0.3, Gr=0.1, Br=0.1, M=0.1, Nd=2, Nb=0.5, Nt=0.3, Le=2, Ld=0.1, m=2.

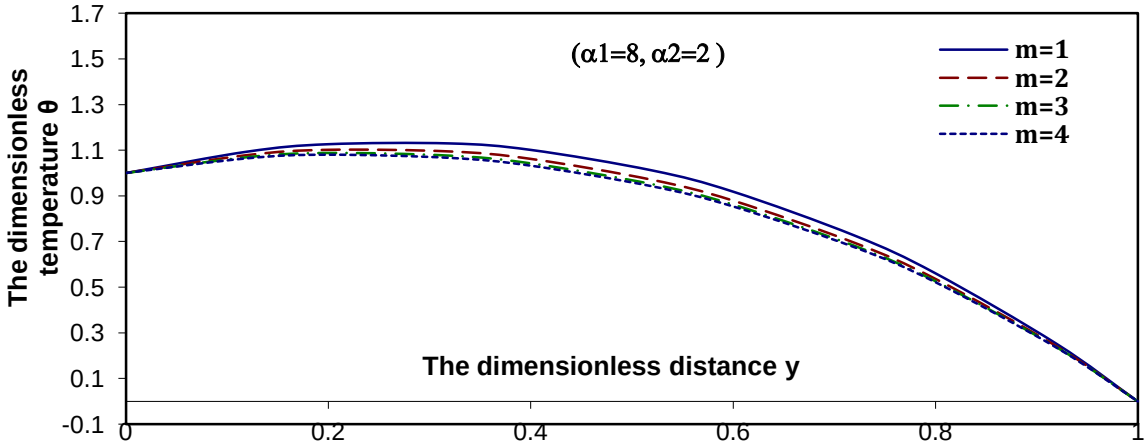

FIG. b-13: Profiles of the temperature θ(y) for a pure Couette flow with various values of m for a system have the particulars Pr=0.7, Da=1, Fs=0.5=1, Nt=0.3, Gr=0.1, Br=0.1, M=0.1, Nd=2, Nb=0.5, Nt=0.3, Le=2, Ld=0.1, Rc=0.5.

Figures (c-1 – c-13) illustrate the distributions of the concentration profile S at different values of some parameters of the problem. It is seen that, the concentration decreases by increasing each of local nanoparticle Grashof B_r, local temperature Grashof number G_r, Sort number L_d, Lewis number L_e, Brownian motion parameter N_b, Dufour number N_d, Thermophoresis parameter N_t, Prandtl number P_r, and Chemical reaction parameter R_c. And, as Darcy number D_a increases, the concentration decreases in the region $0 \leq y \leq 0.6$ and, it returns increase to $0.6 \leq y \leq 1$. But, as Forchheimer number F_s increases, the concentration increases in the region $0 \leq y \leq 0.7$ and, it returns decrease to $0.7 \leq y \leq 1$. The effect of magnetic field parameter M on the concentration disappears in the region $0 \leq y \leq 0.6$, the concentration returns decrease to $0.6 \leq y \leq 1$ at large values of M. Finally, the concentration increases by increasing Chemical reaction order m.

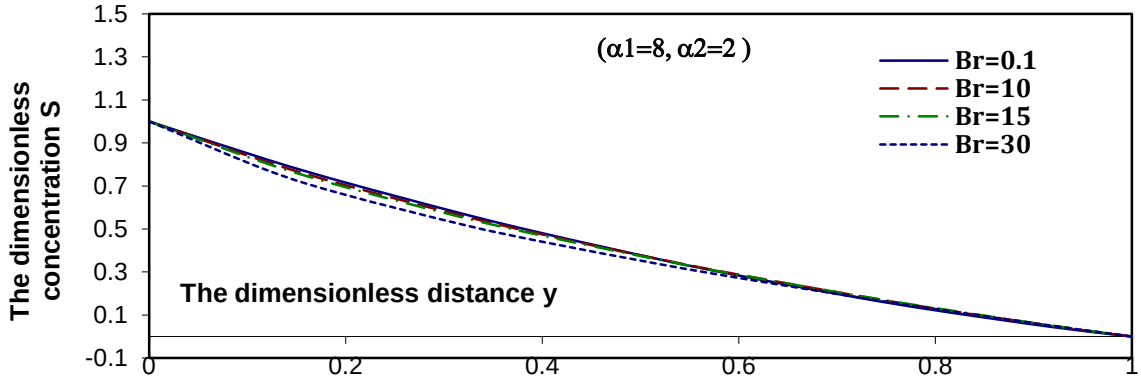

FIG. c-1: Profiles of the concentration S(y) for a pure Couette flow with various values of Br for a system have the particulars M=0.1, Da=1, Fs=0.5, Gr=0.1, Pr=0.7, Nd=2, Nb=0.5, Nt=0.3, Le=2, Ld=0.1, Rc=0.5, m=2.

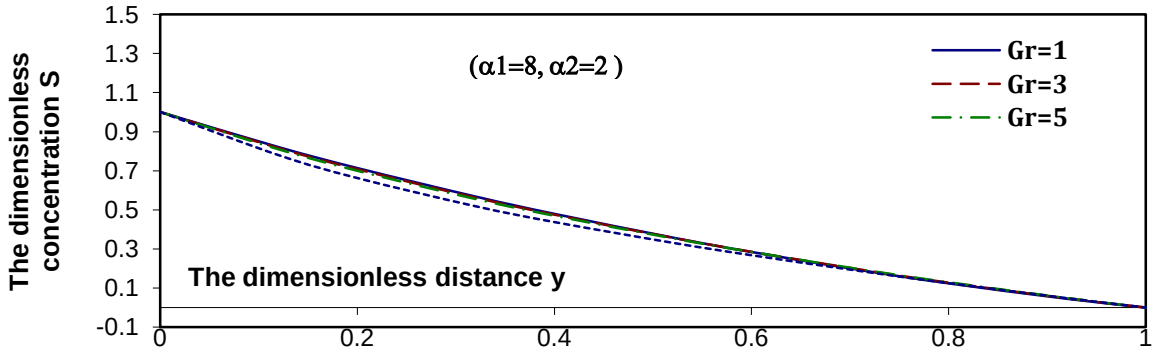

FIG. c-2: Profiles of the concentration S(y) for a pure Couette flow with various values of Gr for a system have the particulars M=0.1, Da=1, Fs=0.5, Br=0.1, Pr=0.7, Nd=2, Nb=0.5, Nt=0.3, Le=2, Ld=0.1, Rc=0.5, m=2.

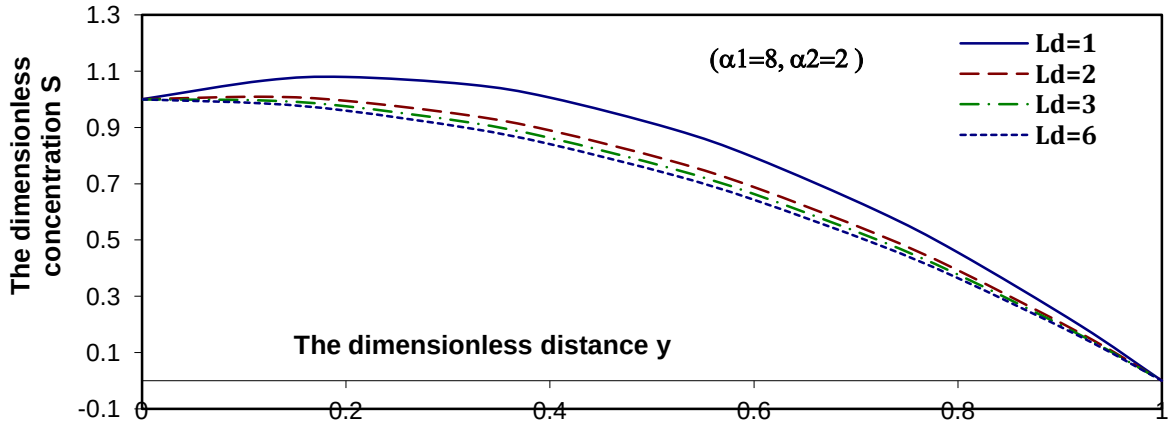

FIG. c-3: Profiles of the concentration S(y) for a pure Couette flow with various values of Ld for a system have the particulars M=0.1, Da=1, Fs=0.5, Gr=0.1, Br=0.1, Pr=0.7, Nd=2, Nb=0.5, Nt=0.3, Le=2, Rc=0.5, m=2.

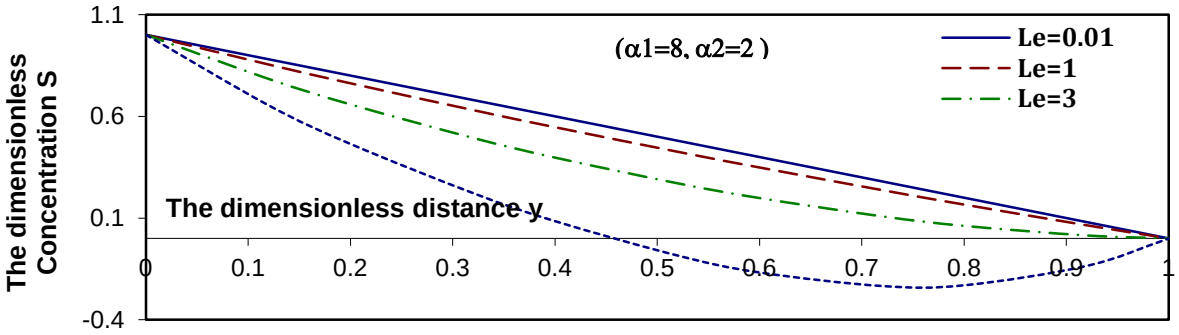

FIG. c-4: Profiles of the Concentration S(y) for a pure Couette flow with various values of Le for a system have the particulars M=0.1, Da=1, Fs=0.5, Gr=0.1, Br=0.1, Pr=0.7, Nd=2, Nb=0.5, Nt=0.3, Ld=0.1, Rc=0.5, m=2.

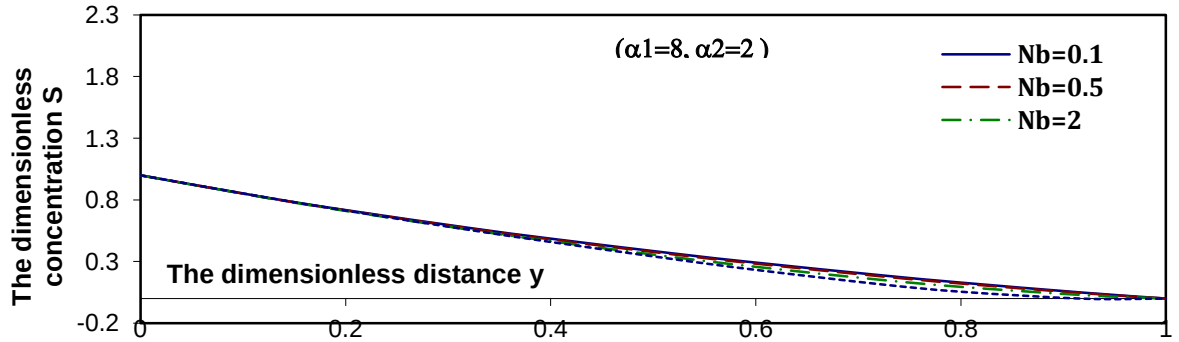

FIG. c-5: Profiles of the concentration S(y) for a pure Couette flow with various values of Nb for a system have the particulars M=0.1, Da=1, Fs=0.5, Gr=0.1, Br=0.1, Pr=0.7, Nd=2, Le=2, Nt=0.3, Ld=0.1, Rc=0.5, m=2.

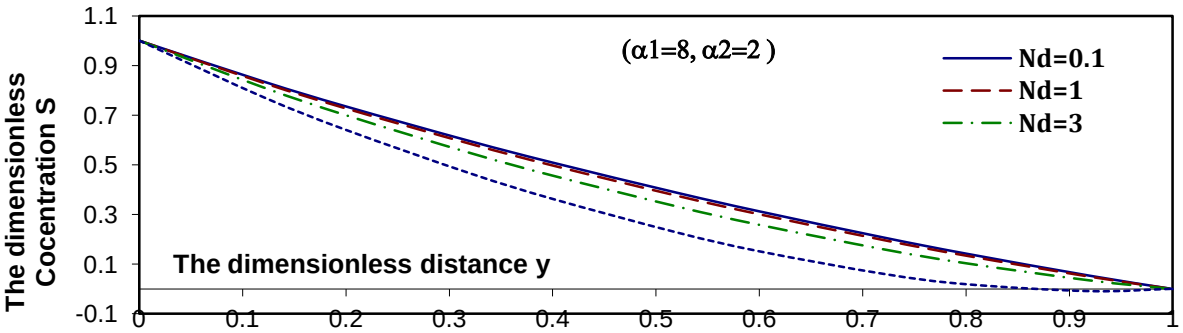

FIG. c-6: Profiles of the Concentration S(y) for a pure Couette flow with various values of Nd for a system have the particulars M=0.1, Da=1, Fs=0.5, Gr=0.1, Br=0.1, Pr=0.7, Nb=0.5, Le=2, Nt=0.3, Ld=0.1, Rc=0.5, m=2.

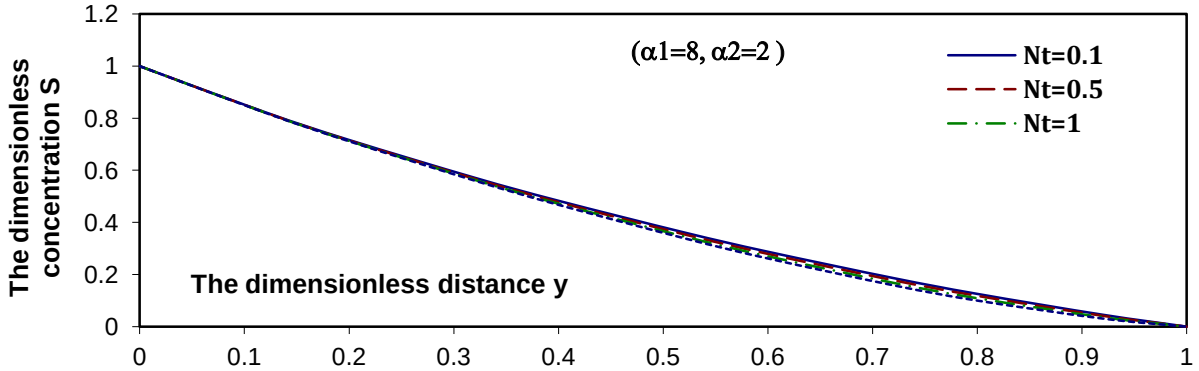

FIG. c-7: Profiles of the Concentration S(y) for a pure Couette flow with various values of Nt for a system have the particulars M=0.1, Da=1, Fs=0.5, Gr=0.1, Br=0.1, Pr=0.7, Nb=0.5, Le=2, Nd=2, Ld=0.1, Rc=0.5, m=2.

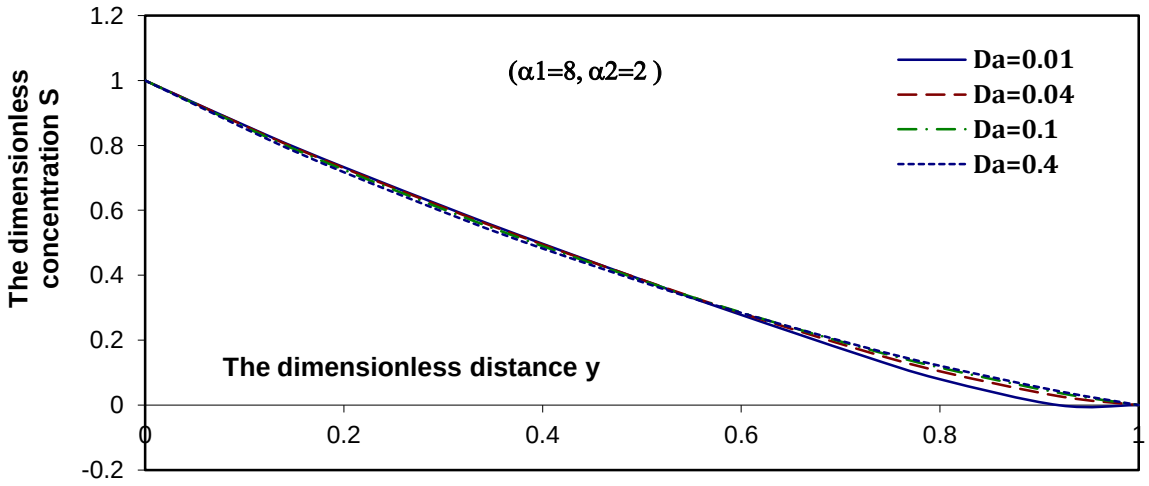

FIG. c-8: Profiles of the concentration S(y) for a pure Couette flow with various values of Da for a system have the particulars M=0.1, Fs=1, Nt=0.3, Gr=0.1, Br=0.1, Pr=0.7, Nd=2, Nb=0.5, Nt=0.3, Le=2, Ld=0.1, Rc=0.5, m=2.

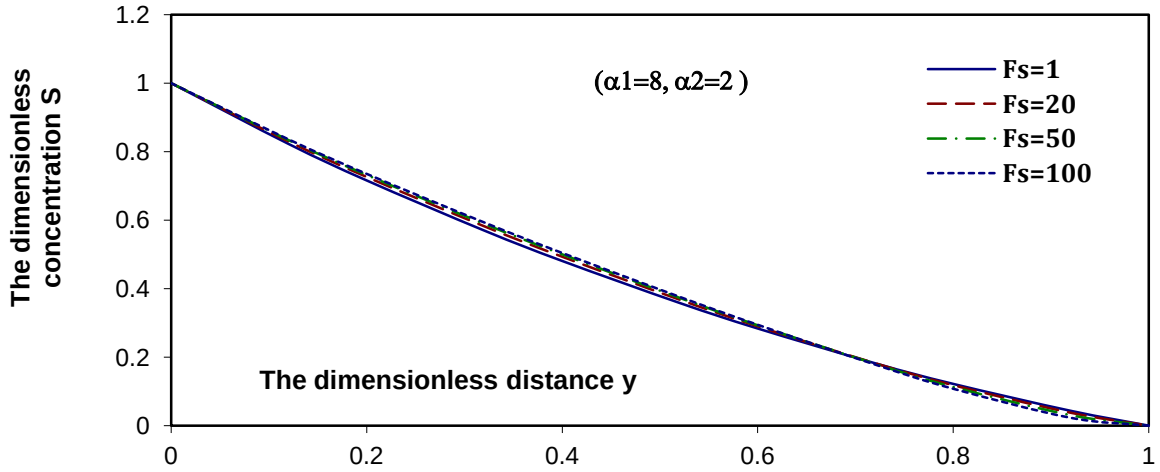

FIG. c-9: Profiles of the concentration S(y) for a pure Couette flow with various values of Fs for a system have the particulars M=0.1, Da=1, Nt=0.3, Gr=0.1, Br=0.1, Pr=0.7, Nd=2, Nb=0.5, Nt=0.3, Le=2, Ld=0.1, Rc=0.5, m=2.

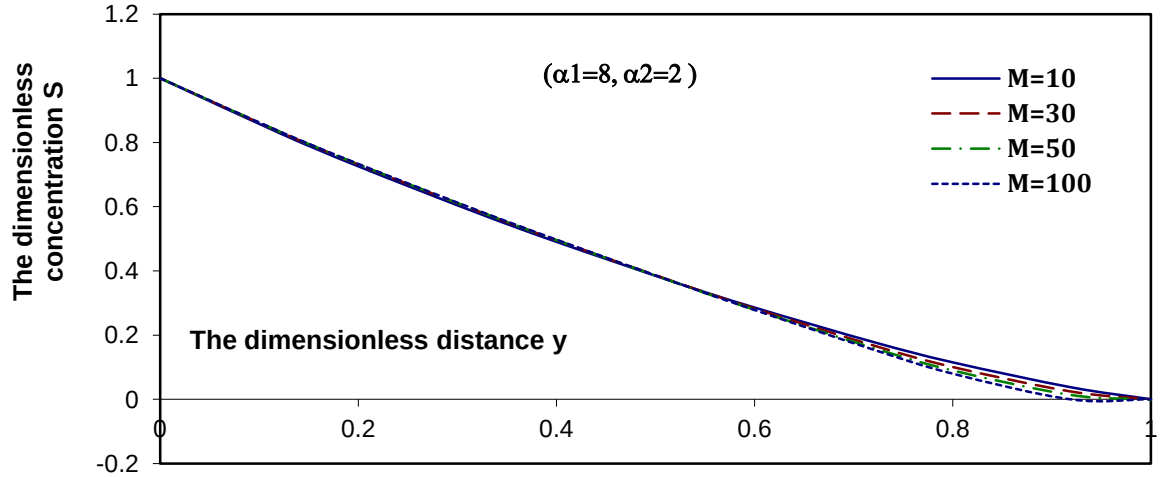

FIG. c-10: Profiles of the concentration S(y) for a pure Couette flow with various values of M for a system have the particulars Da=1, Fs=1, Nt=0.3, Gr=0.1, Br=0.1, Pr=0.7, Nd=2, Nb=0.5, Nt=0.3, Le=2, Ld=0.1, Rc=0.5, m=2.

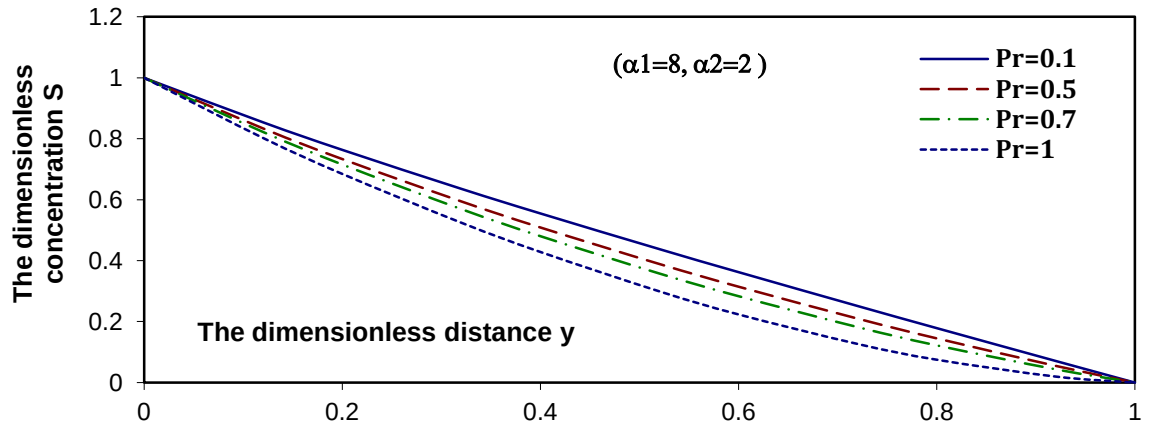

FIG. c-11: Profiles of the concentration S(y) for a pure Couette flow with various values of Pr for a system have the particulars Da=1, Fs=1, Nt=0.3, Gr=0.1, Br=0.1, M=0.1, Nd=2, Nb=0.5, Nt=0.3, Le=2, Ld=0.1, Rc=0.5, m=2.

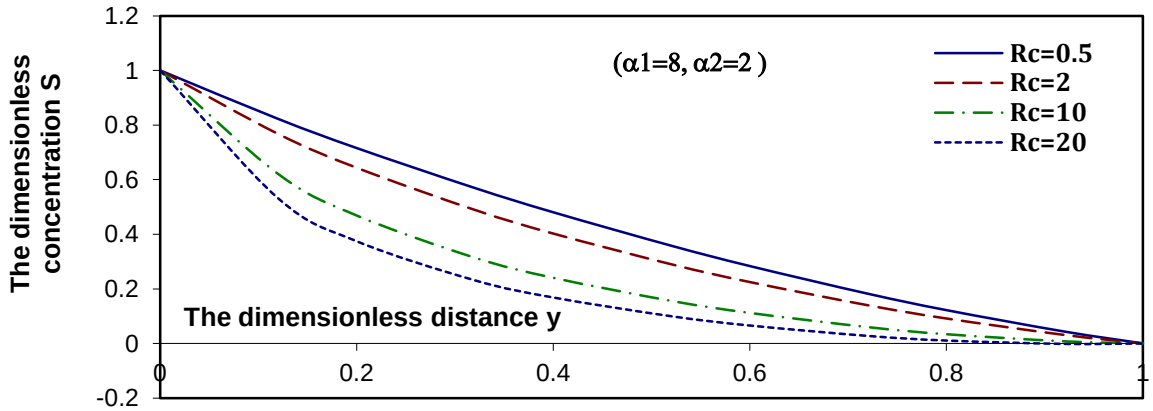

FIG. c-12: Profiles of the concentration S(y) for a pure Couette flow with various values of Rc for a system have the particulars Pr=0.7, Da=1, Fs=1, Nt=0.3, Gr=0.1, Br=0.1, M=0.1, Nd=2, Nb=0.5, Nt=0.3, Le=2, Ld=0.1, m=2.

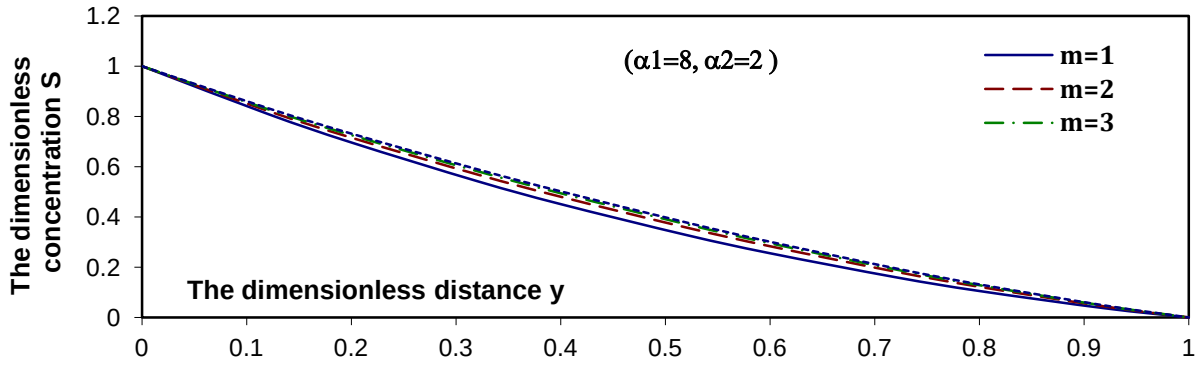

FIG. c-13: Profiles of the concentration S(y) for a pure Couette flow with various values of m for a system have the particulars Pr=0.7, Da=1, Fs=1, Nt=0.3, Gr=0.1, Br=0.1, M=0.1, Nd=2, Nb=0.5, Nt=0.3, Le=2, Ld=0.1, Rc=0.5.

Figures (d-1 – d-13) display the distributions of the nanoparticle profile ϕ at different values of some parameters of the problem. It is clear that, , the nanoparticle decreases by increasing each of local nanoparticle Grashof B_r, local temperature Grashof number G_r, Sort number L_d, Lewis number L_e, Dufour number N_d, Thermophoresis parameter N_t, Prandtl number P_r, and Chemical reaction parameter R_c. But, the nanoparticle increases by increasing Brownian motion parameter N_b. And, as Darcy number D_a increases, the nanoparticle decreases in the region $0 \leq y \leq 0.57$ and, it returns increase to $0.57 \leq y \leq 1$. But, as Forchheimer number F_s increases, the nanoparticle increases in the region $0 \leq y \leq 0.7$ and, it returns decrease to $0.7 \leq y \leq 1$. The effect of magnetic field parameter M on the nanoparticle disappears in the region $0 \leq y \leq 0.5$ and, the

nanoparticle returns decrease to $0.5 \leq y \leq 1$ at large values of M. Finally, the nanoparticle increases by increasing Chemical reaction order m.

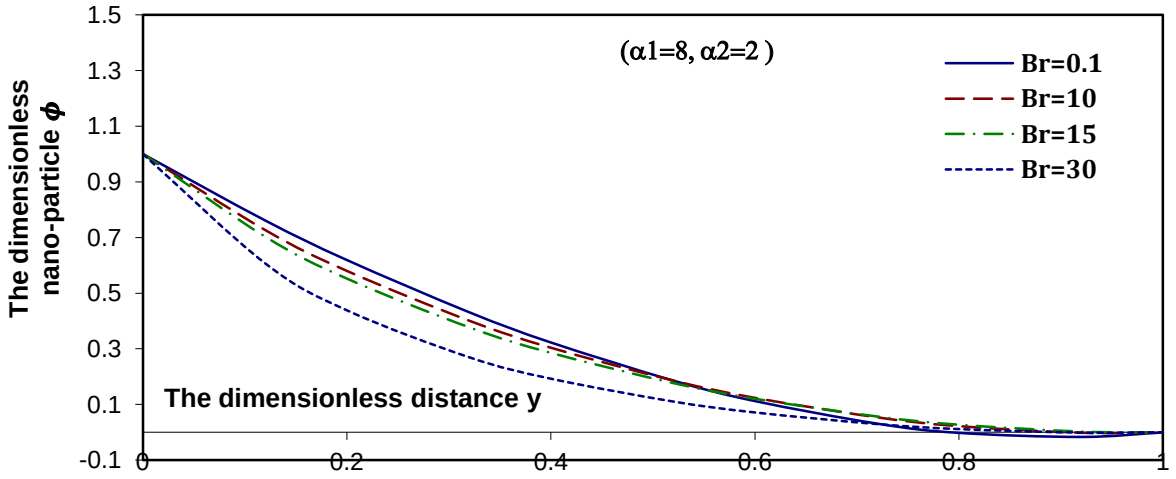

FIG. d-1: Profiles of the nano-particle ϕ(y) for a pure Couette flow with various values of Br for a system have the particulars M=0.1, Da=1, Fs=0.5, Gr=0.1, Pr=0.7, Nd=2, Nb=0.5, Nt=0.3, Le=2, Ld=0.1, Rc=0.5, m=2.

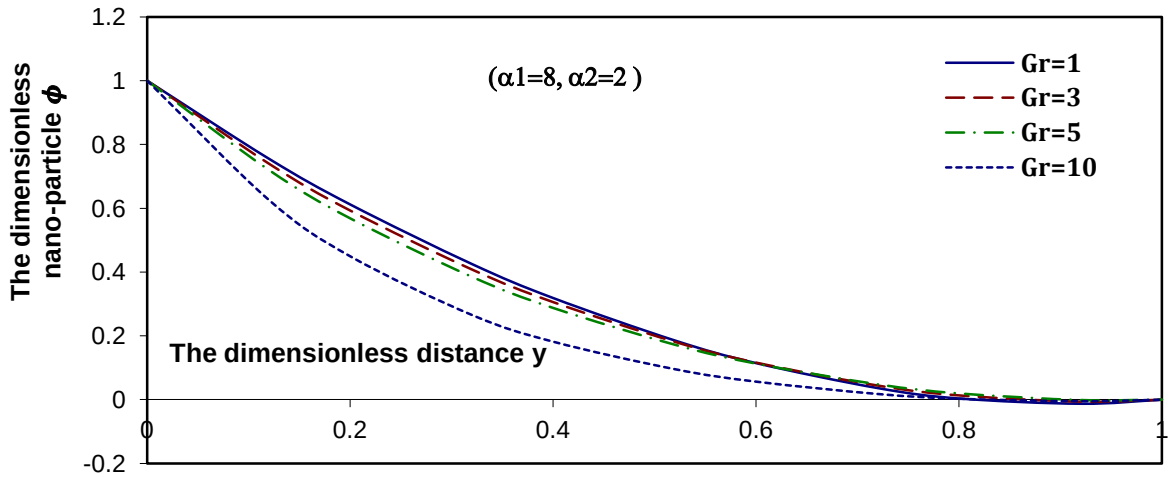

FIG. d-2: Profiles of the nano-particle ϕ(y) for a pure Couette flow with various valuesof Gr for a system have the particulars M=0.1, Da=1, Fs=0.5, Br=0.1, Pr=0.7, Nd=2, Nb=0.5, Nt=0.3, Le=2, Ld=0.1, Rc=0.5, m=2.

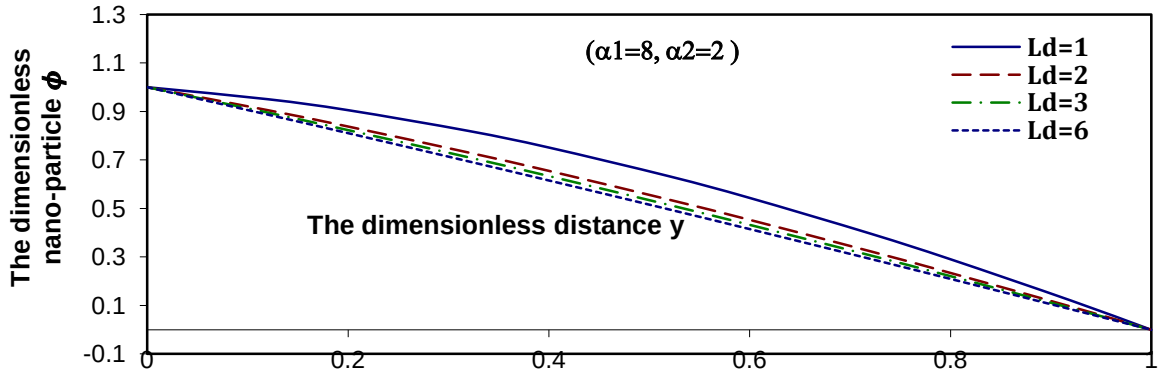

FIG. d-3: Profiles of the nano-particle ϕ(y) for a pure Couette flow with various values of Ld for a system have the particulars M=0.1, Da=1, Fs=0.5, Gr=0.1, Br=0.1, Pr=0.7, Nd=2, Nb=0.5, Nt=0.3, Le=2, Rc=0.5, m=2.

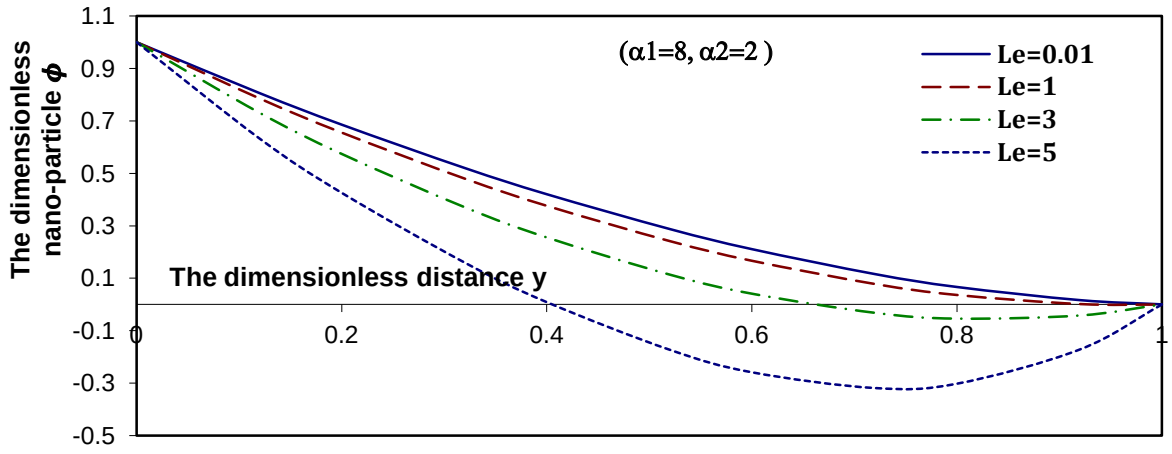

FIG. d-4: Profiles of the nano-particle ϕ(y) for a pure Couette flow with various values the Le for a system have the particulars M=0.1, Da=1, Fs=0.5, Gr=0.1, Br=0.1, Pr=0.7, Nd=2, Nb=0.5, Nt=0.3, Ld=0.1, Rc=0.5, m=2.

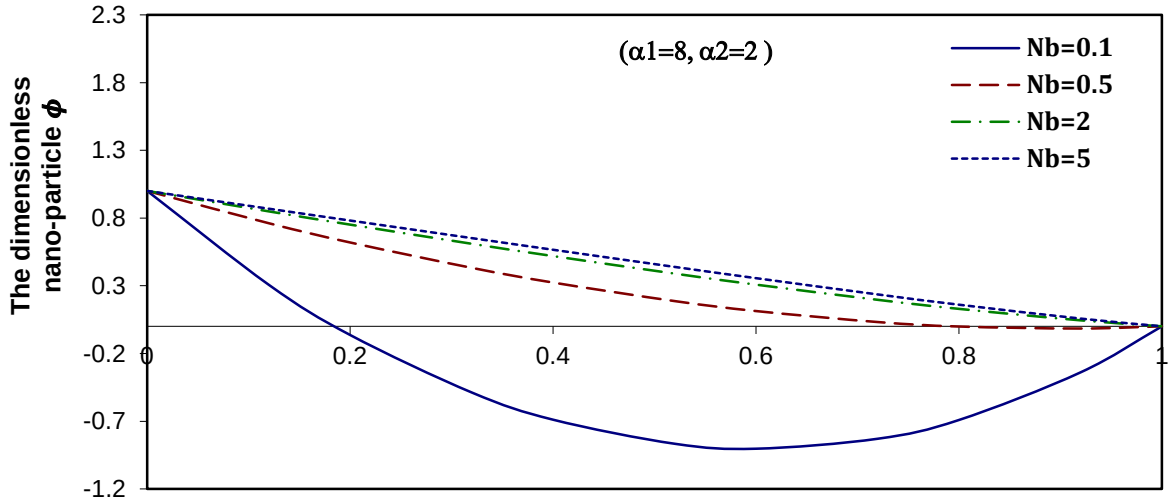

FIG. d-5: Profiles of nano-particle ϕ(y) for a pure Couette flow with various values of Nb for a system have the particulars M=0.1, Da=1, Fs=0.5, Gr=0.1, Br=0.1, Pr=0.7, Nd=2, Le=2, Nt=0.3, Ld=0.1, Rc=0.5, m=2.

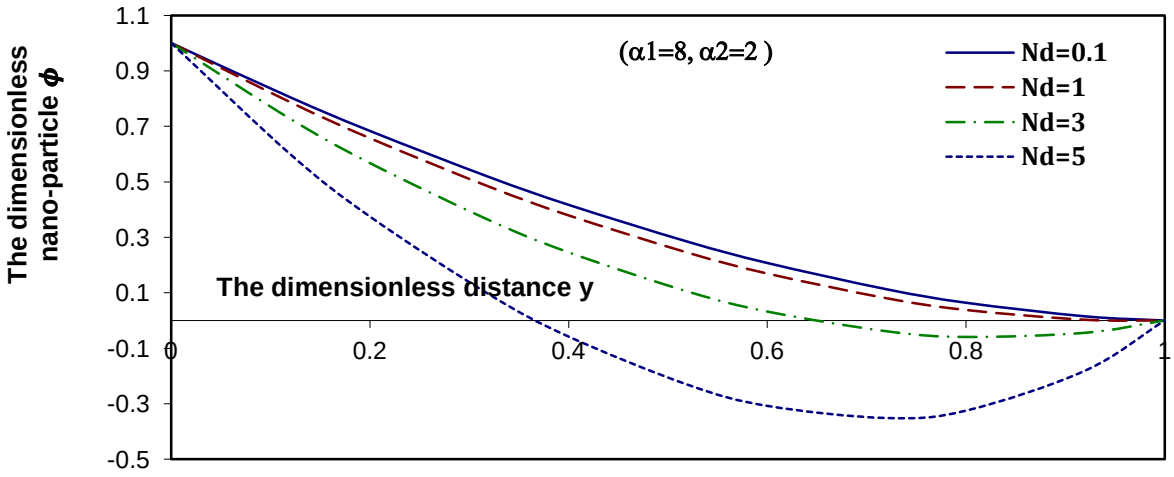

FIG. d-6: Profiles of the nano-particle ϕ(y) for a pure Couette flow with various values of Nd for a system have the particulars M=0.1, Da=1, Fs=0.5, Gr=0.1, Br=0.1, Pr=0.7, Nb=0.5, Le=2, Nt=0.3, Ld=0.1, Rc=0.5, m=2.

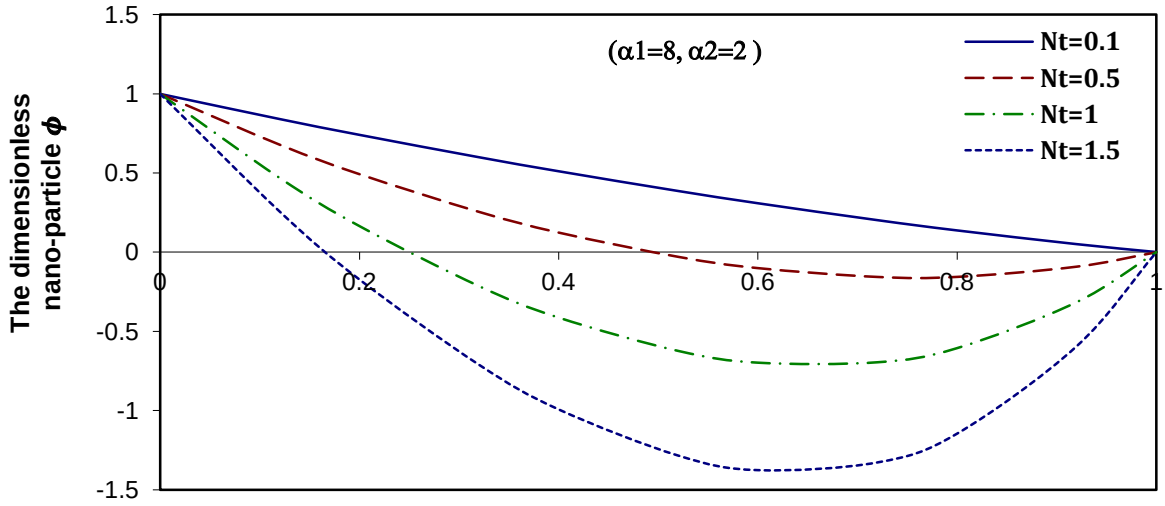

FIG. d-7: Profiles of the nano-particle ϕ(y) for a pure Couette flow with various values of Nt for a system have the particulars M=0.1, Da=1, Fs=0.5, Gr=0.1, Br=0.1, Pr=0.7, Nb=0.5, Le=2, Nd=2, Ld=0.1, Rc=0.5, m=2.

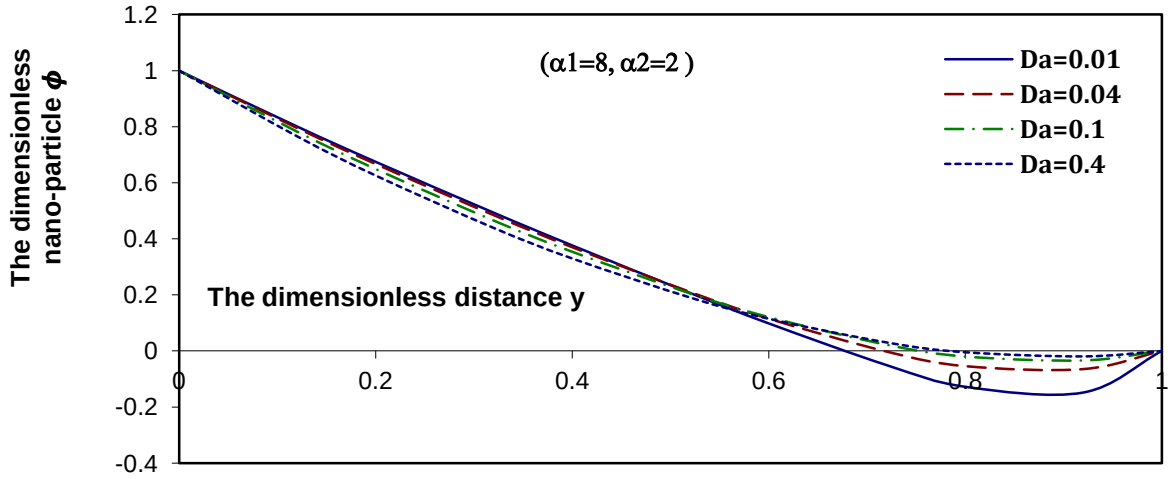

FIG. d-8: Profiles of the nano-particle ϕ(y) for a pure Couette flow with various values of Da for a system have the particulars M=0.1, Fs=0.5, Nt=0.3, Gr=0.1, Br=0.1, Pr=0.7, Nd=2, Nb=0.5, Nt=0.3, Le=2, Ld=0.1, Rc=0.5, m=2.

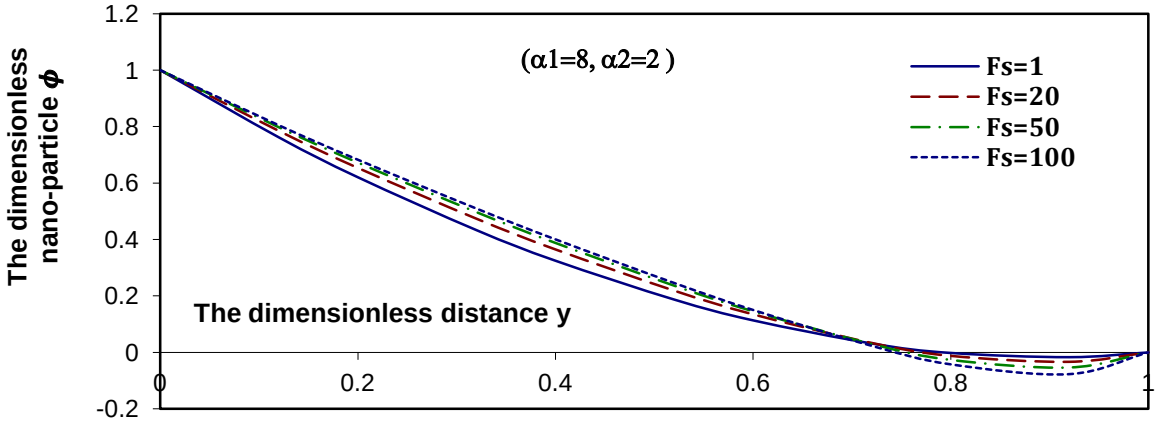

FIG. d-9: Profiles of the nano-particle ϕ(y) for a pure Couette flow with various values of Fs for a system have the particulars M=0.1, Da=1, Nt=0.3, Gr=0.1, Br=0.1, Pr=0.7, Nd=2, Nb=0.5, Nt=0.3, Le=2, Ld=0.1, Rc=0.5, m=2.

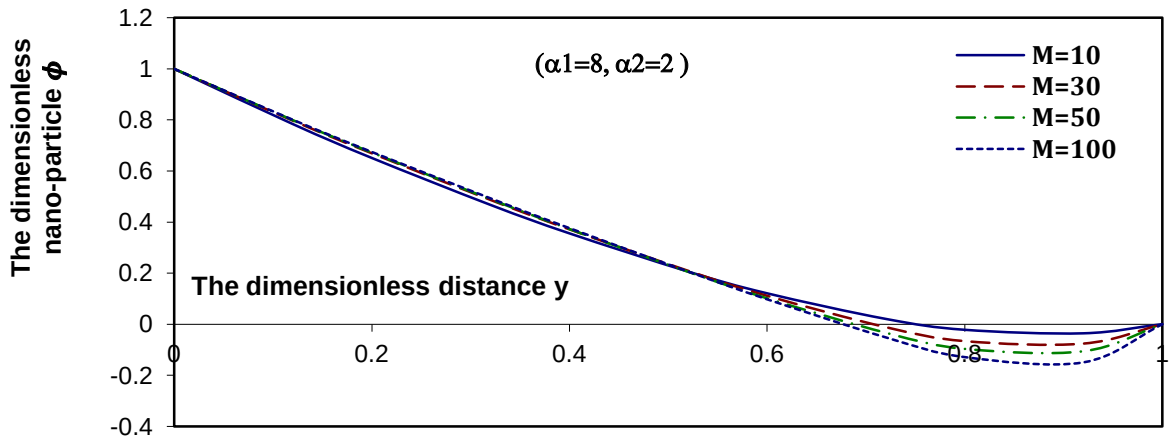

FIG. d-10: Profiles of the nano-particle ϕ(y) for a pure Couette flow with various values of M for a system have the particulars Da=1, Fs=0.5, Nt=0.3, Gr=0.1, Br=0.1, Pr=0.7, Nd=2, Nb=0.5, Nt=0.3, Le=2, Ld=0.1, Rc=0.5, m=2.

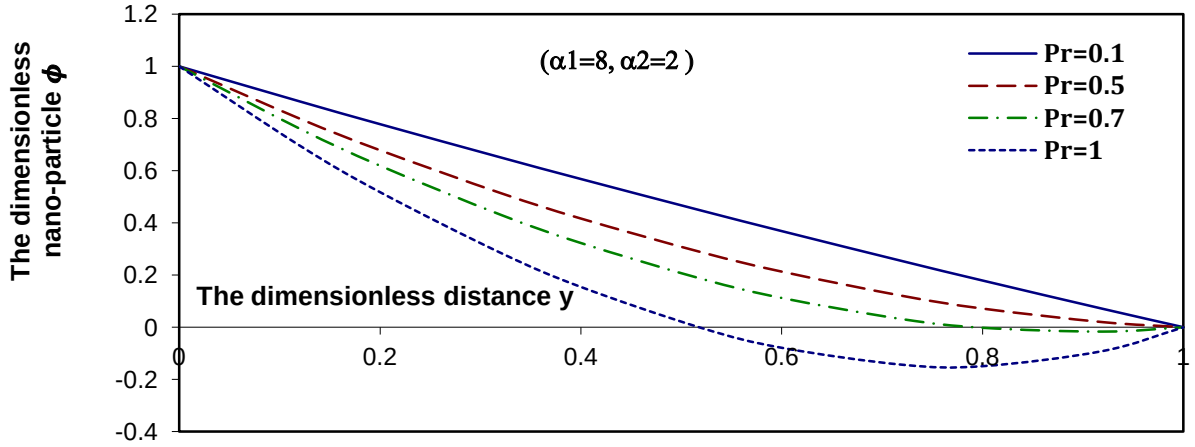

FIG. d-11: Profiles of the nano-particle ϕ(y) for a pure Couette flow with various values of Pr for a system have the particulars Da=1, Fs=0.5, Nt=0.3, Gr=0.1, Br=0.1, M=0.1, Nd=2, Nb=0.5, Nt=0.3, Le=2, Ld=0.1, Rc=0.5, m=2.

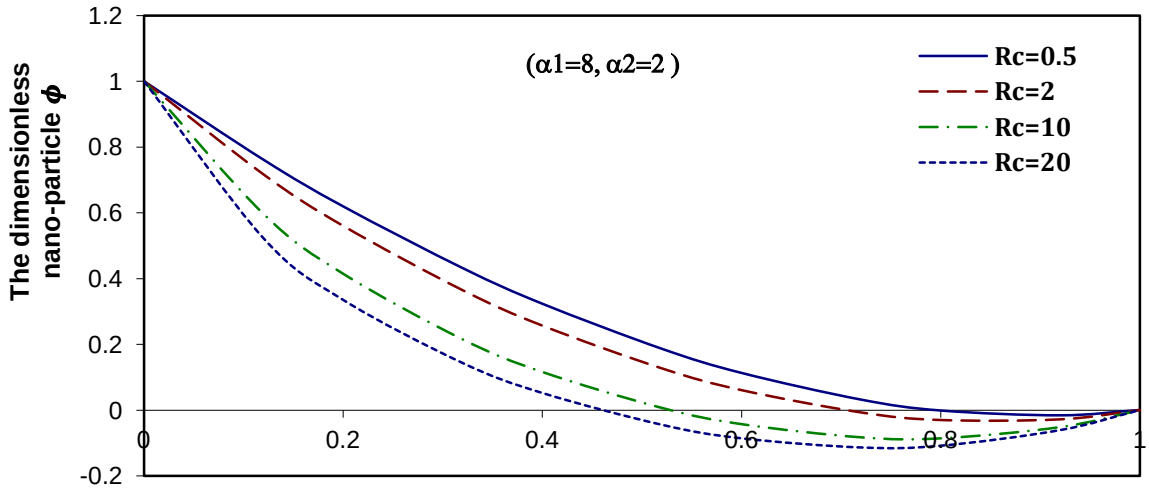

FIG. d-12: Profiles of the nano-particle ϕ(y) for a pure Couette flow with various values of Rc for a system have the particulars Pr=0.7, Da=1, Fs=0.5, Nt=0.3, Gr=0.1, Br=0.1, M=0.1, Nd=2, Nb=0.5, Nt=0.3, Le=2, Ld=0.1, m=2.

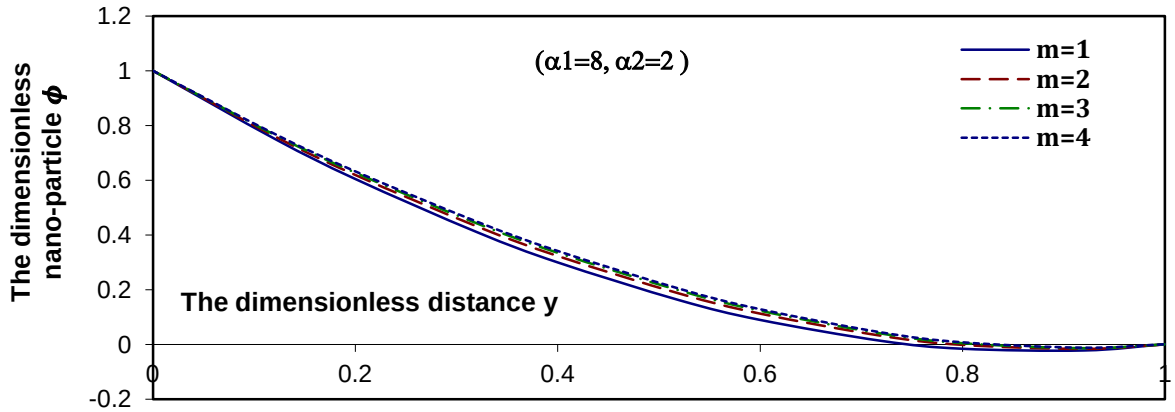

FIG. d-13: Profiles of the nano-particle ϕ(y) for a pure Couette flow with various values of m for a system have the particulars Pr=0.7, Da=1, Fs=0.5, Nt=0.3, Gr=0.1, Br=0.1, M=0.1, Nd=2, Nb=0.5, Nt=0.3, Le=2, Ld=0.1, Rc=0.5.

8.2 Poiseuille flow

Figures (e-1 – e-4) describe the effect of pressure gradient ($\frac{d\hat{P}}{dx}$) on the velocity, the temperature, the concentration, and the nanoparticle distributions. It is clear that, the velocity, the concentration, and the nanoparticle decrease with increasing ($\frac{d\hat{P}}{dx}$), while the temperature increases with increasing ($\frac{d\hat{P}}{dx}$).

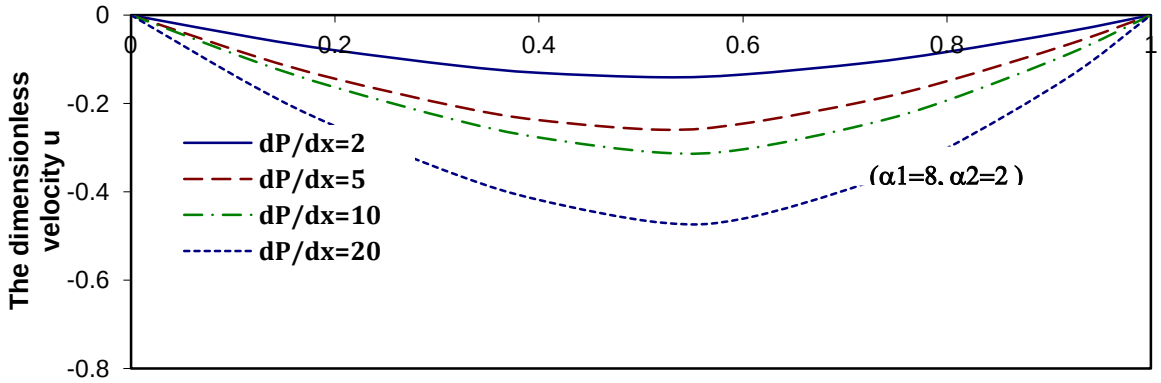

FIG. e-1: Profiles of the velocity u(y) for a pure Poiseuille flow with various values of dP/dx for a system have the particulars M=0.1, Da=1, Fs=0.5, Gr=0.1, Br=0.1, Pr=0.7, Nd=2, Nb=0.5, Nt=0.3, Le=2, Ld=0.1, Rc=0.5, m=2.

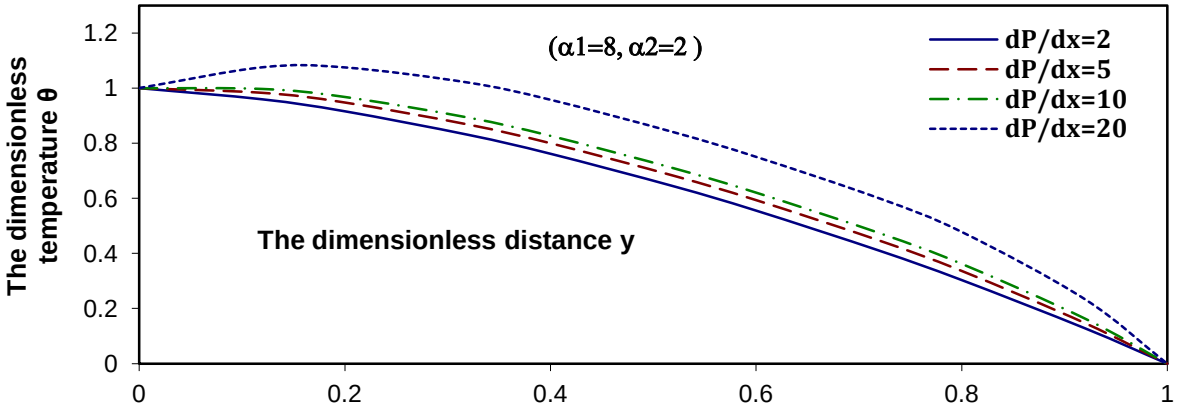

FIG. e-2: Profiles of the temperature θ(y) for a pure Poiseuille flow with various values of dP/dx for a system have the particulars M=0.1, Da=1, Fs=0.5, Gr=0.1, Br=0.1, Pr=0.7, Nd=2, Nb=0.5, Nt=0.3, Le=2, Ld=0.1, Rc=0.5, m=2.

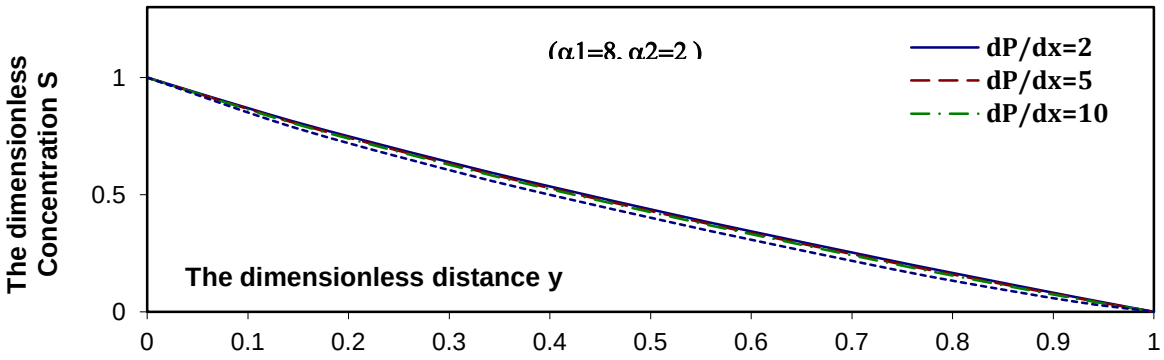

FIG. e-3: Profiles of the concentration S(y) for a pure Poiseuille flow with various values of dP/dx for a system have the particulars M=0.1, Da=1, Fs=0.5, Gr=0.1, Br=0.1, Pr=0.7, Nd=2, Nb=0.5, Nt=0.3, Le=2, Ld=0.1, Rc=0.5, m=2.

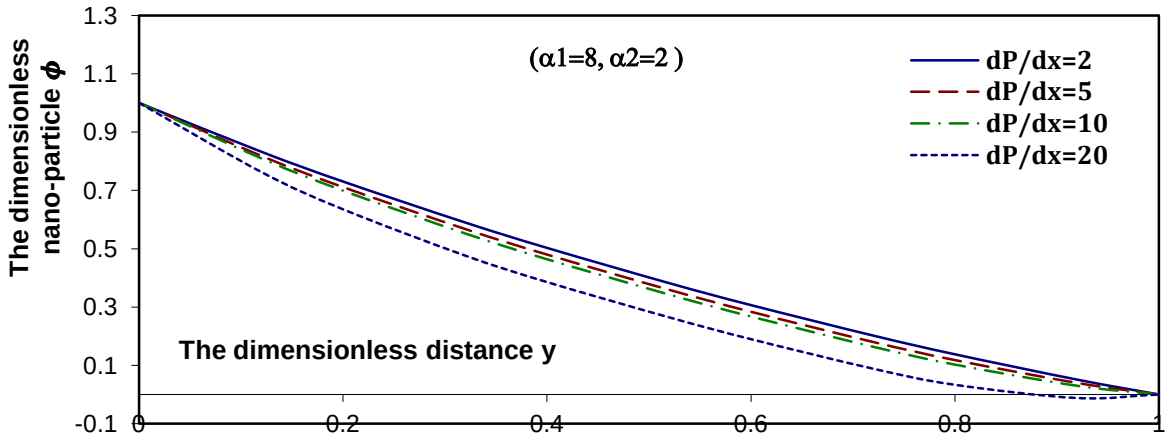

FIG. e-4: Profiles of the nano-particle ϕ(y) for a pure Poiseuille flow with various values of dP/dx for a system have the particulars M=0.1, Da=1, Fs=0.5, Gr=0.1, Br=0.1, Pr=0.7, Nd=2, Nb=0.5, Nt=0.3, Le=2, Ld=0.1, Rc=0.5, m=2.

8.3 Generalized Couette flow

If the flow of an Oldroyd 6-constant fluid between two parallel plates is driven by both the motion of the top plate and a constant pressure gradient in the direction parallel to the plates, a generalized couette flow is formed for ($\frac{d\hat{P}}{dx} \neq 0$, $U_0=1$). Numerical results for such a generalized couette flow are illustrated in figures (f-1 – f-4).

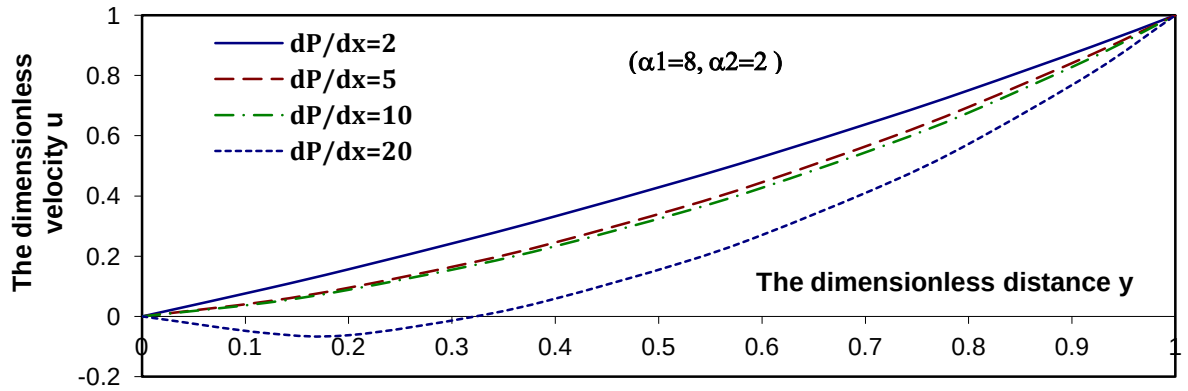

FIG. f-1: Profiles of the velocity u(y) for a generalized Couette flow with various values of dP/dx for a system have the particulars M=0.1, Da=1, Fs=0.5, Gr=0.1, Br=0.1, Pr=0.7, Nd=2, Nb=0.5, Nt=0.3, Le=2, Ld=0.1, Rc=0.5, m=2.

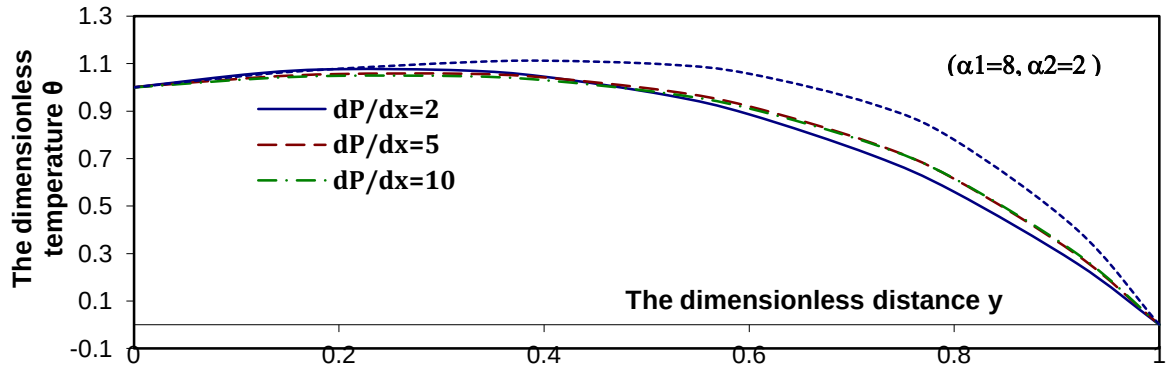

FIG. f-2: Profiles of the temperature θ(y) for a generalized Couette flow with various values of dP/dx for a system have the particulars M=0.1, Da=1, Fs=0.5, Gr=0.1, Br=0.1, Pr=0.7, Nd=2, Nb=0.5, Nt=0.3, Le=2, Ld=0.1, Rc=0.5, m=2.

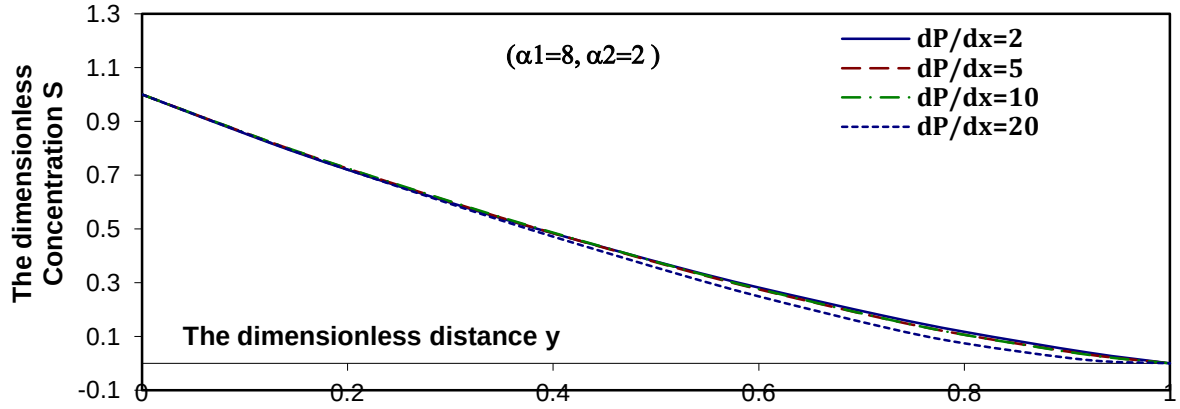

FIG. f-3: Profiles of the concentration S(y) for a generalized Couette flow with various values of dP/dx for a system have the particulars M=0.1, Da=1, Fs=0.5, Gr=0.1, Br=0.1, Pr=0.7, Nd=2, Nb=0.5, Nt=0.3, Le=2, Ld=0.1, Rc=0.5, m=2.

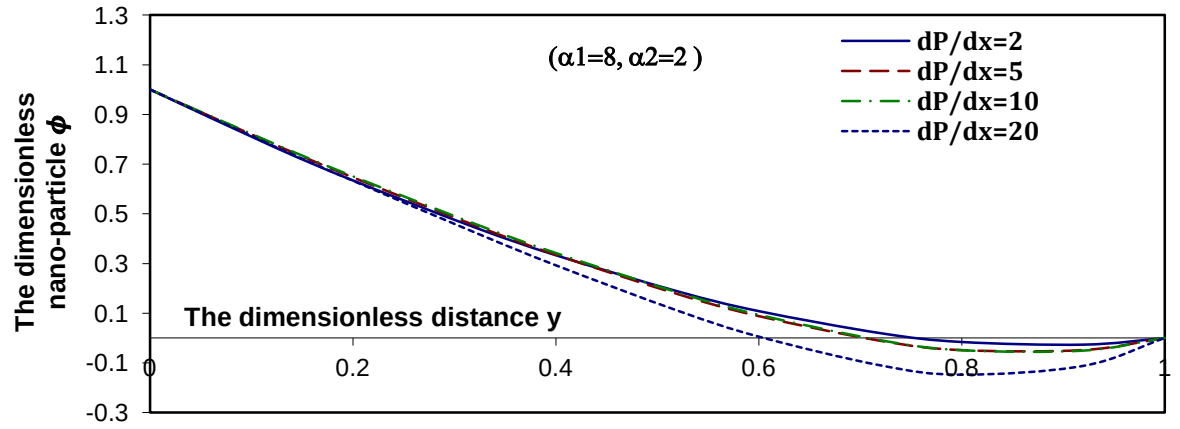

FIG. f-4: Profiles of the nano-particle ϕ(y) for a generalized Couette flow with various values of dP/dx for a system have the particulars M=0.1, Da=1, Fs=0.5, Gr=0.1, Br=0.1, Pr=0.7, Nd=2, Nb=0.5, Nt=0.3, Le=2, Ld=0.1, Rc=0.5, m=2.

Figures (f-1 – f-4) display the variation of the velocity, the temperature, the concentration, and the nanoparticle distributions for several values of the pressure gradient for ($\frac{d\hat{P}}{dx}$). It is observed that, the velocity, the concentration, and the nanoparticle decrease with increasing ($\frac{d\hat{P}}{dx}$), while the temperature increases with increasing ($\frac{d\hat{P}}{dx}$).

IX. CONCLUSION

In this work, we have studied magnetohydrodynamic flows of an Oldroyd 6-constant nano-fluid through a non-Darcy porous medium with heat and mass transfer. The governing boundary value problem was solved numerically by an Explicit Finite-Difference method. We concentrated our work on obtaining the velocity, the temperature, the concentration, and the nanoparticle distributions which are illustrated graphically at different values of the parameters of the problem in three cases, pure Couette flow, pure Poiseuille flow, and generalized Couette flow. Global error estimation is also obtained using Zadunaisky technique. We used 26 points to find the interpolating polynomial of degree 25 in interval [0,1] and the results are shown in table (1). We notice that, the error in table (1) is good enough to justify the use of resulting numerical values. The main findings from the current study can be summarized as follows:

1- By increasing B_r, G_r, and D_a, the velocity u increases, whereas it decreases by increasing each of F_s, and M in the case of Couette flow at $(\alpha_1 = 8, \alpha_2 = 2)$. And, the other parameters doesn't have any effect on the velocity.

2- By increasing B_r, G_r, and D_a, the temperature θ increases at the first part $(0 \le y \le 0.58)$ while, it decreases at the second part $(0.58 \le y \le 1)$. And, by increasing L_d, L_e, N_b, N_d, N_t, P_r, and R_c the temperature increases, while by increasing m, the temperature decreases. By increasing F_s, the temperature decreases at the first part $(0 \le y \le 0.7)$ while, it increases at the second part $(0.7 \le y \le 1)$. Also, By increasing M, the temperature decreases at the first part $(0 \le y \le 0.5)$ while, it increases at the second part $(0.5 \le y \le 1)$. All these results are given in the case of Couette flow at $(\alpha_1 = 8, \alpha_2 = 2)$.

3- By increasing Br, Gr, Ld, Le, Nb, Nd, Nt, Pr, and Rc, the concentration S decreases, while by increasing m, the concentration increases. By increasing Da, the concentration decreases at the first part $(0 \le y \le 0.6)$ while, it increases for $(0.6 \le y \le 1)$. But, by increasing Fs, the concentration increases in the first part $(0 \le y \le 0.7)$ while, it decreases at the second part $(0.7 \le y \le 1)$. And, by increasing M, the concentration doesn't have any change at the first part $(0 \le y \le 0.6)$ while, it decreases at the second part $(0.6 \le y \le 1)$ at large values of M. All these results are given in the case of Couette flow at $(\alpha_1 = 8, \alpha_2 = 2)$.

4- By increasing B_r, G_r, L_d, L_e, N_d, N_t, P_r, and R_c, the nanoparticle $\boldsymbol{\phi}$ decreases, while by increasing N_b, and m, the nanoparticle increases. By increasing Da, the nanoparticle decreases at the first part $(0 \le y \le 0.57)$ while, it increases for $(0.57 \le y \le 1)$. But, by increasing Fs, the nanoparticle increases in the first part $(0 \le y \le 0.7)$ while, it decreases at the second part $(0.7 \le y \le 1)$. And, by increasing M, the nanoparticle doesn't have any change at the first part $(0 \le y \le 0.5)$ while, it decreases at the second part $(0.5 \le y \le 1)$ at large values of M. All these results are given in the case of Couette flow at $(\alpha_1 = 8, \alpha_2 = 2)$.

5- By increasing $\frac{d\hat{P}}{dx}$, the velocity, the concentration, and the nanoparticle decrease, while the temperature increases in the case of Poiseuille flow at $(\alpha_1 = 8, \alpha_2 = 2)$.

6- By increasing $\frac{d\hat{P}}{dx}$, the velocity, the concentration, and the nanoparticle decrease, while the temperature increases in the case of generalized Couette flow at $(\alpha_1 = 8, \alpha_2 = 2)$.

REFERENCES

[1] A. Mushtaq, M. Mustafa, T. Hayat, and A. Alsaedi, "Nonlinear radiative heat transfer in the flow of nanofluid due to solar energy: A numerical study", J. Taiwan Inst. Chem. Eng. , Vol. 45, Pp. 1176-1183, 2014.

[2] C. Guillope, and JC. Saut, "Global existence and one-dimensional non-linear stability of shearing motions of viscoelastic fluids of Oldroyd type, RAIRO Model", Math Anal Numer, Vol. 24, Pp. 369-401, 1990.

[3] F. Trieb, and J. Nitsch, "Recommendations for the market introduction of solar thermal power stations, Renew Energy", Vol. 14, Pp. 17-22, 1998.

[4] G. Pontrelli, "Longitudinal and torsional oscillations of a rod in an Oldroyd-B fluid with suction or injection", Acta Mech. , Vol. 123, Pp. 57-68, 1997.

[5] G. Pontrelli, and K. Bhatnagar, "Flow of a viscoelastic fluid between two rotating circular cylinders subject to suction or injection", Int. J. Numer. Maths. Fluids, Vol. 24, Pp. 337-349, 1997.

[6] H. C. Saxena, "Examples in finite differences and numerical analysis:, S. Chand & Company Ltd, Ram Nagar, New delhi, 1991.

[7] H. Masuda, A. Ebata, K. Teramae, and N. Hishinuma, (1993), Alteration of thermal conductivity and viscosity of liquid by dispersing ultra-fine particles, Netsu Bussei, Vol. 7: 227-233.

[8] J. Bear, (1972), Dynamics of fluids in Porous media, Elsevier, New York.

[9] J. Bungiorno, (2006), Convective transport in nanofluids, ASME J. Heat Transfer, Vol. 128: 240-250.

[10] J. N. Kapur, (1973), An Introduction of fluid dynamics, Indian Institute of Technology.

[11] JG. Oldroyd, (1951), The motion of an elastic-viscous liquid contained between coaxial cylinders, Quart. J. Mech. Appl. Math., Vol. 4: 271-282.

[12] K. Vajravelu, K. V. Prasad, and S. Abbasbandy, (2013), Convection transport of nanoparticle in multi-layer fluid flow, Appl. Math. Mech. Eng. Ed., Vol. 34(2): 177-188.

[13] KR. Rajagopal, (1996), On an exact solution for the flow of Oldroyd-B fluid, Bull Tech. Univ. Istanbul, Vol. 49: 617-623.

[14] M. A. Rana, A. M. Siddiqui, and R. Qamar, (2009), Hall effects on hydromagnetic flow of an Oldroyd 6-constant fluid between concentric cylinders, Chaos, Solitons and Fractals, Vol. 39: 204-213.

[15] Md. Shakhaoath Khan, Ifsana Karim, and Md. Sirajul Islam, (2014), Possessions of chemical reaction on MHD Heat and Mass Transfer Nanofluid Flow on a Continuously Moving Surface, Amer. Chem. Sci. J., Vol. 4(3): 401-415.

[16] Mohamed Y. Abou-zeid, Abeer A. Shaaban and Muneer Y. Alnour, (2015), Numerical treatment and global error estimation of natural convective effects on gliding motion of bacteria on a power-law nanoslime through a non-Darcy porous medium, J. Porous Media, Vol. 18(11): 1091-1106.

[17] Nabil T.M. El-dabe, Abeer A. Shaaban, Mohamed Y. Abou-zeid, and Hemat A. Ali, (2015), MHD non-Newtonian nanofluid flow over a stretching sheet with thermal diffusion and diffusion thermo effects through a non-Darcy porous medium with radiation and chemical reaction, J. Compu. Theor. Nanoscience, Vol. 12(11):1-9.

[18] P. A. Davidson, (2001), An Introduction to magnetohydrodynamics, Cambridge University Press.

[19] P. E. Zadunaisky, (1976), On the Estimation of Errors Propagated in the Numerical Integration of Ordinary Differential Equations, Numer. Math., Vol. 27: 21-29.

[20] R. M. Saldanha da Gama, (2005), A new mathematical modelling for describing the unsaturated flow of an incompressible liquid through a rigid porous medium, Int. J. Non-Linear Mec., Vol. 40: 49-68.

[21] S. Baris, (2001), Flow of an Oldroyd 6-constant fluid between intersecting planes, one of which is moving, Acta Mech. Vol. 147: 128-135.

[22] S. Choi, (2009), Enhancing thermal conductivity of fluids with nanoparticles, In: Siginer DA, Wang HP, editors. Dev. Appl. Non-Newtonian flows, Vol. 231: 99-105.

[23] T. Hayat, M. Khan, and M. Ayub, (2004), Couette and Poiseuille flows of an Oldroyd 6-constant fluid with magnetic field, J. Math. Anal. Appl. , Vol. 298: 225-244.

[24] T. Hayat, M. Khan, and M. Ayub, (2007), the effect of the slip condition on flows of an Oldroyd 6-constant fluid, J. Comp. Appl. Math. , Vol, 202: 402-413.

[25] T. Hayat, M. Khan, and S. Asghar, (2004), Magnetohydrodynamic flow of an Oldroyd 6-constant fluid, Appl. Math. Comp. , Vol. 155: 417-425.

[26] T. Hayat, R. Ellahi, and F. M. Mahomed, (2009), Exact solution of a thin film flow of an Oldroyd 6-constant fluid over a moving belt, Comm. Nonlinear Sci. Num. Sim. , Vol. 14: 133-139.

[27] U. Farooq, T. Hayat, A. Alsaedi, and Shijun Liao, (2014), Heat and mass transfer of two-layer flows of third-grade nano-fluids in a vertical channel, Appl. Math. Comp., vol. 242: 528-540.

[28] Y. Wang, and T. Hayat, (2008), Fluctuating flow of a Maxwell fluid past a porous plate with variable suction, Nonlinear Analysis: R. W. Appl., Vol. 9: 1269-1282.

[29] Y. Wang, T. Hayat, and K. Hutter, (2004), Magnetohydrodynamic flow of an Oldroyd 8-constant fluid in a porous medium, Can. J. Phys., Vol. 82: 965-980.

[30] Y. Wang, T. Hayat, and K. Hutter, (2005), On non-linear magnetohydrodynamic problems of an Oldroyd 6-constant fluid, Int. J. Non-Linear Mech. Vol. 40: 49-58.

Analytical Study on RC Framed Structures on effect of Performance of Different types of Piles in Seismic Region

Sindhu P[1], Manohar K[2]

[1]M TECH, Department of Civil Engineering, Sahyadhri college of Engineering and Management, Mangalore
[2]Asst. Professor, Department of Civil Engineering, Sahyadhri college of Engineering and Management, Mangalore

Abstract-*This thesis includes Analytical Study on RC Framed Structures on effect of Performance of Pile Foundation in Seismic Region. For our design section of a RC framed residential high rise building we are comparing mass irregularities and vertical irregularities with respect to Time period, Frequency, Displacement, Storey Drift Ratio and Storey Shear for Friction pile and End Bearing Pile.*

Keywords- End Bearing Pile, Friction Pile, Mass Irregularity, Pile Foundation, Vertical irregularity.

I. INTRODUCTION

Piles are long and thin individuals which exchange the heap to further soil or shake of high bearing limit keeping away from shallow soil of low bearing limits the principle sorts of materials utilized for heaps are Wood, steel and cement. Heap establishments are the structure used to convey and exchange the heap of the structure to the bearing ground situated at some profundity UG surface. The principle segments of the establishment are the heap top and the heaps. Heaps worked from these materials are driven, penetrated or jacked into the ground and associated with heap tops. In view of sort of soil, heap material and load transmitting trademark heaps are arranged appropriately.

II. CLASSIFICATION OF PILES

Classification of pile with respect to load transmission and functional behaviour

- End bearing piles /point bearing piles
- Friction piles / cohesion piles
- Combination of friction and cohesion piles

2.1 End Bearing Piles

These stacks trade their load on to a firm stratum arranged at a broad significance underneath the base of the structure and they surmise the larger part of their passing on farthest point from the invasion resistance of the soil at the toe of the store (see figure 1-1). The load goes about as a standard fragment and should be arranged hence. In fact, even in frail soil a stack won't slump by catching and this effect require simply be considered if some segment of the store is unsupported. Load is imparted to the soil through disintegration or union. Regardless, occasionally, the soil including the store may hold fast to the surface of the stack and causes "Negative Skin Friction" on the pile. This, at times has amazing effect on the farthest point of the pile. Negative skin contact is delivered by the leakage of the ground water and mix of the soil. The building up significance of the store is impacted by the delayed consequences of the site investigate and soil test.

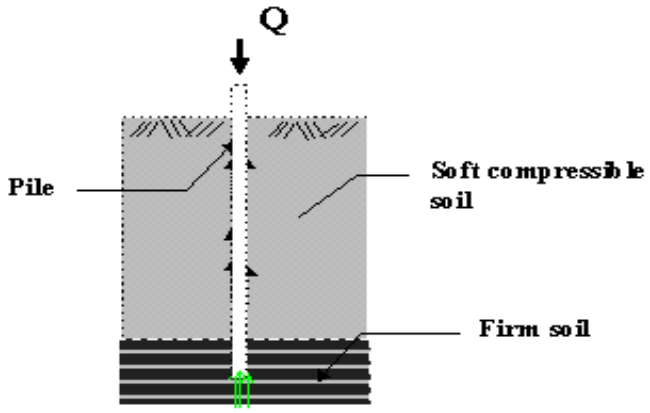

2.2 Friction or Cohesion Piles:

These piles trade their load to the ground along the skin contact. The path toward driving such stacks does not insignificant the soil basically. These sorts of load foundations are normal as floating store foundations.

Contact store is used when the hard strata are connecting underneath a versatile significance and the rubbing of stack surface with the soil is used to withstand the load of the structure. Right when a load is collided with soil of truly uniform consistency and the tip is not arranged in a hard layer, the pile passing on cut-off of the stack is create by skin contact. The pile is moved to the associating soil by contact between the load and the neighboring soil. The load is convey diving and at the edge to the earth is called contact stack.

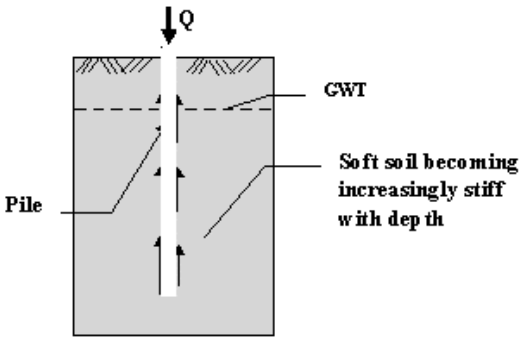

2.3 Combination of Friction Piles and Cohesion Piles

An expansion of the end bearing heap when the bearing stratum is not hard, for example, firm mud. The heap is driven far adequate into the lower material to create imperative frictional resistance. Other than variety of the end bearing heap is heaps with open up bearing ranges. This is achieved by pushing a globule of cement into the delicate stratum immediately over the firm layer to concede an augmented base. A homogeneous impact is delivered with exhausted heaps by building up an expansive cone or ringer at the base with a one of a kind reaming apparatus. Exhausted heaps which are contributed with a chime have a high rigidity and can be utilized as pressure heaps.

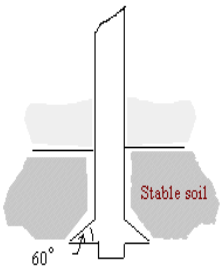

III. OBJECTIVES

- To study the earthquake response of multi storied building with End bearing pile and friction pile foundation by response spectrum analysis.
- To study the earthquake response of Multi storied Building having End bearing pile and friction pile foundation with mass irregularities by response spectrum analysis.
- To study the earthquake response of Multi storied Building having End bearing pile and friction pile foundation with vertical irregularities by response spectrum analysis.

IV. BUILDING DESCRIPTION

The analysis of 3Dimensional multi storey structure with pile foundation resting on Medium soil subjected to seismic load (response spectrum) according to the seismic code IS: 1893-2002(part 1) are carried out.

- Multi-storeyed building:
- Height of each floor = 3m
- Total height of the building = 14.4m
- Software = E-Tabs, AutoCAD

The building given is to be used for residential purpose. Plinth + 3Upper Floors + Roof + Overhead Water tank. The height of the ground floor is 3m and typical floor height is 3 m .Total height of the building is 14.4m above the plinth and each floor of the building comprises of one house, each floor consist of one Living room, one Master Bedroom, one Kitchen, one Dining room, toilet, staircase and balcony.

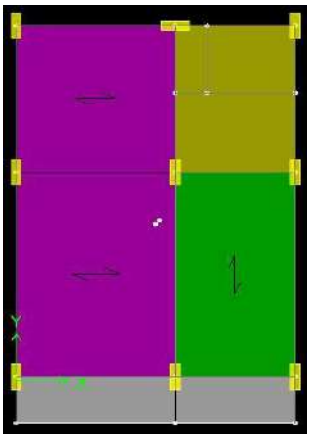

FIG.1: E-TABS MODEL- PLAN

Material of Construction

A. Concrete mix for columns: M25
B. Concrete mix for beams: M25
C. Concrete mix for all slabs: M25

TABLE 1
DENSITIES OF THE MATERIALS USED.

Density of Reinforced Concrete	25.0 kN/m^3
Density of Plain Concrete	24.0 kN/m^3
Density of Steel	78.5kN/m^3

TABLE 2
LIVE LOAD:

Live load on Typical slab	1.5 kN/m^2
Live Load on Typical Floor (Lobby, Balcony, Staircase etc...)	4 kN/m^2
Live Load on Terrace slab	1.5 kN/m^2

TABLE 3
FLOOR FINISHING:

All rooms , Kitchen Toilet and Balconies	2kN/m^2
Stairs	3 kN/m^2
Toilet and Balconies	1.5 kN/m^2
Terrace	3.25kN/m^2

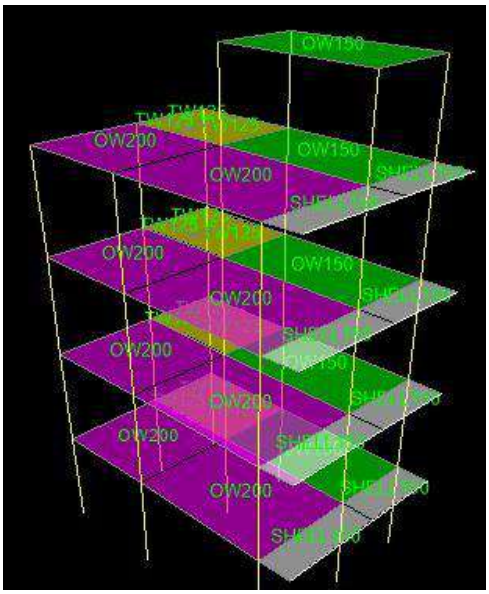

FIG.2: E-TABS MODEL- 3D

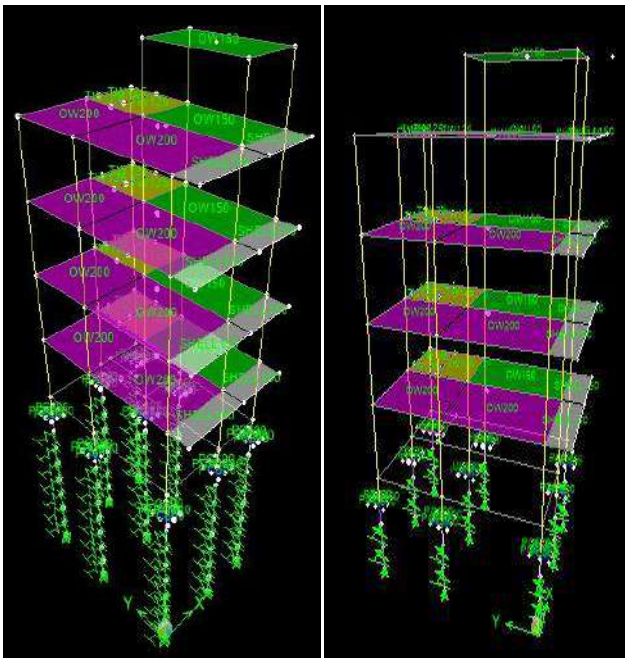

FIG.3:3D VIEW OF END BEARING PILE AND FRICTION PILE

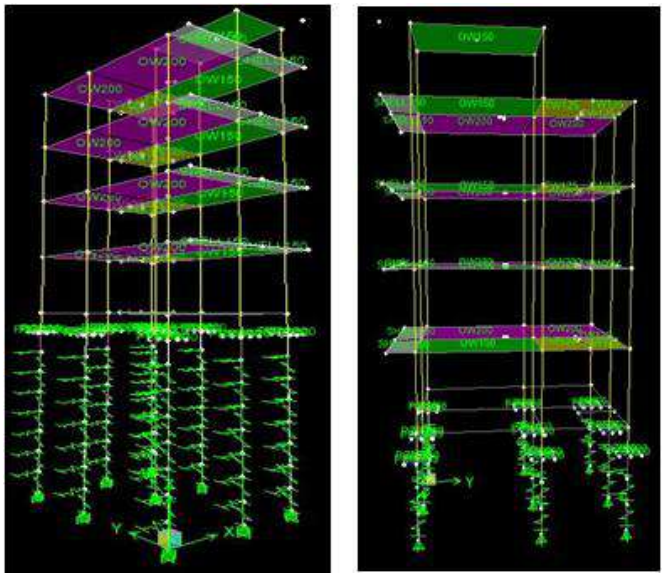

FIG.4:3D VIEW OF END BEARING PILE AND FRICTION PILE WITH MASS IRREGULARITY

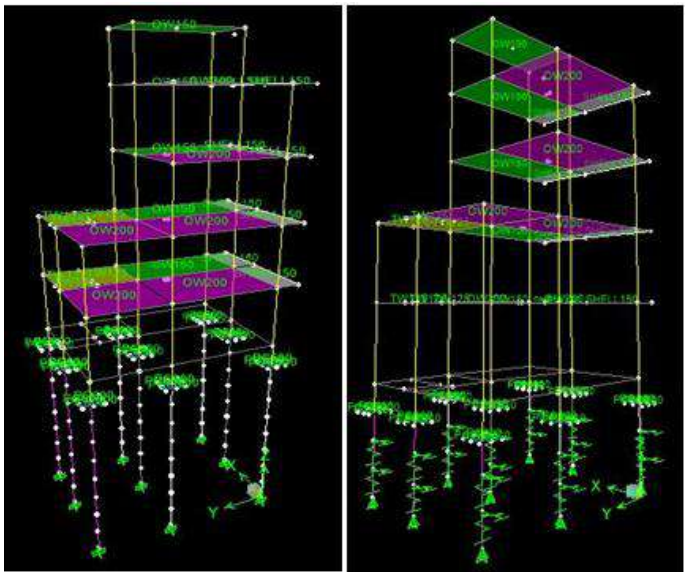

FIG.5:3D VIEW OF END BEARING PILE AND FRICTION PILE WITH VERTICAL IRREGULARITY

V. RESULTS AND DISCUSSIONS

The result of the comparison of structural response between the friction and end bearing pile condition are presented as such.

The following five parameters of multi storey structure with friction and end bearing pile are studied

- Time period
- Frequency
- Displacement
- Storey drift ratio
- Storey shear

5.1 Time Period

TABLE 4
TIME PERIOD (SEC)

MODES	TP-T3	TP-T4
1	2.143443	2.272337
2	1.827572	1.489942
3	1.619822	1.45759
4	0.573636	0.56833
5	0.396024	0.365583
6	0.376887	0.352494
7	0.303306	0.297921
8	0.256555	0.243009
9	0.230866	0.222011
10	0.209686	0.204293
11	0.186548	0.176406
12	0.179459	0.170225

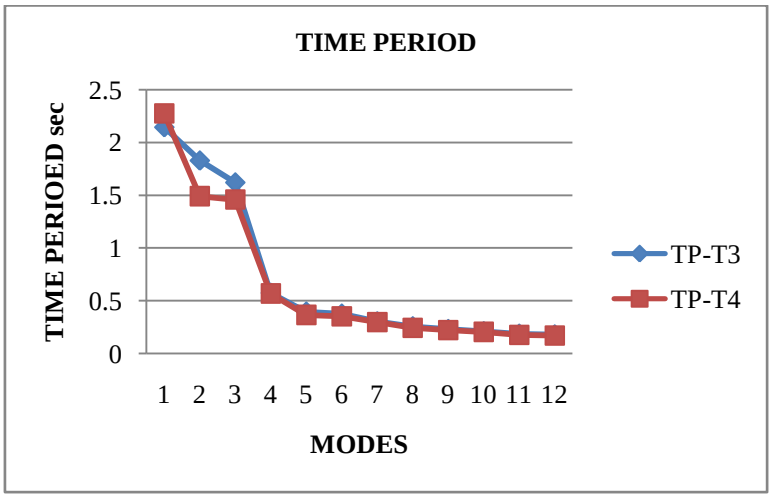

GRAPH 1: TIME PERIOD

- The Time Period for Friction Pile is more when compared to End Bearing Pile.
- A Time Period is the time needed for one complete cycle of vibration to pass a given point.
- Time period mainly depends on two important factors i.e., Mass and Flexibility of the structure.
- As the flexibility increases time period also increases.

5.2 Frequency

TABLE 5
FREQUENCY (cyc/sec)

MODES	FR-T3	FR-T4
1	0.466539	0.440076
2	0.547174	0.671167
3	0.617352	0.686064
4	1.743266	1.759541
5	2.525099	2.735357
6	2.653315	2.836928
7	3.297	3.356595
8	3.8978	4.115074
9	4.331517	4.504281
10	4.769036	4.89493
11	5.360551	5.668741
12	5.572303	5.874578

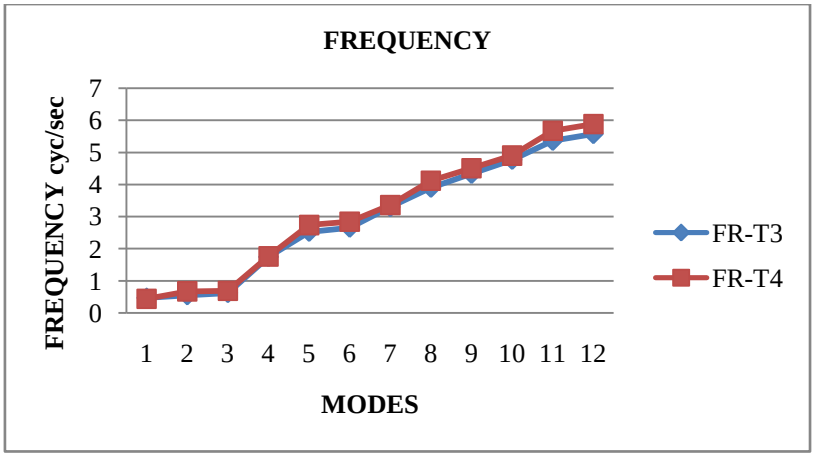

GRAPH 2: FREQUENCY

The Frequency of End Bearing Pile and Friction Pile are as shown in the graph

- The Frequency is defined as the ratio of time period. i.e., f= 1/T
- The Frequency for End Bearing Pile is more when compared to Friction Pile.
- As the frequency of a wave increases, the time period of the wave decreases.

5.3 Displacement

TABLE 6
EARTH QUAKE IN X-DIRECTION

STOREY	UX-T3	UX-T4
SHR	10.6265	10.8649
ROOF	10.7338	10.6879
3RD	10.2643	10.2078
2ND	9.565	9.5982
1ST	8.4772	8.594

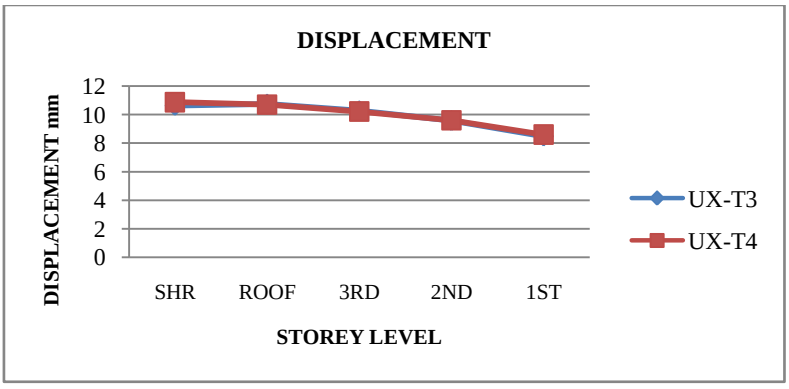

GRAPH 3: DISPLACEMENT

- The lateral displacement is more for Friction Pile in x-direction and End Bearing in y-direction.
- Increase in displacement decreases the stability and durability of the building.

Hence this is not good for human comfort.

5.4 Storey Drift Ratio

TABLE 7
EARTH QUAKE IN X-DIRECTION

STOREY	Drift X-T3	Drift Y-T3	Drift X-T4	Drift Y-T4
SHR	0.000588	0.000205	0.000555	0.000192
ROOF	0.000442	0.000389	0.000403	0.000366
3RD	0.000625	0.000408	0.000575	0.00039
2ND	0.000724	0.000371	0.000698	0.00037
1ST	0.000811	0.000288	0.000761	0.000381
PLINTH	0.001027	0.000327	0.001658	0.000471

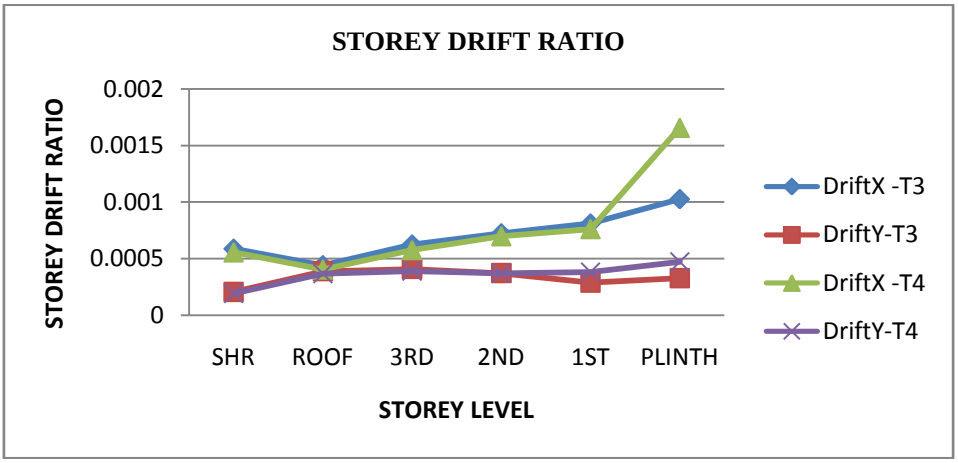

GRAPH 4: STOREY DRIFT RATIO

- Storey drift is the displacement of one level relative to the other level above or below.
- Storey drift ratio is more for friction pile in x-direction and End Bearing Pile in y-direction.
- Storey drift creates strain, stress and torsion in local elements such as beam and column which is most dangerous.

5.5 Storey Shear

TABLE 8
EARTH QUAKE IN X-DIRECTION

STOREY	VX-T3	VX-T4
SHR	3.03	2.76
ROOF	15.01	13.45
3RD	26.48	23.69
2ND	35.06	31.4
1ST	42.68	38.3
PLINTH	46	41.34
PC	47.74	42.56

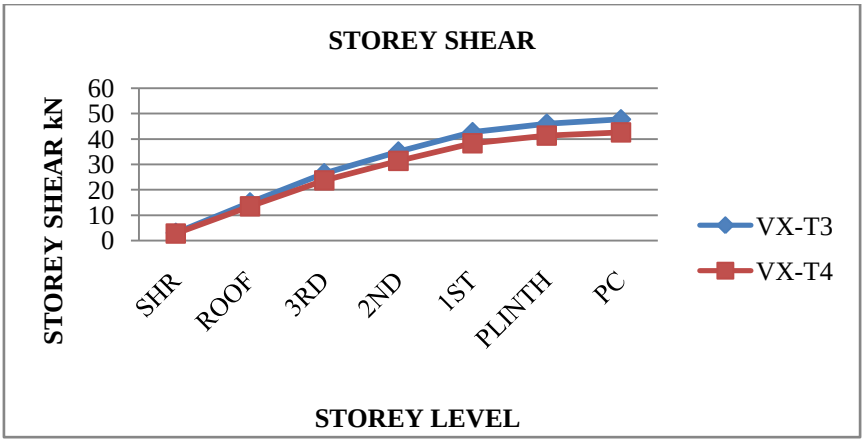

GRAPH 5: STOREY SHEAR

- Storey Shear is the sum of all the horizontal forces at the base.
- There is a slight increase in Storey shear for End Bearing Pile when compared to Friction Pile in x-direction.
- If earthquake acts in x-direction then End Bearing Pile gives good result when compared to friction pile.

VI. CONCLUSION

The Current Study makes an effort to estimate the effect of performance of End Bearing Pile and Friction Pile in seismic region of a multi storey structure situated in zone V on medium type of soil. The study also spreads to find the structural parameters like Time Period, Maximum Lateral Displacement, Storey Drift ratio and Storey Shear.

The Study leads to following conclusions:

6.1 Time Period

By considering all the three cases Friction pile is giving good result than compared to End Bearing Pile.

6.2 Frequency

- In all the three cases, the Frequency for End Bearing Pile is more when compared to Friction Pile.
- As the frequency of a wave increases, the time period of the wave decreases.

6.3 Maximum Lateral Displacement

By considering all the three cases,

- Earthquake response of the building in x-direction is reduced in End Bearing Pile.
- Earthquake response of the building in y-direction is reduced in Friction Pile.

6.4 Storey Drift Ratio

- For case one - End Bearing Pile is giving good result for both x-direction and y- direction.
- For case two - End Bearing Pile is giving good result in x-direction.

  Both End Bearing Pile and Friction Pile are giving similar results in y- direction.

For case three - End Bearing Pile is giving good result for both x-direction and y- direction.

6.5 Storey Shear

- If earthquake acts in x-direction then End Bearing Pile gives good result when compared to friction pile.
- If earthquake acts in y-direction then Friction Pile gives good result when compared to End Bearing pile.

Overall it is concluded that End Bearing Pile performs better than Friction Pile in most of the above stated parameters.

REFERENCE

[1] Mohammed M. Salman, "The effect of improvement surrounding soil on bored pile Friction capacity," vol.7, Issue 1, Jan-Feb 2016, pp. 260-273.

[2] Khaled E. Gaaver, "Uplift capacity of single piles and pile groups embedded in cohesion less Soil," Engineering Structure (2013) 52, 365-372, 2013.

[3] S.K. Arun Kamaraj, "Experimental investigation on buckling behaviour of axially Loaded Prestressed concrete piles in sand," Engineering and Applied Sciences 2(9): 1394-1398, 2007

[4] Suchart Limkatanyu, "Response of Reinforced Concrete Piles including Soil-Pile Interaction effect," vol. II, no. Engineering Structure 31(2009)1976-1986, p. 11, 2009.

[5] G. Sandro Carbonari, "Linear Soil Structure Interaction of coupled Wall-frame Structures on Pile Foundations," vol. II, no. Soil Dynamics and Earthquake Engineering 31(2011)1296- 1309, 2011.

[6] IS: 456-2000, Code of practice for plain and reinforced Concrete, New Delhi, India: Bureau of Indian Standards.

[7] IS1893:2002(Part 1), Criteria for earthquake resistance Design of Structure, Part 1-General Provisions and Buildings, New Delhi, India: Bureau of Indian Standards fifth revision.

A Study on Seismic Response of an Irregular Structure with Different Angle of Incidence

Thanuja D[1], Manohar K[2]

[1]Department of Civil Engineering, Sahyadri College of Engineering and Management, VTU University, Belagavi - 590 018
[2]Assistant Professor, Department of Civil Engineering, Sahyadri College of Engineering and Management, VTU University, Belagavi - 590 018

Abstract— *Earthquakes are a natural calamity, feared by most and cause great destruction in and around the seismic zone where they occur. In seismic design of buildings, the earthquake motions are considered in principle directions of building which may not be true in all cases. The present study is focused on the earthquake incidence angle and its effect on the structure's column axial force and to obtain the critical angle using Non Linear Time History Analysis. A set of values from 0 to 90 degrees, with an increment of 10 degrees, have been used for angle of excitation. An asymmetrical structure of 10 storeys was considered. It can see that the critical angle may vary the column axial force from column to column. The models are analysed using ETABS 15 software. The structural parameters such as column axial force, displacement and story shear in columns are studied. The paper concludes that the internal forces of structural elements depend on the angle of incidence of seismic wave data. There are different critical angles for different parameters, not necessarily that it should be the same of the column axial force.*

Keywords— Incidence angle, Non Linear Time History, Column axial force, Displacement, Story shear.

I. INTRODUCTION

Earthquakes are natural hazards under which disasters are mainly caused by damage to or collapse of buildings and other man-made structures. Experience has shown that for new constructions, establishing earthquake resistant regulations and their implementation is the critical safeguard against earthquake-induced damage. As regards existing structures, it is necessary to evaluate and strengthen them based on evaluation criteria before an earthquake. Earthquake damage depends on many parameters, including intensity, duration and frequency content of ground motion, geologic and soil condition, quality of construction, etc. Building design must be such as to ensure that the building has adequate strength, high ductility, and will remain as one unit, even while subjected to very large deformation. Sociologic factors are also important, such as density of population, time of day of the earthquake occurrence and community preparedness for the possibility of such an event. Up to now we can do little to diminish direct earthquake effects. However we can do much to reduce risks and thereby reduce disasters provided we design and build or strengthen the buildings so as to minimize the losses based on the knowledge of the earthquake performance of different building types during an earthquake. Observation of structural performance of buildings during an earthquake can clearly identify the strong and weak aspects of the design, as well as the desirable qualities of materials and techniques of construction, and site selection. The study of damage therefore provides an important step in the evolution of strengthening measures for different types of buildings.

1.1 Earthquake Incidence Angle

Earthquakes are well known for the damage and destruction that they leave behind. Present scenario demands the need for designing the structures to withstand seismic forces. In seismic design of structures, the earthquake motions are considered in principle directions of structure. Insalmostdall seismic design codes, consideration of simultaneous effects of two horizontal components of earthquake excitations is taken into account by applying 100% of earthquake lateral forces in the direction of one of the structure main axes and 30% of those forces in the direction of other main axis. In reality the direction of the dominant component of excitations might not be one of the main directions of the structure axes and applying the main component in a direction other than main axes direction may lead to higher internal forces and stresses in the structure's

structural elements. Therefore the structure should be resistant under different excitation angles of earthquake. Some researchers have worked on the effect of angle of excitation on the response values since mid-80s. Over the period of time, Time History Analysis has become an important tool is assessing the behavior of a structure subjected to seismic loads. Time History Analysis is a method by which earth motion input of a particular earthquake can be used to determine the response of the structure. The main advantage of using this method is that the accuracy of the system response is higher when compared to Response Spectrum analysis, as the actual earth motion record from an earthquake can be used to simulate the structure.

II. METHODOLOGY

2.1 Project Details

Multi-storeyed apartment, Safe bearing capacity of soil (SBC) = 300 KN/mm2, Height of each floor = 2.95m (typical),Height of basement = 3.3m,Height of ground floor = 4.05m,Total height of the structure = 41.4m, Software = E-Tabs, AutoCAD. The structure given is to be used for residential purpose. Basement + Earth+ 13 Upper Floors + Overhead Water tank. The height of the basement and earth floor is 3.3m and typical floor height is 2.95 m .Total height of the structure is 41.1m above the plinth and each floor of the structure comprises of six houses, where four of them have one Living room, one Master Bedroom and two other Bedrooms with three toilets, one foyer, one Kitchen and one Dining room, one balcony and one utility and two of them have one Living room, one Master Bedroom and one Bedroom with two toilets, one foyer, one Kitchen and one Dining room, one balcony and one utility.

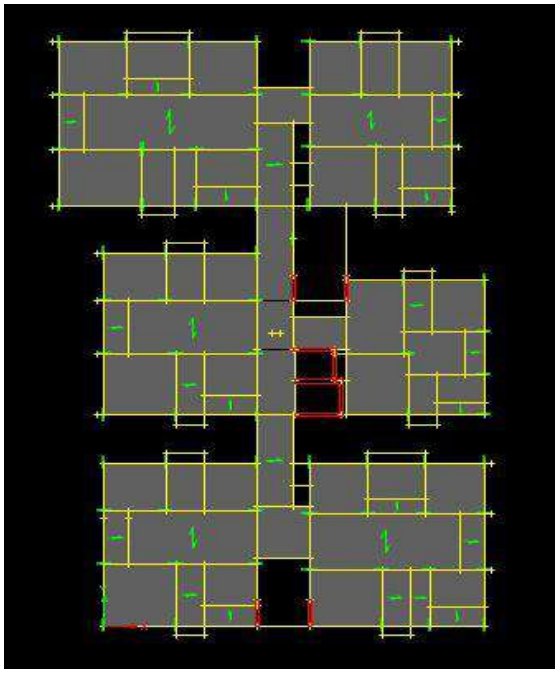

FIG. 1: E-TABS MODEL- PLAN

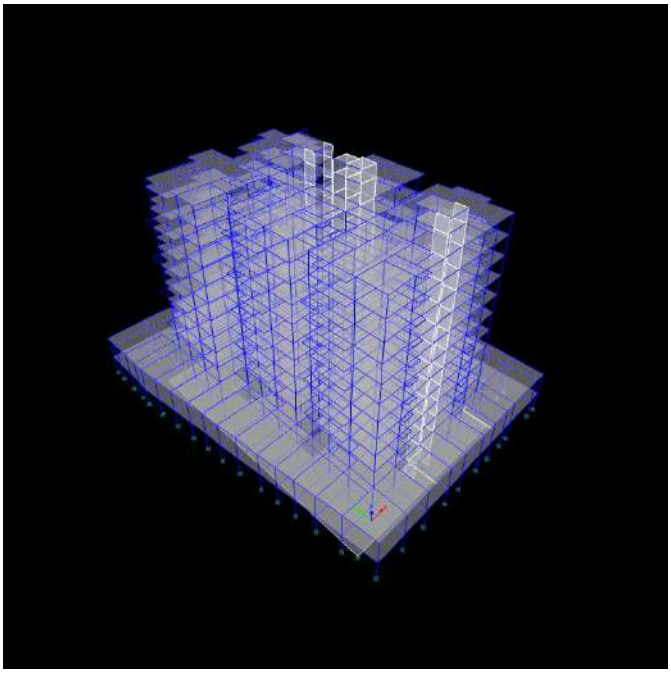

FIG. 2: E-TABS MODEL- 3D

III. RESULTS AND DISCUSSION

The results of Time History Analysis in the form of maximum column forces, column moments, maximum displacement and storey shear were studied.

3.1 Maximum Column Forces

The values of maximum column forces and the variation with incidence angle is shown in Table 1.The max column force was found to be -3693.42 kN for the load combination 1.5(TDL-ELX-0.3ELY) Max for column C-20 at the basement-1at 70^0 angle.

TABLE 4.1
COLUMN FORCES FOR ALL THE ANGLE OF INCIDENCE (0°- 90°)

Story	Column	Unique Name	Load Case/Combo	P	Angle
				kN	Deg.
Basement-1	C20	2578	0.9TDL+1.5(0.3THX-THY) Min	-2217.3	0
Basement-1	C20	2578	1.2(TLD+LL+0.3THX-TY) Min	-3232.67	0
Basement-1	C20	2578	1.5(TDL+0.3EX-EY) Min	-3693.38	0
Basement-1	C20	2578	0.9TDL+1.5(0.3THX-THY) Min	-2217.35	10
Basement-1	C20	2578	1.2(TLD+LL+0.3THX-TY) Min	-3232.7	10
Basement-1	C20	2578	1.5(TDL+0.3EX-EY) Min	-3693.42	10
Basement-1	C20	2578	0.9TDL+1.5(-0.3THX-THY) Min	-2217.33	20
Basement-1	C20	2578	1.2(TLD+LL-0.3THX-TY) Min	-3232.69	20
Basement-1	C20	2578	1.5(TDL-0.3EX-EY) Min	-3693.41	20
Basement-1	C20	2578	0.9TDL+1.5(-0.3THX-THY) Min	-2217.24	30
Basement-1	C20	2578	1.2(TLD+LL-0.3THX-TY) Min	-3232.62	30
Basement-1	C20	2578	1.5(TDL-0.3EX-EY) Min	-3693.32	30
Basement-1	C20	2578	0.9TDL+1.5(-0.3THX-THY) Min	-2217.05	40
Basement-1	C20	2578	1.2(TLD+LL-0.3THX-TY) Min	-3232.47	40
Basement-1	C20	2578	1.5(TDL-0.3EX-EY) Min	-3693.13	40
Basement-1	C20	2578	0.9TDL+1.5(-THX-0.3THY) Min	-2217.11	50
Basement-1	C20	2578	1.2(TLD+LL-THX-0.3TY) Min	-3232.51	50
Basement-1	C20	2578	1.5(TDL-0.3EX-EY) Min	-3692.85	50
Basement-1	C20	2578	0.9TDL+1.5(-THX-0.3THY) Min	-2217.27	60
Basement-1	C20	2578	1.2(TLD+LL-THX-0.3TY) Min	-3232.64	60
Basement-1	C20	2578	1.5(TDL-EX-0.3EY) Min	-3693.35	60
Basement-1	C20	2578	0.9TDL+1.5(-THX-0.3THY) Min	-2217.34	70
Basement-1	C20	2578	1.2(TLD+LL-THX-0.3TY) Min	-3232.7	70
Basement-1	C20	2578	1.5(TDL-EX-0.3EY) Min	-3693.42	70
Basement-1	C20	2578	0.9TDL+1.5(-THX+0.3THY) Min	-2217.37	80
Basement-1	C20	2578	1.2(TLD+LL-THX+0.3TY) Min	-3232.72	80
Basement-1	C20	2578	1.5(TDL-0.3EX+EY) Min	-3691.77	80
Basement-1	C20	2578	0.9TDL+1.5(-THX-0.3THY) Min	-2217.3	90
Basement-1	C20	2578	1.2(TLD+LL-THX-0.3TY) Min	-3232.67	90
Basement-1	C20	2578	1.5(TDL-EX-0.3EY) Min	-3693.38	90

3.2 Maximum Column Moments

The values of maximum column moments and the variation with incidence angle is shown in Table 2. The maximum moment was in 1ST FLOOR for the column C-32 with the load combination 1.2(TLD+LL-0.3THX+TY) Max of 225.3083 kN-m for an incidence angle of 80°.

TABLE 2
COLUMN MOMENTS FOR ALL THE ANGLE OF INCIDENCE (0°- 90°)

Story	Column	Load Case/Combo	P	M3	Angle
			kN	kN-m	Deg.
Ground floor	C32	0.9TDL+1.5(THX-0.3THY) Min	-1621.179	-95.8313	0
1st Floor	C32	1.2(TLD+LL-THX+0.3TY) Max	-2028.8649	225.2589	0
Ground floor	C32	1.5(TDL+EX+0.3EY) Min	-2696.5294	-159.1	0
Ground floor	C32	0.9TDL+1.5(THX-0.3THY) Min	-1621.3585	-95.8373	10
1st Floor	C32	1.2(TLD+LL-THX+0.3TY) Max	-2028.8187	225.2588	10
Ground floor	C32	1.5(TDL+EX+0.3EY) Min	-2696.6017	-159.108	10
Ground floor	C32	0.9TDL+1.5(THX+0.3THY) Min	-1621.3182	-95.8335	20
1st Floor	C32	1.2(TLD+LL-THX+0.3TY) Max	-2028.913	225.2804	20
1st Floor	C32	1.5(TDL-EX+0.3EY) Max	-2211.2698	150.3738	20
Ground floor	C32	0.9TDL+1.5(THX+0.3THY) Min	-1621.2853	-95.8191	30
1st Floor	C32	1.2(TLD+LL-THX+0.3TY) Max	-2028.8427	225.2352	30
Ground floor	C167	1.5(TDL-EX+0.3EY) Min	-469.6913	-239.32	30
Ground floor	C32	0.9TDL+1.5(THX+0.3THY) Min	-1621.0826	-95.7812	40
1st Floor	C32	1.2(TLD+LL-THX+0.3TY) Max	-2028.9545	225.1234	40
Basement-1	C32	1.5(TDL-0.3EX-EY) Min	-2966.8733	-70.2712	40
Ground floor	C32	0.9TDL+1.5(THX+0.3THY) Min	-1620.7625	-95.7169	50
1st Floor	C32	1.2(TLD+LL-0.3THX+TY) Max	-2029.8786	225.0561	50
Basement-1	C32	1.5(TDL-0.3EX-EY) Min	-2967.814	-70.4311	50
Ground floor	C32	0.9TDL+1.5(-0.3THX-THY) Min	-1619.9548	-95.7232	60
1st Floor	C32	1.2(TLD+LL-0.3THX+TY) Max	-2029.4102	225.2217	60
Basement-1	C32	1.5(TDL-0.3EX-EY) Min	-2968.5768	-70.5425	60
1st Floor	C32	0.9TDL+1.5(-0.3THX+THY) Max	-1324.0325	91.6141	70
1st Floor	C32	1.2(TLD+LL-0.3THX+TY) Max	-2029.1073	225.3066	70
Ground floor	C32	1.5(TDL+0.3EX-EY) Min	-2696.2622	-159.065	70
1st Floor	C32	0.9TDL+1.5(-0.3THX+THY) Max	-1323.8518	91.6161	80
1st Floor	C32	1.2(TLD+LL-0.3THX+TY) Max	-2028.9627	225.3083	80
Ground floor	C32	1.5(TDL+0.3EX-EY) Min	-2696.497	-159.082	80
Ground floor	C32	0.9TDL+1.5(0.3THX-THY) Min	-1621.1683	-95.8352	90
1st Floor	C32	1.2(TLD+LL+0.3THX+TY) Max	-2028.8649	225.2589	90
Ground floor	C32	1.5(TDL+0.3EX-EY) Min	-2696.5294	-159.1	90

3.3 Maximum Story Displacement

The values of maximum story displacement and the Comparison between displacements for different angles is shown in Figure 3 and Table 3.Displacement is more in 40° in x-direction 5.47mm and 20°in y-direction 2.73mm for the combo 1.5(TDL+0.3EX-EY).

TABLE 3
COMPARISON BETWEEN DISPLACEMENTS FOR DIFFERENT ANGLES

Angle	X direction(mm)	Y direction(mm)
10	2.58	5.63
20	2.73	5.76
30	2.84	5.47
40	2.96	5.47
50	2.81	5.39
60	2.7	5.49
70	2.5	5.53
80	2.56	5.54
90	2.503	5.526

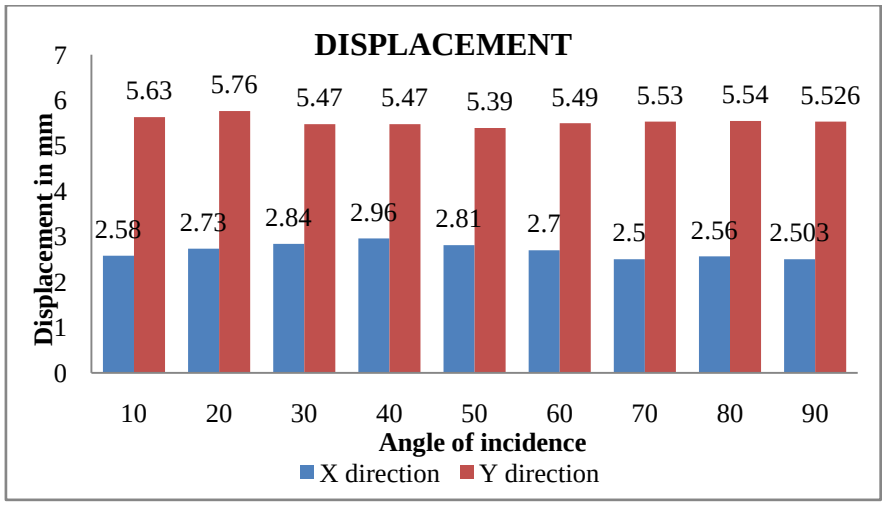

FIGURE 3: COMPARISON BETWEEN DISPLACEMENTS FOR DIFFERENT ANGLES

3.4 Maximum Story Shear

The values of maximum story shear and the Comparison between story shear for different angles is shown in Figure 4 and Table 4. Story shear is more in 70° with 128 kN in x-direction and 50° with 105kN in y-direction for the combo 1.5(TDL+0.3EX-EY).

TABLE 4
COMPARISON BETWEEN STORY SHEAR FOR DIFFERENT ANGLES

Angle	X direction(kN)	Y direction (kN)
10	128	57
20	127	73
30	123.6	87
40	115	101
50	120	105
60	126	93
70	128	78
80	126	61
90	126	46

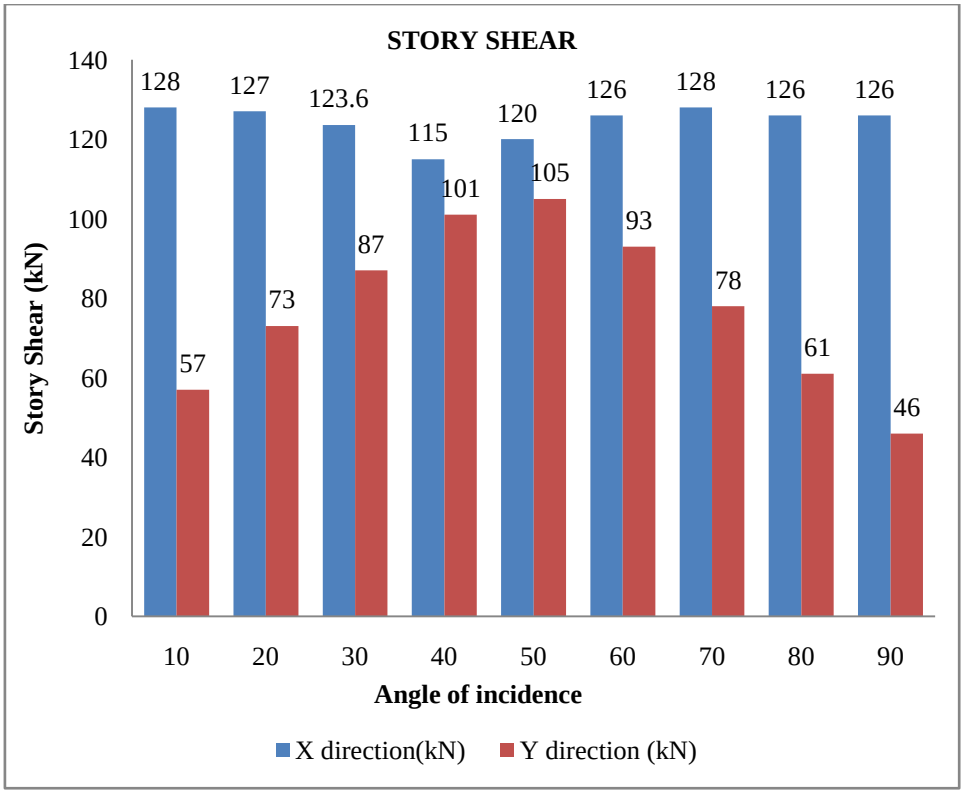

FIGURE 4: COMPARISON BETWEEN STORY SHEAR FOR DIFFERENT ANGLES

IV. CONCLUSION

- The internal forces of structural elements depend on the angle of incidence of seismic wave data.
- There are different critical angles for different parameters, not necessarily that it should be the same of the column axial force.
- The maximum displacement and maximum column axial forces are of same angle i.e. 70° for EL CENTRO earthquake data.
- The critical angle depends on the geometry of the structure.
- The objective of this study is to highlight that, the earthquake motions are considered in principle directions of structure but excitations might not be in one of the main directions of the structure axes.

REFERENCES

[1] Bhatnagar U. "Seismic performance on skewed bridges under orthogonal earth motion components" Journal of Structural Engineering, 2013, pp.1-94.

[2] Salemi, M. H. "Studying the Effect of Earthquake Excitation Angle on the Internal Forces of Steel Structures Elements by Using Non Linear Time History Analysis". 14th World Conference on Earthquake Engineering, 2008, pp.1-8.

[3] Poursha, F. K."Responses of Three Dimensional Structures under Bidirectional and Unidirectional Seismic Excitations". 13th World Conference on Earthquake Engineering, 2004, No 55.

[4] M. Sri Kanya, "Effect of Earthquake Incidence Angle on Seismic Performance of RC Buildings". International Journal of Research in Engineering and Technology, vol 4, Issue 13, 2006, pp.156-161.

[5] M. Sri Kanya, (2006) "Effect of Earthquake Incidence Angle on Seismic Performance of RC Buildings". International Journal of Research in Engineering and Technology, vol 4, Issue 13, pp.156-161.

Analysis and Comparative Study of Unbonded Post-tensioned Cast-In-Place Parking Floor on the Effects of Tendon Layout using Safe

Nethravathi S.M[1], Darshan prasad[2]

Department of Civil Engineering, Sahyadhri college of Engineering and Management, Mangalore

Abstract— *In recent years post-tensioned floors are commonly used for parking purposes in residential and commercial high rise buildings. This paper includes result on a study of un-bonded post tensioned cast-in-place parking floor subjected to various arrangements of tendon layout based on FEM analysis. Modelling and analysis of post-tensioned flat plate is done by using SAFE software. Equivalent loads based on cable profiles are applied to the flat plate according to the tendon layout. Design moments, service moments, hyper-static moments, short term deflection, long term deflection, and punching shear are compared for the various tendon layouts at service and ultimate limit state.*

Keywords— Post-Tensioned flat plate, SAFE, Tendons.

I. INTRODUCTION

In recent days post-tensioned parking floor is common in residential and commercial high rise buildings. Usage of post tensioned floors provide beneficial advantages over reinforced concrete floors in terms of reduction in thickness of slab, construction speed, rapid fixing services and also offers superior structural performance and other advantages. Here we used load balancing techniques for the design of PT flat plate, and this method is mainly dependent on tendon arrangements. This paper shows the comparative study and behavior of PT flat plate by the effects of tendon layout at service and ultimate limit state.

II. POST-TENSIONED FLAT PLATE

Post-tensioning concrete slabs is a method in which tendons are stressed after the concrete is poured around it. Post-tensioned concrete slab is a method for overcoming concretes natural weak in tension. In Post- tensioned floors, compressive stress is already introduced in it, before the slab is put in to service, because of the nature of the stress, the top part of the slab will be in tension and bottom part will be in compression. In PT slabs stresses gets nullified with load acting and it makes the slab in which stresses opposite to loads are introduced. Now the opposite stresses in PT slabs are introduced using high tensile steel strands which can take more load than reinforced concrete slabs.

2.1 Post-tensioning is of two types,

2.1.1 Bonded post-tensioning system

Bonded post-tensioning system are those in which pre-stressing steel strand is bonded to the concrete after it is tensioned by injecting cement grout inside of a duct in which the tendon is placed. This method mainly prevents corrosion of tendons.

2.1.2 Unbonded post-tensioning system:

Unbonded post-tensioning system are those in which pre-stressing steel strand is preventing from bonding to the concrete and thus free to move relative to the concrete. The force is transferred to the concrete by the mechanical assembly only.

2.2 Advantages of Post-tensioning

- Simple form work
- Speedier construction
- Steel quantity is reduced
- Larger span
- Reduced cracks in slab

- Freezing and thawing is higher than RC slab systems
- Improved deflection criteria
- Superior and economical design
- Reduced moments and stresses than compare to RC slab systems

III. MODELING AND ANALYSIS

SAFE-2D Post-tensioned flat plate models shown in Fig.1.

Case I: Banded and Distributed tendon layout

Case II: Distributed and Distributed tendon layout

Case III: Banded and Banded layout

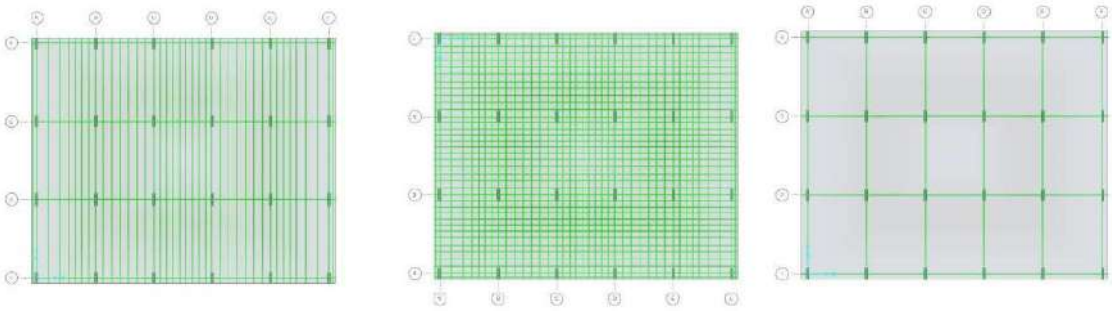

FIG.1: PT FLAT PLATE 2D MODEL FOR CASE I, II, & III

3.1 Model Description

PT flat plate modeled in SAFE V12 Floor slab having dimension of size 41.2m x 25.2m center to center. Model is analyzed for uniform LL of 3.125 kN/m2. Detailed descriptions of PT flat plate for different cases have been mentioned in the below tables.

IV. RESULTS AND ANALYSIS

From the results the following observations are made:

- **Service moments:** By considering all the three cases of tendon layout case 1 i.e, Banded and distributed tendons gives less elastic moment values than case 2 and case 3. It means banded and distributed tendons can improve the flexural capacity of a member at service limit state. Banded tendons are more effective in reducing punching failure, whereas distributed tendons are effective in reducing punching failure of a member. Banded/distributed tendons are more effective in reducing flexure of a member at service limit state.
- **Design moments:** By considering all the three cases of tendon layout case 2 i.e, distributed and distributed tendons gives less design moment values than case 1 and case 3. It means the tendons are closely placed here in both directions. Hence the load capacity of the member increased here than compare to case 1 and case 3, as I said earlier distributed tendons are more effective in reducing flexure of a member in case 2 tendons are running in both the directions, hence load capacity of a member is increased than compare to other two cases at ultimate limit state.
- **Hyper-static moments:** By considering all the three cases of tendon layout, case 2 i.e, Distributed and distributed tendons gives less secondary moment values than case 1 and case 3. It means the tendons are closely placed here in both directions. Hence the load capacity of the member increased here than compare to case 1 and case 3.
- **Short term deflection:** By considering all the three cases of tendon layout, case 1 i.e. Banded and distributed tendons gives less immediate deflection values than case 2 and case 3 and it is shown in Fig.2
- **Long term deflection:** By considering all the three cases of tendon layout, case 1 i.e. Banded and distributed tendons

gives less deflection values than case 2 and case 3 and it is shown in Fig.3. Total/final deflection values in all the 3 cases are within the permissible limit hence our design is safe.

- **Punching shear:** Here punching values in all 3 cases at some points it is exceeding than permissible limit hence for our design shear reinforcement is required at that points. By considering all the three cases of tendon layout, case 3 i.e, Banded and banded tendons punching shear capacity ratio values are better than case 1 and case 2, this is because banded tendons runs along both the directions and they are more effective in reducing punching failure than distributed tendons.

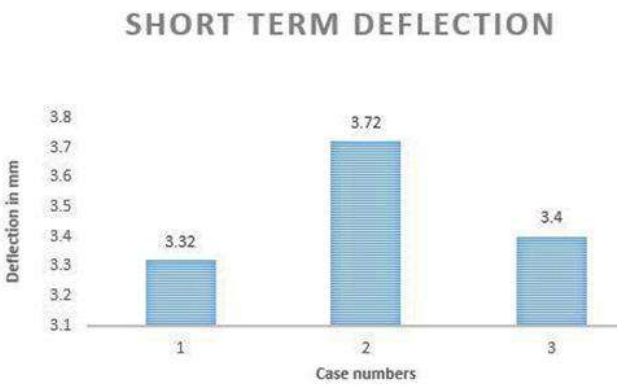

FIG.2: SHORT TERM DEFLECTION IN mm

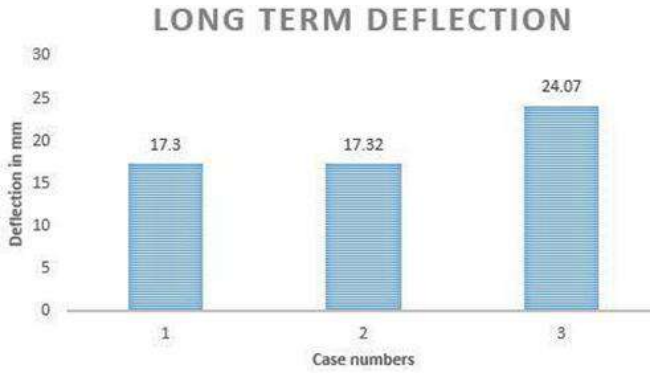

FIG.3: LONG TERM DEFLECTION IN mm

TABLE 1
DESCRIPTION FLAT PLATE MODEL

CASE	GRADE (MPA)	SLAB THICKNESS(mm)	LONG SPAN (m)	SHORT SPAN (m)
I	40	200	8	8
II	40	200	8	8
III	40	200	8	8

TABLE 2
ANALYSIS RESULTS OF POST-TENSIONED FLAT PLATE MODELS

	Critical Service Moment in kN-m	Critical Design Moment in kN-m	Critical Hyper-static Moment in kN-m
CASE I	(+M)108.41	(+Mu)258.52	(Max)125.76
	(-M)91.02	(-Mu)341.62	(Min)-2.95
	(+M)130.64	(+Mu)249.77	(Max)108.30
CASE II	(-M)96.29	(-Mu)341.62	(Min)-26.03
	(+M)105.11	(+Mu)259.76	(Max)137.74
	(-M)113.68	(-Mu)340.89	(Min)-32.91
	CASE I	CASE II	CASE III
	3.32	3.72	3.40
DEFLECTION (mm)	17.30	17.32	24.07

TABLE 3
ANALYSIS RESULTS OF POST-TENSIONED FLAT PLATE MODELS

PUNCHING	1.34	1.42	1.20	1.20	1.42	1.34
SHEAR CAPACITY	0.94	1.44	1.23	1.23	1.44	0.94
RATIO	0.94	1.44	1.23	1.23	1.44	0.94
VALUES OF CASE I	1.34	1.42	1.20	1.20	1.42	1.34
PUNCHING SHEAR	1.40	1.44	1.25	1.25	1.44	1.40
CAPACITY	0.99	1.37	1.21	1.21	1.37	0.99
RATIO	0.99	1.36	1.19	1.19	1.36	0.99
VALUES OF CASE II	1.41	1.44	1.26	1.26	1.44	1.41
PUNCHING SHEAR	1.27	1.32	1.13	1.13	1.32	1.27
CAPACITY	0.92	1.44	1.24	1.24	1.44	0.92
RATIO	0.92	1.44	1.24	1.24	1.44	0.92
VALUES OF CASE III	1.27	1.32	1.13	1.13	1.32	1.27

V. CONCLUSION

- Moment distributions across the slab panels may vary significantly between different tendon layouts, resulting in different signs at critical sections at service limit states.
- Moment distributions across the slab panels are almost similar between different tendon layouts, at ultimate limit states.
- Load carrying capacity of a case 1 FEM model is more than compare to case 2 and case 3 at service limit state.
- Load carrying capacity of a case 2 FEM model is more than compare to case 1 and case 3 at ultimate limit state.
- Load carrying capacity of a case 2 FEM model is more than compare to case 1 and case 3 to withstand hyper -static moments (secondary moments).
- Total deflection including effect of temperature, creep and shrinkage, the deflection values are within the permissible limit for all the 3 cases. But, case 1 gives fewer values than compare to case 2 and case 3.
- The punching shear capacity ratio values in case 3 are better than compare to case 1 and case 2, at some points it is exceeding than permissible limit at that point shear reinforcement is required.
- Overall by seeing the results obtained from analysis, case 2 (distributed and distributed tendons) behaving good at ultimate limit state than case 2 and case 3. Here strength and serviceability considerably increased; hence I am concluding case 1 is better option for constructing un-bonded post-tensioned parking floor slabs.

REFERENCES

[1] Andre j schokker and Andrew Scanlon "Analytical study of the effects of tendon layout on the performance of post-tensioned two way slab systems". 4th Structural Specialty Conference of the Canadian Society for Civil Engineering 2002.

[2] Min Sook Kim and Young Hak Lee "Flexural Behavior of Posttensioned Flat Plates Depending on Tendon Layout". Hindawi Publishing Corporation Advances in Materials Science and Engineering Volume 2016.

[3] V.G Mutalikdesai and MD J. Shaikh. "Comparative Analysis of Flat Slab and Post-Tensioned Flat Slab Using SAFE". International Advanced Research Journal in Science, Engineering and Technology ISO 3297:2007 Certified Vol. 3, Issue 8, August 2016.

[4] Shriraj S. Malvade and P.J. Salunke "Analysis of Post-Tensioned Flat Slab by using SAFE" International Journal of Scientific Engineering and Applied Science (IJSEAS) – Volume-3, Issue-3, March 2017.

[5] Boskey Vishal Bahoric and Dhananjay K. Parbat, "Analysis And Design Of RCC And Post-Tensioned Flat Slabs Considering Seismic Effects", IACSIT International Journal of Engineering and Technology, Vol. 5, No. 1, February 2013.

[6] N.H. Burns and R. Hemakom, "Test of PT flat plate with banded tendons," Journal of Structural Engineering, vol.111, no.9,pp.1899– 1915,1985.

[7] IS 1343:1980, "Indian standard code of practice for pre stressed concrete", New Delhi.

[8] IS 456:2000, "Indian standard code of practice for plain and reinforced concrete", New Delhi.

Kinematic Surface Generated by an Equiform Motion of Astroid Curve

H. N. Abd-Ellah[1], M. A. Abd-Rabo[2]

[1]Department of Mathematics, Faculty of Science, Assiut Univ., Assiut, 71516, Egypt
[2]Department of Mathematics, Faculty of Science, Al-Azhar Univ., Assuit branch, Assiut 71524, Egypt

Abstract— *In this paper, a kinematic surface using equiform motion of an astroid curve in Euclidean 3-space E^3 is generated. The main results given in this paper: the surface foliated by equiform motion of astroid curve has a constant Gaussian and mean curvatures if motion of astroids is in parallel planes. Also, the geodesic curves on this surface are obtained. Additionally, special Weingarten of such surface is investigated. Finally, for some special cases new examples are constructed and plotted.*

2010 Mathematics subject classification:53A10, 53A04, 53C22 and 53A17.

Keywords— Kinematic surfaces; equiform motion; Gaussian, mean and geodesic curvatures, Weingarten Surfaces.

I. INTRODUCTION

The kinematic geometry is dedicated to the study of geometrical and temporal characteristics of movement procedures, mechanical aspects such as masses, forces, and so on remain unconsidered. With additionally neglect of the temporal aspect, one can speak more exactly of kinematic geometry. Regarding the relations to the mechanics and to technical applications in mechanical engineering, the kinetics were turned originally to the movements of rigid systems in the Euclidean plane and the three-dimensional Euclidean space and arrived here in the second half of the 19 Century and at the beginning of the last century too more largely.

In recent years interesting applications of kinematics have, for example, been made in areas as diverse as: animal locomotion, biomechanics, geology, robots and manipulators, space mechanics, structural, chemistry and surgery [1].

In [2] R. Lopez proved that cyclic surfaces in Euclidean three-dimensional space with nonzero constant Gaussian curvature are surfaces of revolution. In the case that the Gaussian curvature vanishes on the surface, then the planes containing the circles must be parallel. In [3] Fathi M. Hamdoon studied the corresponding kinematic three-dimensional surface under the hypothesis that its scalar curvature K is constant. In the eighteenth century, Euler proved that the catenoid is the only minimal surface of revolution. In 1860, Riemann found a family of embedded minimal surfaces foliated by circles in parallel planes. Each one of such surfaces is invariant by a group of translations and presents planar ends in a discrete set of heights [4]. At the same time, Enneper proved that in a minimal cyclic surface, the foliating planes must be parallel [5]. As a consequence of Euler, Riemann and Enneper's works, we have that the catenoid and Riemann minimal examples are the only minimal cyclic surfaces in Euclidean space. A century later, Nitsche [6] studied, in 1989, cyclic surfaces with nonzero constant mean curvature and he proved that the only such surfaces are the surfaces of revolution discovered by Delaunay in 1841 [7].Several special motions in equiform planar kinematics have been investigated by [8, 9] and [10]. For more treatment of cyclic surfaces see [11, 12] and [13].

An equiform transformation in the 3-dimensional Euclidean space E^3 is an affine transformation whose linear part is composed of an orthogonal transformation and a homothetical transformation. This motion can be represented by a translation vector d and a rotation matrix A as the following.

$$\bar{x} \to \rho A x + d, \tag{1}$$

where $AA^t = A^t A = I, \quad .2cm\bar{x}, x \in E^3$ and ρ is the scaling factor [3, 14]. An equiform motion is defined if the parameters of (1)- including ρ - are given as functions of a time parameter t. Then a smooth one-parameter equiform motion moves a point x via $\bar{x}(t) = \rho(t)A(t)x(t) + d(t)$. The kinematic corresponding to this transformation group is called an equiform kinematic.

The purpose of this paper is to describe the kinematic surface obtained by the motion of an astroid curve whose Gaussian and mean curvatures K and H are constant, respectively. As a consequence of our result, we prove:

A kinematic 2-dimensional surface obtained by the equiform motion of an astroid curve has a zero Gaussian and mean curvatures if a motion of astroids is in parallel planes. Moreover, using the motion of such surface, the kinematic geometry of geodesic lines is determined. Special Weingarten kinematic surface is studied. Finally, some examples are provided.

II. BASIC CONCEPTS

Here, and in the sequel, we assume that the indices $\{i, j\}$ run over the ranges $\{1,2\}$. The Einstein summation convention will be used, that is, repeated indices, with one upper index and and one lower index, denoted summation over its range. Consider M a surface in E^3 parameterized by

$$X = X(u^i) = X(u,v), \tag{2}$$

and let **N** denote the unit normal vector field on M given by

$$N = \frac{X_1 \wedge X_2}{| X_1 \wedge X_2 |}, \qquad X_i = \frac{\partial X}{\partial u^i}, \qquad X_{ij} = \frac{\partial^2 X}{\partial u^i \partial u^j}, \tag{3}$$

where $\wedge$ stands of the cross product of E^3. The metric $\langle\ ,\ \rangle$ in each tangent plane is determined by the first fundamental form

$$I = g_{ij} du^i du^j, \tag{4}$$

with differentiable coefficients

$$g_{ij} = \langle X_i, X_j \rangle. \tag{5}$$

The shape operator of the immersion is represented by the second fundamental form

$$II = -\langle dN, dX \rangle = h_{ij} du^i du^j, \tag{6}$$

with differentiable coefficients

$$h_{ij} = \langle N, X_{ij} \rangle. \tag{7}$$

With the parametrization of the surface (2), the Gaussian and mean curvatures are given by

$$K = Det(h_{ij})/Det(g_{ij}), \tag{8}$$

and

$$H = \frac{1}{2} tr(g^{ij} h_{ij}), \tag{9}$$

respectively, where, (g^{ij}) is the associated contravariant metric tensor field of the covariant metric tenser field (g_{ij}), i.e., $g^{ij} g_{ij} = \delta^i_j$.

The surface M generated by an astroid curve is represented by

$$M : X(u,v) = c(u) + r(u)(\cos^3 v\ t(u) + sin^3 v\ n(u)), \tag{10}$$

where $r(u)$ and $c(u)$ denote the radius and centre of each u-astroid of the foliation, $v \in [0,2\pi]$. Let $\Phi = \Phi(u)$ be an orthogonal smooth curve to each u-plane of the foliation and represented by its arc length u. We assume that the planes of the

foliation are not parallel. Let **t**, **n** and **b** be unit tangent, normal and binormal vectors, respectively, to Φ. Then, Frenet equations of the curve Φ are

$$\begin{pmatrix} t' \\ n' \\ b' \end{pmatrix} = \begin{pmatrix} 0 & k & 0 \\ -k & 0 & \tau \\ 0 & -\tau & 0 \end{pmatrix} \begin{pmatrix} t \\ n \\ b \end{pmatrix}, \qquad ' = \frac{d}{du}, \tag{11}$$

where k and τ are the curvature and torsion of $\Phi(u)$, respectively. Observe that $k \neq 0$ because $\Phi(u)$ is not a straight-line. Also, putting

$$c' = \alpha t + \beta n + \gamma b, \tag{12}$$

where α, β, γ are smooth functions in u [2].

III. CONSTANT GAUSSIAN CURVATURE OF M

In this section we will study the constancy of Gaussian curvature K of the surface generated by equiform motion which is locally parameterized by the equation(10).

Putting in $(2.8)\ W = Det(g_{ij})$, we have

$$KW^2 = K_1, \tag{13}$$

where

$$K_1 = [X_1, X_2, X_{11}][X_1, X_2, X_{22}] - [X_1, X_2, X_{12}]^2. \tag{14}$$

Consider now that the surface M is a surface with constant Gauss curvature. After a homothety, it may be assumed, without loss of generality, that the Gaussian curvature is $K = \hat{A}0, 1$ or -1.

3.1 Case *K*=0

Using equation (13) we can express K_1 by trigonometric polynomial on $\cos nv$ and $\sin nv$. Exactly, there exists smooth functions on u, namely A_n and B_n such that (8) writes as

$$0 = KW^2 - K_1 = A_0 + \sum_{i=1}^{16} (A_n \cos iv + B_n \sin iv). \tag{15}$$

Since this is an expression on the independent trigonometric terms $\cos nv$ and $\sin nv$, all coefficients A_n , B_n vanish identically.

After some computations, the coefficients of equation (15) are

$$A_{16} = \frac{-27r(u)^6 \tau(u)^4}{32768},$$

$$B_{16} = A_{15} = B_{15} = 0.$$

This leads to $\tau(u) = 0$.

Now, the coefficients

$$A_{16} = B_{16} = \cdots A_9 = B_9 = 0,$$

$$A_8 = -\frac{27}{128} r(u)^3 \gamma(u)(4k(u)^2 r(u)\gamma(u) + r^{'}(u)\gamma^{'}(u) - \gamma(u)r^{''}(u)),$$

$$B_8 = -\frac{27}{64} r(u)^3 \gamma(u)(2k(u)\gamma(u)r'(u) + r(u)(\gamma(u)k'(u) - k(u)\gamma'(u))),$$

$$B_8 = -\frac{27}{64} r(u)^3 \gamma(u)(k(u)\beta(u)\gamma(u) - \gamma(u)\alpha'(u) + \alpha(u)\gamma'(u)).$$

The above coefficients equal to zero in the following two cases

(i) $\gamma(u) = 0,$ **therefore, we have**

$$A_5 = B_5 = \cdots A_1 = B_1 = A_0 = 0,$$

(ii)

$$4k(u)^2 r(u)\gamma(u) + r^{'}(u)\gamma^{'}(u) - \gamma(u)r^{''}(u) = 0,$$

$$2k(u)\gamma(u)r'(u) + r(u)(\gamma(u)k'(u) - k(u)\gamma'(u)) = 0,$$

$$k(u)\beta(u)\gamma(u) - \gamma(u)\alpha'(u) + \alpha(u)\gamma'(u) = 0,$$

This system of nonlinear ODEs is of second order. Thus, their general solution is much more complicated and can only be solved in special cases. Thus, their solution is also $\gamma(u) = 0.$

Therefore, one can see all coefficients are vanished. Thus we have the proof of the following theorem:

Theorem 3.1 *The surface foliated by equiform motion of astroid curve has a zero Gaussian curvature if a motion of astroid is in parallel planes.*

3.2 Case *K*=1

From (13) similarly as in above case, we have

$$0 = KW^2 - K_1 = A_0 + \sum_{i=1}^{20}(A_n cos iv + B_n sin iv). \tag{16}$$

A routine computation of the coefficients yields

$$A_{20} = \frac{81r(u)^8 \tau(u)^4}{524288},$$

$$B_{20} = A_{19} = B_{19} = 0.$$

By solving the coefficient A_{20}, we have $\tau(u) = 0$. Now, the coefficients

$$A_{20} = B_{20} = A_{19} = B_{19} = 0$$

$$A_{16} = -\frac{81r(u)^4}{32768}(16k(u)^4 r(u)^4 - 24k(u)^2 r(u)^2 r^{'}(u)^2 + r^{'}(u)^4),$$

$$B_{16} = -\frac{81}{4096}(4k(u)^3 r(u)^7 r'(u) - k(u)r(u)^5 r'(u)^3).$$

By solving system A_{16}, B_{16}, we have $k(u) = 0$, $r(u) = r(constant)$. Now, the coefficients

$$A_{16} = B_{16} = ... = A_{13} = B_{13} = 0,$$

$$A_{12} = -\frac{81}{2048} r^4 (\alpha(u)^4 - 6\alpha(u)^2 \beta(u)^2 + \beta(u)^4),$$

$$B_{12} = -\frac{81}{512} r^4 \alpha(u)\beta(u)(\alpha(u)^2 - \beta(u)^2).$$

This gives

$$\alpha(u) = \beta(u) = 0.$$

Thus we have

$$A_{12} = B_{12} = ... = A_9 = B_9 = 0,$$

$$A_8 = -\frac{81 r(u)^4 \gamma(u)^4}{128},$$

which leads to

$$\gamma(u) = 0.$$

then, one can see all coefficients are vanished. Thus, the conclusion of the above case is: if $K = 1$ or -1 then $r(u) = r$ and $\tau(u) = k(u) = \alpha(u) = \beta(u) = \gamma(u) = 0.$ This implies that c is a point $c_0 \in R^3$.

IV. CONSTANT MEAN CURVATURE OF M

In this section, we will study the constancy of the mean curvature H of the surface generated by equiform motion which is locally parameterized by equation(9).

By a manner similar to the previous section 3, we put

$$H^2 = \frac{H_1^2(\cos nv, \sin iv)}{4W^3(\cos iv, \sin iv)}, \tag{17}$$

where

$$H_1 = g_{22}[X_1, X_2, X_{11}] - 2g_{12}[X_1, X_2, X_{12}] + g_{11}[X_1, X_2, X_{22}]. \tag{18}$$

According to (17), we discuss two cases.

4.1 Case *H*=0

Thus one can get

$$H_1^2 = \sum_{i=0}^{13} (A_n \cos iv + B_n \sin iv). \tag{19}$$

Since this is an expression of the independent trigonometric terms $\cos nv$ and $\sin nv$, all coefficients A_n, B_n must vanish identically.

Here, after some computations, the coefficients of the equation (19) are

$$A_{13} = 0,$$

$$B_{13} = \frac{9 r(u)^5 \tau(u)^3}{1024}.$$

In view of the expression of B_{13}, there is one possibility

$$\tau(u) = 0,$$

which leads to the following

$$A_{13} = B_{13} = \cdots = A_9 = B_9 = 0,$$

$$A_8 = \frac{27}{128} r(u)^2 (r(u)r'(u)\gamma'(u) + \gamma(u)(r'(u)^2 - r(u)r''(u))),$$

$$B_8 = \frac{2}{64} r(u)^4 (\gamma(u)k'(u) - k(u)\gamma'(u)).$$

By solving A_8 of $\gamma(u)$, we discuss two cases:

(I) $\gamma(u) = 0.$ This leads to all coefficients are vanished.

(II) $\gamma(u) = \frac{C_1 r'(u)}{r(u)} \neq 0$

$$A_8 = 0,$$

$$B_8 = \frac{2}{64} r(u)^4 (k(u)r'(u)^2 + r(u)(k'(u)r'(u) - k(u)r''(u))).$$

By solving B_8 , we have two cases:

(1) $r'(u) = 0$, this is contradiction.

(2) $k(u) = \frac{C_2 r'(u)}{r(u)}$, then, we have

$$B_8 = 0,$$

$$A_7 = -\frac{9}{64} C_1 r(u)(r'(u)(C_2\beta(u)r'(u) + 3r(u)\alpha'(u)) + \alpha(u)(r'(u)^2 - 3r(u)r''(u))).$$

By solving A_7 , we have two cases:

(a) $C_1 = 0$, this is contradiction.

(b) $\beta(u) = -\frac{1}{C_2 r'(u)^2}(3r(u)r'(u)\alpha'(u) + \alpha(u)(r'(u)^2 - 3r(u)r''(u))).$

Then,

$$A_7 = 0,$$

$$B_7 = -\frac{9C_1 r(u)}{64C_2 r'^2}(3r(u)r'(u)(-9r(u)r''(u)\alpha'(u) + 3r(u)r'(u)\alpha''(u) + 5r'(u)^2\alpha'(u)) +$$
$$\alpha(u)((C2^2 + 1)r'(u)^4 + 27r(u)^2 r''(u)^2 - 9r(u)^2 r^{(3)}(u)r'(u) - 15r(u)r'(u)^2 r''(u)))$$

$$A_6 = B_6 = 0,$$

$$A_5 = \frac{27}{8} C_1 r(u)^2 (-r'(u)\alpha'(u) + \alpha(u) r''(u)).$$

By solving A_5, we have $\alpha(u) = C_3 r'(u)$,

this leads to

$$B_7 = \frac{9C_1}{64C_2}(1+C_2^2) C_3 r(u) r'(u)^3.$$

From B_7 we discuss one possibilities, $C_3 = 0$, then,

$$B_7 = A_6 = B_6 = A_5 = B_5 = 0,$$

$$A_4 = \frac{9C_1}{8r(u)}(C_1^2 + (1+C_2^2) r(u)^2) r'(u)^3,$$

this leads to $r'(u) = 0$, this is contradiction.

From the previous results, we have the proof of the following theorem:

Theorem 4.1 *The surface foliated by equiform motion of astroid curve is a minimal surface if motions of astroid are in parallel planes.*

4.2 Case H^2=1

Thus one can get

$$0 = 4H^2 W^3 - H_1^2 = A_0 + \sum_{i=1}^{30} (A_n \cos iv + B_n \sin iv). \tag{20}$$

After some computations, we have

$$A_{30} = \frac{729}{134217728} r(u)^{12} \tau(u)^6.$$

$$B_{30} = 0$$

In view of the expression for A_{30}, there is one possibility

$$\tau(u) = 0.$$

Thus, we obtain

$$A_{30} = B_{30} = \cdots = A_{25} = B_{25} = 0,$$

$$A_{24} = -\frac{729}{2097152} r(u)^6 (64k(u)^6 r(u)^6 - 240k(u)^4 r(u)^4 r'(u)^2 + 60k(u)^2 r(u)^2 r'(u)^4 - r'(u)^6),$$

$$B_{24} = -\frac{729}{524288} r(u)^7 r'(u)(48k(u)^4 r(u)^4 - 40k(u)^2 r(u)^2 r'(u)^2 + 3r'(u)^4)$$

. By solving system A_{24}, B_{24}, This implies that $k(u) = 0,\ r(u) = r,$ which leads to the following

$$A_{24} = B_{24} = \cdots = A_{19} = B_{19} = 0,$$

$$A_{18} = -\frac{729}{32768} r(u)^6 (\alpha(u)^6 - 15\alpha(u)^4 \beta(u)^2 + 15\alpha(u)^2 \beta(u)^4 - \beta(u)^6),$$

In view of the expression of A_{18}, there are six possibilities

$\alpha(u) = \pm\beta(u)$, $\alpha(u) = \pm 2\beta(u) \pm \sqrt{3}\beta(u)$

(a) $\alpha(u) = -2\beta(u) - \sqrt{3}\beta(u)$. Thus we have

$$B_{18} = -\frac{729}{512}(26+15\sqrt{3}) r(u)^6 \beta(u)^6,$$

Therefore, $\beta(u) = 0,$

$$B_{18} = A_{17} = \cdots = A_{13} = B_{13} = 0,$$

$$A_{12} = \frac{729}{512} r(u)^6 \gamma(u)^6,$$

Solving A_{12} implies that $\gamma(u) = 0.$

As a consequence, we have the coefficients

$$A_{12} = B_{12} = \cdots = A_1 = B_1 = A_0 = 0.$$

By direct computation, one can see that all remaining possibilities of $\alpha(u)$ conclude the same results.

Remark 4.2 *The surface foliated by equiform motion of astroid curve has nonzero constant mean curvature* $H = 1$ *or* -1 *if* $r(u) = r$ *and* $\tau(u) = k(u) = \alpha(u) = \beta(u) = \gamma(u) = 0$ *which implies that c is a point* $c_0 \in R^3$.

V. GEODESIC CURVES ON M

In this section, we construct and obtain the necessary and sufficient conditions for a curve on the kinematic surface to be a geodesic $(K_g = 0)$. For this purpose, we recall the following definition:

Definition 5.1 *A curve* $\Gamma = \Gamma(u)$ *on* $M \in R^3$ *is a geodesic of M provided its acceleration* Γ'' *is always normal to M [15].*

Making use of the equation (10), the curve $\Gamma(u)$ can be expressed in the form

$$\Gamma(u) = X(u, f(u)), \quad .v = f(u). \tag{21}$$

Since the curve $\Gamma(u)$ is a regular curve on the surface M in E^3, not necessary parameterized by arc length, **N** is the unit normal vector field of the M, the geodesic curvature k_g is given by [16]

$$k_g = \frac{[N, \Gamma'(u), \Gamma''(u)]}{|\Gamma'(u)|^3}. \tag{22}$$

The above equation can be written in the following form

$$k_g |\Gamma'(u)|^3 = Q, \tag{23}$$

where $Q = [N, \Gamma'(u), \Gamma''(u)]$, then

$$0 = k_g \,|\,\Gamma'(u)\,|^3 - Q = A_0 + \sum_{i=1}^{12}(A_n \cos iv + B_n \sin iv). \tag{24}$$

Hence, after some computations, the coefficients of the equation (24) are given as

$$A_{12} = 0,$$

$$B_{12} = \frac{3}{2048} r(u)^4 \tau(u)^4 = 0,$$

which implies $\tau(u) = 0$.

Consequently,

$$A_{11} = B_{11} = A_{10} = B_{10} = A_9 = B_9 = 0,$$

$$\begin{aligned} A_8 = &-\frac{9}{128} r(u)(k(u)^3 r(u)^2 r'(u) + k(u)^2 r(u)^2(-11 f'(u)r'(u) + 4r(u) f''(u)) \\ &+ k(u)(-4r(u)^3 f'(u)k'(u) + 7r(u)^2 f'(u)^2 r'(u) + 2r'(u)^3 - r(u)r'(u)r''(u) \\ &+ r'(u)(3r(u)^2 f'(u)^3 - 2 f'(u)r'(u)^2 + r(u)(k'(u)r'(u) - r'(u) f''(u) + f'(u)r''(u)))) \end{aligned}$$

$$\begin{aligned} B_8 = &\frac{9}{64} r(u)^2 (k(u)^4 r(u)^2 - 3k(u)^3 r(u)^2 f'(u) + f'(u)r'(u)(r(u)k'(u) - 2 f'(u)r'(u)) \\ &- k(u)^2 (r(u)^2 f'(u)^2 - 2r'(u)^2 + r(u)r''(u)) + k(u)r(u)(3r(u) f'(u)^3 \\ &+ k'(u)r'(u) - 2r'(u) f''(u) + f'(u)r''(u))), \end{aligned}$$

This system of nonlinear ODEs is of the second order. Since the cases where this system can be explicitly integrated are rare, a numerical solution of the system is in general the only way to compute points on a geodesic. Thus, for simplicity, we consider the two cases

(I) **Case** $r(u) = r$ (constant) : We have

$$A_8 = \frac{9}{32} r^4 k(u)[- f'(u)k'(u) + k(u) f''(u)] = 0,$$

$$B_8 = \frac{9}{64} r^4 k(u)(k(u)^3 - 3k(u)^2 f'(u) - k(u) f'(u)^2 + 3 f'(u)^3) = 0.$$

This implies $k = \pm f'(u)$ or $k = 3 f'(u)$. Therefore, we consider the following cases

(a) $k = 3 f'(u)$: Then we have

$$A_8 = B_8 = A_7 = B_7 = A_6 = B_6 = 0,$$

$$A_5 = \frac{27}{8} r^3 f'(u)[(7\alpha(u) f'(u)^2 + f'(u)\beta'(u) - \beta(u) f''(u)] = 0\,,$$

$$B_5 = \frac{27}{8} r^3 f'(u)[7\beta(u) f'(u)^2 - f'(u)\alpha'(u) + \alpha(u) f''(u)] = 0\,,$$

$$\begin{aligned} A_4 = &-\frac{9}{8} r^2[-\alpha(u) f'(u)\alpha(u) - \beta(u) f'(u)\beta'(u) + \alpha(u)^2 f''(u) + \beta(u)^2 f''(u) \\ &+ 2\gamma(u)(f'(u)\gamma(u) + \gamma(u) f''(u))] = 0 \end{aligned}.$$

Similarly as solving A_8 and B_8 we consider $f'(u) = c$ where c is constant. Thus we have

$$A_5 = \frac{27}{8}c^2r^3(7c\alpha(u) + \beta'(u)) = 0,$$

$$B_5 = \frac{27}{8}c^2r^3(7c\beta(u) - \alpha'(u)) = 0.$$

Thus we obtain

$$\alpha(u) = c_1\cos(7cu) + c_2\sin(7cu),$$

$$\beta(u) = c_2\cos(7cu) - c_1\sin(7cu),$$

where c_1 , c_2 are constants.

From this we obtain

$$A_4 = 9/4cr^2\gamma(u)\gamma'(u) = 0,$$

$$A_4 = 9c^2r^2(-c_1^2 - c_2^2 + 9c^2r^2 + \gamma(u)^2) = 0.$$

This implies $\gamma(u) = \gamma(constant) = \sqrt{9c^2r^2 - c_1^2 - c_2^2}$. Therefore, we obtain

$$A_0 = (12cr(-c_1^2 - c_2^2 + 9c^2r^2)(c_2\cos(7cu - f(u)) - c_1\sin(7cu - f(u)))\sin(2f(u))).$$

This leads to $r = \frac{\sqrt{c_1^2 + c_2^2}}{3c}$, i.e., $\gamma = 0.$ Then

$$B_4 = A_3 = B_3 = A_2 = B_2 = A_1 = B_1 = A_0 = 0.$$

(b) $k = \pm f'(u)$, gives the same result as in case (a).

(II) **Case** $k(u) = k$ (constant): The same results as in (I) are obtained.

Now, we give the following theorem

Theorem 5.2 *The geodesic curves on the surface M have the following representations*

$\Gamma(u) = X(u, f(u))$,

M: $X(u,v) = c(u) + r(u)(\cos^3 v\ t(u) + sin^3 v\ n(u))$,

$c(u) = \{\xi_1 t(u) + \xi_2 n(u)\}$,

where $v = f(u) = cu + h$,

$$\xi_1 = \frac{1}{27c^3(-1+49c^2)}\big((1-49c^2) f\cos(u) - 9c^2(1+21c^2)b\cos(7cu) - e\sin(u) + 49c^2 e\sin(u) + 9c^2 a\sin(7cu) + 189c^4 a\sin(7cu)\ \big),$$

$$\xi_2 = \left(\frac{(-1+49c^2)e\cos(u) + 90c^3 a\cos(7cu) - f\sin(u) + 49c^2 f\sin(u) + 90c^3 b\sin(7cu)}{9c^2(-1+49c^2)}\right),$$

$t(u) = \{-Sin(3cu), Cos(3cu), 0\},$

$n(u) = \{-Cos(3cu), -Sin(3cu), 0\},$

a, b, c, f and h are constants.

VI. SW-SURFACE

In this section, we construct and obtain the necessary and sufficient conditions for a surface M to be a special Weingarten surface. For this purpose, we recall the following definition:

Definition 6.1 *A surface M in Euclidean 3-space* R^3 *is called a special Weingarten surface if there is relation between its Gaussian and mean curvatures such that* $U(K, H) = 0$*, and we abbreviate it by SW-surface [17].*

We can express this as the following condition:

$$aH + bK = c, \tag{25}$$

where a, b and c are constants and $a^2 + b^2 \neq 0$. We can rewrite The Gaussian and mean curvatures of a surface M as the following forms By using the equations (13) and (17),without loss of generality we can take $a = 1$, the condition (25), can be written in the following form

$$\frac{H_1}{2W^{3/2}} + b\frac{K_1}{W^2} = c, \tag{26}$$

or, equivalently

$$H_1 W^{1/2} = 2(cW^2 - bK_1). \tag{27}$$

Squaring both sides, we have

$$H_1^2 W - 4(cW^2 - bK_1)^2 = 0. \tag{28}$$

6.1 Case *c*=2

In this case, we discuss the equation (28) at $c = 0$, thus it become as a form

$$H_1^2 W - 4(bK_1)^2 = 0 \tag{29}$$

By using equation (14), (18) and a manner similar to the previous sections, we can express (29) as the form

$$\sum_{i=0}^{36}(A_n \cos(iv) + B_n \sin(iv)) = 0. \tag{30}$$

After some computations, the coefficients of equation (30) are

$$A_{36} = -\frac{729a^2 r(u)^{14} \tau(u)^8}{2147483648},$$

$$B_{36} = A_{35} = B_{35} = 0.$$

This gives us one possibility, $\tau(u) = 0.$ Then

$$A_{36} = B_{36} = ...B_{25} = 0,$$

$$A_{24} = \frac{6561a^2}{8388608} r(u)^6(-32k(u)^3 r(u)^6\gamma(u)k'(u)\gamma'(u) + 16k(u)^4 r(u)^6\gamma(u)^2 - 8k(u)r(u)^3\gamma(u)k'(u)r'(u)$$
$$(-3r(u)r'(u)\gamma'(u) - 2\gamma(u)(r'(u)^2 - r(u)r''(u))) + r'(u)^2(-4r(u)^4\gamma(u)^2k'(u)^2 + \gamma(u)^2 r'(u)^4$$
$$+ 2r(u)\gamma(u)r'(u)^2(r'(u)\gamma'(u) - \gamma(u)r''(u)) + r(u)^2(r'(u)\gamma'(u) - \gamma(u)r''(u))^2)$$
$$+ 4k(u)^2 r(u)^2(4r(u)^4\gamma(u)^2k'(u)^2 - \gamma(u)^2 r'(u)^4 + 2r(u)\gamma(u)r'(u)^2(-3r'(u)\gamma'(u)$$
$$+ \gamma(u)r''(u)) - r(u)^2(6r'(u)^2\gamma'(u)^2 - 6\gamma(u)r'(u)\gamma'(u)r''(u) + \gamma(u)^2 r''(u)^2))).$$

Here, we discuss two possibilities

(i) $\gamma(u) = 0$. Then, one can see that all coefficients are vanished.

(ii) $\gamma(u) = \dfrac{C_1\sqrt{4k(u)^2 r(u)^2 - 4k(u)r(u)r'(u) - r'(u)^2}}{r(u)} \neq 0$, then, we have

$$B_{24} = \frac{6561a^2C_1^2 r(u)^6(4k(u)^2 r(u)^2 + r'(u)^2)^2(k(u)r'(u)^2 + r(u)(k'(u)r'(u) - k(u)r''(u)))^2}{(1048576(4k(u)^2 r(u)^2 - 4k(u)r(u)r'(u) - r'(u)^2))},$$

also, this gives us two possibilities

(a) $(4k(u)^2 r(u)^2 + r'(u)^2) = 0$, i.e. $k(u) = 0,\ r'(u) = 0,$

this implies $\gamma(u) = 0$, this is contradiction.

(b) $k(u)r'(u)^2 + r(u)(k'(u)r'(u) - k(u)r''(u)) = 0.$

By solving above deferential equation we get $k(u) = \dfrac{C_2 r'(u)}{r(u)}$, then

$$A_{22} = -\frac{729a^2C_1^2(-1 - 4C_2 + 4C_2^2)}{2097152} r(u)^4 r'(u)^2(9r(u)^2 r'(u)^2((-1 + 4C_2^2)\alpha'(u)^2 + 8C_2\alpha'(u)\beta'(u)$$
$$+ (1 - 4C2^2)\beta'(u)^2) + 6r(u)\beta(u)r'(u)(r'(u)^2(C_2(3 + 4C_2^2)\alpha'(u) + \beta'(u)) + 3r(u)(-4C_2\alpha(u)$$
$$+ (-1 + 4C_2^2)\beta(u))r''(u)) - \alpha(u)^2((1 + 3C_2^2 + 4C_2^4)r'(u)^4 - 6r(u)r'(u)]^2 r''(u) + 9(1 - 4C_2^2)$$
$$r(u)^2 r''(u)^2) + \beta(u)^2((1 + 3C_2^2 + 4C2^4)r'(u)^4 - 6r(u)r'(u)^2 r''(u) + 9(1 - 4C_2^2)r(u)^2 r''(u)^2)$$
$$+ 2\alpha(u)(2C2\beta(u)(r'(u)^2 - 6r(u)r''(u))((1 + 2C_2^2)r'(u)^2 - 3r(u)r''(u)) - 3r(u)r'(u)(r'(u)^2(\alpha(u)$$
$$- C_2(3 + 4C_2^2)\beta'(u)) + 3r(u)((-1 + 4C_2^2)\alpha'(u) + 4C_2\beta'(u))r''(u)))).$$

The solution of this deferential equation is very difficult, thus $(-1 - 4C_2 + 4C_2^2) = 0$ i.e., $C_2 = \dfrac{1}{2} \pm \dfrac{1}{\sqrt{2}}$ or $r'(u) = 0$, in two cases $\gamma(u) = 0$, thus, this is contradiction.

This leads to the following theorem:

Theorem 6.2 *The kinematic surface generated by an equiform motion of astroid curve is a special Weingarten surface with condition* $H + bK = 0$ *if and only if motion of astroid is in parallel planes.*

6.2 Case $c \neq 0$

By the same way in above subsection, we can express(28) as the following form

$$\sum_{i=0}^{40}(A_n \cos(iv) + B_n \sin(iv)) = 0. \tag{31}$$

After some computations, the coefficients of equation (31) are

$$A_{40} = -\frac{6561c^2 r(u)^{16}\tau(u)^8}{137438953472}$$

$$B_{40} = A_{39} = B_{39} = 0.$$

This gives us one possibility $\tau(u) = 0$ Then

$$A_{32} = -\frac{6561c^2}{536870912} r(u)^8 (256k(u)^8 r(u)^8 - 1792k(u)^6 r(u)^6 r'(u)^2 + 1120k(u)^4 r(u)^4 r'(u)^4$$

$$-112k(u)^2 r(u)^2 r'(u)^6 + r'(u)^8),$$

$$B_{32} = -\frac{6561c^2}{33554432} k(u) r(u)^9 r'(u)(64k(u)^6 r(u)^6 - 112k(u)^4 r(u)^4 r'(u)^2 + 28k(u)^2 r(u)^2 r'(u)^4 - r'(u)^6),$$

By solving these two deferential equations, we obtained $r(u) = r(constant),\ \ k(u) = 0,$

$$A_{24} = -\frac{6561c^2}{2097152} r^8(\alpha(u)^8 - 28\alpha(u)^6\beta(u)^2 + 70\alpha(u)^4\beta(u)^4 - 28\alpha(u)^2\beta(u)^6 + \beta(u)^8),$$

$$B_{24} = \frac{6561c^2}{262144} r^8 \alpha(u)\beta(u)(\alpha(u)^6 - 7\alpha(u)^4\beta(u)^2 + 7\alpha(u)^2\beta(u)^4 - \beta(u)^6).$$

By solving these two equations, we obtained $\alpha(u) = 0,\ \ \beta(u) = 0,$ then

$$A_{16} = -\frac{6561c^2 r^8 \gamma(u)^8)}{8192}.$$

Thus, $\gamma(u) = 0$, and therefore, one can see all coefficients are vanished.

Remark 6.3 *The kinematic surface generated by an equiform motion of astroid curve is a special Weingarten surface with condition* $H + bK = c$ *if and only if it has nonzero constant Gaussian and mean curvatures.*

VII. EXAMPLES

In this section to illustrate our investigation, we give two examples:

Example 1 (zero Gaussian curvature) : Consider the circle Φ given by

$$\Phi(u) = \{cos(u), sin(u), 0\}.$$

Using (12), (10)and after some computations, we have

$$c(u) = \{-cos(6u), sin(6u), 0\}.$$

Therefore, the representation of the surface generated by the astroid curve is

$$X(u,v) = \{-cos(6u) - r(cos(u)cos(v)^3 + sin(u)sin(v)^3),$$

$$-r\,cos(v)^3\,sin(u) + sin(6u) + r\,cos(u)\,sin(v)^3, 0\}$$

Thus, Fig. 1 displays the surface with zero Gaussian curvature.

For geodesic curves on a surface, we give the following example:

Example 2 (zero geodesic curvature) : Consider the curve Φ given by

$$\Phi(u) = \{3c\cos(3cu), 3c\sin(3cu), 0\}.$$

After some computations, we have the representation of the surface generated by the astroid curve as

$$X(u,v) = \{\frac{1}{27c^3}(-\frac{9}{4}c^2\sqrt{a^2+b^2}(\sin(3cu-3v)+3\sin(3cu+v))-\sin(3cu)\zeta_1-3c\cos(3cu)\zeta_2),$$
$$\frac{1}{27c^3}(\frac{9}{4}c^2\sqrt{a^2+b^2}(\cos(3cu-3v)+3\cos(3cu+v))+\cos(3cu)\zeta_1-3c\sin(3cu)\zeta_2),0\}$$

$$\Gamma(u) = \{\frac{1}{27c^3}(-\frac{9}{4}c^2\sqrt{a^2+b^2}(3\sin(4cu+h)+\sin(3cu-3(cu+h)))-\sin(3cu)\zeta_1-3c\cos(3cu)\zeta_2),$$
$$\frac{1}{27c^3}(\frac{9}{4}c^2\sqrt{a^2+b^2}(3\cos(4cu+h)+\cos(3cu-3(cu+h)))+\cos(3cu)\zeta_1-3c\sin(3cu)\zeta_2),0\},$$

$$\zeta_1 = \frac{1}{49c^2-1}\left(189ac^4\sin(7cu)+9ac^2\sin(7cu)-9b\left(21c^2+1\right)c^2\cos(7cu)\right.$$
$$\left.+49c^2e\sin(u)+\left(f-49c^2f\right)\cos(u)-e\sin(u)\right),$$

$$\zeta_2 = \frac{\left(90ac^3\cos(7cu)+90bc^3\sin(7cu)+\left(49c^2-1\right)e\cos(u)+49c^2f\sin(u)-f\sin(u)\right)}{49c^2-1}.$$

The geodesic curves are shown in Figs. $(2-4)$.

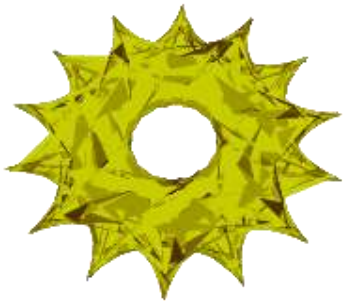

FIGURE 1: THE SURFACE M WITH ZERO GAUSSIAN CURVATURE AT $r = 5$.

FIGURE 2: THE GEODESIC CURVE $\Gamma(u)$ **ON THE SURFACE M AT** $a = b = c = e = f = h = 1$.

FIGURE 3: THE GEODESIC CURVE $\Gamma(u)$ **ON THE SURFACE M AT** $a = b = c = e = f = h = 0.1$.

FIGURE 4: THE GEODESIC CURVE $\Gamma(u)$ **ON THE SURFACE M AT** $a = b = e = f = h = 0.1$, $c = 0.135$.

VIII. CONCLUSION

In this study, a kinematic surface generated by an equiform motion of astroid curve is considered. Constant Gaussian and mean curvatures of such surface are established. Therefore, the surface foliated by equiform motion of astroid curve has a constant Gaussian and mean curvatures if motion of astroid is in parallel planes. Moreover, the necessary and sufficient

conditions for a curve on the kinematic surface M to be a geodesic are given. Using a new technique which is different from that in our papers [18, 19, 20], for SW-surface and it is introduced from a different angle and aspect of [17]. Finally, some examples are given. The field is developing rapidly, and there are a lot of problems to be solved and more work is needed to establish different results of new kinematic surfaces.

ACKNOWLEDGEMENTS

We wish to express our profound thanks and appreciation to professor, Dr.Nassar H. Abdel All, Department of Mathematics, Assiut University, Egypt, for his strong support, continuous encouragement, revising this paper carefully and for his helpful suggestions. We would like also to thank Dr. Fathi M. Hamdoon, Department of Mathematics, Faculty of Science, Al-Azhar University, Assuit branch, Egypt, for his critical reading of this manuscript, helpful suggestions and making several useful remarks.

REFERENCES

[1] F. M. Hamdoon, Ph. D. Thesis, Math. Dept., Faculty Sci, Assiut University (2004).

[2] R. L o' pez, Cyclic surfaces of constant Gauss curvature, Houston Journal of Math., Vol 1. 27, No. 4 (2001), 799-805.

[3] F. M. Hamdoon, Ahmed T. Ali, Constant scalar curvature of the three dimensional surface obtained by the equiform motion of a sphere, International Electronic Jornal of Geometry, Vol 6, No 1, PP: 68-78 (2013).

[4] B. Riemann, $\ddot{U}$ ber die Fl$\ddot{a}$chen vom kleinsten Inhalt bei gegebener Begrenzung, Abh. K$\ddot{o}$nigl. Ges. d. Wissensch. G$\ddot{o}$ttingen, Mathema. Cl. 13, PP: 329-333 (1868).

[5] A. Enneper, Die cyclischen Flächen,Z. Math.. Phys. 14 (1869), 393-421.

[6] J.C.C. Nitsche, Cyclic surfaces of constant mean curvature, Nachr. Akad. Wiss. Gottingen Math. Phys, II $1\,(1989),\ 1-5.$

[7] C. Delaunay, Sur la surface de revolution dont la courbure moyenne est constant, J. Math. Pure Appl. 6, PP: 309-320, (1841).

[8] A. Gfrerrer, J. Lang, Equiform bundle motions in E^3 with spherical trajectories I, Contributions to Algebra and Geometry, Vol. 39 No. 2, PP: 307-316, (1998)..

[9] A. Gfrerrer, J. Lang, Equiform bundle motions in E^3 with spherical trajectories II, Contributions to Algebra and Geometry, Vol. 39, No. 2, PP: 317-328, (1998).

[10] A. Karger, Similarity motions in E^3 with plane trajectories, Aplikace Math., 26, PP: 194-201, (1981)..

[11] A. Caylay, On the cyclide, The collected mathematical papers of Arther Cayley, Vol. IX, Cambridge Univ. Press, Cambridge PP: 64-78, (1896).

[12] V. Chandru, D. Dutta and C. Hoffmann, On the geometry of Dupin cyclide, Visual Computer 5 PP: 277-290, (1989).

[13] R. L o' pez, Cyclic hypersurfaces of constant curvature, Advanced Studies in Pure Mathematics, 34 PP: 185-199, (2002).

[14] N. H. Abdel-All, Areej A Al-Moneef, Local study of singularities on an equiform motion, Studies in Mathematical Sciences, Vol. 5, No. 2 (2012), $26-36.$

[15] B. O Neill, Elementary Differential Geometry, Academic Press Inc, New York (2006).

[16] N. H. Abdel-All, Differential Geometry, El-Rushd Publishers, KSA (2008).

[17] R. López, Special Weingarten surfaces foliated by circles, Monatsh Math 154, PP: 289-302, (2008).

[18] R. A. Abdel-Baky, H. N. Abd-Ellah, Ruled W-surfaces in Minkowski 3-space R_1^3 Arch. Math., Tomus 44 (2008), 251-263.

[19] R. A. Abdel-Baky, H. N. Abd-Ellah, Tubular surfaces in Minkowski 3-space, J. Adv. Math. Stud. Vol. 7, No. 2 (2014), 1-7.

[20] H. N. Abd-Ellah, Translation L/W-surfaces in Euclidean 3-space E^3, In Press, J. Egyptian Math. Soc. (2015).

AD Publications
Sector-3, MP Nagar, Bikaner,
Rajasthan, India
www.adpublications.org, info@adpublications.org